More than skin deep: Utilising an ATG16L1 mouse model to study skin homeostasis and pigmentation dynamics

---

Shannon Colleen Conway

A thesis submitted to the University of East Anglia in accordance with the requirements for the degree of Doctor of Philosophy (Ph.D.)

University of East Anglia
School of Chemistry, Pharmacy & Pharmacology
2024

Abstract

The skin, comprising the epidermis, dermis, and hypodermis, serves as a barrier against environmental and biological threats. This barrier function relies on the layered structure and constant turnover of the epidermis. Within the epidermis, melanocytes and keratinocytes are crucial for photoprotection and barrier integrity, respectively.

Autophagy is a highly conserved self-eating process that is initiated in response to nutrient starvation, delivering damaged intracellular proteins and organelles to lysosomes for degradation. It is essential for skin barrier function, melanogenesis, and melanosome processing. LC3-associated phagocytosis (LAP) is a related process that utilises some autophagy components, conjugating LC3 to single-membraned phagosomes. LAP plays a role in the innate immune response, protecting tissue from pathogens and aiding in tissue homeostasis. Its versatile capability to engulf diverse cargoes, spanning from fungi and viruses to apoptotic cells, emphasises its significance in cellular physiology. So far, the relationship between skin homeostasis, pigmentation, and LAP remains unclear.

To examine this relationship, I utilised the ATG16L1$^{\Delta WD}$ mouse model (ΔWD), which harbours a mutated WD domain in *ATG16L1*, rendering it LAP-deficient but autophagy-competent. This study aimed to evaluate the role of LAP in skin homeostasis and determine if LAP-defective mice (ΔWD) exhibit a cutaneous phenotype. Additionally, it investigated the involvement of LAP in melanosome trafficking and processing in primary cultures of mouse skin keratinocytes.

Findings revealed that ΔWD mice exhibit no signs of impaired barrier function, yet aged ΔWD mice demonstrated an accelerated decline in biomechanical properties compared to littermate controls. Assessment of the melanosome dynamics in ΔWD primary keratinocyte cultures indicated that melanosomes are internalised and trafficked to the supranuclear region in keratinocytes and subsequently stored in lysosomal compartments, surrounded by LC3. This suggests that melanosomes are processed in keratinocytes in an autophagy-driven manner, with melanin later stored in the lysosome for long-term storage.

The work presented here offers a comprehensive description of the cutaneous phenotype of the ΔWD mouse model and offers a unique *in vitro* system for studying pigmentation dynamics in an autophagy-competent, but LAP-deficient environment.

Access Condition and Agreement

Each deposit in UEA Digital Repository is protected by copyright and other intellectual property rights, and duplication or sale of all or part of any of the Data Collections is not permitted, except that material may be duplicated by you for your research use or for educational purposes in electronic or print form. You must obtain permission from the copyright holder, usually the author, for any other use. Exceptions only apply where a deposit may be explicitly provided under a stated licence, such as a Creative Commons licence or Open Government licence.

Electronic or print copies may not be offered, whether for sale or otherwise to anyone, unless explicitly stated under a Creative Commons or Open Government license. Unauthorised reproduction, editing or reformatting for resale purposes is explicitly prohibited (except where approved by the copyright holder themselves) and UEA reserves the right to take immediate ‘take down’ action on behalf of the copyright and/or rights holder if this Access condition of the UEA Digital Repository is breached. Any material in this database has been supplied on the understanding that it is copyright material and that no quotation from the material may be published without proper acknowledgement.

Declaration

The research within this thesis was designed and conducted by the author under the guidance of the primary supervisors Dr Chris Morris and Dr Derek Warren and secondary supervisor Professor Thomas Wileman. The author was at no time registered for any other university award, degree, or qualification during the registration for the degree of Doctor of Philosophy. All experiments were conducted between the laboratories of Dr Derek Warren and Professor Thomas Wileman at the Biomedical Research Centre, between October 2020 and December 2023. The research was funded by the internal Science Faculty PhD Programme.

Word Count: 51,691 *Shannon Colleen Conway*

Dedication

I dedicate this thesis to my two wonderful Grandas, Sean McGeown (1938-2004) and Hugh Conway (1935-2022). Granda Sean, though our time together was brief, I am grateful for every moment we shared. Granda Hugh, thank you for always believing in me and being my biggest supporter. I will forever cherish our memories. You are both always in our hearts and prayers. Lots of Love, Shannon xx.

Table of Contents

Abbreviations

α-MSH – alpha-melanocyte-stimulating hormone

A.U – Arbitrary units

AMP – Adenosine monophosphate

AMPK – Adenosine monophosphate activated protein kinase

ATG – Autophagy-related genes

BM – Basement membrane

BMP – Bone morphogenetic proteins

BPE – Bovine pituitary extract

Ca^{2+} - Calcium

cAMP – cyclic adenosine monophosphate

CCD - Coiled-coil domain

CD63 – Tetraspanin cell surface antigen

CE – Cornified envelope

CER – Ceramide

CHOL – Cholesterol

CRE – cAMP response element

CREB – CRE-binding protein

DAPI – 4’,6 – diamidino-2-phenylindole

DC – Dermal condensate

DCT – Dopachrome tautomerase

Dermal DC – Dermal Dendritic Cell

DETC – Dendritic epidermal T cell

Dkk1 – Dickkopf 1

DMEM – Dulbecco’s Modified Eagle Media

DP – Dermal papilla

DSC – Desmocollin

DSG – Desmoglein

dWAT – Dermal white adipose tissue

E. – Embryonic day

ECM – Extracellular matrix

EEA1 – Early endosome antigen 1

EGF – Epidermal growth factor

ER – Endoplasmic reticulum

EtBr – Ethidium Bromide

EVPL – Envoplakin

FBS – Foetal bovine serum

FFA – Free Fatty Acid

FGF – Fibroblast growth factors

FGFR – Fibroblast growth factor receptor

H&E – Haematoxylin & Eosin

HiCa – High Calcium

ICC - Immunocytochemistry

IHC – Immunohistochemistry

ILC – Innate Lymphoid Cell

INV – Involucrin

IRS – Inner root sheath

KBM – Keratinocyte basal medium

KGFR – Keratinocyte growth factor receptor

KO – Knock out

LAMP1 – Lysosomal-associated membrane protein 1

LAP – LC3-associated phagocytosis

LB – Lamellar body

LC – Langerhans cells

LC3 – Microtubule-associated protein 1 light chain 3

LoCa – Low Calcium

LOR – Loricin

MC1R – Melanocortin 1 receptor

MC – Mast cell

MEF – Mouse embryonic fibroblast

MEK – Murine epidermal keratinocytes

MITF – Microphthalmia-associated transcription factor

MMP – Matrix Metalloproteinase

mTORC1 – Mammalian target of rapamycin complex 1

NADPH – Nicotinamide adenine dinucleotide phosphate

NBF – Neutral Buffered Formalin

NFW – Nuclease free water

NSB – Non-specific binding

OA1 – Ocular albinism type 1

P/S – Penicillin/Streptomycin

PAMP – Pathogen-associated molecular pattern

PAR – Protease-activated receptor

PBS – Phosphate Buffered Saline

PC – Pearson’s coefficient

PCM – Panniculus Carnosus muscle

PCNA – Proliferating cell nuclear antigen

PCR – Polymerase Chain Reaction

PE – Phosphatidylethanolamine

PFA – Paraformaldehyde

PI3K – class III phosphatidylinositol-3-kinase

PI3P – Phosphatidylinositol-3-phosphate

PKA – Protein kinase A

PMEL – pre-melanosome protein

POMC - Proopiomelanocortin

PPL – Periplakin

PtdSer – Phosphatidylserine

PVDF – Polyvinylidene difluoride

ROI – Region of interest

ROS – Reactive oxygen species

RUBCN – Rubicon

SCID – Severe combined immunodeficiency

SE – Standard Error

SEM – Scanning Electron Microscopy

SF – Sodium Fluorescein

SIK – Salt-inducible kinase

SPR – Small proline-rich protein family

TA – Transient amplifying

TB – Toluidine Blue

TBS – Tris-Buffered Saline

TE – Tris-EDTA

TGase – Transglutaminase

TLR – Toll-like receptors

TYR – Tyrosinase

TYRP – Tyrosinase-related protein

ULK1 – Unc-52-like autophagy-activating kinase

UV - Ultraviolet

UVRAG – UV radiation resistance-associated gene protein

WB – Western Blot

List of Figures

List of Tables

Acknowledgements

Wow! What a journey this has been, but it would not have been possible without the support and encouragement given by so many in my life. I cannot express in enough words how appreciative and thankful I am to every one of you for helping me along this journey. Thank you to the Science Faculty at the University of East Anglia for funding this research project and giving me a chance to do a PhD.

First and foremost, I would like to extend my heartfelt gratitude and appreciation to my primary supervisor, Dr Chris Morris, for his invaluable mentorship, guidance, and encouragement. He has been a pillar of support throughout this PhD, and I would sincerely like to thank him for being so caring and understanding, when times were tough. Moreover, despite his relocation to UCL, he remained dedicated and committed to this PhD project, and never failed to meet me for in person meetings on campus. Thank you so much for your continued support and countless BIO loading bay drop offs, I am forever grateful for all the opportunities and everything you have done for me.

I would like to express my sincere gratitude to Professor Tom Wileman and the entire Wileman lab, particularly Sophia, for the tremendous help and support I have received over the past three years. Working on this unique mouse model has been an absolute pleasure, and I am grateful for all the valuable advice you have shared with me throughout this journey. Thank you, Tom, and Chris, for giving me the opportunity to be a part of your teams. I will always be thankful for this experience.

Dr Derek Warren, I want to extend my heartfelt gratitude to you for welcoming me into the Warren lab with open arms during my second year. Your mentorship has been invaluable, and I am so appreciative for everything you have done for me. Thank you for your caring and supportive nature, especially during times when I needed it the most. Working with you has been an absolute pleasure, and I will fondly remember the crazy bus rides home after a fun night at the pub.

I would like to extend a special thank you to Dr Matthew Jefferson, for all his help and guidance with the $ATG16L1^{\Delta WD}$ mouse model. Despite him always saying I do not do much, none of this work would have been possible without the countless hours he spends upstairs in the DMU. Thank you for all your support, and most importantly your friendship, I honestly would have been lost without you.

Dr James McColl, I wanted to express my heartfelt gratitude for your invaluable guidance and support over the past year. It has been an absolute pleasure collaborating with you. Your advice and guidance have been incredibly enlightening, and I am forever thankful for your generosity in sharing your time and expertise with me.

I would also like to thank the Morris lab, past and present, for all the support and technical advice they have given me throughout this journey. Randa, Hassan, and Summer, this could not have been possible without you!

I would like to thank Dr Nicole Ball, Dr Darrell Green and Dr Isabelle Piec for their help and advice with the Cobas Calcium analysis. A special thank you to Darrell for making me an honorary member of the Green lab and inviting me to BCRT charity events and letting me feature in BBC interviews! Thank you for our friendship over the last 3 years!

Thank you to the technical team of the BMRC, especially Andy Loveday and Glen Mitchell. The work could not have been done without your help and keeping the place up and running. A special thank you to Glen, for his catch ups, especially when I was feeling homesick. Your hugs have meant so much to me, and I will forever remember your kind nature.

I am so grateful I got to share the countless hours at the lab bench with two of my closest friends, Emma Bull, and Paul Lonsdale. I do not believe you both truly understand how much I have cherished the support and friendship you have provided me over the past four years. I consider myself incredibly fortunate to have shared this journey with both of you.

An incredibly special thank you goes out to Lisa, Adam, and Abdul at Crown Place. They have watched my journey since the day I started in the Morris lab. They are and have been my extended Norwich family, and I am so grateful for their support and care over the years. Especially Lisa, what a wonderful person she is. Thank you for everything you do and continue to do for me.

Jaz, Frazer, and Charlotte thank you for your tremendous support, encouragement, and weekends away at the seaside. Your help has been invaluable in getting me through my writing and the final stages of my PhD. I couldn't have asked for better friends to support me along the way. I can't thank you enough for everything you have done for me.

I have lived in Norwich for nine years now and have had the privilege of getting to know some remarkable people here. I would like to express a very special thank you to the Nichols/McGhee family. They have welcomed me with open arms into their family and have made my experience in Norwich so much more enjoyable. Steph and David, your care and support have meant the world to me. I appreciate and love you both so much.

Caolan, Elisabeth, and Connor, thank you from the bottom of my heart for all the care packages, Connor videos, love, and support. Connor, I love you so much, you have brought so much joy to my life, which has helped me throughout this difficult journey. Caolan and Elisabeth, you have both encouraged me to keep going and never give up on what you are passionate about. Caolan, as my big brother, I admire and look up to you immensely. Thank you for being an incredible role model and for your continued support. Ech hun Ierch all ganz vill gäer, merci fir alles!

An incredibly special thank you to my wee nephew Rían for all his love, cuddles, and support, you mean the world to me. Granny Ann and Granny Maureen, thank you both for always believing in me and keeping me company. I appreciate you both so much, and I could not have done it without you. Love you both so much!

Mommy and Daddy, I am filled with profound gratitude for your enduring love and support. This has kept me going, while living away from home and facing the most challenging experience of my life. I cannot thank you enough for everything you have done and continue to do for me daily. This PhD could not have been possible without your guidance, support and Sunday facetimes. Reflecting on 2015, when I made the decision to move to Norwich and pursue my studies at UEA; I am reminded of your unwavering support. Your encouragement allowed me to pursue my passion for scientific research, for which I am eternally grateful. I extend my heartfelt gratitude to you both and appreciate and love you both immensely.

Last, but certainly not least, Matthew. I want to express my heartfelt appreciation for the love, laughter, and support you have shown me over the past eight years. You have been my rock, and I am deeply grateful for our time together in Norwich. Your unwavering love and support have meant everything to me, guiding me through both the good times and the challenges. I cannot thank you enough for being by my side through it all. I love you deeply, and I am immensely grateful to you.

Awards and Publications

Publications containing work from this thesis

Results from Chapter 3 and Chapter 4 are included in this publication. Conway et al. 2024 has been stated in the legends representing figures from this publication.

Conway, S., Jefferson, M., Warren, DT., Wileman, T., Morris, CJ., The WD domain of Atg16l1 crucial for LC3-associated phagocytosis is not required for preserving skin barrier function in mice, *JID Innovations* (2024), doi: https://doi.org/10.1016/j.xjidi.2024.100283.

Awards during this project

- **Winner Poster Prize May 2022** – Molecular & Tissue Pharmacology School of Pharmacy Symposium
- **Winner Poster Prize June 2023** – Molecular & Tissue Pharmacology School of Pharmacy Symposium

Poster/Oral presentations containing work from this thesis

- Poster Presentation School of Pharmacy Symposium May 2022
- PHA Research Seminar November 2022
- Poster Presentation School of Pharmacy Symposium June 2023
- Poster Presentation at Autophagy UK Network June 2023
- Cell, Development & Molecular Biology Seminar Invited Speaker May 2024

Chapter 1: General Introduction

1. Introduction

1.1 The functional anatomy of the mammalian skin

The skin is the largest and most intricate organ that forms the first protective barrier of all mammals (Zomer and Trentin, 2018). It is persistently challenged by a wide variety of external factors, which make it highly susceptible to trauma. The skin consists of specialised layers that are fundamental for its protective function. These layers include an innermost hypodermis, dermis, and outermost epidermis (Figure 1.1) (Ali et al., 2015; Alonso and Fuchs, 2003; Watt and Fujiwara, 2011). The epidermis, a stratified epithelium, mainly consists of keratinocytes, along with melanocytes, Langerhans, and Merkel cells. Together, these cells form the chemical, physical and microbial barrier, responsible for regulating water loss and thermoregulation (Zingkou et al., 2022). The connective tissue of the dermis is formed by fibroblasts along with an extracellular matrix, abundant in collagen and elastic fibres (Dellambra et al., 2019). Moreover, blood and lymphatic vessels, as well as sebaceous glands, sweat glands, hair follicles and nerve endings invaginate the dermis from the epidermis (Dellambra et al., 2019). Found beneath the dermal layer, lies the hypodermis, responsible for producing cytokines and growth factors and serving as the insulating and shock absorbing barrier (Jin et al., 2022; Nguyen and Soulika, 2019).

The mouse (*Mus musculus*) is widely employed as a mammalian model organism to address questions relating to human health (Chen and Roop, 2008). They are readily available, easily maintained and handled, and experience rapid reproducibility, whilst being economical (Bedell et al., 1997; Wong et al., 2011). In many respects, the mouse skin shares several similarities with human skin, making mouse models a convenient tool to study skin diseases (Figure 1.1) (Chen and Roop, 2008). The mouse genome has been sequenced for several commonly used laboratory mouse strains, with around 99% of mouse genes having a corresponding human homolog (Chinwalla et al., 2002). This underscores the relevance of the mouse model as an invaluable tool for studying skin biology. So far, there are more than 5000 mouse genotypes that model around 1000 human diseases, including many inherited human skin diseases, such as skin cancer and inflammatory skin disorders (Liakath-Ali et al., 2014; Salgado et al., 2017).

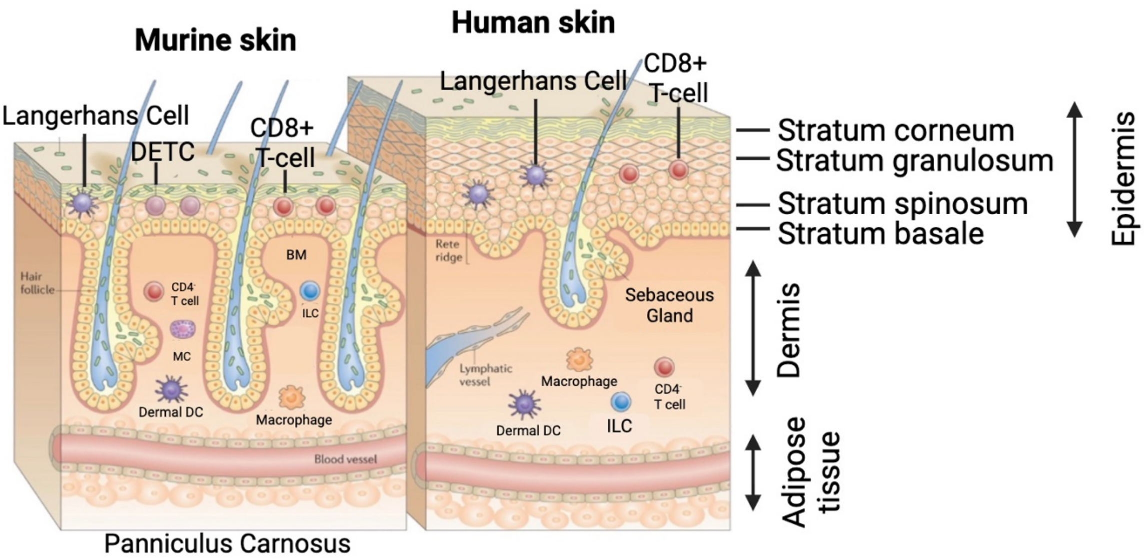

Figure 1.1 Anatomy of the mouse and human skin. Schematic representation of the overview of murine skin and human skin. BM: Basement membrane; Dermal DC: Dendritic cell; MC: Mast cell; ILC: Innate lymphoid cell; DETC: Dendritic epidermal T cell. Figure adapted from Pasparakis et al. (2014). Figure created in BioRender.com.

Despite its genetic similarities, mouse skin also exhibits striking differences such as the human epidermis being much thicker (i.e., > 50 μm) than the murine epidermis (i.e., < 25 μm), with generally more cell layers (Pasparakis et al., 2014). Human epidermal skin exhibits around 6-10 keratinocyte layers, while mouse epidermis constitutes only 3 keratinocyte layers (Gudjonsson et al., 2007). Moreover, mouse skin is densely packed with hair follicles, whereas human skin has a greater area of interfollicular skin, covered sparsely by hair follicles (Liu et al., 2021). Epidermal renewal and hair cycle in mouse skin is around 8-10 days, while in human skin epidermal renewal lasts around 26-28 days (Dellambra et al., 2019). Moreover, melanocytes in human skin are distributed in the hair follicles and epidermal basal layer, while in mice they are mainly confined to the hair follicle (Dellambra et al., 2019). The dermis is thicker in humans than in mice and is characterised by downward projections of epidermal rete ridges, which also contribute to the re-epithelisation of the skin (Liu et al., 2021). Nevertheless, the mouse skin remains a very valuable tool to investigate many areas of biomedical research, due to its substantial similarities with human physiology and pathology. Next, it is critical to explore the individual skin layers in a greater depth, starting with the innermost hypodermal dermal.

1.1.1 The hypodermis

The innermost layer of the skin, also known as the subcutaneous fat layer or dermal white adipose tissue (dWAT), is predominantly composed of adipose tissue, loose fibrous connective tissue, and larger blood vessels (Calabro et al., 2011; Wong et al., 2016). Moreover, various immune cells are also found within the hypodermal layer, which include fibroblasts and macrophages (Wong et al., 2016). The hypodermis fulfils numerous essential functions including thermoregulation, protection, hair follicle cycling and wound healing (Alexander et al., 2015).

1.1.2 The dermis

Above the subcutaneous fat layer lies the dermal matrix, which is characterised by an intricate arrangement of collagen fibres interlaced with elastin fibres, proteoglycans, and fibronectin (Wong et al., 2007). Dermal fibrils primarily consist of type I collagen, supplemented by other collagen types, such as collagen III (Breitkreutz et al., 2013; Lynch et al., 2017). Contained within the collagenous network reside fibroblasts, mast cells and other transiently migratory cells that have pivotal roles in proliferation and migration, as well as paracrine and autocrine signalling (Ghetti et al., 2018; Wong et al., 2007). Fibroblasts are responsible for maintaining the structural integrity of the connective tissue by secreting precursors of the ECM, including collagens, fibronectin, elastins, laminins, proteoglycans and integrins (Ghetti et al., 2018). Additionally, mast cells originating from the bone marrow, exert immunoregulatory functions (Harvima and Nilsson, 2011). The dermis can be classified into the papillary and reticular dermis, with the papillary dermis representing a thinner area of the dermis and being interconnected to the epidermis (Salazar et al., 2023). The papillary dermis exhibits a loose connective tissue and high cell density, allowing blood vessels to nourish the epidermis and Schwann cells to project their dendrites into the upper epidermis enabling sensation (Korosec et al., 2019). Conversely, the reticular dermis is composed of a dense distribution of collagens and other connective tissue proteins, allowing the skin to undergo stretching and resilience, by resisting deformation forces (Korosec et al., 2019). These mechanical and structural properties, such as skin layer thickness and elasticity, adjust with age and between anatomical locations (Wang et al., 2013).

Together, the dermis and the skin appendages (including the sebaceous glands, hair follicles and excretory glands) provide the skin with mechanical and tensile strength, as well as thermoregulation (Salazar et al., 2023). Moreover, the extensive vasculature in the dermis is responsible for thermoregulation, and delivery of oxygen and nutrients whilst removing toxins and waste products (Weng et al., 2020).

1.1.3 The dermal-epidermal junction & basement membrane

The boundary between the dermal and epidermal compartment is formed by a thin layer of highly organised ECM proteins that form the dermal-epidermal junction (DEJ) (Rousselle et al., 2022). This ECM is categorised as a supramolecular matrix arrangement that is termed the basement membrane (BM), anchoring the epidermal layer to the papillary dermis (Breitkreutz et al., 2013). The BM is primarily composed of type IV collagen, nidogen, proteoglycans, laminin, calcium-dependent integrins and glycosaminoglycans

(Brohem et al., 2011). Collagen IV is largely responsible for the mechanical properties of the BM (Rousselle et al., 2022). The BM is responsible for the bidirectional trafficking of bioactive molecules and binds to a plethora of growth factors and cytokines, ensuring a stable reservoir for controlled release during repair processes and physiological remodelling (Brohem et al., 2011). Collagen XVII, $\alpha 6\beta 4$ integrin and laminin isoform 332 act as the anchoring filaments, also known as the hemidesmosomes, which span the entire BM and are responsible for attaching the basal keratinocytes to the BM, ensuring a reinforced cohesion (Rousselle et al., 2022). Collagen VII aims to anchor the upper papillary dermis to the BM (Lohi, 2001; Rousselle et al., 2022).

Skin diseases have been associated with defects in collagen XVII and VII, with mutations affecting collagen XVII and VII causing epidermolysis bullosa (Gatseva et al., 2019). The absence of collagen VII and XVII in the ECM matrix affects the anchoring fibrils, resulting in a weakened BM and blistering (Nishimura et al., 2015).

1.1.4 The epidermis

The interfollicular epidermis can be subdivided into several layers, including the stratum basale, stratum spinosum, stratum granulosum and stratum corneum (Figure 1.1) (Zingkou et al., 2022). Each layer is formed predominantly by keratinocytes, with proliferating and less differentiated keratinocytes found in the basal layer, while terminally differentiated keratinocytes are found in the suprabasal layers. There are two other important cell types in the epidermis, which include the melanocytes and Langerhans cells (Wickett and Visscher, 2006). Melanocytes are the pigment-producing cells of the skin and hair in mammals, while the Langerhans cells are the dendritic antigen-presenting cells of the skin. Together, these cells exert many functions that include adhesion of the epidermis to the underlying BM, replenishing the cells that shed through terminal differentiation and desquamation, and providing the immune barrier to the epidermis (Forni et al., 2012). To fulfil these functions the cells must maintain a stringent balance between proliferation and quiescence, which begins during embryonic development.

1.2 The epidermis- An overview of epidermal and hair follicle development

1.2.1 Embryonic origins of the murine epidermis

Following gastrulation, the embryo surface arises as a single layer of neuroectoderm, destined to give rise to both the nervous system and the skin epithelium (Fuchs, 2007). The pivotal factor for this decision is Wnt signalling, which inhibits the ectoderm's responsiveness to the fibroblast growth factors (FGF). Consequently, in the absence of FGF signalling, the cells initiate the expression of bone morphogenetic proteins (BMPs), thus committing to epidermal fate. The embryonic epidermis that arises is formed of a single layer of multipotent epithelial cells that undergo stratification to give rise to a functional barrier at birth (Fuchs, 2007; Sotiropoulou and Blanpain, 2012). In mice, the surface ectoderm is loosely integrated into the basal lamina, which begins at embryonic day 8.5 (E8.5) (Figure 1.2) (Forni et al., 2012). The periderm acts as the early epidermal barrier, protecting the developing skin from the amniotic fluid. During the early stages of stratification, which typically occur between E12.5 to E15.5 in mice, cell proliferation is primarily localised to the basal layer, with differentiated keratinocytes found in the spinous layer, denoted by their keratin 1 immunoreactivity (Figure 1.2) (Bazzi et al., 2007). The main structural proteins found within the basal keratinocytes are keratins 5 and 14, which are known to be found in cells displaying proliferative potential (Figure 1.2) (Fuchs and Green, 1980). Keratin 1 expression is governed by Notch signalling that directs spinous cells to continue to differentiate, mature and migrate towards the cornified layer (Hu et al., 2018). Concurrently, the skin appendages, such as hair and sweat glands arise from the embryonic ectoderm (O'Shaughnessy and Christiano, 2004). At E15.5, the granular layer keratinocytes arise from the differentiating keratinocytes of the spinous layer and begin to express the cornified envelop precursor protein loricrin (Figure 1.2) (Bazzi et al., 2007). These stages are primarily governed by the increases in extracellular Ca^{2+} concentrations (Hu et al., 2018). By E18.5, the epidermis is fully mature and the periderm, serving as the initial protective layer, is shed; thus, establishing the first line of defence for the mouse (Jacob et al., 2023).

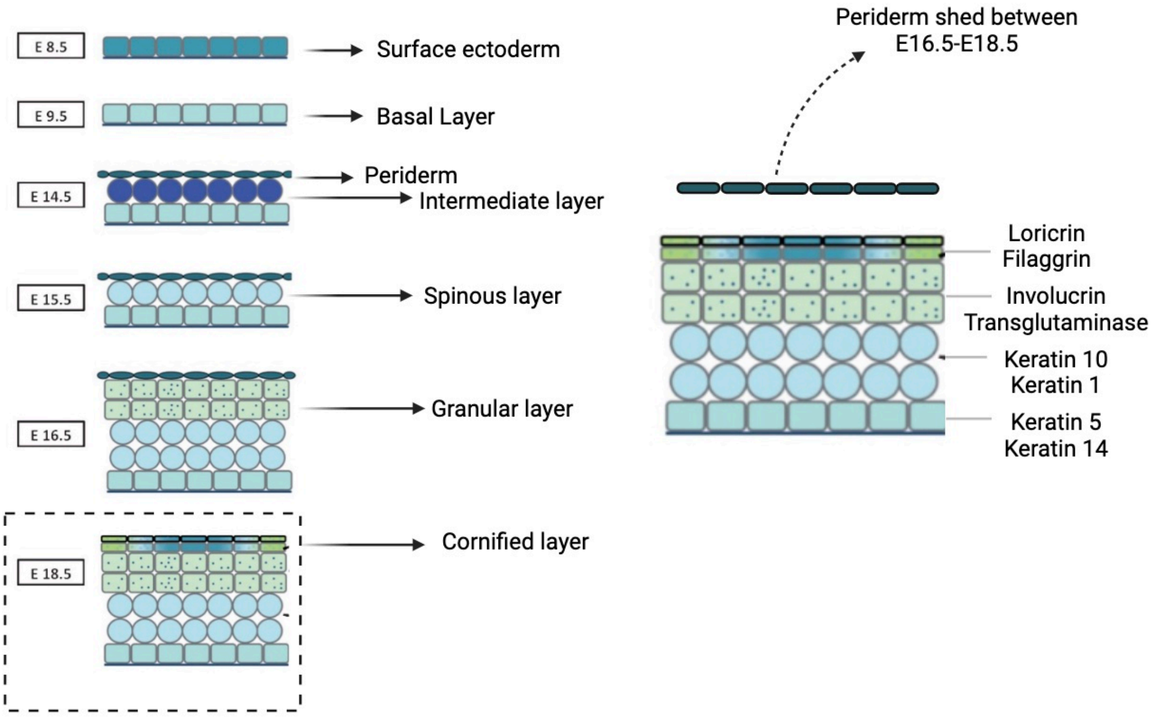

Figure 1.2 Timeline representing the formation of the epidermis during embryonic development. The stratification of the epidermis begins at E8.5 with a single layer of ectoderm. The development of the mouse epidermis from the ectoderm begins at E9.5, with the formation of a single basal layer of epidermal cells that are overlayed by a structure known as the periderm. From E13.5 onwards the single layer of epidermal cells, known as keratinocytes, develop into a stratified epithelium. A complete barrier is formed before birth at E16.5-E17, when the periderm is shed. The fully stratified epidermis is complete at E18.5. Loricrin and Filaggrin are markers for the cornified layer. Involucrin and Transglutaminase are markers for the granular layer. Keratin 10 and Keratin 1 are expressed in the spinous layer. Keratin 5 and Keratin 14 are expressed in the basal layer. Figure taken and adapted from Forni et al. (2012). Figure created in BioRender.com.

1.2.2 Embryonic origins of the murine epidermal appendages

Development of the hair follicles and other skin appendages is intrinsically related to the stratification of the embryonic epidermis, as stated above (Forni et al., 2012; O'Shaughnessy and Christiano, 2004). Three stages are involved in this process, which begin with the induction of hair placode formation at E14, hair follicle organogenesis occurring at E15.5-E17.5, followed by cytodifferentiation taking place at E18.5 (Lin et al., 2022). These stages are coordinated by several signalling pathways, such as Wnt/β-catenin, hedgehog, notch, and BMP pathways (Houschyar et al., 2020; Hu et al., 2018). Canonical Wnt signalling determines hair follicle fate, as studies have demonstrated that lack of epidermal Wnt/β-catenin or expression of the Wnt inhibitor Dickkopf 1 (Dkk1), result in the absence of hair follicle induction (Andl et al., 2002).

During the first stage, epithelial cells that have activated Wnt/β-catenin signalling, collect dermal cell signals to gradually thicken and form the hair follicle basal placodes, leading to FGF20 secretion that is required for dermal condensates (DCs) (Lin et al., 2022; Park, 2022). These dermal condensates are the result of mesenchymal cell clustering, which aggregate under these hair placodes, forming a new hair follicle at this aggregation point (Lin et al., 2022). In the second stage, the dermal cells send signals to induce the hair follicle basal plate to expand downwards, forming a hair germ and hair peg, causing the hair follicle structure to enter the dermis and begin to form hair buds (Park, 2022; Van der Veen et al., 1999). These hair buds become columnar structures that accumulate many dermal fibroblasts (Houschyar et al., 2020). Upon entering the final stage, keratinocytes are arranged in a columnar shape around the hair buds, which continue to thicken, and dermal cells collect under the hair placode to form the dermal papillae (DP) (Houschyar et al., 2020). Following formation of the DP, the hair bulge begins to form with the DP, inducing the proliferation of the hair matrix cells that differentiate into the hair shaft and inner root sheath (IRS) (Park, 2022). Hair follicle accessory organs, such as the sebaceous gland, and other hair follicle structures have all differentiated from the epithelial cells and have formed a fully mature hair follicle (Lin et al., 2022). These hair follicles express a range of keratins, including keratin 5 and 14, expressed in the outer root sheath and keratin 10 is expressed in the IRS (Hu et al., 2018).

1.2.3 Hair cycle

Throughout the entire lifespan of mammalian organisms, hair follicles demonstrate a high capacity for self-renewal and undergo periodic growth cycles (Lin et al., 2022). The cycle comprises three stages: anagen (growing phase), catagen (regression phase) and telogen (resting phase) (Shin et al., 2020). C57BL/6 mice exhibit a precise time scale of each cycle, with newborn mice entering catagen stage in the second week after birth, while telogen and anagen occur in the third and fourth week, respectively (Lin et al., 2022).

1.2.4 Key cell types in the murine epidermis

1.2.4.1 Melanocytes

Melanocytes are highly specialised neural crest-derived cells that can synthesise the pigment melanin, which is contained within a fully mature intracellular organelle derived from early endosomal membranes, called a melanosome (discussed in more detail in 1.3.1) (Domingues et al., 2020; Lin and Fisher, 2007). Melanin granules, produced by melanocytes, are distributed to adjacent keratinocytes, forming a specific supranuclear cap (Thingnes et al., 2012). This cap protects the keratinocytes from ultraviolet (UV)-induced damage. Together with the keratinocytes, the melanocytes form the epidermal melanin unit, which is involved in the release of any paracrine factors that act upon the melanocytes in response to UV-stimulated and unstimulated conditions (discussed in more detail in 1.3.1) (Nordlund, 2007). There are key differences in melanocyte characteristics between mice and humans, with mouse melanocytes being primarily found either in the bulge and bulb regions of hair follicles, while in humans they are localised to the basal layer and hair follicles (Michalak-Mićka et al., 2022).

1.2.4.2 Langerhans cells

Langerhans cells (LCs) are members of the dendritic cell/macrophage family that are primarily found in the epidermis and upon activation can migrate to skin draining lymph nodes, thereby playing a role as antigen presenting cells (Neagu et al., 2022). LCs are not attached to other cell types in the epidermis and thus can participate in the immune response, where they sense the microenvironment and respond to stress by presenting antigens to the cells of the adaptive immune system (Deckers et al., 2018; Rajesh et al., 2019). In the steady state, LCs are replenished in the epidermis via the local proliferation of skin resident LCs, where mature LCs possess an intrinsic ability to enter a cell division cycle (Neagu et al., 2022).

1.2.4.3 Merkel cells

Merkel cells are also derived from the neural crest and are mechanosensitive cells that contain neuropeptides and neurotransmitter-like substances (e.g., substance P), which enable them to fulfil their roles in somatosensation, chemosensation and endocrine function (Munde et al., 2013).

1.2.4.4 Keratinocytes

Keratinocytes make up around 95% of the epidermal cell population (Eckhart et al., 2000). Self-renewing, undifferentiated epidermal stem cells give rise to daughter transient amplifying (TA) cells, which constitute most of the proliferative cell population (Wang and Yang, 2013). TA cells undergo a finite number (3-5 times) of cell divisions before committing to terminal differentiation (Nakamura et al., 2014). This process is regulated by the balance between cell proliferation in the basal layer and keratinocyte differentiation into corneocytes, leading to the formation of the cornified layer, which acts as a mechanical barrier crucial for skin function (Eckhart et al., 2000; Nakamura et al., 2014). Terminal differentiation enables the epidermis to carry out essential functions, such as minimising passive water loss from the body, preventing the entry of microorganism, and blocking the absorption of chemicals from the external environment (Jiang et al., 2020). Moreover, keratinocytes harbour many anti-inflammatory properties, where they produce a variety of antimicrobial peptides, such as β-defensins, cathelicidins, S100 proteins (e.g., psoriasin and calprotectin) and RNase 7, which protect the skin from infection (Piipponen et al., 2020).

1.2.5 Terminal differentiation in murine epidermal skin

To fulfil the essential roles of the epidermis, the stratified epithelium must undergo continuous re-epithelisation, division, and differentiation in a basal to superficial direction

(Wikramanayake et al., 2014). These processes are crucial for maintaining skin integrity and function and protect against dehydration and infection. The maintenance of skin integrity and function relies on a tightly regulated mechanism termed terminal differentiation (Hu et al., 2018). Excessive proliferation can lead to skin disorders, such as psoriasis, while inadequate growth results in skin thinning (Fuchs and Horsley, 2008). Overall, in mice, the differentiation process is estimated to span approximately 8-10 days (Hu et al., 2018).

Basal keratinocytes, characterised by their columnar shape, consist mainly of mitotically active keratinocytes, including epidermal stem cells and TA cells, which express keratins 5 and keratin 14 (Eckhart et al., 2000; Wikramanayake et al., 2014). These basal keratinocytes are functionally and structurally linked to components of the underlying BM, through a cell-extracellular matrix junction known as the hemidesmosome and integrins (e.g., $\alpha3\beta1$ and $\alpha6\beta4$), thus providing the tissue integrity and strong cell-cell adhesions in the epidermal barrier (Müller et al., 2021; Nakamura et al., 2014). Desmosomes are intercellular junctions, which help strengthen the barrier by linking the intermediate filaments of adjoining cells (Johnson et al., 2014). The fundamental constituents of the desmosome comprise cadherins such as desmogleins (DSG1-4) and desmocollins (DSC1-3), armadillo proteins like plakoglobin and plakophilins, and a plakin known as desmoplakin (Figure 1.3) (Johnson et al., 2014). The fundamental adhesive unit of desmosomes is represented by the DSG/DSC heterodimers, whose cytoplasmic domain bind to plakoglobin and plakophilins (Müller et al., 2021). Plakoglobins and plakophilins interact with desmoplakin, to enable the connection of desmosomes with the keratin filament network (Figure 1.3). Commonly, basal keratinocytes express DSC2/3 and DSG2/3, while the differentiated cells tend to express DSC1 and DSG1/4 (Figure 1.3). The basal desmosomes are dynamic and maintain the proliferative capacity of the basal layer.

As the TA cells exit the cell cycle and lose their capacity to adhere to the BM, due to the decreased expression of crucial integrins, the process of terminal differentiation begins (Eckhart et al., 2000). As the keratinocytes migrate to the spinous layer, they become polyhedral, larger, and more flattened and downregulate keratin 5 and 14 expression and switch on keratin 1 and 10 expression (Candi et al., 2005). Upon entry into the granular layer, the keratinocytes remain nucleated with their cytoplasm filled with basophilic keratohyalin granules, primarily composed of profilaggrin and loricrin, thereby prohibiting

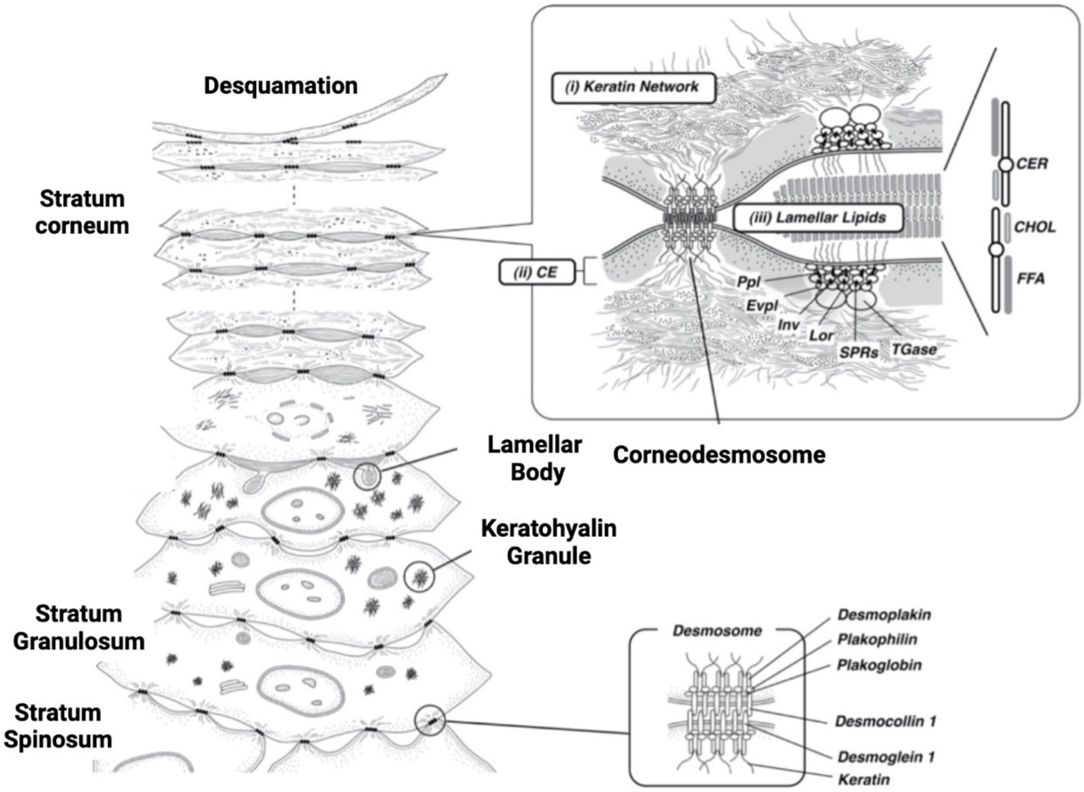

Figure 1.3 Overview of epidermal barrier formation. Three major events occur during terminal differentiation and the formation of the cornified layer. (i) The formation of the keratin network, (ii) the formation of the cornified envelope (CE) by the crosslinking of lipids and proteins and (iii) the creation of intercellular lipids (i.e., Lamellar bodies). Desquamation is the process, where the corneocytes in the stratum corneum are eventually shed. TGase: transglutaminase; SPRs: small proline-rich protein family; Lor: loricin; Inv: Involucrin; Evpl: envoplakin; Ppl: periplakin; FFA: free fatty acid; CHOL: cholesterol; CER: ceramide. Figure adapted from Matsui and Amagai, (2015). Figure created in BioRender.com.

cell division and enabling them to undergo cornification instead (Figure 1.3) (Candi et al., 2005). Here, in addition to keratins, membrane-bound vacuoles, known as Lamellar Bodies (LBs), containing phospholipids, cholesterol, sphingomyelin, and glucosylceramides, provide additional support to the barrier function (Figure 1.3) (Feingold, 2012). These LBs deliver pro-barrier lipids and lipid processing enzymes to the intercellular space of the corneocytes, found in the stratum corneum (Menon et al., 2018). In addition, they secret corneodesmosin, which provides cohesion to the stratum corneum (Figure 1.3). In the differentiated layers, desmosomes provide the stable cell-cell adhesion, aiding in the developing cornified envelope, thus protecting the epidermis from mechanical and chemical stresses (Green et al., 2019). The final stage of terminal differentiation concludes in the stratum corneum, where keratinocytes lose their cytoplasmic organelles and nucleus, but retain the keratin filaments (Eckhart et al., 2000). The influx of calcium activates transglutaminase 1 to catalyse the crosslinking of involucrin and loricrin, which leads to the formation of the cell envelope, thereby forming a corneocyte (Eckert and Rorke, 1989). During this process, lipids are released into the intercellular space, forming a continuous lipid matrix (Wikramanayake et al., 2014). This matrix creates a ‘bricks and mortar’ structure, which effectively seals the corneocytes together, providing the epidermis with its mechanical and chemical protection. Dissociated corneocytes are later shed off by a process known as desquamation (Figure 1.3).

1.2.6 Importance of calcium (Ca^{2+}) in the formation and maintenance of the skin barrier

The initiation of keratinocyte differentiation and maintenance of epidermal functions, relies on extracellular Ca^{2+} (Tu and Bikle, 2013). Studies have demonstrated the presence of a Ca^{2+} gradient within the epidermis, with low levels of Ca^{2+} ions found in the basal, spinous layer and cornified layer, and progressively more in the granular layer (Ahn et al., 1999; Lee et al., 1998; Snoeck, 2020). This data suggests that extracellular Ca^{2+} ions, in the granular layer, are involved in regulating LB secretion, lipid synthesis and in epidermal barrier function recovery (Ahn et al., 1999; Lee et al., 1998). By elevating the extracellular Ca^{2+}, an increase in intracellular Ca^{2+} is triggered, which is responsible for inducing cell-cell adhesion in the epidermal barrier (Tu and Bikle, 2013). Intracellular Ca^{2+} is released from

Ca^{2+} stores, such as the endoplasmic reticulum (ER) and Golgi apparatus (Lee and Lee, 2018). The disruption of Ca^{2+} gradients result from a compromised epidermal permeability barrier, whereas the reestablishment of these gradients has been linked to the recovery of the barrier function (Menon et al., 1992). This indicates that the Ca^{2+} gradient is crucial for the fully functional epidermal skin barrier (Ahn et al., 1999). Patients with Hailey-Hailey and Darier disease, both genetic disorders causing blisters, keratotic papules, and erosions of the skin, are due to defects in the Golgi Ca^{2+} pump (ATP2C1) and ER calcium pump (ATP2A2) (Bikle et al., 2012). Both conditions display lower levels of Ca^{2+} concentration in their basal keratinocytes, causing decreased cell adhesion and disruption to keratinocyte differentiation, preventing the exchange of keratin 14 expression to keratin 10 (Bikle et al., 2012).

Several studies have shown that primary cultures of mouse keratinocytes can be cultured *in vitro* to be proliferative or differentiated using extracellular Ca^{2+} (Hennings et al., 1980; Huang et al., 2006). Protocols for proliferating keratinocytes, which display basal cell phenotypes, are commonly cultured in low Ca^{2+} concentrations (< 0.07 mM), whereas increased Ca^{2+} gradients (above 0.1 mM) induce differentiation (Bikle et al., 2013). The onset of differentiation prompts morphological alterations in keratinocytes, involving redistribution of desmoplakin to form desmosomes, as well as occludins and claudins, which constitute tight junctions (Elsholz et al., 2014). Additionally, E-cadherin, in conjunction with catenins and kinases, form the adherens junctions (Bikle et al., 2013). Together, these junctions not only facilitate cell adhesion, but also create a signalling complex involved in modulating actin distribution and sustaining elevated intracellular calcium levels (Hennings et al., 1980; Bikle et al., 2013).

1.2.7 Proliferation markers in the basal cell layer of the epidermis

Proliferating cell nuclear antigen (PCNA) and Ki67 are well-established markers for assessing cellular proliferation (Prabhu et al., 2022). Ki67 is a non-histone nuclear protein associated with the cell cycle, present in all proliferating cells but absent in resting cells. It is often used as a diagnostic tool for tissue proliferation in many forms of malignant tumours, including lymphomas, breast, colorectal and prostate cancers (Mansy et al., 2020). PCNA contributes to cell proliferation by mediating DNA polymerase activity and exists in the nucleus of all eukaryotic cells. It is integral to nucleic acid synthesis and metabolism and has a fundamental role in recombination, replication, chromatin assembly and excision repair (Moore et al., 2004). Elevated expression of this proliferative marker has been observed in the S, G2, and M phases of cell mitosis in both healthy and cancerous tissues. It is widely used and has demonstrated relevance in clinical dermatology, by comparing and characterising proliferating cell populations in normal, benign, premalignant and malignant human skin lesions (Moore et al., 2004). Reports showed that PCNA distribution was primarily confined to the basal layer in normal skin, with variable patterns of expression exhibited in malignancies and other dermatologic diseases (Moore et al., 2004).

1.3 Overview of pigmentation dynamics

1.3.1 Melanin, Melanogenesis and melanosome transfer

As previously stated, melanocytes are the melanin-producing cells found in the basal layer of the epidermis (d'Ischia et al., 2015). Melanin, the biological macromolecule produced by melanocytes, holds a broad spectrum of biological activities, including photoprotection against UV radiation and being the natural skin pigment (Solano, 2014).

Melanogenesis is the biological and biochemical pathway of melanin biosynthesis, involving an enzymatic reaction in which tyrosinase family proteins (i.e., tyrosinase (TYR), TYR-related protein (TYRP-1) and TYRP-2) convert tyrosine into eumelanin and pheomelanin in melanocytes (Figure 1.4) (Hida et al., 2020; Hirobe, 2014). In response to UV-induced DNA damage in keratinocytes, the alpha-melanocyte-stimulating hormone (α-MSH) a product of proopiomelanocortin (POMC) processing, activates the melanocortin 1 receptor (MC1R) on the melanocytes (D’Mello et al., 2016; Maddaleno et al., 2021). This activation increases the cyclic adenosine monophosphate (cAMP) synthesis, thereby causing activation of protein kinase A (PKA), which phosphorylates CRE-binding protein (CREB), acting as a transcription factor of microphthalmia-associated transcription factor (MITF) (D’Mello et al., 2016; Vachtenheim and Borovanský, 2010). MITF regulates the expression of the key melanogenesis proteins that include TYR, TYRP1, TYRP2, ocular albinism type 1 (OA1), dopachrome tautomerase (DCT) and pre-melanosome protein 17 (PMEL17) (Maddaleno et al., 2021). OA1 is an integral membrane glycoprotein that is solely expressed by melanocytes and is detectable on the membrane of the melanosomes, which are membrane-bound organelles, involved in the synthesis, storage, and distribution of melanin (D'Mello et al., 2016; Palmisano et al., 2008). The N-terminal of OA1 is predominantly localised in the lumen of the melanosome, while the C-terminal is localised to the cytoplasmic side (Chen et al., 2016).

A series of well-defined steps prompt the formation of melanosomes in vertebrates, whereby melanosome development can be classified into four stages, according to their morphological features and degree of melanin deposition (Hirobe, 1995; Schiaffino, 2010). Non-pigmented and undifferentiated melanosomes are found within stages I and II, with proteinaceous fibrils beginning to form in the lumen of the organelle during stage II (Figure 1.5 A) (Schiaffino, 2010). Once the fibrils have wholly formed, the melanosome adopts an ellipsoidal shape that expresses PMEL17/gp100, representing the main structural constituent of the fibrils (Schiaffino, 2010). During stages III and IV, electron-dense melanin is synthesised and gradually deposited in the fibrils until the melanosome is entirely obscured at the end of stage IV (Figure 1.5 B) (Schiaffino, 2010).

OA1 appeared broadly distributed across all stages of melanosomal development and maturation, but the bulk (around 24%) of was observed in regions with high PMEL17 expression, corresponding to premelanosomal stage II (Chen et al., 2016; Giordano et al., 2009).

Once the melanosomes are fully mature and pigmented, they move bidirectionally along microtubules under actin-dependent transport and migrate towards the cell periphery where they interact with the cortical actin cytoskeleton (Futter et al., 2004). Microtubules serve as the tracks of transport for several intracellular organelles, including melanosomes, lysosomes, and sorting vesicles (Watabe et al., 2008). This trafficking of vesicles to the target organelles is governed by microtubule-associated motor proteins, such as kinesins and cytoplasmic dyneins. Cytoplasmic dyneins drive the minus-end motility of the microtubules, while the kinesins drive the plus-end directed mobility. The interaction with the actin cytoskeleton is mediated through a complex with Rab27a, a small GTPase that is involved in melanosome transfer, myosin and melanophilin, where myosin Va binds to actin and Rab27a binds to the melanosomes (Figure 1.5 B) (Hume et al., 2001). Melanophilin acts as the linker between myosin Va and Rab27a (Hume et al., 2001). A study on melanocytic cells in *Xenopus laevis* indicated that myosin Va counteracts dynein-mediated motor transport more than kinesin- mediated transport, leading to the eventual

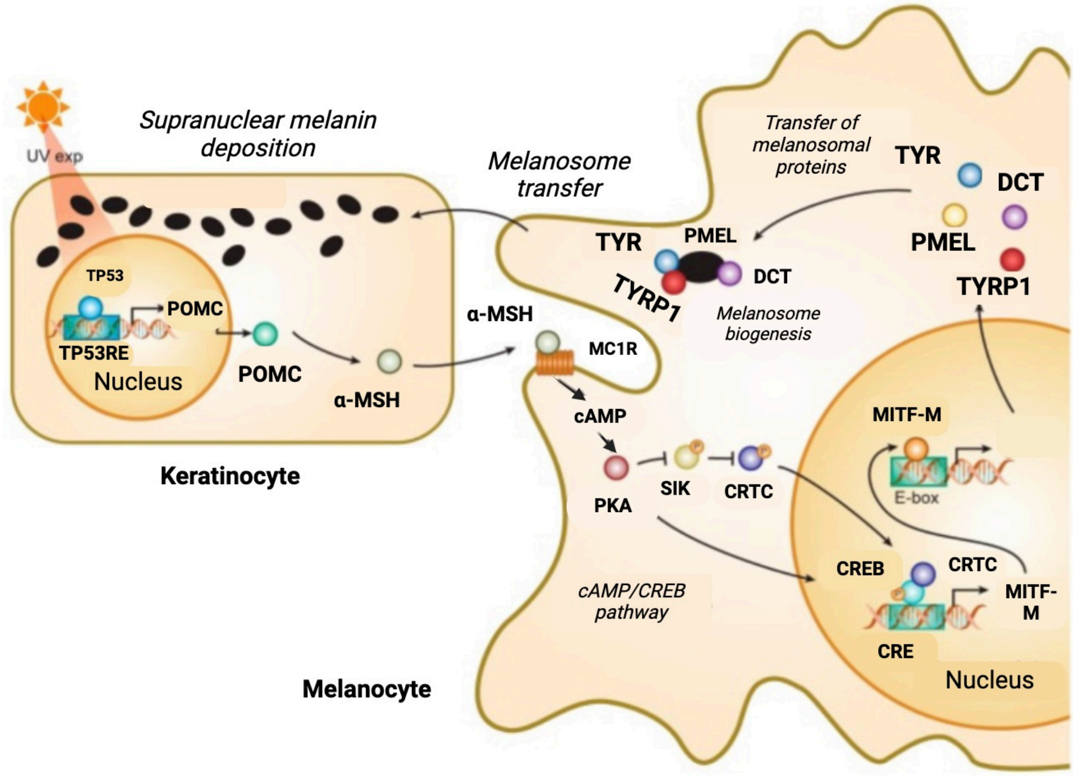

Figure 1.4 Overview of the cascade of melanogenesis in human skin. UV damages DNA in keratinocytes, which activate TP53 that initiates the transcription of *POMC.* POMC is cleaved into α-MSH, which is secreted by the keratinocyte and binds to the MC1R on the melanocytes, thereby increasing cAMP. PKA is activated by cAMP, resulting in the CREB transcriptional activity, which can occur in two ways: (i) by phosphorylating CREB or (ii) inhibiting SIK. CREB activates the transcription of MITF-M, leading to the transcription of key melanogenesis genes including *TYR*, *TYRP1*, *DCT* and *PMEL*. These proteins are transported to melanosomes, with mature melanosomes eventually being transported from melanocytes to keratinocytes, accumulating at the supranuclear region, thereby blocking UV light. α-MSH: alpha-melanocyte-stimulating hormone; cAMP: cyclic adenosine monophosphate; CRE: cAMP response element; CREB: CRE-binding protein; CRTC: CREB-regulated transcriptional coactivator; MC1R: melanocortin 1 receptor; MITF: microphthalmia-associated transcription factor; PKA: protein kinase A; SIK: salt-inducible kinase; POMC: proopiomelanocortin; TYR: Tyrosinase; TYRP1: Tyrosinase-related protein 1. Figure adapted from Hida et al. (2020). Figure created in BioRender.com.

localisation of mature melanosomes in the cell periphery, rather than cell centre (Gross et al., 2002). Once the melanosomes reach the cell periphery, they are transferred to neighbouring keratinocytes, in four suggested mechanisms, which remains poorly understood (Figure 1.5) (Bruder et al., 2012; Wu and Hammer, 2014).

The process of melanosome transfer has been widely studied by many cellular biologists over the past decades, yet the exact process remains ambiguous. Several studies using brightfield time-lapse imaging, immunolabelling, and electron microscopy have proposed numerous potential mechanisms of melanosomal transfer (Bruder et al., 2012).

A proposed mechanism, termed cytophagocytosis, involves phagocytosis of a viable cell or intact region of a viable cell and was demonstrated by Okazaki and co-workers (Okazaki et al., 1976). They determined that melanin transfer was achieved through the keratinocyte engulfing the melanosome-rich dendritic tip of the melanocyte (Figure 1.5 A). In the initial stages, the melanocyte extends its dendrites, connecting with the nearby keratinocytes, resulting in the keratinocyte engulfing the melanocyte membrane, using villus-like cytoplasmic projections. Once the keratinocyte consumes the dendrite tip, it is pinched off leading to the formation of a cytoplasmic pouch containing the melanosomes. Okazaki et al. (1976) suggested that this cytoplasmic sack is degraded where it later disintegrates the load further into smaller vesicles containing single melanin granules or aggregates of melanin granules that are evenly dispersed in the cytoplasm.

In 2002, a novel mechanism of melanosome transfer was established using high-resolution time-lapse microscopy (Scott et al., 2002). Scott and co-workers documented that melanosomes move along actin-based filopodia, most likely in the presence of myosin Va. Furthermore, this transfer was believed to be stimulated by the small GTP-binding protein CDC42 and driven by the motor protein kinesin. The protease-activated receptor 2 (PAR-2), identified on keratinocytes, has been suggested to act as a phagocytic receptor. Upon exposure to UV irradiation, PAR-2 expression increases, facilitating the engulfment of melanosomes by keratinocytes (Scott et al., 2002; Van den Bossche et al., 2006).

More recently, Wu and colleagues determined that melanocytes package their melanosomes into globules and release them at their periphery, which are later phagocytosed by the plasma membrane of the keratinocyte (Figure 1.5 A) (Wu et al., 2012). Ando and co-workers also revealed that melanosome-rich globules were found at the periphery of melanocyte dendrites and attached to the microvilli of adjacent keratinocytes

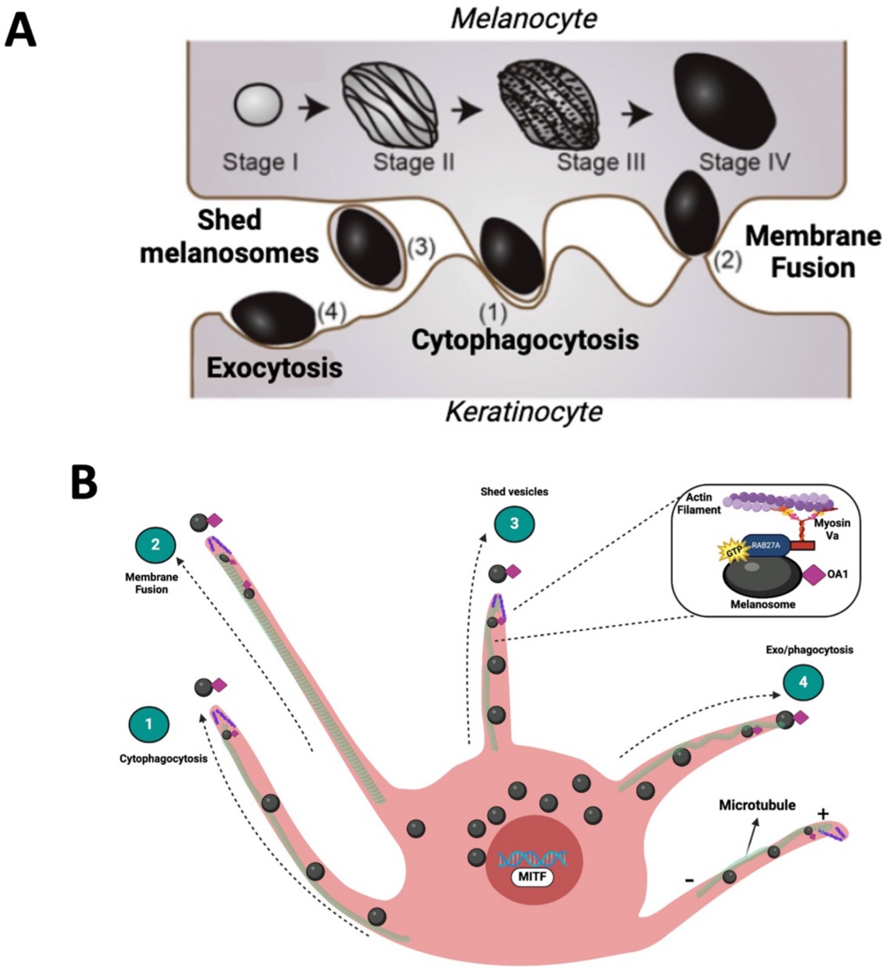

Figure 1.5 Melanosome development and transfer. (A) Melanosome development is categorised into four stages. During stages I and II, melanosomes are non-pigmented. During stage II, striations begin to form in the melanosome, while in stage III, melanin begins to be deposited in the fibrils. Once in stage IV, melanosomes are fully matured and pigmented, which can then be transported to neighbouring keratinocytes. Yet, the exact mechanism of transport remains poorly understood, and four suggested mechanisms have been proposed by scientists. (1) Cytophagocytosis of filopodia or dendrite tips by keratinocytes. (2) Immediate transfer through a ‘membrane channel’. (3) Shedding of vesicles containing the melanosome, followed by keratinocyte engulfment. (4) Exocytosis-mediated secretion of naked melanin. Figure adapted from Tian et al. (2020). Figure created in BioRender.com. **(B)** Graphical representation showing melanosome bidirectional trafficking, along microtubules, in melanocytes. At the cell periphery, melanosomes are attached to the actin cytoskeleton, through a Rab27A and myosin Va complex. Figure created in BioRender.com.

(Ando et al., 2012). Remnants of these globules were also observed within the keratinocytes favouring this proposed mechanism.

The final suggested transfer process includes the exocytosis of melanin, lacking a membrane, from the melanocyte dendritic tip to the keratinocyte (Figure 1.5 A). Here, melanosomal membrane fusion with the melanocyte plasma membrane results in the release of extracellular melanin, which is internalised by bordering keratinocytes (Yamamoto and Bhawan, 1994). It is believed that melanin is released from the melanosomes within the melanocytes by exocytosis, as melanocytes express many molecules, including SNAREs (e.g., SNAP23/25; VAMP2; syntaxin4/6) and Rab GTPases (e.g., Rab3) that exhibit crucial roles in exocytosis (Van den Bossche et al., 2006). Rab27a has a suggested role in aiding in the exocytosis of melanin from the melanocytes, as it is known that Rab27a facilitates the docking of melanosomes to the plasma membrane of the dendritic tips of melanocytes, which is an essential step in exocytosis.

Several mechanisms for melanosome transfer have been proposed, with most involving keratinocyte phagocytosis (Cardinali et al., 2008; Seiberg et al., 2000; Sharlow et al., 2000). Melanosomes range in size from 0.5 μm to 2 μm, making phagocytosis and micropinocytosis the likely pathways for their internalisation into keratinocytes (Moreieras et al., 2021). One of the most well-studied receptors involved in keratinocyte phagocytosis is PAR-2, which has been implicated in skin pigmentation by promoting melanin uptake (Babiarz-Magee et al., 2004; Bento-Lopes et al., 2023; Lin et al., 2008; Scott et al., 2002; Seiberg et al., 2000). It has been suggested that autophagy plays a role in the degradation of melanin in primary human keratinocytes, with autophagy inducers reducing melanin levels and inhibitors enhancing melanin accumulation (Murase et al., 2013). In other epithelial cells, such as kidney tubular cells, PAR-2 has been shown to inhibit autophagy through the PI3K/Akt/mTOR signalling pathway (Zhang et al., 2017). This raises the possibility that PAR-2 may similarly regulate autophagic inhibition in murine keratinocytes after melanin internalisation via phagocytosis, thus permitting the long-term storage of melanin within these cells.

1.3.2 Melanin internalisation and degradation within keratinocytes

Following the transfer of melanosomes from the melanocytes to the keratinocytes, little is known about the destiny of melanosomes after incorporation into keratinocytes (Murase et al., 2013). Given the size of the melanosomes (0.3-0.5 µm) several studies have indicated that macropinocytosis and phagocytosis can enable the internalisation of such cargo (Benito-Martinez et al., 2021; Moreiras et al., 2021). The widely known receptor, involved in melanin ingestion by keratinocytes is PAR-2 (Seiberg et al., 2000). PAR-2 expression has been shown to correlate with skin phototype, with darker skin exhibiting higher PAR-2 expression compared to lighter skin (Babiarz-Magee et al., 2004). Other receptors such as TLR-3 and fibroblast growth factor receptor 2/keratinocyte growth factor receptor (FGFR-2/KGFR) have been linked to melanin phagocytosis by keratinocytes (Belleudi et al., 2010; Koike et al., 2019). A study by Koike and co-workers determined that TLR3 stimuli enhanced PAR-2 expression in keratinocytes and activated RHO GTPase RHOA and CDC42, which are both involved in endocytosis and melanosome transfer from melanocytes through filopodia (Koike et al., 2019; Scott et al., 2002). Additionally, a c-type lectin receptor known as MelLec was shown to recognise fungal melanin on endothelial and myeloid cells (Stappers et al., 2018). Interestingly, keratinocytes express a further c-type lectin receptor known as Dectin-1, which is known to be involved in keratinocyte-mediated innate immune responses and wound re-epithelisation (Van den Berg et al., 2014). Dectin-1 has demonstrated a role as receptor for a non-canonical autophagy pathway, called LC3-associated phagocytosis, which will be discussed in further detail in the next sections. Up until now the link between this receptor and the phagocytosis of human/mouse melanin remains unclear.

The mechanism of melanin processing remains elusive, with several studies proposing that melanin degradation is controlled by a process called autophagy (Murase et al., 2013; Kim et al., 2020). These studies are described in greater detail in 1.4.4. Research by Hurbain and colleagues revealed that melanin accumulates in moderately acidic compartments, indicated by low levels of LysoTracker (marker for lysosomes), with low degradative capacity (Hurbain et al., 2018). It was further suggested that melanin-containing compartments, called melanokerasomes, are specialised compartments for the long-term melanin storage inside keratinocytes (Correia et al., 2018). They maintain the unique features of melanosomes, such as low acidity and degradative capacity, and exhibit characteristics of late endosomes/lysosomes, such as LAMP1/2 and CD63 (Correia et al., 2018; Hurbain et al., 2018). Is has been proposed that melanin is not degraded at all, given its protective properties and favours the assumption of melanokerasomes storing the pigment (Bento-Lopes et al., 2023). Fungal melanin was shown to inhibit LC3-associated phagocytosis in *Aspergillus fumigatus,* thus promoting pathogenicity (Akoumianaki et al., 2016; Chamilos et al., 2016). Therefore, the link between LC3-associated phagocytosis and melanin internalisation and processing should be investigated.

1.4 Phagocytosis & Canonical Autophagy

1.4.1 Phagocytosis

Phagocytosis is an evolutionarily conserved cellular process, which involves the ingestion and elimination of pathogens and apoptotic cells (> 0.5 µm) into a plasma membrane derived vesicle, referred to as a phagosome (Rosales and Uribe-Querol, 2017). This cellular process is essential for maintaining tissue homeostasis of an organism, through the removal of both self and foreign particles. It is the first step in prompting host defence and inflammation, eradicating vast numbers of senescent cells that die every day (Aderem, 2003).

Phagocytosis can be split into three stages that include microbial recognition, phagosome formation and phagolysosome maturation (Rosales and Uribe-Querol, 2017). Only a specialised group of cells, known as professional phagocytes, perform phagocytosis with high efficiency (Rosales and Uribe-Querol, 2017; Uribe-Querol and Rosales, 2020). Among these professional phagocytes are macrophages, monocytes, neutrophils, dendritic cells, and osteoclasts (Uribe-Querol and Rosales, 2020). These cells are actively involved in the removal of microorganisms and present them to the cells of the adaptive immune system (Rosales and Uribe-Querol, 2017). Non-professional phagocytes include all remaining cell types, capable of performing phagocytosis (i.e., fibroblasts and epithelial cells) (Lim et al., 2017).

The recognition of microbial pathogens is achieved through the engagement of pattern recognition receptors (PRR), that recognise molecular patterns related to a microorganism (Aderem, 2003). Upon recognition, the receptors then trigger signalling cascades, which favour and initiate phagocytosis. These signalling cascades prompt the remodelling of the actin cytoskeleton and lipids in the membrane, which allow the membrane to extend and cover the particle (Uribe-Querol and Rosales, 2020). The membrane eventually closes at the distal end, thereby creating the phagosome, which internalises the particle. The nascent phagosome undergoes a sequence of fusion and fission events with endocytic organelles (i.e., early or sorting endosomes, late endosomes, and lysosomes), resulting in modifications to both the limiting membrane and luminal contents (Levin et al., 2016). This process ultimately leads to the maturation of the phagosome (i.e., late phagosome). This late phagosome has a more acidic luminal pH, due to proton-pumping V-ATPase, which can fuse with a lysosome, thereby creating a phagolysosome (Lee et al., 2020). This phagolysosome is highly acidic, oxidative and contains a variety of lytic enzymes that aid in the degradation of the foreign material.

Similar processes, such as canonical autophagy and non-canonical autophagy (i.e., LC3-associated phagocytosis) are also highly conserved processes that are involved in the removal of unwanted or foreign material from the organism.

1.4.2 Canonical Autophagy

Canonical autophagy, hereafter referred to as autophagy, was first proposed by Christian de Duve in 1963 and is an evolutionary conserved mechanism, responsible for degrading and recycling damaged subcellular organelles and proteins (Liu et al., 2021; Zhang et al., 2015). It is crucial for the maintenance of cell metabolism and homeostasis during development, differentiation, and starvation (Zhang et al., 2015). There are three major types of autophagy, known as macroautophagy, microautophagy and chaperone-mediated autophagy, which all function by promoting the degradation of cytosolic components via lysosomes (Zhang et al., 2015).

Macroautophagy, known as autophagy, is an intracellular lysosome-mediated degradation process that is characterised by the formation of intracellular double-membrane autophagosomes (Akinduro et al., 2016; Kim et al., 2022). These autophagosomes are responsible for removing intracellular materials, such as lipids, organelles, DNA, and invading pathogens. The formation of these autophagosomal structures involves autophagy-related genes (ATGs) and can be split into five steps – initiation, elongation, maturation, fusion, and degradation (Figure 1.6) (Sun et al., 2013).

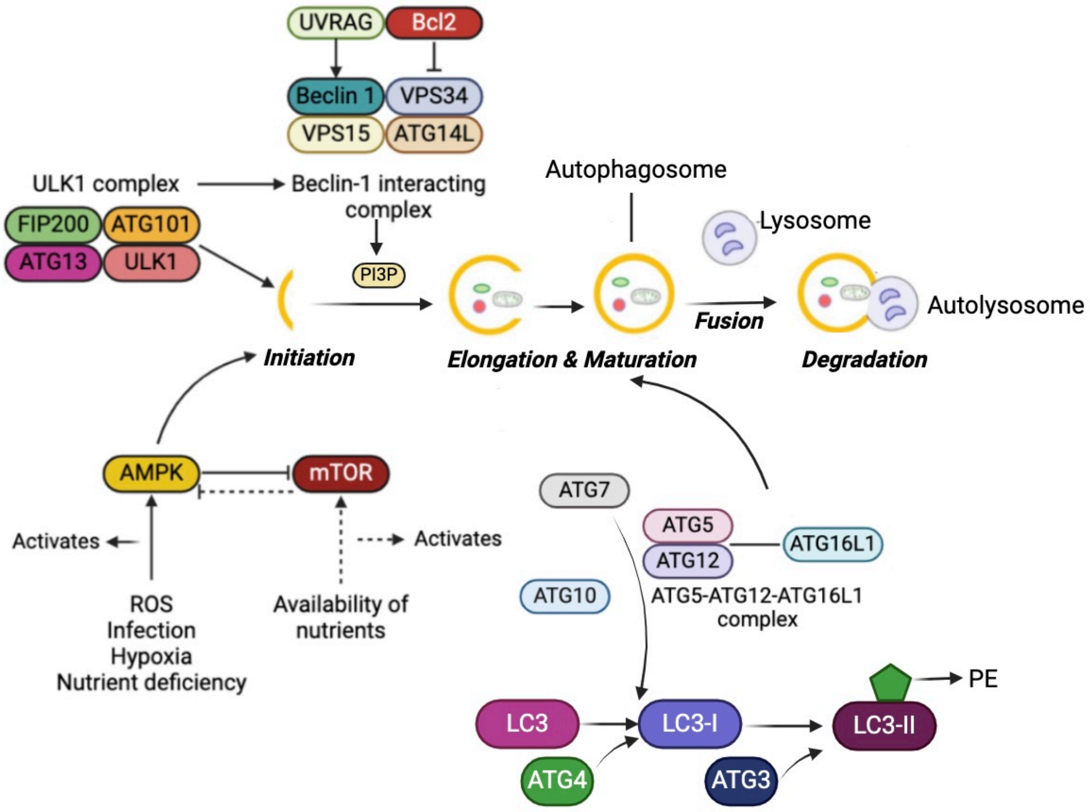

Figure 1.6 Overview of canonical autophagy. Autophagy is initiated by the formation of the pre-initiation complex, consisting of ULK1, FIP200, ATG13 and ATG101. This complex can be suppressed by mTOR or initiated by AMPK, in the presence of starvation and nutrient deprivation. The Beclin 1 class II PI3K complex, comprised of Beclin 1, VPS34, ATG14L and VPS15 is activated to produce PI3P, responsible for recruiting downstream ATG proteins that aid in the development of the autophagosome. This complex can be promoted by UVRAG but can be inhibited by the Bcl2 family proteins. During the elongation and completion steps of autophagosome formation, ATG12 conjugated to ATG5, in the presence of ATG7 and ATG10, resulting in the subsequent binding to ATG16L1, forming the ATG5-ATG12-ATG16L1 complex. LC3 is cleaved by ATG4 to generate the cytosolic LC3-I form, which with the help of ATG7 and ATG3 enzymes is conjugated to the cellular lipid PE, to give rise to the membrane-associated LC3-II. LC3-II is embedded into the outer and inner membranes of the mature autophagosome. In the final degradation step, the mature autophagosome fuses with the lysosome, resulting in the degradation and recycling of the unwanted material. Figure adapted from Liu et al. (2021). Figure created in BioRender.com.

The initiation step includes the assembly of core machinery involving the Unc-51-like autophagy-activating kinase (ULK1) complex, consisting of ATG13, FIP200 and ATG101 (Figure 1.6) (Jeong et al., 2020; Sun et al., 2013). The initiation of this assembly is prompted by the inhibition of mammalian target of rapamycin complex 1 (mTORC1). This inhibition can occur either through the activation of adenosine monophosphate (AMP)-activated protein kinase (AMPK), or in response to various factors such as nutrient deficiency, reactive oxygen species (ROS), infection, or hypoxia (Figure 1.6) (Jeong et al., 2020). Vice versa, the availability of nutrients activates the mTORC1 complex, leading to the inhibition of the ULK1 complex by phosphorylation (Münz, 2022). The activation of the ULK1 complex results in the further initiation of downstream complexes, including the Beclin-1 interacting complex, consisting of VPS34, ATG14L and p150 (Liu et al., 2021; Sun et al., 2013). UV radiation resistance-associated gene protein (UVRAG) can promote the formation of the Beclin-1 complex, while the Bcl2 family proteins can inhibit the complex through their interaction (Figure 1.6) (Kovacs et al., 2022; Levy et al., 2017). Moreover, the activation of the Beclin-1 complex generates phosphatidylinositol-3-phosphate (PI3P), which is crucial for nucleation of the autophagic vesicles (Leidal and Debnath, 2021). The elongation and maturation of autophagosomes, requires the activity of two further complexes: the ATG5-ATG12 complex and ATG5-ATG12-ATG16L1 complex (Parzych and Klionsky, 2013). In the elongation step, ATG5-ATG12 complex conjugates to ATG16, thereby forming the ATG5-ATG12-ATG16L1 complex, involved in the expansion of the autophagosome membrane (Levy et al., 2017). The diameter of the autophagosomes differ among organisms, with autophagosomes in yeast ranging between 0.4 – 0.9 μm and 0.5 – 1.5 μm in mammals (Parzych and Klionsky, 2013). ATG3, ATG4B and ATG7 bind phosphatidylethanolamine (PE) to LC3-I, which is converted to LC3-II, and recruited into the expanding outer and inner autophagosome membrane (Figure 1.6) (Levy et al., 2017; Jeong et al., 2020). LC3-II serves as a marker for autophagosomes and is required alongside other key molecules, such as Rab7, SNAREs and LAMPs, for the subsequent fusion with lysosomes, whereby the contents of the autophagosomes are subsequently degraded and recycled (Sil et al., 2018).

1.4.3 The role of autophagy in the skin barrier

Several studies have highlighted roles of autophagy in keratinocyte biology and skin barrier function (Akinduro et al., 2016; Haruna et al., 2008; Rossiter et al., 2013).

A study in 2008 by Haruna and co-workers briefly described the first report of LC3 in human epidermal skin differentiation (Haruna et al., 2008). They reported that LC3-I and LC3-II expression increased during calcium-induced differentiation, with LC3 distribution mainly being distributed in the granular layers, following the initiation of terminal differentiation. They next investigated skin affected by psoriasis vulgaris and found that LC3 expression was downregulated in psoriatic skin, suggesting that autophagy in the granular layer contributes to the normal keratinisation of the granular layer.

Akinduro and colleagues showed that during foetal development, several autophagy markers (i.e., ULK1, beclin-1, WIPI 1 and ATG5-ATG12 complex) are active in the development of the skin barrier (Akinduro et al., 2016). Low levels of LC3, ULK1, beclin-1 and WIPI 1 were found before granular layer development and increased as granular layer development commenced. They also demonstrated that the inhibition of mTORC1 in the epidermis, resulted in the increased expression of autophagy markers (e.g. LC3; WIPI1; ULK1; Beclin-1 and ATG5-ATG12), which was consistent with the induction of autophagy in the upper epidermis. To conclude their analysis, they performed a detailed examination of the cell morphology in differentiated keratinocytes and found that the keratinocytes exhibited misshapen and irregular nuclei, which were positive for LAMP2 and LC3 aggregates, following degradation of nuclear material. Moreover, they found that p62 expression was elevated in differentiating keratinocytes in comparison to undifferentiated keratinocytes, suggesting that during differentiation keratinocytes employ nucleophagy to eliminate nuclear material. They further examined the association of autophagy markers on skin disorders such as psoriasis and found that LC3, ULK1 and WIPI1 exhibited a reduced expression in lesional psoriatic skin, compared to healthy adult epidermis. They concluded that these patients may benefit from treatment with mTORC1 inhibitors, which would drive autophagy in their lesions, restore epidermal differentiation, and thereby reduce inflammation and hyperproliferation. Altogether, their data reveals a significant importance for the presence and location of autophagy in epidermal development and differentiation, and outlines the significance of autophagy in ensuring healthy epidermal function and homeostasis.

Rossiter and co-workers examined the effects of an inactivated autophagy gene *ATG7* in keratin 14 expressing tissues, on skin barrier function (Rossiter et al., 2013). The research findings revealed that mice deficient in ATG7 displayed similar epidermal morphology, thickness, and expression of differentiation markers compared to their ATG7 littermate controls. Skin barrier integrity was assessed by toluidine blue uptake assay, which demonstrated that ATG7 defective mice display a fully functioning and intact skin barrier. Altogether, these findings demonstrate that despite these mice displaying defective autophagy, the mouse epidermis morphology and function is not compromised. This work was followed up with a study by Yoshihara and co-workers, who employed skin grafts from ATG7-deficient mice and transplanted them onto the dorsal skin of severe combined immunodeficiency (SCID) mice, to examine the effects of ATG7 deficiency on skin barrier function (Yoshihara et al., 2015). Findings revealed that skin grafts from the ATG7-deficient mice exhibited hyperkeratosis and acanthosis (thickening of the skin). Terminal differentiation markers, such as loricrin, filaggrin and involucrin were all found to be downregulated in the mutant mouse, when compared to their littermate controls, again suggesting a role of autophagy in the keratinisation pathway. This was further validated by the reduced number of keratohyalin granules in the skin of ATG7-deficient mice. Overall, findings suggested that the absence of autophagy has a dramatic effect on the granular layer, compared to other layers of the skin. They propose that the ATG7-deficiency delays granular layer differentiation and thus causes several skin conditions, such as acanthosis.

Work by Douroudis and colleagues, demonstrated that polymorphisms in the human ATG gene *ATG16L1* have been associated with skin conditions, such as psoriasis vulgaris and palmoplantar pustulosis (Douroudis et al., 2012; Douroudis et al., 2011). A study by Van Hove and co-workers examined the role of autophagy in mice that lack ATG16L1 in keratinocytes (Δ^{Ker}*atg16l1),* as ATG16L1 deficient mice die shortly after birth (Van Hove et al., 2023). To examine the function of autophagy in keratinocytes, these mice with a floxed *ATG16L1* gene were crossed to the keratin 5 (KRT5) Cre line, thereby generating the Δ^{Ker}*atg16l1* mice. Overall, the mice exhibited a normal skin phenotype, yet showed a thickened stratum corneum, giving an indication to potential defects in desquamation. The epidermal permeability barrier of the Δ^{Ker}*atg16l1* mice was not compromised. Findings reported that ATG16L1 deficiency in keratinocytes promotes epidermal inflammation upon treatment with a topical inflammatory agent (TPA- 12-O-tetradecanoylphorbol-13-acetate), shown by the presence of increased erythema and scaling compared to the control. Moreover, the Δ^{Ker}*atg16l1* mice, subjected to DMBA (2, 4-dimethoxybenzaldehyde) a tumour promoting agent, appeared more sensitised to inflammation-driven carcinogenesis, with higher number of tumours forming relative to their controls.

Overall, studies have demonstrated key roles of autophagy in regulating epidermal turnover, yet the exact role of non-canonical autophagy in this process remains ambiguous.

1.4.4 The involvement of autophagy in melanosome maturation and degradation

While autophagy has been widely studied in keratinocyte biology and skin barrier function, it has also demonstrated roles in melanogenesis and melanin degradation (Ganesan et al., 2008; Ho et al., 2011; Kalie et al., 2013).

In a study by Ganesan and colleagues, where the authors conducted a genome wide siRNA screen, findings revealed that multiple autophagy components were identified as novel regulators for melanogenesis (Ganesan et al., 2008). Results demonstrated that depletion of WIPI1, LC3 or Beclin 1 resulted in decreased levels of melanin in MNT-1 melanoma cells. Moreover, the authors found that autophagy proteins LC3 and ATG5 were colocalised with melanosomal marker PMEL17 in mature melanosomes and have suggested that the autophagy machinery, required for autophagosome formation, may be implicated in the biogenesis of melanin.

Findings by Ho and co-workers demonstrated that WIPI1 depletion inhibited the transcription of MITF and MITF-M target genes (Ho et al., 2011). Additionally, they showed that WIPI1 depletion resulted in less accumulated melanin and reduced numbers of mature melanosomes (stages III and IV). However, WIPI1 depletion led to the accumulation of early melanosomes, stages I and II, with increased levels of LC3-II and p62, suggesting that WIPI1 is involved in controlling melanogenesis. By pharmacologically activating autophagy, using a low dose of rapamycin, consequently suppressing mTOR, MITF and TYR transcription were stimulated. Moreover, following autophagy stimulation by rapamycin, the authors demonstrated a decreased accumulation of p62 (marker for early melanosomes), increased build-up of LC3-II (a marker for early and late melanosomes) and an increase in mature melanosomes (stages III and IV). Collectively, the authors concluded that autophagy signalling is involved in the transcription of melanogenic enzymes and the maturation of melanosomes.

Similarly, a study by Kalie and colleagues determined that ULK1 depletion in MNT-1 cells causes an increase in melanin levels, through upregulation of melanogenesis, which is accompanied by an increased MITF expression (Kalie et al., 2013). However, they revealed that important autophagy components that associate with the ULK1 complex, FIP200 and ATG13, did not influence melanin levels, suggesting that ULK1 is involved in melanogenesis in a manner that is independent from its role in autophagy.

The balance between number of melanosomes and phagocytic activity of keratinocytes gives rise to skin colour (Kim et al., 2020; Murase et al., 2013). Many regulators of autophagy are involved in melanogenesis, as previously discussed, but also in the degradation of melanosomes in the keratinocytes (Murase et al., 2013). Low levels of basal autophagy activity are observed in keratinocytes from individuals with darker skin, compared to keratinocytes from Caucasians, which exhibit higher basal autophagic activity. The levels of basal autophagy influence melanosome degradation and thus give rise to several different skin pigmentation phenotypes.

A study by Kim and colleagues has proposed an autophagy-inducing agent (PTPD-12) that promotes melanosome degradation without disturbing the biochemical signals that are associated with melanogenesis (Kim et al., 2020). PTPD-12 is an autophagy-regulating peptide, which causes significant upregulation of LC3-II, and dose-dependent decrease of p62 expression in primary human epidermal keratinocytes; thus, confirming that PTPD treatment induces autophagic flux. Their findings further confirmed previous reports that increased autophagy can induce melanosome degradation in melanocytes but here also in keratinocytes.

1.4.5 The role of autophagy in skin ageing

The skin, as the outermost organ of the human body, is highly susceptible to damage from environmental factors, such as UV-radiation, air pollution, and cigarette smoking. This damage can lead to skin ageing, known as extrinsic ageing (Gu et al., 2020). Intrinsic ageing occurs in all tissues and is typically observed in areas of the skin not exposed to sunlight. During intrinsic ageing, the number of dermal fibroblasts decreases, and the ability to synthesise collagen and elastin in the ECM is diminished. This leads to the thinning of the dermis, loss of elasticity, and an increase in wrinkles and skin fragility. Both extrinsic and intrinsic ageing contribute to a decline in the structural integrity and physiological function of the skin (De Araújo et al., 2019).

Reactive oxygen species (ROS), which are continuously produced as by-products of mitochondrial aerobic metabolism, are considered major contributors to intrinsic ageing. ROS activates various signalling pathways that lead to reduced collagen production and synthesis, as well as the activation of matrix metalloproteinases (MMPs) responsible for degrading connective tissue (Shin et al., 2023).

Autophagy exhibits several roles in maintaining skin homeostasis, by targeting different types of organelles and proteostasis pathways in skin cells, including melanogenesis, nucleophagy (removal of nucleus in differentiating keratinocytes), and anti-inflammation (Murase et al., 2020). A study by Demirovic and colleagues revealed that basal autophagy was upregulated in human facial skin fibroblasts *in vitro* following the Hayflick system, a common method used to study the phenomenological and mechanistic aspects of ageing (Demirovic et al., 2015). Here, LC3 expression was found to be 5-fold greater in aged fibroblasts, in comparison to young. Tashiro and co-workers discovered that the number of autophagosomes increases in dermal fibroblasts with age, and they demonstrated that LC3-II was significantly higher in dermal fibroblasts cultured from the skin of elderly women compared to those from young women (Tashiro et al., 2014). They also showed that autophagy was disrupted at the degradation step in aged fibroblasts. To further investigate the impact of this autophagy disruption on the dermis, they treated young fibroblast cells with leupeptin and pepstatin A, major lysosomal protease inhibitors, to mimic the autophagy-suppressed state of aged cells. Their results indicated that age-dependent changes in autophagy occur in dermal fibroblasts, and that leupeptin and peptstatin A treated fibroblasts exhibited reduced levels of type I procollagen, hyaluronan and elastin, along with increased levels of MMP-1, an MMP known to induce collagen fragmentation. Scanning electron microscopy revealed broken collagen fibrils in the collagen lattice of treated fibroblasts. Overall, their findings suggest that impaired autophagic function leads to a decrease in dermal components, resulting in the collapse of dermal structure and increased skin fragility.

However, the connection between autophagy and intrinsic skin ageing, particularly in the dermis, remains poorly understood, highlighting the need for further research to determine the extent of autophagy in various skin cell types.

Numerous abnormalities in the autophagic machinery have been associated with inflammation, pigmentation issues and autoimmune disorders. However, it is plausible that some of these abnormalities are associated with an alternative, non-canonical autophagy pathway, known as LC3-associated phagocytosis, rather than conventional autophagy. The studies outlined in section 1.3.1-1.3.2 and 1.4.3-1.4.5 highlight an essential role of autophagy in maintaining healthy skin homeostasis, which prompted us to examine the roles of non-canonical autophagy on healthy skin function.

1.5 Non-canonical Autophagy – LC3-associated phagocytosis (LAP)

In recent years, a further pathway for ingestion of particulate structures has been established, called LC3-associated phagocytosis (LAP) (Herb et al., 2020). LAP is present in phagocytic cells, such as epithelial cells, macrophages, and endothelial cells (Asare et al., 2020; Heckmann et al., 2017). It has a critical role in resolving inflammation, pathogen clearance, preventing autoimmunity and immune-mediated tissue damages, as well as being responsible for promoting wound healing. It is a process that is triggered upon phagocytosis of foreign particles or apoptotic cells that engages with cell surface receptors, such as toll-like receptors (TLR) (i.e., TLR1/2, TLR2/6 and TLR4), TIM4, or FcγR (Heckmann et al., 2017). This recognition prompts the recruitment of some, but not all, members of the autophagy machinery to a single-membraned phagosome (Figure 1.7) (Hooper et al., 2022; Martinez, 2020; Schille et al., 2018). Detection of LAP by confocal microscopy using LC3-GFP-expressing cells revealed that the localisation of LC3 can be detected as early as 15 minutes post phagocytosis, while the fusion of the phagosome with the lysosome can occur after 45 minutes (Martinez, 2020). The detectability of LAP occurs much more rapidly

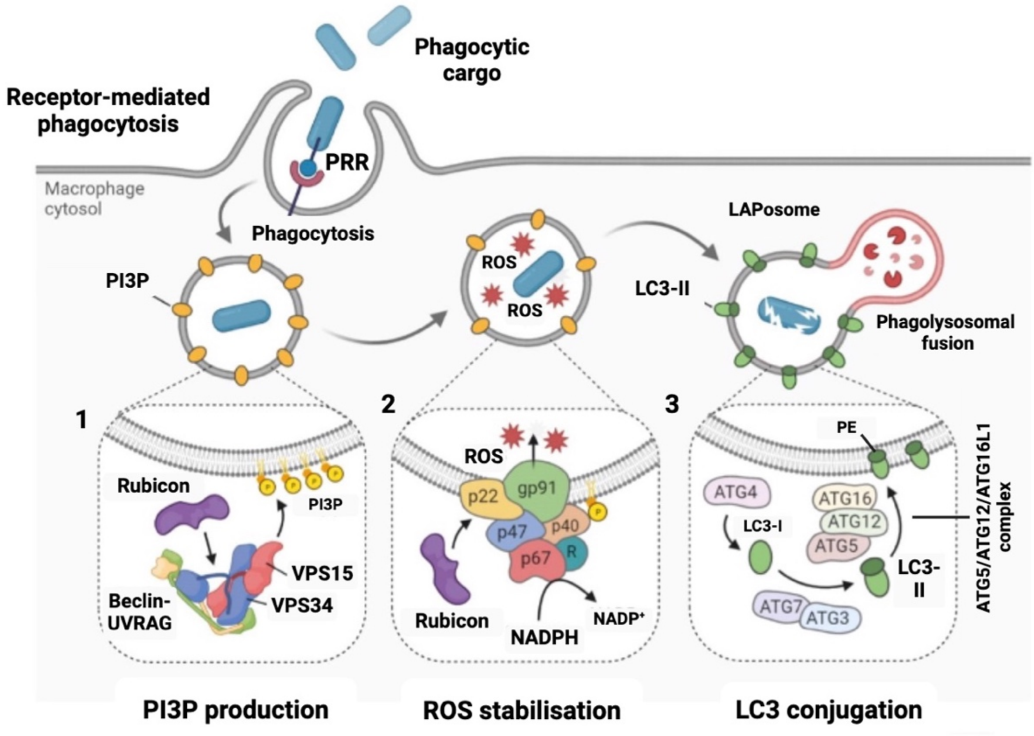

Figure 1.7 Overview of non-canonical autophagy – LC3-associated phagocytosis. (1) LAP is activated upon surface-specific receptor (TLRs, FcγR, dectin-1) recognition by Pattern Recognition Receptors (PRR). Initially, Rubicon is recruited and initiates the formation of the UVRAG-containing class III PI3K complexes, consisting of Beclin-1, VPS34, VPS15, Rubicon and UVRAG. The stability of the complex is maintained by Rubicon, which sustains the production of phosphatidylinositol 3-phosphate (PI3P) on the phagosome membrane. **(2)** PI3P production is critical for the stabilisation of the NOX2 complex (NOX2; Rac1; p47^{phox}; p40^{phox} and p67^{phox}), which favours the production of reactive oxygen species (ROS) in the lumen of the phagosome and enables the recruitment of the conjugation systems that participate in the processing and ligation of LC3 into the lumen of the phagosome. **(3)** The ATG5-ATG12-ATG16L and LC3-PE conjugation systems are both required for LC3 lipidation, which is a necessary step in the degradation of components by LAP. Cytosolic LC3 is conjugated by ATG4, to form LC3-I, which is then lipidated by ATG5-ATG12-ATG16L1 and ATG7-ATG3 to form LC3-II on the phagosomal membranes. Once the phagosome is decorated with the lipidated LC3-II, it can fuse with lysosome and thereby degrade the unwanted target material. Figure adapted from Grijmans et al. (2022). Figure created in BioRender.com.

than autophagy, which is commonly characterised by the presence of LC3-II puncta in the cytosol after 4 hours post autophagy induction (Martinez, 2020).

1.5.1 Mechanisms of LAP

Unlike autophagy, activation of LAP is not dependent on the regulation of the mTORC1-ULK1-ATG13 system, with LAP appearing unresponsive to nutrient starvation and other autophagic cues associated with ULK1 activation (Sanjuan et al., 2007). Instead, it is initiated by receptors located in the plasma membrane of the phagocyte, such as TLR (e.g., TLR1-TLR2 heterodimer, TLR2-TLR6 heterodimer and TLR4), TIM4 and FcγR (Sil et al., 2018). These receptors are present on the surface of certain cells – including, among others, macrophages, dendritic cells, and neutrophils (Figure 1.7). The initiation of LAP is activated in response to the ligation of cell surface receptors with apoptotic cells or pathogens during phagocytosis (Heckmann et al., 2017). For instance, pattern recognition receptors (PRR) engage with the pathogen-associated molecular patterns (PAMPs) on pathogens, while immunoglobulin receptors specifically bind to antigens (Figure 1.7). Similarly, TIM4 receptors target phosphatidylserine (PtdSer) found on apoptotic cells (Sil et al., 2018).

Following receptor recognition in LAP, the first complex to associate with the budding of the phagosome is the PI3K complex (Figure 1.7) (Grijmans et al., 2022; Lei and Klionsky, 2022). Here, the PI3K complex of LAP is composed of VPS34, VPS15, UVRAG, Rubicon and Beclin-1 (Figure 1.7) (Lei and Klionsky, 2022). Following TLR signalling, Rubicon binds to p22phox subunit of the nicotinamide adenine dinucleotide phosphate (NADPH) oxidase complex (NOX2; Rac1; $p47^{phox}$; $p40^{phox}$ and $p67^{phox}$), leading to the generation of reactive oxygen species (ROS) in the lumen of the phagosome (Figure 1.7) (Yuan et al., 2022).

Concurrently, following activation by VPS15 and Beclin-1, VPS34 generates PI3P, which creates a binding site for the N-terminal of p40phox, thereby stabilising the NADPH complex (Figure 1.7) (Wang et al., 2022). Moreover, PI3P molecules distribute throughout the phagosome membrane, creating a label for future LC3-conjugation (Grijmans et al., 2022). ROS formation is a critical intermediatory step exclusive to LAP, as it is crucial for LC3 lipidation on phagosomes (Heckmann et al., 2017). The stabilisation of the NADPH complex maintains a stable generation of ROS, which results in the increase of the pH inside the lumen of the phagosome (Wang et al., 2022). It is believed that this pH increase, and ROS production causes the recruitment of the ATG12-ATG5-ATG16L1 complex to the phagosome, required for the conjugation of LC3 to PE (Figure 1.7) (Wang et al., 2022). Now that the phagosome is decorated with LC3-II, it can be termed the LAPosome, with LC3-II mediating the rapid fusion of the LAPosome with the lysosome (Figure 1.7) (Romao and Münz, 2014).

1.5.2 *ATG16L1*

As previously mentioned, LAP requires E3-like activity of the ATG12-ATG5-ATG16L1 (~ 800 kDa) complex, which enables the binding of LC3 to membranes. The mammalian *ATG16L1* gene is situated on the long arm of chromosome 2 at position 37.1 (2q37.1) (Li et al., 2017). It encodes ATG16L1, a crucial component of a large protein complex that is necessary for autophagy (Moazeni-Roodi et al., 2019). It can be separated into three key domains that collaborate to fulfil the distinct functions of ATG16L1 (Gammoh, 2021). The key domains include an N-terminal region containing the ATG12-ATG5 conjugate, a middle region comprised of a coiled-coil domain (CCD) that can bind to WIPI2 and seven WD40 repeats, located in the C-terminal (Figure 1.8).

ATG16L1 can function as a molecular hub by utilising various domains that enable it to fulfil both functions in canonical and non-canonical autophagy (Hooper et al., 2022). During autophagy, ATG16L1 uses its CCD containing the WIPI2 and FIP200 binding sites, to form double-membraned autophagosomes (Figure 1.8) (Lei and Klionsky, 2022; Moazeni-Roodi et al., 2019). Recently, a study by Fletcher and co-workers discovered the uncertain role of the WD domain within ATG16L1 (Fletcher et al., 2018). They revealed that the WD domain of ATG16L1 is crucial for LC3 recruitment to endolysosomal membranes during LAP. Results further demonstrated that a K490A point mutation did not appear to influence canonical autophagy, thus providing the first means to genetically distinguish between canonical and non-canonical autophagy.

1.5.3 ATG16L1^{E230} mouse model

For some time, it proved difficult to study the effects of LAP on cellular and tissue homeostasis *in vivo*. Former PhD student Dr Maryam Arasteh, from the Wileman lab, generated the first LAP-deficient mouse model that enabled research for LAP-deficiency to be conducted *in vivo* (Arasteh, 2012). This was done by inserting two stop codons in frame at the end of the CCD domain of *ATG16L1*, which permits the translation of the E230 glutamate residue, yet prevents the translation of the linker region and WD domain of ATG16L1, required for LAP function (Figure 1.8) (Rai et al., 2019). This mouse model was later named the ATG16L1^{E230} model, which will be described as ΔWD for the remainder of this thesis, as it lacks the WD domain of ATG16L1. Rai and colleagues revealed that these mice exhibit normal growth and body weights, as well as fully functioning autophagy (i.e., maintained levels of LC3 and SQSTM1/p62), when compared to their littermate controls (Rai et al., 2019). The ΔWD mouse model has been widely used to examine the effects of the removal of the WD domain of ATG16L1 on tissue homeostasis, influenza infection and neurodegenerative disorders (Heckmann et al., 2020; Rai et al., 2019; Wang et al., 2021).

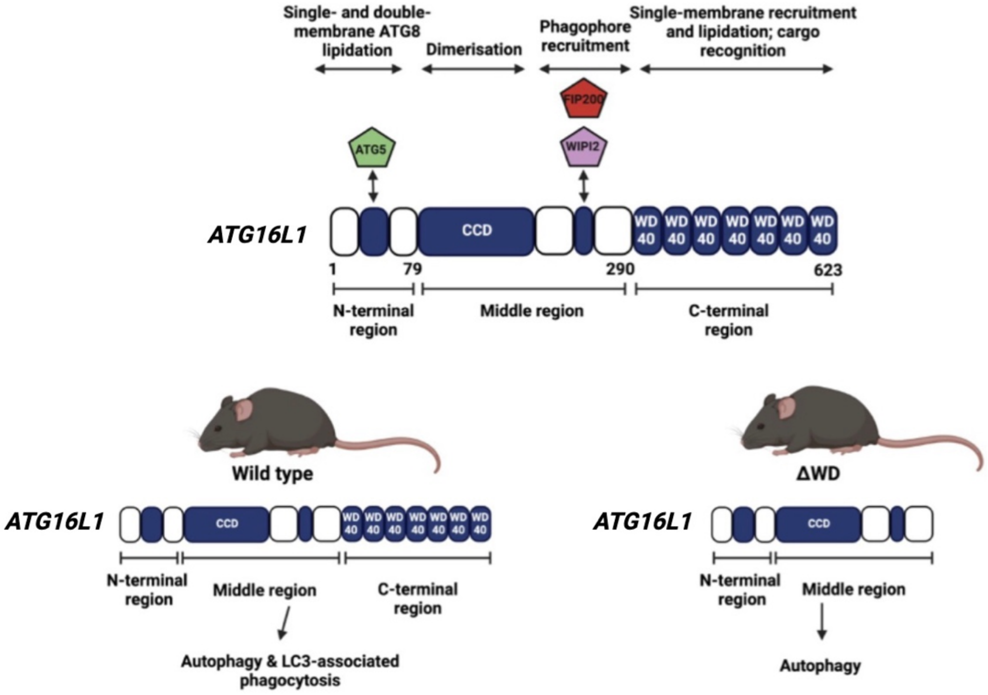

Figure 1.8 Graphical representation of *ATG16L1*, highlighting the key domains required for canonical autophagy and LC3-associated phagocytosis. Overview of *ATG16L1* showing N-terminal and CCD region required for autophagy. The WD domain in the C-terminal have been shown to be required for LAP but dispensable for autophagy. All three domains are present in WT ATG16L1^{E230} mice, while in the ATG16L1^{E230} (known as ∆WD) the WD domain is absent, therefore causing LAP deficiency. Figure created in BioRender.com. Figure taken from Conway et al. (2024).

1.5.4 The role of LAP in inflammation, infection & tissue homeostasis

The principal objective of phagocytosis is the degradation extracellular cargoes, such as pathogens and apoptotic cells, aiming to preserve homeostasis. It is believed that LAP has a key role in the clearance of pathogens, as studies have demonstrated that Dectin-1 is involved in fungal clearance, with zymosan inducing LAP (Sanjuan et al., 2007). Moreover, *Aspergillus fumigatus* and *Candida albicans* are also recognised by the phagocytic receptor Dectin-1, leading to the internalisation of the fungi, resulting in the increase in ROS production and simultaneous Rubicon recruitment and LC3 processing (Sanjuan et al., 2007; Sprenkeler et al., 2016). The function of LAP in skin pigmentation and melanin transfer has not yet been studied; however, it has been investigated in the context of fungal melanin (Akoumianaki et al., 2016; Kyrmizi et al., 2018). Research on *Aspergillus fumigatus* has shown that fungal cell melanin can induce LAP blockage by preventing NOX2 recruitment and inhibiting the NADPH oxidase complex (Akoumianaki et al., 2016; Kyrmizi et al., 2018).

Additionally, previous work has demonstrated that influenza A virus-induced LC3 lipidation was independent from FIP200 required for autophagy and emphasised that LAP was activated upon influenza A virus infection via a M2 protein channel-dependent mechanism (Beale et al., 2014; Fletcher et al., 2018). This was further confirmed *in vivo* using the ∆WD LAP-deficient mouse model, which demonstrated that loss of LAP from all tissues render the mice highly susceptible to influenza A virus infection (Wang et al., 2021).

Macrophages play a fundamental role in eliminating apoptotic cells, through a process known as efferocytosis, a critical component for the maintenance of tissue homeostasis (Asare et al., 2020). Efferocytosis is a term that is commonly used to describe the engulfment and clearance of apoptotic cells by phagocytes. Moreover, it is believed that elements of autophagy are recruited and participate in phagosome formation during efferocytosis. This phenomenon occurs as neighbouring cells release signals, consequently enhancing the efficiency of the engulfment process (Asare et al., 2020). A study by Cunha and colleagues revealed that aberrations in LAP restrict tumour immunosuppression afforded by efferocytosis, indicating that LAP may be an influential contributor to the signals that are released upon engulfment of apoptotic cells during efferocytosis (Cunha et al., 2018). LAP mediates immunoregulation in response to apoptotic cells, with LAP deficient mice (∆WD) accumulating apoptotic bodies in their tissues, and within the cytosol of phagocytic cells, thereby creating a tumour-supporting environment in acute myeloid leukaemia (Moore et al., 2022).

With regards to tissue homeostasis, as previously discussed, LAP defective mice (ΔWD) exhibit comparable body weights and normal growth rates, when compared to their littermate controls (Rai et al., 2019). In addition, they maintain tissue homeostasis (e.g., brain, liver, and kidney) independently from LAP, with comparable levels of autophagy markers (i.e., LC3 and p62) expressed across the LAP-deficient tissues.

1.6 Hypothesis and Project Aims

The mammalian skin undergoes constant cellular turnover to maintain its crucial function of protecting the body from mechanical stresses, pathogens, and thermoregulation. Prior work has focused on the involvement of autophagy on epidermal homeostasis and melanogenesis, yet much of the work had been done prior to the characterisation of the WD domain of *ATG16L1* and its involvement in LAP. LAP plays a fundamental role in facilitating the clearance of apoptotic cells and pathogens. Its versatile capability to engulf diverse cargoes, spanning from fungi and viruses to apoptotic cells, emphasises its significance in cellular physiology. We know that several studies have indicated that melanosomes enter the keratinocytes via phagocytosis and are subsequently transported to the perinuclear region where they are degraded. Studies have also demonstrated that autophagy is active during the process of terminal differentiation, giving rise to the epidermal permeability barrier.

Therefore, this PhD work aims to use the ΔWD mouse model to investigate the specific role and function of LAP in (1) preserving epidermal homeostasis, and (2) the uptake and trafficking of melanosomes by epidermal keratinocytes. The ΔWD mouse model will allow the analysis to be conducted both *ex vivo* and *in vitro,* by utilising primary mouse cultures and skin tissue. We hypothesise that the removal of the WD domain of *ATG16L1* will result in an impaired epidermal barrier. Moreover, we believe that melanosomes will be internalised by keratinocytes in a single-membraned vacuole, decorated with LC3.

The specific objectives within the project were:

1. To examine the overall histology of the integumentary system of WT and LAP-deficient mice.
2. To characterise the impact of the removal of the WD domain of *ATG16L1* on the overall of the skin barrier function.
3. To determine the impact of the loss of the WD domain of *ATG16L1* on the dermal biomechanics.
4. To examine the effects of the removal of WD domain of *ATG16L1*, resulting in LAP-deficiency, on melanosomal uptake and trafficking in primary keratinocytes and their subsequent processing.

By furthering our understanding of the role of LAP in epidermal homeostasis and pigmentation, this work will aid in identifying future therapeutic targets for pigmentation and skin disorders.

Chapter 2: Materials and Methods

2.1 Laboratory consumables

2.1.1 Chemicals, reagents, and materials

All chemicals and reagents were obtained from ThermoFisher (UK), Sigma-Aldrich (UK), PCR Biosystems (UK), Lonza (UK), Cell Signalling Technology (UK) and Proteintech (UK), unless stated otherwise. For detailed product description, please refer to Table 2.1-2.4.

2.1.2 Lab instruments

Table 2.1. Lab instruments used within project.

Instrument	**Supplier**
Centrifuge 5424R	Eppendorf
Centrifuge 5810R	Eppendorf
ChemiDoc Imaging System	Bio-Rad
ChemiDoc-It®2 810 Imager	Ultra-Violet Products Ltd
Cobas 6000	Roche
Cutometer MPA580	Courage and Khazaka Electronic GmbH
Dry block heating system QBD series	Grant
Incubator	Fisherbrand
Microm EC 350 Modular Tissue embedding center	ThermoFisher Scientific
Microtome HM 355S	Leica Microsystems
Nanodrop 2000	Thermo Scientific
Odyssey CLx Imager	LI-COR Biosciences
Platform shaker	Stuart Scientific
PowerPac™ Basic Power Supply	Bio-Rad
QuantStudio™ 3 Real-Time PCR System	Thermo Scientific
Shaking incubator	ThermoFisher Scientific
SpectraMax M2 spectrophotometer	Molecular Devices
Thermo-cycler, Veriti 96 well	Applied Biosystems
Tissue Lyser	Qiagen

Trans-Blot Cell	Bio-Rad
Ultrasonic homogeniser Soniprep 150	MSE
Vortex	Scientific industries
Water bath sonicator	Fisherbrand
Wheel rotator	Marshall Scientific
Xcell SureLock Mini	ThermoFisher Scientific

2.1.3 Lab consumables

Table 2.2. List of consumables used within project.

Lab consumables	**Supplier**	**Product code**
40 µm cell strainer	Corning	352340
70 µm cell strainer	Corning	352350
96-well plate	Greiner	650160
BioLite 6-well multidish	ThermoFisher Scientific	130184
Bolt™ 4-12% Bis-Tris, 1.0 mm Mini Protein Gel, 10 well	Invitrogen	NW 0412 BOX
Coverslips rectangle	Dixon	NPS09/1818
Eppendorf Safe-lock tubes	Fisher Scientific	10430423
Histology Cassette	Simport	M490-12
Immobilon Transfer Membrane (PVDF)	Sigma	IPFL0010
Inoculating loop	Fisher Scientific	12870155
MicroAmp optical 96-well reaction plate	Applied Biosystems	N8010560
MicroAmp optical adhesive film	Applied Biosystems	4311971
Microscope Coverslips circular 13 mm	VWR	MARI0111530
Microtome bladed MX35 Ultra	Epredia	3053835
Millex 0.20 µm pore size filter	Sigma	SLGSM33SS

Nunc 24-well plate	ThermoFisher Scientific	140682
Nunc 6-well plate	ThermoFisher Scientific	140680
Nunc™ Lab-Tek™ II Chamber slides 2 well	ThermoFisher Scientific	154852PK
Petri-dish	ThermoFisher Scientific	11901518
T25 cell culture flask Nunc EasYFlask	Fisher Scientific	12034917
T75 cell culture flask Nunc EasYFlask	Fisher Scientific	10538931
Tungsten Carbide bead	Qiagen	69997

2.1.4 Lab reagents

Table 2.3. List of lab chemicals and reagents used within project.

Chemical/Reagent	**Supplier**	**Product code**
0.1 M DTT	Invitrogen	18080093
0.25 % Trypsin/EDTA	Invitrogen	25200072
10 % Neutral Buffered Formalin	Sigma	HT 501128
100X antibiotic-antimycotic	ThermoFisher Scientific	15240096
10X DreamTaq Buffer with MgCl2	Fisher Scientific	EP0702
18S primer	Sigma	custom order
4’,6-diamidino-2-phenylindole (DAPI)	ThermoFisher Scientific	62248
5X first strand buffer	Invitrogen	18080093
Acetic Acid, glacial	Fisher Scientific	11337558
Agarose	Fisher Scientific	10688973
Ampicillin	Sigma	A9393-5G
β-mercaptoethanol	Sigma	444203
Bovine Serum Albumin (BSA)	Sigma	A7906
Bradford Reagent	Sigma	B6919-500 mL
Bromophenol blue	Sigma	B5525
Calcium chloride dihydrate	Fisher Scientific	10403265
Calcium Gen 2	Cobas (Roche)	05061482 190
Calcium-free MEM Eagle with Earle's BSS	Lonza	BE 06-174G
Chelex-100 sodium form	Sigma	C7901
Chloroform	Fisher Scientific	10219900

Clarity Western ECL Substrate	Bio-Rad	1705061
Collagen Type I Rat Tail	BD Biosciences	354236
cOmplete Inhbitor tablets, mini EASYpack	Roche	4693124001
dNTP (25 mM)	Fisher Scientific	R1121
DPX mounting medium	Fisher Scientific	SP 15-100
DreamTaq DNA Polymerase	Fisher Scientific	EP0702
Dulbecco's Modified Eagle Media (DMEM) GlutaMAX	Gibco	31966-021
Eosin Y solution aqueous	Sigma	HT110232-1L
Ethanol absolute	Fisher Scientific	10233962
Ethidium bromide	Fisher Scientific	11416750
Ethylenediaminetetraacetic acid (EDTA)	Fisher Scientific	10213570
Fetal bovine serum	Sigma	F7524
Fluoromount-G	Invitrogen	00-4958-02
Glycerol	Fisher Scientific	10021083
Glycine	Fisher Scientific	10061073
Glycoblue (20 µg/ µl)	Invitrogen	AM 95-15
Histoclear II	National Diagnostics	HS 202
Hydrochloric Acid	Fisher Scientific	10053023
Hydrogen peroxide	Acros Organics	202460010
Hyperladder	Bioline	BIO-33053
Kanamycin (50 mg/mL)	ThermoFisher Scientific	J67354-AE
KBM Keratinocyte serum-free media & SingleQuots	Lonza	CC-3104
KiCqstart SYBR Green Primers	Sigma	KSPQ12012
L-glutamine	Gibco	A29168-01
LB agar Miller	Formedium	LMM 0202
LB broth Miller	Formedium	LMM 0102
Lipofectamine 2000	Invitrogen	11668-027
LysoTracker™ Blue DND-22	ThermoFisher Scientific	L 7525
Mayer's Haematoxylin	Sigma	1.09249.1000
Methanol	Fisher Scientific	L13255
Nuclease-free water	Invitrogen	AM9932
Nuclease-free water	Stemcell	79001
NuPAGE™ MES SDS Running Buffer (20X)	Invitrogen	NP 0002
Opti-MEM reduced serum free medium	Gibco	31985-047
Orange G	Sigma	O3756
PageBlue Protein Staining Solution	ThermoFisher Scientific	24620
Paraffin wax	Sigma	P3558
Paraformaldehyde	Sigma	158127-500G
Penicillin-streptomycin	Gibco	15140-122
Phosphate Buffered Saline	Oxoid	BR0014G
Ponceau S	Sigma	P7170
Precision Plus Protein Dual Colour Standard	Bio-Rad	1610374

qPCRBIO SyGreen Mix Lo-ROX	PCR Biosystems	PB20.11-05
Random hexamers 50 µm	Invitrogen	N8080127
RNAase OUT recombinant	Invitrogen	1077019
RNAlater	ThermoFisher Scientific	AM7021M
RPMI-1640	Sigma	R0883-500 mL
Skimmed milk powder	Oxoid	LP0031
Sodium chloride	Fisher Scientific	10316943
Sodium deoxychloate	Sigma	D6750
Sodium dodecyl sulfate (SDS)	Fisher Scientific	10356463
Sodium fluorescein	Sigma	46960
Superfrost™ Plus Adhesion Microscope Slides	Epredia	J1800AMNZ
SuperScript II RT	Invitrogen	18080093
Tetracycline hydrochloride	Sigma	T7660-25G
Toluidine Blue O	Sigma	T3260
Tri-sodium citrate (dihydrate)	Fisher Scientific	10396430
Tris base	Fisher Scientific	10336793
Tris-EDTA (TE) buffer	Fisher Scientific	BP 2473
Triton X-100	Sigma	T8787-100 mL
TRIZol Reagent	Invitrogen	15596018
Trypsin 0.25% without EDTA in hank's salts	Speciality Media	SM-2001-C
Trypsin-EDTA 0.25%	ThermoFisher Scientific	25200056
Tween 20	Fisher Scientific	10419000
Urea	Fisher Scientific	11469493
Vectashield with DAPI	Vector Labs	H-1200
Videne	Ecolab	3030440
β-mercaptoethanol	Sigma	7154

2.1.5 Kits

Table 2.4. List of kits used.

Kit	**Manufacturer & Product Code**
GenElute Total RNA Purification Kit	Sigma-Aldrich, RNB100
qPCRBIO SyGreen Mix Lo-ROX	PCR Biosystems
Maxi Prep	Macherey Nagel (740416.2)
Calcium Gen.2	Roche Cobas C 111

2.1.6 Frequently used buffers and solutions

Solutions used throughout the PhD were prepared with double dH_2O unless stated otherwise (Table 2.5).

Table 2.5. Compositions of solutions and buffers. All solutions are made up with double dH_2O unless stated otherwise.

Reagent	Formula	Reagent	Formula
DNA Lysis Buffer (Genotyping)	100 mM Tris-HCL pH 8.5, 5 mM EDTA pH 8.0, 0.2% SDS, 200 mM NaCl, 100 μg/mL Proteinase K in nuclease free water (NFW)	10X TBS-T	1.5 M NaCl, 200 mM Tris Base, 1% Tween-20
50X TAE Buffer	242 g Tris Base, 100 mL 0.5 M EDTA pH 8.0, 57.1 mL Acetic Acid	1X NuPAGE MES Running Buffer	50 mL 20X NuPAGE MES Running Buffer
Ethidium Bromide (EtBr) Solution	1X TAE, 30 μl EtBr solution	10X Transfer Buffer	250 mM Tris Base, 1.92 M Glycine, 20% Methanol
DNA Loading Buffer Orange G	50% (v/v) Glycerol, 1X TAE, 0.25 g Orange G	Blocking Buffer WB	5% semi-skimmed milk powder in 1X TBS-T 5% BSA in 1X TBS-T
0.02 M Acetic acid	Glacial Acetic Acid in 500 mL ddH_2O	Blocking Buffer IHC	10% Goat Serum in 1X PBS
0.06 M Calcium chloride	0.88 g calcium chloride in 1X PBS	Blocking Buffer ICC	5% Goat Serum, 0.3% Triton X-100 in 1X PBS
10 mg/mL Tetracycline hydrochloride	0.1 g Tetracycline Hydrochloride (Sigma) in 10 mL 70% Ethanol	Antibody Dilution Buffer IHC	1% BSA, 0.3% Triton X-100 in 1X PBS
6.5 M Urea Buffer	7.808 g Urea, 1 mM DTT, 50 mM Tris-HCL pH 7.4, 2 cOmplete Inhibitor tablets, Mini *EASYpack* (Roche)	0.1 M Citrate Buffer	10 mM tri-sodium citrate, 0.05% Tween-20 pH 6.0
1X PBS	10 Phosphate Buffered Saline Tablets in 1 L double dH_2O	Permeabilisation Solution IHC	0.5% Tween-20 in 1X PBS
RIPA Buffer	1% Triton X-100, 0.5 g Na Deoxycholate, 0.1 g SDS, 0.6 g Tris Base, 0.88 g NaCl & 2 cOmplete Inhibitor tablets, Mini *EASYpack* (Roche)	PCR Reaction Mix Genotyping	Primer Mix (10 mM), 10 X DreamTaq Buffer (ThermoFisher Scientific), dNTP (25 mM), DreamTaq Polymerase, NFW, DNA 1:20

2.1.7 Oligonucleotides used

Table 2.6. List of KiCqStart SYBR Green primers (Sigma) used.

Gene	**Sequence (5’-3’)**
18S	Forward: GCCGCTAGAGGTGAAATTCTTG Reverse: CATTCTTGGCAAATGCTTTCG
KRT5	Forward: GTGATGTTGAAGAAGGATGTG Reverse: TTCATGAAGTTGATCTCGTC
KRT10	Forward: CAATCAGAAGAGCAAGGAAC Reverse: CAGTGATTTCAGACTTATGGC
KRT1	Forward: CTACCAAATGGAAATGTCTCAG Reverse: GTAAAAGGTCTCAGCTTCAG
IVL	Forward: CTGTGAGTTTGTTTGGTCTAC Reverse: GAAAGCCCTTCTCTTGAATC

2.1.8 Plasmids used

Table 2.7. List of plasmids used.

Plasmid	**Plasmid size (kb)**	**Insert size (bases)**	**Resistance**
Ocular Albinism type 1 (OA1)-mCherry (Gifted from Professor Elena Oancea, Brown University, USA)	5.100	1074	Ampicillin

2.1.9 Primary and Secondary Antibodies used

Table 2.8. List of antibodies used with their desired dilutions.

Primary/Secondary	**Name**	**Dilution**	**Manufacturer**
Primary	Rabbit polyclonal LC3AB	1:1000 (WB) 1:500 (ICC)	Cell Signaling Technology (CST) (4108)
Primary	Rabbit LC3B	1:500 (IHC)	Sigma Aldrich (L7543)
Primary	Rabbit anti-Cytokeratin 10	1:10000 (WB) 1:500 (IHC)	Abcam (76318)
Primary	Rabbit Anti-Keratin 5	1:1000 (WB)	Sigma Aldrich (SAB4501651)
Primary	Rat LAMP1	1:500 (IHC)	Abcam
Primary	Rabbit Rab27a	1:800 (IHC)	Cell Signaling Technology (CST) (69295)
Primary	Mouse ATG16L	1:1000 (WB)	MBL (M150-3)
Primary	Rabbit SQSTM1/P62	1:1000 (WB)	Cell Signaling Technology (5114S)
Primary	Rabbit Akt	1:1000 (WB)	Cell Signaling Technology (9272S)
Primary	Mouse p-Akt (Ser 473)	1:1000 (WB)	Proteintech (66444-1-IG)
Primary	Mouse β-actin	1:10000 (WB)	Sigma (A1978)
Primary	Rabbit PCNA	1:200 (IHC)	Proteintech (24036-1-AP)
Primary	Phalloidin Atto 647N	1:400 (IHC)	Sigma (65906)
Secondary	Goat anti-rat Alexa Fluor 405	1:1000 (IHC)	Abcam (ab 175673)
Secondary	Goat anti-rabbit Alexa Fluor 488	1:1000 (IHC)	Invitrogen (2110498)

Secondary	Donkey anti-rabbit Alexa Fluor 594	1:1000 (IHC)	Invitrogen (A21207)
Secondary	800CW Goat anti mouse IgG H+L	1:10000 (WB)	Li-Cor (926-32210)
Secondary	680RD Goat anti-rabbit IgG H+L	1:10000 (WB)	Li-Cor (926-68071)
Secondary	Anti-rabbit IgG HRP-linked antibody	1:10000 (WB)	Cell Signaling Technology (7074P2)
Secondary	Anti-mouse IgG, HRP-linked antibody	1:10000 (WB)	Cell Signaling Technology (7076S)

2.1.10 Culture media – mammalian cell culture

Table 2.9. Cell culture growth medias.

Cell Line/Primary Cell	**Composition**
1014 murine melanoma	RPMI-1640, 10% (v/v) heat inactivated Fetal Bovine Serum (FBS), 1% penicillin/streptomycin (P/S), 1% L-glutamine (2 mM).
ATG16L1 KO Mouse embryonic fibroblasts (MEF)	Dulbecco’s Modified Eagle Media (DMEM), GlutaMAX, high glucose (4.5 g/l), 10% heat inactivated FBS, 1% P/S.
XB-2 Mouse Keratinocytes (ATCC)	DMEM, GlutaMAX, high glucose (4.5 g/l), 20% heat inactivated FBS, 1% P/S, 1% L-glutamine (2 mM).
Primary Mouse Keratinocytes (ATG16L1$^{\Delta WD}$)	Low calcium keratinocyte media (0.05 mM): EMEM without L-glutamine, 10% heat inactivated chelated FBS, 1% P/S, 1X Antibiotic-Antimycotic KBM Keratinocyte serum-free media with SingleQuots™ Supplements (concentrations are proprietary).

HEK-293	Dulbecco's Modified Eagle Media (DMEM), GlutaMAX, high glucose (4.5 g/l), 10% heat inactivated FBS, 1% P/S.

2.1.11 For bacterial growth

LB broth Miller was used for the culture of *E. coli* (DH5α). LB agar Miller was used for pouring agar plates. All bacteria were grown in a concentration of 10 μg/mL of Ampicillin.

2.2 Methods

2.2.1 Genotyping

2.2.1.1 Mice

All experiments were performed in accordance with UK Home Office guidelines and under the UK Animals (Scientific procedures) Act 1986. The generation of the ATG16L1$^{\Delta WD}$ mice has been previously described (Rai et al., 2019). Generation and breeding of mice for the genotype was approved by the University of East Anglia Animal Welfare and Ethical Review Body and performed under UK Home Office Project License 70/8232.

2.2.1.2 Extraction of mouse genomic DNA

Mouse tails were digested overnight at 55 °C in 100 µl of DNA lysis buffer (Table 2.5) The following day, the lysates were vortexed vigorously and diluted 1:20 in nuclease free water.

2.2.1.3 Primer information and Polymerase Chain Reaction (PCR) set-up

Table 2.10. Primer information and PCR cycle set-up.

Oligonucleotide Primers **(290 - 291)**	**290 (forward):** 5'-CAAATATGCCTTCAGAACTG **291 (reverse):** 5'-GCTGTAGTTCCAATCCCTAA
PCR Program: Touchdown PCR (The Annealing temperature decreases from 65°C to 56°C at a rate of 1°C/cycle)	95°C – 3 minutes 95°C – 45 seconds 10 Cycles 65°C – 45 seconds (decreases 1°C/cycle) 72°C – 1 minute 25 Cycles 95°C – 45 seconds 55°C – 45 seconds 72°C- 1 minute 72°C- 10 minutes 4°C – forever (hold)

As per manufacturer's instructions of the DreamTaq Polymerase PCR kit, 3 μl of the 1:20 diluted tail lysate was used per 50 μl of total PCR reaction mix. This was used as a template for the PCR using the defined oligonucleotide primers shown in the table above (Table 2.10). The PCR reaction mix was prepared according to table 2.5 and the Touchdown PCR program (Table 2.10) was performed using the thermo-cycler. PCR products were either stored at 4°C until further processing or were processed immediately.

2.2.1.4 Agarose Gel Electrophoresis

The agarose gel was cast by boiling 1% agarose in 1X TAE buffer (Table 2.5). Prior to loading, each PCR product was mixed with 10 μl Orange G loading dye (Table 2.5). Samples were separated by gel electrophoresis alongside a 1 kb standard DNA size hyperladder. Samples were run at a constant 150 V for 40 minutes, using the PowerPac™ and stained in ethidium bromide solution (Table 2.5) for 30 minutes. Gels were visualised with a

ChemiDoc-It®2 810 Imager, equipped with an ultraviolet light source and camera that enabled the imaging of DNA bands.

2.2.2 Timed mating of WT and ΔWD E18.5 embryos

All ATG16L1$^{\Delta WD}$ mice (C57BL/6) were sourced from the Biomedical Research Centre animal facility. For the timed pregnancy, the trio-mating method (one male with two females per genotype) was used. Mating was set up the evening before the start of the dark cycle. Females were separated from the male mouse upon confirmation of a vaginal plug the following day. This is considered as gestation day 0.5 (E0.5). If no plug was observed the female mouse was re-housed with the same sire for a maximum of five days. Embryos were harvested and sacrificed by anesthetic overdose (Euthatal, pentobarbital sodium, 200 mg in 1 ml) at E18.5, one day before birth to ensure the full development of the skin barrier, without the presence of hair follicles.

2.2.3 Recovering plasmid DNA from filter paper for transfection

2.2.3.1 Recovering plasmid DNA from filter paper

To recover plasmid DNA from filter paper, the marked circle area that contains the dried plasmid DNA was cut out. Using sterile tweezers, the filter paper was placed into a 1.5 mL Eppendorf, and 100 μl of Tris-EDTA (TE) buffer was added and vortexed thoroughly. The mixture was left to incubate for 5 minutes at room temperature. Following 5-minute incubation the mixture was vortexed again. 10 μl of the supernatant was removed for the transformation of bacteria and the preparation of a plasmid stock.

2.2.3.2 Transformation of DH5α with OA1-mCherry plasmid

DH5α competent cells were used for plasmid propagation. Here, DH5α were taken out of the – 80°C freezer and thawed on ice for 20-30 minutes. Ampicillin (10 μg/mL) agar plates were placed in the 37°C incubator to allow to heat up and the water bath was set to 42°C. 0.5 μl of OA1-mCherry plasmid DNA was mixed with 50 μl of DH5α competent cells in an Eppendorf. The mixture was gently mixed by flicking the bottom of the tube and was incubated on ice for 30 minutes. The solution was exposed to heat shock in the 42°C water bath for 45 seconds, followed by incubation on ice for 2 mins. 500 μl of LB broth Miller with no selection antibiotic was added to the DH5α competent cells and was left to grow at 37°C in a shaking incubator for 45 minutes. The incubated mixture was spread onto the Ampicillin (10 μg/mL) LB agar plates with a sterile inoculating loop and was incubated at 37°C overnight (12-18 hours). A single culture was inoculated following the method described in 2.2.3.3.

2.2.3.3 Inoculating a liquid bacteria culture

The following day, LB broth Miller was added to a 50 mL falcon tube and using a sterile tip, a single colony was selected from the LB agar plate. The tip was dropped into the liquid LB containing Ampicillin (10 μg/mL) and was mixed before loosely covering the culture with sterile cap that is not airtight. The bacterial culture was incubated at 37 °C for 8 hours in a shaking incubator at 300 rpm. After 8 hours, 300 mL of LB with Ampicillin (10 μg/mL) was inoculated with 300 μl starter culture. This was then further shaken at 300 rpm overnight (12- 18 hours) at 37°C.

2.2.3.4 Plasmid DNA purification - Maxi-Prep

Large-scale isolation of plasmid DNA was achieved using the Maxi-Prep kit from Macherey Nagel according to manufacturer’s instructions. Cells were pelleted at 4 °C by centrifugation at 6000 g for 15 minutes. The pellet was resuspended in 12 mL of resuspension buffer + RNase A S1. 12 mL of lysis buffer S2 was added to the suspension and was mixed by inverting the tube 6-8 times. The mixture was incubated at room temperature for 2-3 minutes. Pre-cooled (4 °C) neutralisation buffer S3 was added to the suspension and was mixed by inverting the lysate 6-8 times until a homogenous suspension containing an off-white flocculate was formed. The suspension was then incubated on ice for 5 minutes. The NucleoBond xtra column was equilibrated by applying the equilibration buffer N2 to the rim of the column filter. The bacterial lysate was loaded onto the wet filter and the filter was washed with 15 mL of N2 buffer. The filter was then removed, and the column was washed with 25 mL of wash buffer N3. The plasmid was eluted using the elution buffer N5 and collected in a new sterile falcon tube. 10.5 mL of room temperature isopropanol was added and vortexed thoroughly to precipitate eluted plasmid DNA. The eluted plasmid DNA was centrifuged at 15,000 g for 30 minutes at 4 °C. The supernatant was discarded, and 4 mL of room temperature 70% ethanol was added to the pellet. This was centrifuged at room temperature for 5 minutes at 15,000 g. The ethanol was carefully removed and the pellet was left to dry at room temperature for around 15-30 minutes. The dry pellet was later resuspended in 10 μl sterile deionized H_2O.

2.2.4 Tissue harvest and processing

2.2.4.1 Tissue harvest and preservation

Dissected mouse skin was placed in a histology cassette and fixed in 10% neutral buffered formalin (NBF) overnight at room temperature. The following day, the tissue was washed, dehydrated through a graded series of ethanol solutions (50% - 100%) and incubated in paraffin wax (Table 2.11). For the embedding process the Microm EC 350 tissue embedding center was used. Following overnight storage in paraffin wax, tissues were mounted one by one, in the correct orientation on top of a thin layer of partially solidified paraffin wax, in a designated plastic mould. The embedding cassette was placed over the tissue and covered in molten paraffin wax to finish the embedding process. Moulds were placed on a cooling platform to ensure the solidification of the wax, surrounding the tissue. This process enables the generation of a solid cuboidal block containing the skin tissue, which can be easily mounted onto a microtome HM355S and stored at 4°C for long-term storage.

Table 2.11. Processing method for fixed mouse skin tissue.

Time	**Solution**
90 min	PBS
45 min	50% Ethanol
45 min	70% Ethanol
45 min	95% Ethanol
90 min	100% Ethanol
45 min	Histoclear II

45 min	Fresh Histoclear II
45 min	Paraffin Wax
Overnight	Fresh Paraffin Wax

2.2.4.2 Tissue processing - Microtome

Prior to sectioning the tissue paraffin blocks were chilled at 4 °C for 1 hour. 5 µm tissue sections were cut using the microtome. For this, the microtome blades (MX35 Ultra) were used to cut the sections, which were floated on a warm water (42 °C) bath to remove any creases from the section. These sections were later carefully transferred onto coated glass slides (Superfrost™ Plus) and left to dry overnight at room temperature. Slides were labelled and stored at 4°C until further processing.

2.2.4.3 Haematoxylin and Eosin (H&E) stain

Tissue sections were H&E stained by dewaxing and rehydrating the slides in histoclear II and ethanol solutions (Table 2.12). Following rehydration, the slides were submerged in Mayers haematoxylin and Eosin Y solutions (Table 2.12). The slides were dehydrated prior to mounting them using coverslips and mounting medium (DPX). Sections were examined under the brightfield Apotome 3 Imager.Z2 microscope.

Table 2.12. H&E staining procedure for NBF fixed tissue embedded in paraffin wax.

Step Nr	**Solution**	**Time**
1	Histoclear II	2 min
2	100% Ethanol	20 s
3	95% Ethanol	20 s
4	80% Ethanol	20 s
5	70% Ethanol	20 s
6	50% Ethanol	20 s
7	Mayers Haematoxylin	4 min
8	Distilled water	20 s
9	0.5% Eosin Y + Acetic Acid	30 s
10	50% Ethanol	20 s
11	70% Ethanol	20 s
12	80% Ethanol	20 s

13	95% Ethanol	20 s
14	100% Ethanol	20 s
15	100% Ethanol	20 s
16	Histoclear II	5 min
17	Histoclear II (fresh)	5 min

2.2.5 Mammalian cell culture

2.2.5.1 Cell lines and their corresponding growth conditions and maintenance

1014 murine melanoma melanocytes, HEK 293, and primary WT and ΔWD mouse keratinocytes were cultured in the media listed in Table 2.9 above. The cells were cultured at 37 °C and 5% CO_2. When the cells were confluent, growth media was removed and 5 mL of 1X PBS was added. PBS was removed and replaced with 2 mL of 0.25% Trypsin/EDTA for no longer than 5 minutes at 37 °C and 5% CO_2. Trypsinisation was stopped by adding the appropriate growth media (Table 2.9) to the cells and cells were split to a desired ratio depending on their confluency. For trypsin inactivation in primary keratinocytes, EMEM Low Ca^{2+} media was used. The split cells were resuspended in their culture flasks for further propagation. Every trypsinisation was recorded by passage number.

2.2.5.2 Collagen coating of cell culture plates

6 well plates, T25 cell culture flasks and chamber slides were collagen coated by diluting collagen type I rat tail (3.56 mg/mL) in 0.02 M Acetic Acid (Table 2.5) to a final concentration of 50 μg/mL. The appropriate volume of the mixture was added to the culture dishes and was incubated at room temperature for 2 hours in a laminar flow hood. After 2 hours, the collagen mixture was aspirated, and the surfaces were rinsed with 1X PBS solution. After rinsing with 1X PBS, the solution was again removed, and the cell culture dishes and flasks were left to air dry in the laminar flow hood. Once they were dry, they were either used immediately or repackaged in the original packaging and stored at 4°C for later use.

2.2.5.3 Calcium depletion from fetal bovine serum (FBS) for primary keratinocyte growth media

Chelated serum was achieved by thawing 50 mL aliquot of FBS at 37 °C and adding 2 g of Chelex 100 sodium form. The solution was mixed overnight at 4°C on a wheel rotator. The next day the aliquot was spun at 2000 rpm for 10 minutes at room temperature and filtered through a 0.20 µm pore size filter. The FBS is now considered Ca^{2+} free and is ready to use, yet the calcium concentration was validated before usage in growth media, using the COBAS 6000 analyser.

2.2.5.4 COBAS 6000 – Calcium Gen.2 (CA2)

Calcium concentration was measured using the Calcium Gen.2 kit on the COBAS 6000 analyser. The analysis was kindly performed by Dr Isabelle Piec and Dr Nicole Ball. The measuring range for this kit is 0.20 – 5.0 mmol/L, with anything less than 0.20 mmol/L classified as calcium-free.

2.2.5.5 Primary keratinocyte isolation from mouse tail

To isolate tail skin keratinocytes, male and female mice were sacrificed, and the tail was completely removed. Upon removal, the tail was placed in a 1X PBS and Betadine (1:1) solution for 1 minute, followed by a rinse step in 1X PBS for 30 seconds. After washing the tail in 1X PBS, it was submerged in 70% ethanol and again rinsed with 1X PBS, before storing it in a Kanamycin solution (50 µg/mL) for further processing.

From the next step onwards, sterile conditions were crucial. An incision was made down the full length of the tail, using a scalpel, to expose the tail bone. Using sterile tweezers, the tail bone was removed from the skin and placed epidermal side down in a sterile petri dish. The hypodermal layer was gently removed before the remaining dermis and epidermis were transferred to a new sterile petri dish for trypsin incubation. Ice-cold 0.25% trypsin in hank's salts was added to the sterile petri dish and the tail skin was incubated for 2 hours at 37 °C and 5% CO_2. After incubation, the epidermis was peeled off with curved tweezers. The epidermis was removed and minced with sterile scissors and scalpels until fragments were small enough to pass through the tip of a 10 mL serological pipette. The minced epidermises were transferred into a 50 mL centrifuge tube and resuspended in low calcium (LoCa) keratinocyte growth media (0.05 mM) (Table 2.9). The resulting suspension was triturated and was subsequently spun down at 150 x g for 5 minutes at 4 °C. The supernatant was aspirated, and the pellet was resuspended in LoCa media and filtered through a 70 µm cell strainer into a new 50 mL centrifuge tube. The suspension was spun down again using the same settings, and supernatant was removed. The cell pellet was resuspended in LoCa media and filtered through a 40 µm cell strainer. Cells were counted and plated at a density of 0.3 x 10^6 for 6-well plates or 0.7 x 10^6 for T25 culture flasks. Initial plating of keratinocytes was done in KBM keratinocyte serum-free media (Table 2.9), and primary keratinocytes were incubated at 36°C in an atmosphere of 7% CO_2. Primary mouse keratinocytes were maintained in KBM keratinocyte serum-free media for live-cell imaging experiments.

2.2.5.6 Transfection of 1014 murine melanoma cells with OA1-mCherry plasmid

For method optimisation, the 1014 murine melanoma cells were seeded in antibiotic-free growth media (Table 2.9) at 0.3 x 10^5 cells per well, in a 24-well plate on glass coverslips. Cells were grown overnight at 37 °C and 5% CO_2 until they were around 50-80% confluent. A variety of plasmid concentrations (1; 2; 4 and 6 µg) were used to optimise transfecting OA1-mCherry into 1014 murine melanoma cells and were added to Opti-MEM reduced serum medium. DNA-lipid complexes were formed using Lipofectamine 2000, with 2.5, 3, 4 and 5 µl of Lipofectamine 2000 added to Opti-Mem reduced serum medium. The diluted OA1-mCherry was added to the diluted Lipofectamine 2000 at a 1:1 ratio and was left to incubate for 5 minutes at room temperature. The DNA-lipid complexes were then added to the cells and were left to incubate for 6 hours at 37 °C and 5% CO_2. A non-transfected and Lipofectamine control were run alongside the transfected cells. After 6 hours, the DNA-lipid complexes were removed and replaced with growth media without antibiotics. The media was removed after 24 hours and replaced with growth media with 1 µg/mL tetracycline. Fluorescence was confirmed by visualising the cells under the Zeiss Observer 7 widefield fluorescent microscope.

For the live-cell imaging experiment, a larger scale of OA1-mCherry positive melanosomes needed to be harvested following transfection. In a 6-well plate, 0.1 x 10^6 cells per well were seeded overnight at 37 °C and 5% CO_2 in antibiotic-free growth media. The cells were allowed to reach 70 – 80% confluency. The following day, the media was replaced, and the cells were washed with 1X PBS for 2 minutes. 1 μg of OA1-mCherry plasmid DNA was diluted in Opti-MEM serum-free medium. 2.5 μl of Lipofectamine 2000 was diluted in Opti-MEM serum-free medium and diluted OA1-mCherry was added to the diluted Lipofectamine 2000 at a 1:1 ratio. The DNA-lipid complexes were left to incubate for 5 minutes at room temperature before being added to the cells for 6-hour incubation at 37 °C and 5% CO_2. After 6 hours, the DNA-lipid complexes were removed and replaced with growth media without antibiotics. The media was removed after 24 hours and replaced with growth media with 1 μg/mL tetracycline. Cells were incubated for 3 days at 37 °C and 5% CO_2 before collecting the media for further usage in the live-cell imaging experiment.

2.2.5.7 Adenovirus LC3-GFP amplification

The GFP-LC3B adenovirus was generously gifted by Dr Helena Maier from the Pirbright Institute (Maier et al., 2013). The pAd/CMV/V5-DEST adenoviral expression vector (Invitrogen, V49320) was used by Maier et al. to generate the adenovirus LC3-GFP (Maier et al., 2013). To generate adenovirus LC3-GFP particle stock, HEK-293 cells were grown in two T75 culture flasks in their recommended growth media until they have reached 90% confluency (Table 2.9). The media was removed, and cells were washed with 1X PBS before replacing the media. 10 μl and 20 μl of adenoviral LC3-GFP pellet isolate was added to two T75 culture flask containing the HEK-293 cells. The cells were cultured for 5 days at 37 °C and 5% CO_2 until around 60% of the HEK-293 had lifted. The fluorescence was observed each day across the total of 5 days, to ensure viral infection. The cells were collected and transferred to two 15 mL falcon tubes and were centrifuged at 1000 rpm for 3 minutes. The supernatant was collected as it may contain up to 40% secreted virus. The cell pellets were resuspended in 0.5 mL of PBS and were transferred to a 1.5 mL Eppendorf. A small dry ice-methanol bath and 37 °C water bath was prepared for subjecting the cells to freeze and thaw cycles. The cell mixtures were exposed to 4 rounds of freeze and thaw cycles with each thaw or freeze cycle lasting 5 minutes. The cell mixtures were then centrifuged for 5 minutes at 5,000 g at room temperature. The viral isolate was transferred to a new sterile Eppendorf and were stored at – 80 °C.

2.2.5.8 Adenovirus LC3-GFP titration on 1014 murine melanoma cells

To establish the concentration required for efficient adenoviral transduction the newly acquired adenovirus LC3-GFP pellet isolate stock was titred using 1014 murine melanoma cells. 1014 murine melanoma melanocytes were cultured in a 24-well plate at 0.1 x 10^6 cells per well, at 37 °C and 5% CO_2 until 70-80 % confluency. Here, 2, 4, 6 and 8 μl of the adenoviral LC3-GFP pellet isolate was added to 1014 murine melanoma growth media. The mixture was incubated for 24 hours before confirming adenoviral transduction by fluorescence using the Zeiss Observer 7 fluorescent microscope. A no treatment cell control was run alongside these four concentrations.

2.2.5.9 Transduction of ATG16L1 KO MEF, 1014 murine melanoma cells, XB-2 Mouse keratinocytes and primary mouse keratinocytes

After establishing the optimum concentration required for efficient adenoviral LC3-GFP transduction, 1014 murine melanoma melanocytes, ATG16KO MEFS and XB-2 keratinocytes were cultured at 37 °C and 5% CO_2 in a 24-well plate at a seeding density of 0.1 x 10^6 cells per well. Primary WT and ΔWD keratinocytes were seeded at 0.1 x 10^6 cells per well and were cultured at 36 °C and 7% CO_2. The cells were transduced with 2 μl of adenovirus LC3-GFP pellet isolate and were incubated with the adenovirus LC3-GFP for 24 hours before removing the media and replacing with the required growth media for further processing (Table 2.9).

2.2.5.10 Chloroquine treatment

After adenovirus LC3-GFP transduction, primary mouse keratinocytes were exposed to a lysosomal inhibitor chloroquine. The cells were incubated in growth media with the addition of 100 mM of chloroquine for 2 hours at 36 °C and 7 % CO_2 for mouse primary keratinocytes. Following 2-hour incubation, the chloroquine mixture was removed and replaced with fresh growth media.

2.2.5.11 Live-cell experiment

WT and ΔWD primary keratinocytes were seeded in collagen coated chamber slides at a density of 0.1 x 10^6 cells/ well. Cells were cultured for 3 days and were subsequently transduced with adenovirus LC3-GFP for 24 hours, as described in section 2.2.5.9. The following day, the adenoviral media was removed and replaced with KBM keratinocyte media and LysoTracker™ Blue DND-22 (50 nM) for 30 minutes at 37 °C (Table 2.9). The media was removed and replaced with KBM keratinocyte media and RPMI-1640 OA1-mCherry melanosome media (1:1) that had been previously collected (see section 2.2.5.6). The time-course was captured over 24 hours, imaging every hour, to monitor the melanosomal dynamics within the primary keratinocytes. The timelapse experiment was imaged using the Zeiss LSM 980 Airyscan 2 and analysed using ImageJ2 (v.2.14.0/ 1.54f).

2.2.6 Microscopy and immunofluorescence

All fluorescent, phase, scanning electron microscopy and brightfield images presented within this project were captured using a Zeiss Apotome 3 Imager Z2, Zeiss Axioplan 2, Zeiss Observer 7 widefield, Zeiss Gemini 300 scanning electron microscope and Zeiss LSM 980 Airyscan 2. Software program used to capture images was Zen 3.9. Images in each experiment were captured with the same camera settings, exposure time, and same laser intensity. All exported images were saved as TIFF files for processing in ImageJ (v.2.14.0/1.54f) (Schindelin et al., 2012).

2.2.6.1 Immunohistochemistry on paraffin-embedded tissue sections

5 μm tissue sections mounted on coated-glass slides, were dewaxed, and rehydrated by immersing them through the solutions listed in the table 2.13 below. Once rehydrated, the sections had undergone heat-induced antigen retrieval, to unmask the epitopes that had been tied up in crosslinks formed by formaldehyde fixation. 0.1 M citrate buffer (pH

6.0) was heated to 95 °C and tissue sections were placed in the antigen retrieval buffer for 10 mins at 95 °C. After 10 minutes they were left to cool in the buffer for 25 minutes before proceeding with permeabilisation and blocking. Tissue sections were then washed in 1X PBS for 5 minutes and then permeabilised with permeabilisation solution (Table 2.5) for 15 minutes. Following permeabilisation they were incubated in 3% hydrogen peroxide for 5 minutes. Prior to antibody staining, the tissue sections were blocked with 10% goat-serum for 30 minutes at room temperature. For the tissue immunohistochemistry the following antibodies were used: LC3B, PCNA, keratin 10 (Table 2.8). Tissue sections were stained overnight at 4 °C in the desired primary antibody. The following day, sections were washed 3 times for 5 minutes with 1X PBS before applying the secondary antibody of choice (Donkey anti-rabbit Alexa Fluor 594, 1:1000) for 1 hour at room temperature. After staining with the secondary antibody, the sections were washed again 3 times for 5 minutes in 1X PBS. Vectashield with DAPI was used to mount the coverslips on the sections. Tissue sections were visualised using the Zeiss Apotome 3 Imager Z2 and images were taken at 10x, 20x and 40x magnification. The images were analysed using Zen 3.1 (blue edition) and ImageJ2 (v.2.14.0/ 1.54f).

Table 2.13. List of solutions for dewaxing/rehydration of paraffin embedded tissue sections.

Solution	**Time (min)**
Histoclear II	10
Histoclear II	10
100% Ethanol	5
100% Ethanol	5
70% Ethanol	5
1X PBS	10

2.2.6.2 Immunocytochemistry (ICC) on fixed cell lines and primary keratinocytes

1014 murine melanoma and primary mouse keratinocytes were cultured on 13 mm coverslips and were fixed by adding 100% ice-cold methanol for 10 minutes at -20 °C. For the use of Phalloidin, primary keratinocytes were fixed in 4% paraformaldehyde (PFA) for 10 minutes at room temperature. This was followed by 3 washes in 1X PBS for 5 minutes each. Following fixation, the coverslips were blocked by adding the blocking buffer for ICC (Table 2.5) for 30 minutes at room temperature. The primary antibodies used for ICC are the following and detailed description of their manufacturers can be found in table 2.8. Phalloidin Atto 647N; Rabbit Rab27a; Rabbit LC3A/B and Rat LAMP1 were used for the ICC analysis. Primary antibodies were incubated on cells overnight at 4 °C. The following day, the cells were washed 3 times for 5 minutes in 1X PBS, before incubating with the desired secondary antibody for 2 hours at room temperature. The following secondary antibodies were used: goat anti-rabbit Alexa Fluor 488, donkey anti-rabbit Alexa Fluor 594 and goat anti-rat Alexa Fluor 405. After secondary staining the cells were washed 3 times for 5 minutes in 1X PBS, before proceeding with 4’, 6-diamidino-2-phenylindole (DAPI) (0.02 μg/mL) staining for 10 minutes at room temperature. Coverslips were then mounted with Fluoromount G and stored at 4 °C prior to imaging. The coverslips were visualized with the Zeiss Apotome 3 Imager Z2. Images were taken at 40x and 63x magnification and analysed using Zen 3.1 (blue edition) and ImageJ2 (v.2.14.0/ 1.54f).

2.2.6.3 Sodium fluorescein dye permeation assay

The sodium fluorescein permeation assay was performed on unfixed whole mouse embryo (E18.5) dorsal skin. Embryos were placed dorsal epidermal side down in a petri dish containing 1 mM sodium fluorescein in PBS (pH 7.4) at 37 °C for 1 hour. Following 1 hour incubation, the dorsal skin was removed and fixed in 10% NBF. After fixation, the tissue was dehydrated and processed as seen previously in section 2.2.4.1 – Tissue harvest and preservation. 5μm sections were cut using the microtome as described in 2.2.4.2 - Tissue processing – Microtome. Sodium fluorescein slides were dewaxed and rehydrated (Table 2.13) and imaged with the Zeiss ApoTome 3 Imager Z2. Fluorescent dye uptake was quantified using the straight-line tool in ImageJ2 (v.2.14.0/ 1.54f).

2.2.6.4 Scanning Electron Microscopy of ATG16L1$^{\Delta WD}$ hair

Dorsal hair was plucked from the WT and ΔWD mouse skin and mounted on aluminum stubs covered with conductive carbon tape and then gold coated with a Polaron

SC7640 high resolution sputter coater, manufactured by Quorum Technologies. The hair samples were imaged under vacuum with the Zeiss Gemini 300 scanning electron microscope using the secondary electron (SE) detector. Hair follicle analysis was conducted using ImageJ2 (v.2.14.0/ 1.54f).

2.2.6.5 Image processing

Prior to image analysis, all images were adjusted to ensure the background, brightness and contrasts were equal. These parameters were set for each experiment and were constant across WT and ∆WD images. Images were analysed in ImageJ2 (v.2.14.0/ 1.54f).

2.2.6.6 Thickness analysis – General Histology

Brightfield H&E images were analysed in ImageJ2 (v.2.14.0/ 1.54f) software using the straight-line measurement tool. A total of 20 measurements were taken at each of the distinctive skin layers across three anatomical locations (i.e., dorsal, ventral and tail). This was done on 1-year-old WT and ∆WD mice (N=3).

2.2.6.7 Fluorescent intensity

The mean fluorescent intensity of the LC3B and Keratin 10 immunohistochemistry experiments were calculated using the ImageJ2 (v.2.14.0/ 1.54f) software. As previously stated, all images were adjusted accordingly, to ensure that levels of brightness and contrast were equal. The z-stacks were converted into MAX intensity images in ImageJ. Region of interest (ROI) boxes were added to the areas of analysis (epidermal layer) and the intensity plots were measured (*Analyse – plot profile*). Intensity plots were generated using the mean gray value. For live cell imaging experiment, fluorescent intensity of OA1-mCherry, LC3-GFP and LysoTracker Blue was measured using the straight-line tool in ImageJ2 (v.2.14.0/ 1.54f) software. Again, once the ROIs were set, the intensity plots were measured (*Analyse – plot profile*). To switch between channels in the same ROI, the intensity plot was set to live.

2.2.6.8 "Analyse particles" for Adenovirus LC3-GFP titration

To analyse the number of LC3-GFP positive 1014 murine melanoma melanocytes for the examination of transduction efficiency, images were taken at 10x magnification on the Zeiss Observer 7 fluorescent microscope. The number of cells was calculated using the Analyse particle tool in ImageJ2 (v.2.14.0/ 1.54f). The image was split into individual channels (*Image-Colour-Split Channels*) and each channel was thresholded by eye and kept consistent across images (*Image-Adjust-Threshold*). After thresholding, the parameters in Analyse Particles (*Analyse-Analyse Particles*) were set to a size (pixel^2) of 0-Infinity and circularity of 0.00-1.00. The same was repeated for both DAPI and LC3-GFP.

2.2.6.9 Colocalisation analysis using Coloc2 plug-in ImageJ

For the colocalisation analysis in the live cell imaging experiment, the time-course images were converted into MAX intensity images. From this the individual timepoint images were duplicated (*Image – Duplicate*) and used for the coloc2 plug in (*Analyse-Colocalisation-Coloc2*). ROIs were manually added to the images using the freehand ROI function, and these ROIs were maintained across the time-course. For the colocalisation analysis, OA1-mCherry and LC3-GFP, OA1-mCherry and LysoTracker Blue, and LC3-GFP and LysoTracker Blue were compared. In the third drop down list selection, the ROI manager was selected. Threshold regression was set to Costes. The algorithm that was selected for the analysis was the Spearman's Rank Correlation.

2.2.7 Western Blotting

2.2.7.2 Tissue homogenisation

Adult mouse tail epidermal skin tissue was enzymatically digested from the dermis as previously described in section 2.2.5.5 - Primary keratinocyte isolation from mouse tail. The epidermis was snap frozen in liquid nitrogen and stored at -80 °C until further processing. For western blot, 0.1 g of the skin tissue was homogenised in a mortar and pestle using liquid nitrogen. The ground sample was transferred to a sterile chilled Eppendorf and 400 μl of 6.5 M urea buffer (Table 2.5) was added. The sample was incubated at 37 °C for 30 minutes before sonicating the sample for 10 minutes in a water bath sonicator. The homogenate was spun down at 14,000 g for 20 minutes at 4 °C. The supernatant was later collected and used for further analysis in Western Blot or stored at -20 °C until further processing.

2.2.7.3 Western Blot

1.5 μl and 5 μl of tissue lysate was loaded along with 1:4 of loading buffer (150 mM Tris-HCL pH 6.8; 30% Glycerol; 6% SDS; 3 mM ETDA; 0.03% bromophenol blue; 3% β-mercaptoethanol) and nuclease free water. The lysate was heated at 95 °C for 5 minutes in a heat block. Once the samples were denatured, they were loaded onto precast Bolt™ 4-12% gradient gels, which had been carefully mounted into an electrophoresis running tank. The samples were run in NuPAGE MES SDS running buffer at a constant voltage of 200 V for 30 minutes alongside the Precision Plus Protein Dual Colour Standards. Once the samples had been separated by SDS-PAGE, proteins were transferred onto a polyvinylidene difluoride (PVDF) membrane using the Bio-Rad Trans-Blot Cell at a constant 200 mAmp for 1 hour. Efficiency of protein transfer onto the PVDF membrane was confirmed using Ponceau S solution for 5 minutes at room temperature. After Ponceau S staining, the membrane was washed with 1X TBS-T (Table 2.5) 2 times for 5 minutes. Membranes were then incubated in 5% milk blocking buffer or 5% BSA, respectively, on a platform shaker. After blocking, the desired primary antibodies (Table 2.8) were diluted in 5% milk blocking buffer or 5% BSA, and transferred onto the PVDF membrane and incubated overnight at 4°C with agitation. The next day, membranes were washed 3 times for 5 minutes with 1X TBS-T before being incubated with the required secondary antibody (Table 2.8) at the recommended dilution. For chemiluminescent Western Blot detection, the blots were washed 3 times for 5 minutes in TBS-T, before being developed using the Clarity Western ECL Substrate with a 1:1 ratio of Clarity Western Peroxide reagent and Clarity Western Luminol/Enhancer reagent. The membranes were visualized using the Bio-Rad Chemidoc™ Imaging System. For fluorescent Western Blot detection, the secondary IRDye antibodies are used to detect proteins of interest. Here, the membranes are washed 3 times with 1X TBS-T and imaged using the Odyssey CLx Imager with associated imaging software. Densitometry analysis was conducted using ImageJ2 (v.2.14.0/ 1.54f).

2.2.8 Quantifying relative expression levels of keratinocyte differentiation markers

2.2.8.2 RNA extraction from mouse tissue

For qPCR, mouse tail epidermal skin was cut into small pieces (approx. 2 mm) and transferred to a 2 mL Eppendorf safe-lock tube, containing 600 µl of TRIzol™ solution and one Tungsten Carbide bead. The biopsies were placed in a tissue lyser and were shaken for 10 minutes at 30 Hz. The homogenate was later centrifuged at 14,000 x g for 10 minutes at 4 °C and the supernatant was removed and added to a sterile Eppendorf containing 200 µl of chloroform. The solution was vortexed for 15 seconds and left to incubate at room temperature for 5 minutes. Following incubation, the solution was centrifuged at 14,000 x g for 15 minutes at 4 °C to separate phases. The upper aqueous layer, taking care to not disturb the contaminating interface layer, was removed, and added to a fresh centrifuge tube containing 200 µl of 95% ethanol. The solution was mixed before proceeding with total RNA extraction. Total RNAs were then extracted using the GenElute Total RNA purification kit, following manufacturer's instructions (Table 2.4). The RNA was quality controlled using the Nanodrop 2000.

2.2.8.3 Ethanol precipitation

The most common way to precipitate and purify RNA is by alcohol precipitation. Here 1 µl of glycoblue (20 µg/ µl) was added to the RNA along with 7.5 M ammonium acetate (0.5 x volume of sample) and 100% ethanol (2.5 x volume of sample). The solution was stored in an Eppendorf at – 20 °C overnight to precipitate the RNA from the sample. The following day, the sample was centrifuged at 4°C at 16,000 x g for 30 minutes to pellet the RNA. The supernatant was then removed without disturbing the pellet. 150 µl of 70% ethanol was added to the pellet and centrifuged at 4°C for 2 minutes at 16,000 x g. The supernatant was removed, and this step was repeated. After centrifugation, the supernatant was removed, and the pellet was left to air-dry at room temperature. Once the pellet was dry, it was resuspended in Tris-EDTA (TE) buffer or nuclease-free water. The precipitated RNA was stored at – 80 °C until further processing.

2.2.8.4 cDNA synthesis

RNA was firstly reverse transcribed to cDNA using random hexamers (50 µM), 10 mM dNTPs, 5X first-strand buffer, 0.1 M DTT, SuperScript II RT and 1 ng-5 µg total RNA. A 20 µl reaction volume was used for cDNA synthesis, which was performed in a nuclease-free Eppendorf tube. To this tube 1 µl of random hexamers, 1 µl of dNTPs and 1 ng-5 µg of RNA were added and nuclease-free water was added to make up the 20 µl reaction volume. The mixture was heated for 5 minutes to 65 °C using a dry block heating system. The samples were chilled on ice and 4 µl of 5X first-strand buffer and 2 µl of 0.1 DTT were added. Once the heat block had cooled down to 42 °C, 0.5 µl of SuperScript II RT was added to each sample and incubated for 2 hours. Immediately after the completed 2-hour incubation, enzyme deactivation was performed for 15 minutes at 70 °C. cDNA samples were stored at -20 °C until further processing (for a maximum of 12 months).

2.2.8.5 SYBR green qPCR

The oligonucleotides purchased from Sigma arrived as lyophilised products and were reconstituted in nuclease-free water to a stock concentration of 100 µM (Table 2.6).

For relative quantification of mRNA expression using the five genes of interest, primary mouse tail epidermises were analysed via SYBR green qPCR, following the manufacturer's instructions. Each 20 µl reaction contained 10 µl of the 2x qPCRBIO SyGreen Mix, 0.8 µl of forward primer (10 µM), 0.8 µl of reverse primer (10 µM), < 100 ng cDNA and nuclease-free water. Samples were carried out as technical duplicates alongside no-template controls and positive controls (whole skin of mouse). SYBR Green qPCR was performed using the QuantStudio™ 3 Real-Time PCR System in a MicroAmp optical 96-well reaction plate sealed with a MicroAmp optical adhesive film. The amplification method used is described in Table 2.14. Primers were quality controlled by examining their ability to generate a single product in a qPCR reaction through melt curve analysis. Moreover, primer efficiencies were established by standard curve analysis using serial dilutions of a positive control sample, which consisted of whole skin tissue. Results were collected in the QuantStudio™ 3 Software and analysed using Microsoft Excel version 16.57 and GraphPad Prism version 9.3.1.

Relative quantification was calculated using the $2^{(-\Delta\Delta CT)}$ method using 18S as a reference gene (Livak and Schmittgen, 2001). Statistical analyses were performed using the multiple unpaired t-tests on the relative expression values, as appropriate. Dot plots were plotted with the $2^{(-\Delta\Delta CT)}$ values normalised to the mean of the control group and standard error (SE) was shown by error bars. All statistical analyses were performed using GraphPad Prism version 9.3.1 and for all statistical tests, $p < 0.05$ was considered statistically significant.

Table 2.14. qPCR amplification program on QuantStudio™ 3 Real-Time PCR system.

Step	**Cycle**	**Time (s)**	**Temperature (°C)**
Polymerase Activation	1	120 600	50 95
Denaturation **Anneal/ Extension**	40	15 60	95 60-65
Dissociation	1	1	95
Melt Curve	1	15	65

2.2.9 Skin permeability assessment – Toluidine Blue Assay

Toluidine blue assay was done on unfixed whole mouse embryos (E18.5). The embryos were isolated from the pregnant female at E18.5 and sacrificed by anesthetic overdose (Euthatal, Pentobarbital sodium, 200mg in 1mL) and immersion in ice cold 1X PBS for 30 minutes. The embryos were passed through a chilled methanol gradient (Table 2.15), kept on ice, to allow for toluidine blue penetration. After passing the embryos through methanol they were then immersed in 0.1% toluidine blue solution in water for 2 minutes on ice. The embryos were de-stained in PBS (pH 7.4) until a dye pattern was visible (NB. If a barrier defect is present).

Table 2.15. List of solutions required for 0.1 % toluidine blue staining of E18.5 embryos.

Solution	**Time (mins)**
25 % Methanol	2
50 % Methanol	2

75 % Methanol	2
100 % Ethanol	2
75 % Methanol	2
50 % Methanol	2
50 % Methanol	2
25 % Methanol	2
1X PBS	2
0.1 % Toluidine Blue	2

2.2.10 Elasticity testing

The Cutometer® skin elasticity meter MPA580, kindly borrowed from EnviroDerm, was used in the assessment of the elasticity. The Cutometer® measures the vertical deformation of the skin in millimeters and was used with a 2-mm diameter probe to evaluate the skin elasticity parameters of the 2-month and 17-month WT and ΔWD mouse skin. Prior to testing, the mice were exposed to an acclimatisation period of 10 minutes. The WT and ΔWD mice were immediately assessed post-mortem after euthanasia. The pressure in the probe was set to 400 mBar with 5 second of suction, followed by 5 second of release. A total of 3 mice per genotype and age group were analysed in the dorsal region, with each measurement being repeated a total of 6 times per mouse. To examine the elasticity in further detail, the following parameters were considered: net elasticity (Ur/Ue) and elastic recovery (Ur/Uf). Uf denotes the deformation at the end of the vacuum period, Ue exhibits the extent of skin stretching within the first 0.1 s of the vacuum period and Ur measures the ability of the skin to return to its initial position after deformation (Draaijers et al., 2004). An overview of the parameters can be seen in Table 2.16. Parameters were calculated in the MPA CTplus software associated to the device. A two-way ANOVA with Tukey's post-hoc was used to compare the means among the various groups.

Table 2.16. Overview of Cutometer MPA580 parameters.

Parameter	**Point of measurement**
Uf	Total distance the skin stretches after the suction period
Ue	Distance the skin stretches in the initial 0.1 seconds after suction
Ur	Distance the skin retracts after the first 0.1 seconds of the relaxation phase
Ur/Ue	Elastic part of the suction phase vs. immediate recovery during relaxation phase
Ur/Uf	Proportion of the immediate recovery compared to the amplitude after suction in %

2.2.11 Statistical analysis

Data are expressed as means ± SE of the mean. Statistical analysis was performed in GraphPad Prism version 10.2.0 for Macintosh, GraphPad Software, Boston, Massachusetts USA and in SPSS version 29.0.1.0 (IBM Corp. Released 2022. IBM SPSS Statistics for Macintosh, Version 28.0. Armonk, NY: IBM Corp). Levene's Test for Variance was used for all datasets before performing the unpaired t-test. Shapiro-Wilk test was used to test for normality within the dataset. For the comparison between two means the unpaired t-test was used. Mann-Whitney U test was used for the non-parametrical comparison between two means. Following the analysis of multiple unpaired t-tests, the Bonferroni correction was applied. For the comparison between multiple groups the two-way ANOVA (Tukey's post-hoc) was performed. Statistical significance was determined by a confidence level of 95%, where ns $p > 0.05$; * $p < 0.05$; ** $p < 0.01$ and *** $p < 0.001$.

Chapter 3: Characteristics of the integumentary system of ATG16L1$^{\Delta WD}$ mice

3.1 Introduction

The skin is a multifunctional organ, composed of three primary layers that include the outermost layer termed the epidermis, the middle layer called the dermis and the innermost layer, known as the hypodermis (Joost et al., 2020). Together, these layers form the barrier between the external and internal environment, which functions as a safeguard against extrinsic factors (Joost et al., 2020). Sustaining healthy cellular homeostasis in the skin, is vital for the regulation and maintenance of the fully functioning skin barrier. Processes, such as canonical autophagy, have proven to be involved in the regulation of this cellular homeostasis of the skin (Akinduro et al., 2016, Rossiter et al., 2013).

This catabolic pathway, hereafter referred to as autophagy, is crucial for the degradation of cytoplasmic material that preserves cellular homeostasis (Serramito-Gomez et al., 2020). The process is mediated by a collection of proteins called autophagy-related proteins (ATGs), which include ATG16L1. ATG16L1 is involved in forming the ATG12-ATG5-ATG16L1 complex, required for the recruitment of microtubule-associated protein 1 light chain 3 (LC3) to double-membraned autophagosomes (Schille et al., 2018). Intracellular cargo, such as damaged organelles, protein aggregates or intracellular pathogens, are engulfed by the double-membraned autophagosome and are subsequently degraded by lysosomes. *ATG16L1* is composed of an N-terminal containing an ATG5 binding motif, followed by an extended linker region, leading into a coiled-coil domain (CCD) and a carboxy-terminal linker region that includes seven WD40 repeats (WD domain) (Parkhouse et al., 2013).

Mice lacking the WD domain and linker region of *ATG16L1* were designed and created by former PhD student Dr Julia Maryam Arasteh (Arasteh, 2012). These mice were generated using a targeting vector, which was developed for exon 6 of *ATG16L1,* to insert two stop codons following the glutamate residue E230 in the CCD (Rai et al., 2019). The absent WD domain favours autophagy but prevents these mice from performing the "non-canonical autophagy," known as LC3-associated phagocytosis (LAP), which is characterised by the conjugation of LC3 to phosphatidylethanolamine (PE) on single-membrane phagosomes (Fletcher et al., 2018). The ATG16L1$^{\Delta WD}$ mouse model, hereafter referred to as ΔWD, has been used to study the roles of LAP in maintaining tissue homeostasis *in vivo* and *ex vivo* (Rai et al., 2019, Slowicka et al., 2019).

Age-related changes affect the structure and function of the three layers of the skin. Although, the visible effects of aging have been extensively studied, it primarily impacts the dermis (Lynch et al., 2017). The dermis, primarily consisting of collagen, glycoproteins, and proteoglycans, contributes significantly to the skin's biomechanical properties (Lynch et al., 2017; Prigent et al., 2023). With ageing, the dermis often shows signs of increased stiffness and reduced elasticity at a macroscopic level. Studies have indicated a decrease in autophagy activity in aged individuals, yet the effects of non-canonical autophagy on ageing remain poorly understood (Nakamura et al., 2019).

This chapter aims to investigate the cutaneous phenotype of the ∆WD mouse model. It will discuss the overall morpho-histological differences seen between WT littermate controls and ∆WD mice. Moreover, it will discuss the effects of LAP deficiency on overall elasticity, elastic recovery and dermal function. I hypothesise that the removal of the WD domain of ATG16L1 will impact skin barrier function. I believe that the impaired skin barrier will be due to physiological changes within the strata of the mouse skin. In addition, I anticipate a more rapid decline in elastic properties in the ∆WD mice during intrinsic ageing, due to the truncation in *ATG16L1*; thus, resulting in reduced non-canonical autophagy activity. The chapter will aim to meet the following experimental objectives:

- Confirmation of the genetics of the ∆WD mouse model by genotyping PCR and Western Blot.
- Examine for changes in hair morphology in the ∆WD model.
- Examine for changes in skin histology and barrier function in the ∆WD model.
- Compare the age-related changes in dermal biomechanics between ∆WD and WT mice.

3.2 Results

3.2.1 Genotyping of the ATG16L1^{DWD} mouse model

Confirming the correct genetics of mice, used in each experiment, is one of the fundamental steps prior to comparing mutant mice with WT littermate controls. For the histological examination of the ATG16L1$^{\Delta WD}$ mouse model, male mice were used. Each mouse was genotyped at postnatal day 21 and was additionally confirmed after sacrifice. Only homozygous mutant mice were included in the studies.

PCR analysis of genomic DNA used a primer pair specifically designed for the ΔWD model (Figure 3.1 A). A targeting vector was designed to insert two stop codons at the end of glutamate E230 residue in the CCD of exon 6 of *ATG16L1* (Figure 3.1 A). A WT mouse exhibited a PCR product at 291 bp, due to the 290-291 primer set flanking exon 6 of *ATG16L1* (Figure 3.1 A-B). PCR products from ΔWD mutant mice appeared at 639 bp due to the insertion of the two stop codons and a neomycin resistance cassette (green box) in exon 6, which increased the amplicon size from 291 bp to 639 bp (Figure 3.1 A-B).

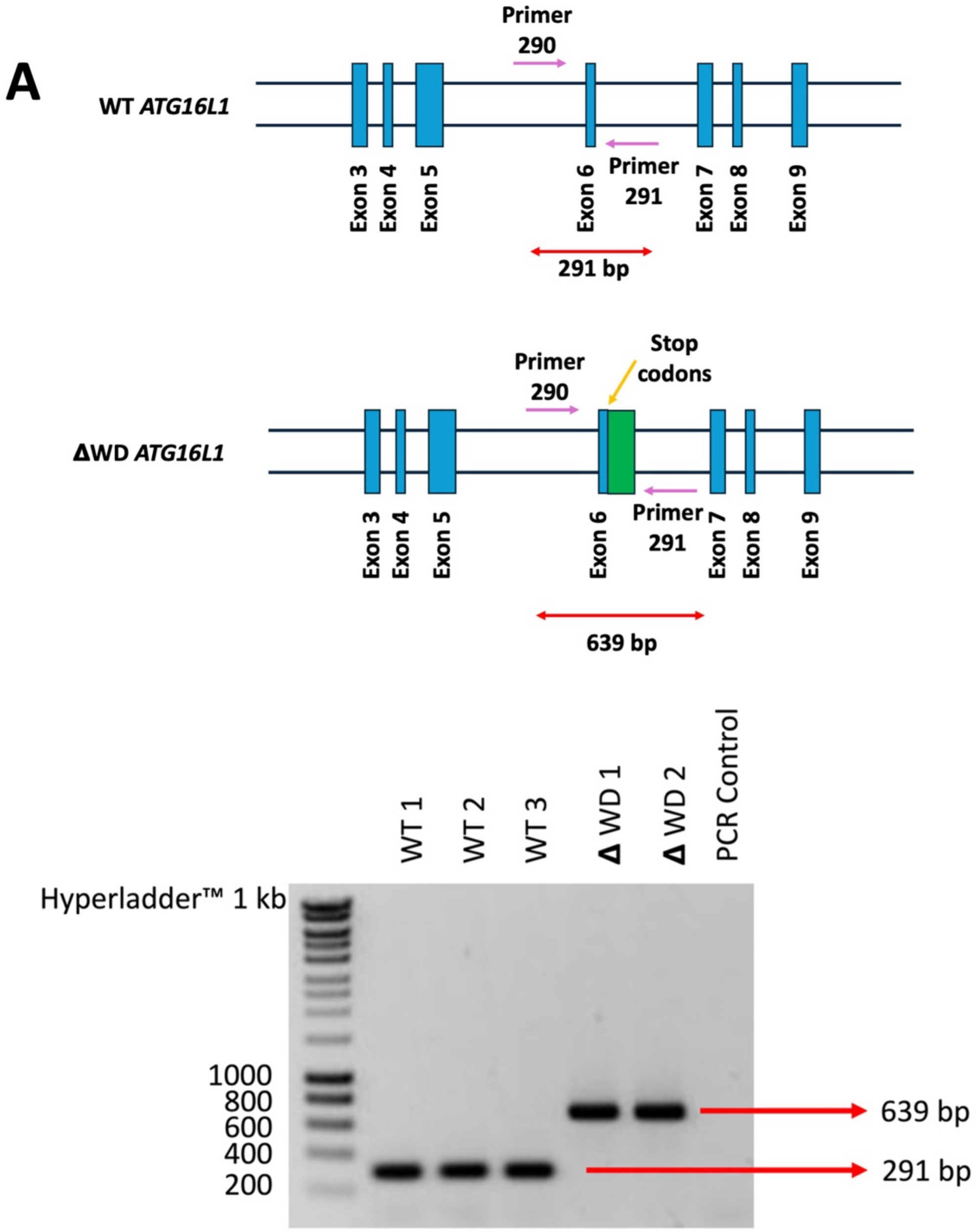

Figure 3.1 Genotyping mice from the ∆WD model. (A) 290 and 291 primer location in WT and ∆WD *ATG16L1* in exon 6**.** The ∆WD allele was generated by inserting a neomycin cassette (green box) containing two stop codons into exon 6. Illustration adapted from (Wang, 2020). **(B)** A representative 1% agarose gel electropherogram showing the WT *ATG16L1* PCR product appearing at 291 bp and the ∆WD *ATG16L1* PCR product at 639 bp due to the insertion increasing the size of the frame. Figure taken from Conway et al. (2024).

3.2.2 Analysis of truncated ATG16L1 expression by Western Blot

ATG16L1 is ubiquitously expressed in mouse tissue. To validate the expression of full-length and truncated ATG16L1 in the respective models, used in these studies, Western blot analysis was performed on protein extracted from epidermal tail skin from both 1-year-old WT and ΔWD mice. Full length ATG16L1 was present in WT epidermal skin lysates yet was not detected in the ΔWD lysates (Figure 3.2 B). Here, the WT tail skin epidermal lysates exhibited a slower migrating β-isoform of ATG16L1, appearing at 75 kDa, while ΔWD skin lysates demonstrated a more rapid migrating β-isoform of ATG16L1, appearing at 25 kDa (Figure 3.2 B). The ATG5 binding domain in the N-terminal and the CCD domain in middle region exhibited a band size of 25 kDa, due to the expression of truncated ATG16L1 in the ΔWD skin (Figure 3.2 A-B). The full length ATG16L1 was only present in lysates from WT tail skin, emphasising the expression of all the domains of ATG16L1 (Figure 3.2 A-B). ATG16L1 α-isoform and ATG16L1 γ-isoform were not detected in the Western blot analysis of skin tissue (Figure 3.2 B). Non-specific binding (NSB) was present suggesting that the concentration of the secondary antibody was too concentrated.

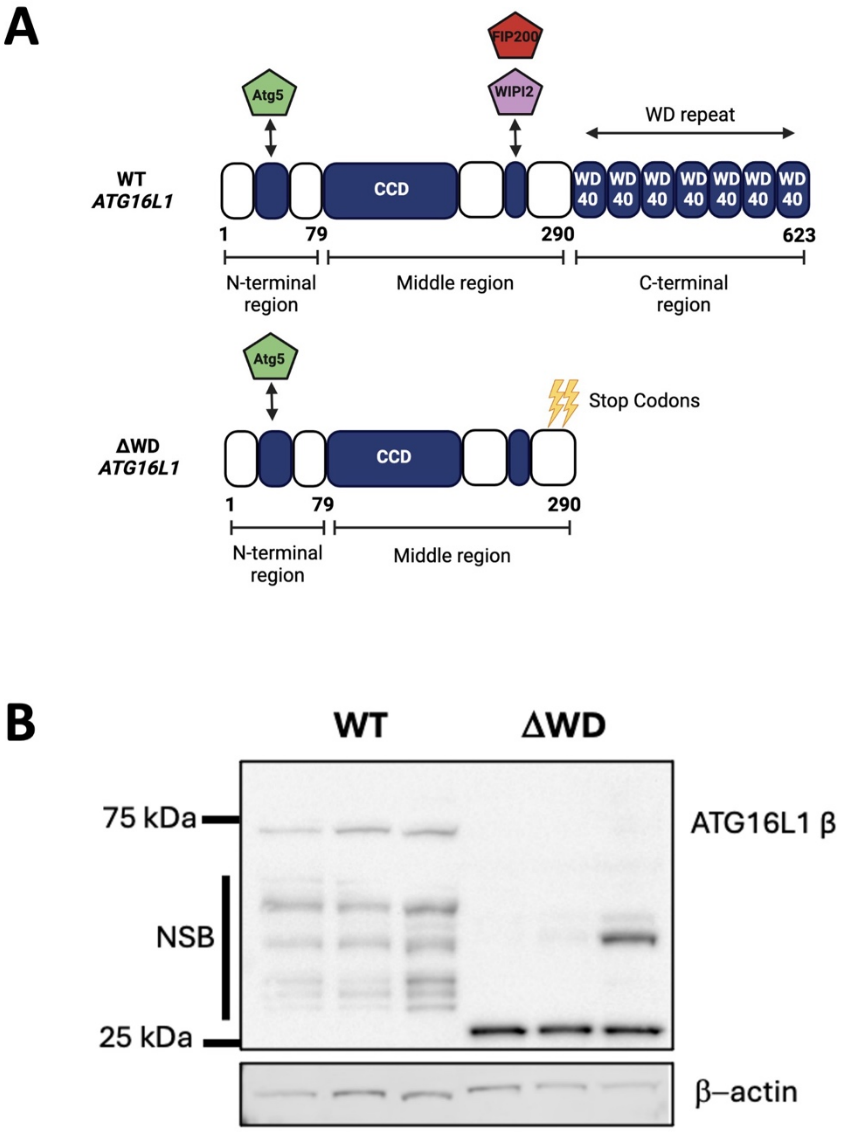

Figure 3.2 Protein characterisation of ATG16L1 in 1-year-old ΔWD mice. (A) Graphical representation of WT *ATG16L1* and ΔWD *ATG16L1*. Figure created in BioRender.com. **(B)** Western Blot analysis of ATG16L1 expression in 1-year old WT and ΔWD mouse epidermal tail skin. Truncated ATG16L1 appears at 25 kDa; full-length ATG16L1-β appears at 75 kDa. Blots representative of three independent experiments with N=3 mice per genotype. NSB: Non-specific binding. Figure taken from Conway et al. (2024).

3.2.3 The assessment of the aged ΔWD mouse skin

3.2.3.1 Overall appearance and body masses

Once a method for confirming the genetic background of the ΔWD mouse model was established, the analysis began with gaining a greater understanding of the overall appearance and histology in the male 1-year old WT and ΔWD mice. Identical fur pigmentation was observed in the aged mice of this model (Figure 3.3 A). Despite being 1-year-old mice, the WT and ΔWD mice still exhibit a dense fur coat, with no signs of thinning (Figure 3.3 A). Moreover, they exhibit the characteristic appearance of the C57BL/6 mouse, with non-agouti black hair and lighter brown hairs around the base of tail and ears (Figure 3.3 A lateral view). Few white hairs can be seen across both genotypes, indicating signs of ageing (Figure 3.3 A lateral view). Both mice display a fully pigmented tail with occasionally unpigmented tail tip (data not shown) (Figure 3.3 A). In addition, the ΔWD mice exhibited a similar size and body weight, as previously described (Figure 3.3 A-B) (Rai et al., 2019).

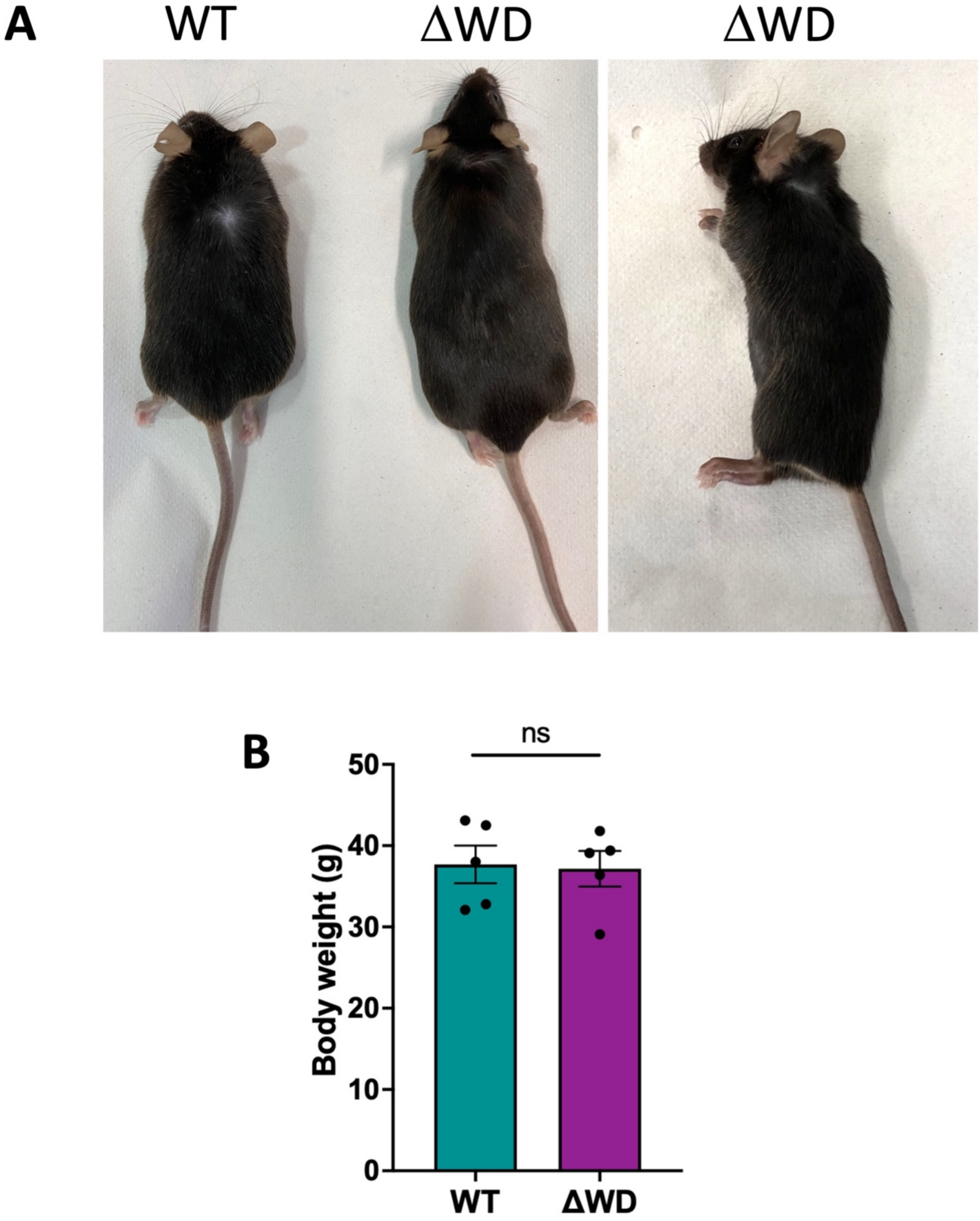

Figure 3.3 General appearance of the ΔWD mouse model at 1-year-old. (A) Representative posterior images of male WT littermate control and ΔWD mutant mouse at 1-year old. Lateral view of male ΔWD mutant mouse at 1-year old. **(B)** Mean bodyweight of 1-year old male mice. N=5 mice per genotype. Error bars are SE. An unpaired t-test, with Welch correction was used to compare the means (ns = not significant).

3.2.3.2 Overall histology of the ∆WD model dorsal hair

The overall architecture of the hair follicle was assessed by plucking hair from the dorsal skin regions, which were examined using the scanning electron microscope (SEM) (Figure 3.4 A). SEM imaging of the dorsal WT and ∆WD hair displayed a coronal, crown like scale pattern, which is commonly observed in the hair of small rodents (Figure 3.4 A; middle panel). Histologically, differences were compared at the tip, isthmus and bulb region using ImageJ and were quantified by measuring the distance outline by the red arrow in the middle panels (Figure 3.4 B). Morphologically, the results revealed no significant changes ($p > 0.05$) between both genotypes, at the various regions, indicating that hair formation was identical in both groups (Figure 3.4 B).

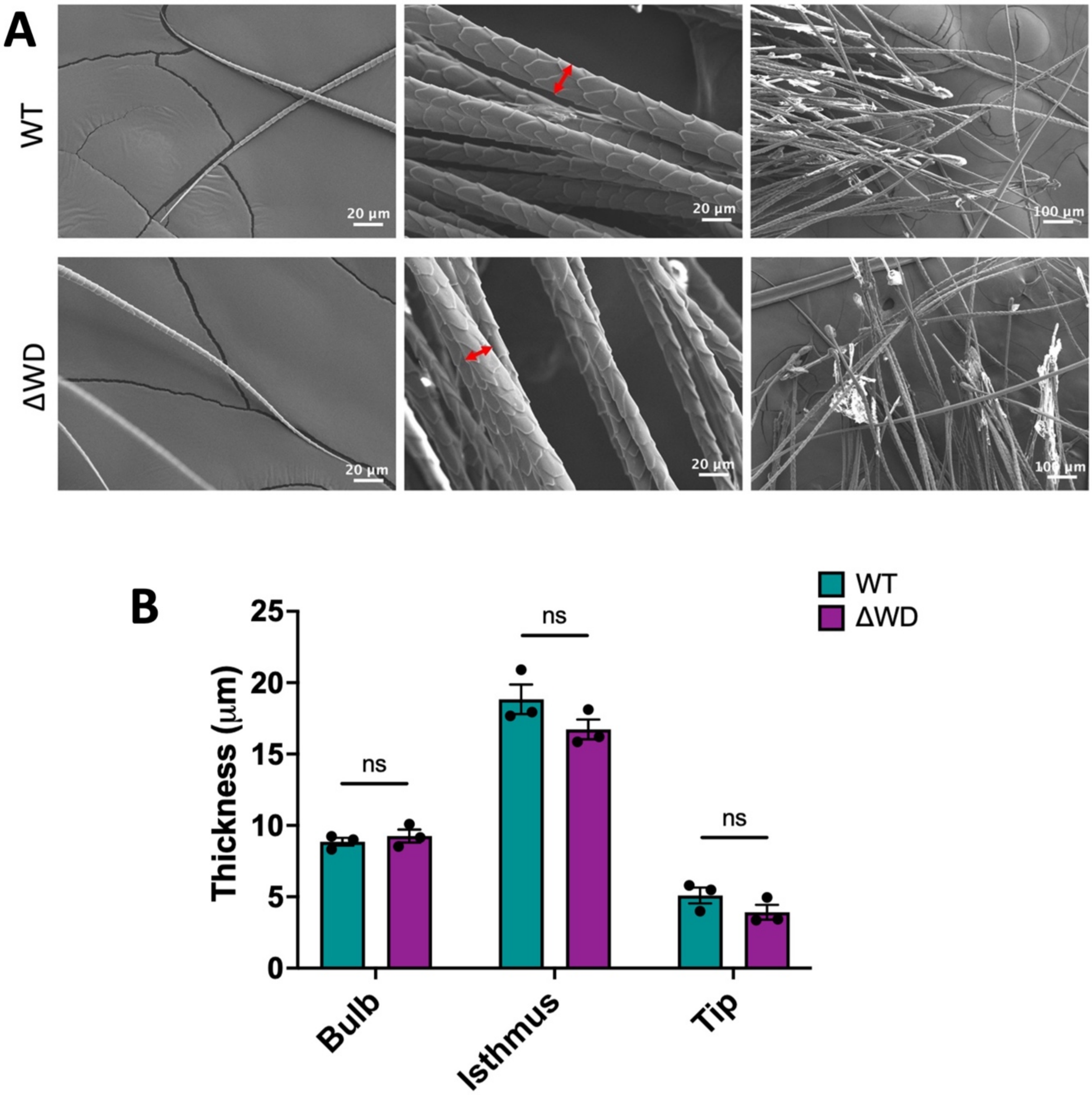

Figure 3.4 Representative SEM images taken from plucked dorsal hair from the ΔWD mouse model. (A) Images captured at the tip region (panel left), isthmus (middle) and bulb region (panel right). Hair shaft thickness was measured as indicated by the red arrow in ImageJ. Scale bar (left and middle) 20 µm and 100 µm (right). **(B)** Hair thickness quantification at three regions. Data shown are means, with error bars represented by SE. A total of n=30 measurements taken per mouse (N=3). Means were compared using the multiple unpaired t-test with Bonferroni correction (ns = not significant). Figure taken from Conway et al. (2024).

3.2.3.3 Histological analysis of 1-year old male WT littermate controls and ΔWD mouse skin

Following the analysis of the overall appearance of the 1-year-old WT and ΔWD mice, I next sought to examine for a cutaneous phenotype in the ΔWD model. The overall structure of the skin was assessed by Haematoxylin & Eosin (H&E) staining. The skin is composed of three layers: the outermost epidermis, the dermis, and the innermost hypodermis (Figure 3.5-3.7). The intermediate layer, known as the basement membrane, is located between the epidermis and the dermis (Figure 3.5). Within the epidermis, keratinocytes are the predominant cell type, characterised as oval purple structures above the basement membrane (Figure 3.5). Both WT and ΔWD mice exhibit a single, uniform, and continuous cell layer of basal keratinocytes (Figure 3.5). Hair follicles are present in both the dermal and epidermal compartments, along with an additional appendage known as the sebaceous gland (Figure 3.5 & 3.7). The dermis, located beneath the epidermis, contains a large arrangement of collagen fibres and scattered dermal cells interlaced within the collagen lattice (Figure 3.6). The innermost layer of the skin, known as the hypodermis, is primarily composed of adipocytes, which form about four cell layers, and appear engorged in both WT and ΔWD ventral skin (Figure 3.7). Beneath the hypodermal layer, a unique striated muscle called the panniculus carnosus muscle can be observed (Figure 3.7).

Table 3.1. Overview of mean skin layer thickness (μm) ± SE at several anatomical locations in 1-year old WT and ΔWD mice (N=3).

Thickness analysis (μm)				
Anatomical Location	**Skin Layer**	**WT**	**ΔWD**	**Adjusted *p* Value**
Dorsal	Epidermis	13.54 ± 1.30	11.05 ± 0.76	> 0.99
	Dermis	251.93 ± 30.90	184.09 ± 32.44	> 0.99
	Hypodermis	277.03 ± 41.96	331.42 ± 13.94	> 0.99
Ventral	Epidermis	11.05 ± 1.84	10.38 ± 0.79	> 0.99
	Dermis	163.83 ± 24.67	111.09 ± 4.84	0.90
	Hypodermis	331.09 ± 88.11	178.49 ± 61.69	> 0.99
Tail	Epidermis	10.76 ± 1.36	10.14 ± 1.70	> 0.99
	Dermis	206.84 ± 16.49	120.97 ± 4.42	0.90
	Hypodermis	250.46 ± 31.27	292.95 ± 19.65	> 0.99

The thicknesses of the epidermis, dermis, and hypodermis in three anatomical regions - dorsal, ventral, and tail – were quantified using ImageJ (Figure 3.8; Table 3.1). Results showed that the ∆WD mice had thinner epidermal and dermal layers in the listed anatomical regions, though these differences were not statistically significant ($p > 0.05$) (Figure 3.9; Table 3.1). Increased hypodermal thickness was observed in the dorsal and tail regions, while the ventral area showed reduced thickness (Table 3.1). However, these changes in hypodermal thickness were not statistically significant ($p > 0.05$) (Figure 3.9).

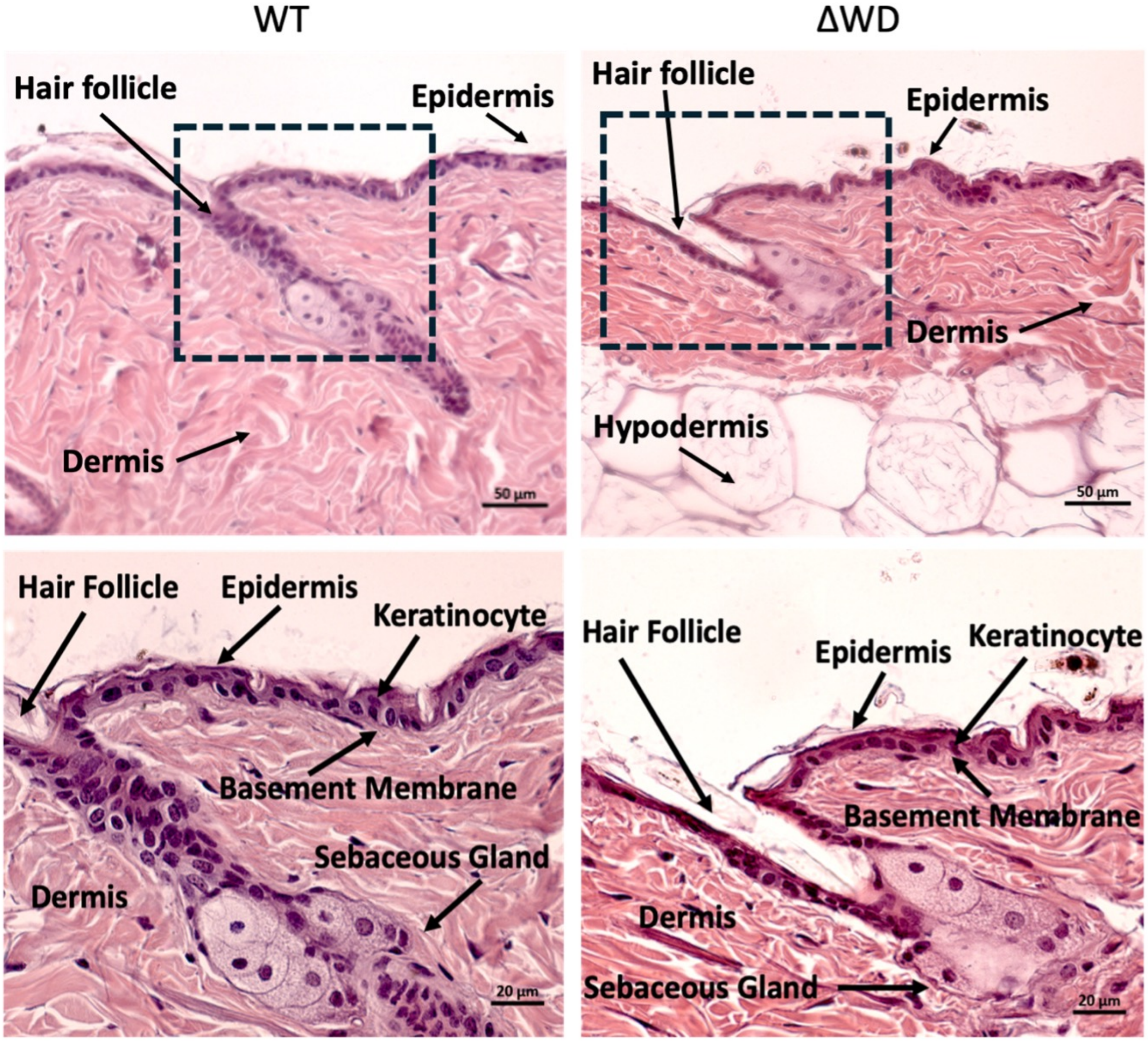

Figure 3.5 Overview of 1-year-old WT littermate controls and ΔWD dorsal epidermal histology. Representative H&E images showing the general epidermal and hair follicle histology. Magnified images of epidermal layer, in the areas marked by the black dashed box, are shown below. Magnified images show keratinocytes, basement membrane, hair follicle and sebaceous gland. Images taken on Zeiss Apotome 3 Imager Z.2. Upper panel images: scale bar: 50 µm. Lower panel images: scale bar: 20 µm. Figure taken from Conway et al. (2024).

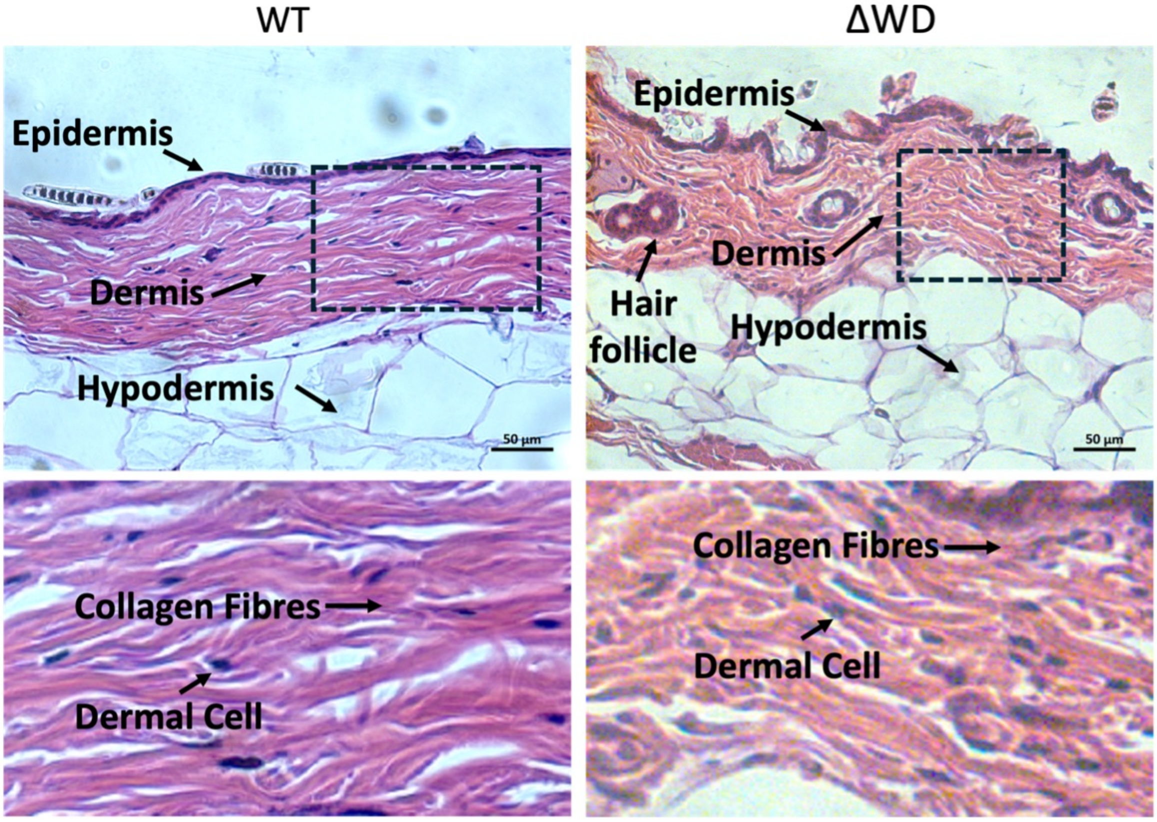

Figure 3.6 Overview of 1-year-old WT littermate controls and ΔWD ventral dermal histology. Representative H&E images showing the ventral skin histology. Magnified images of dermal layer, in the areas marked by the black dashed box, are shown below. Magnified image shows the collagen fibres and dermal cells. Images taken on Zeiss Apotome 3 Imager Z.2. Upper panel images: scale bar: 50 μm.

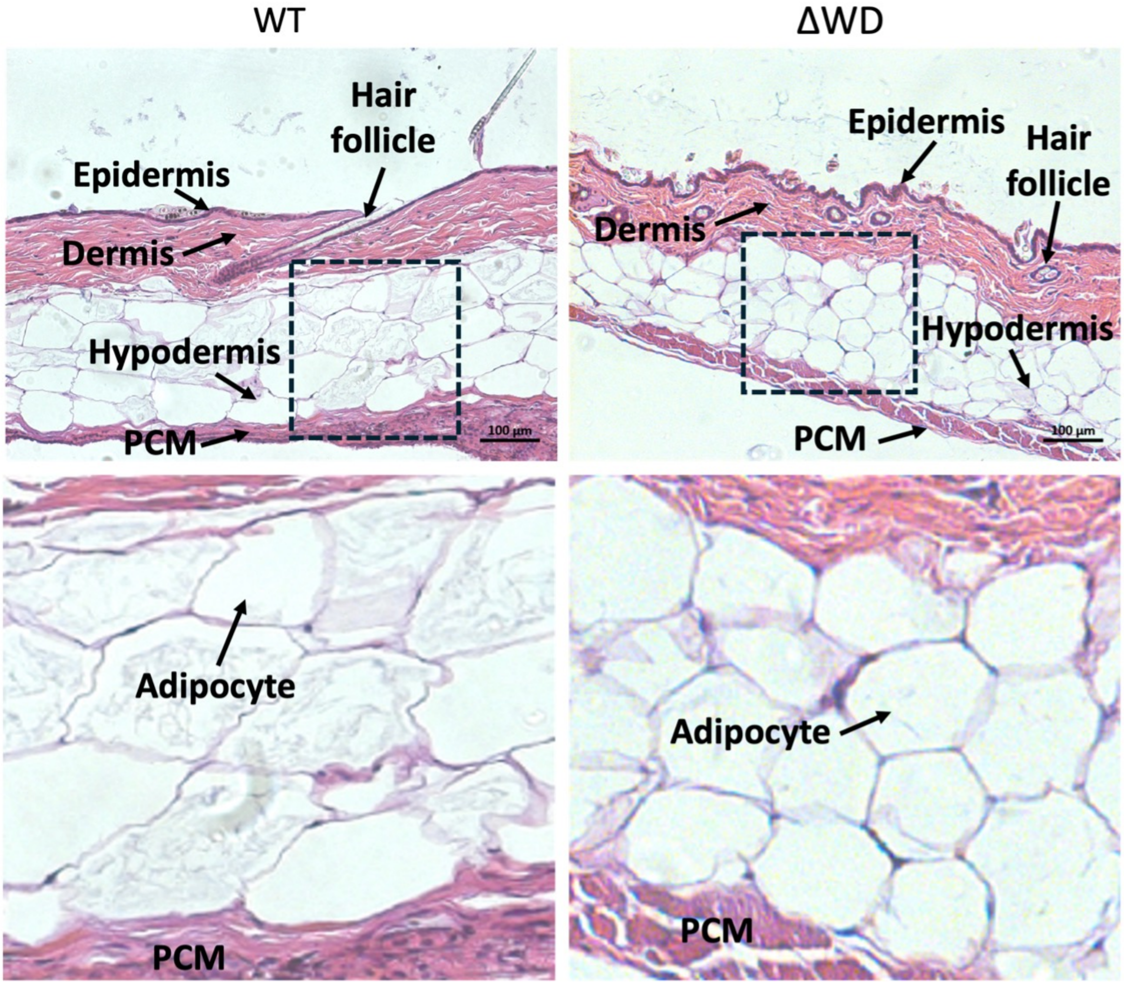

Figure 3.7 Overview of 1-year-old WT littermate controls and ΔWD ventral hypodermal histology. Representative H&E images showing the ventral skin histology. Magnified images of hypodermal layer, in the areas marked by the black dashed box, are shown below. Magnified images show the hypodermal adipocytes and panniculus carnosus muscle (PCM). Images taken on Zeiss Apotome 3 Imager Z.2. Upper panel images: scale bar: 100 μm.

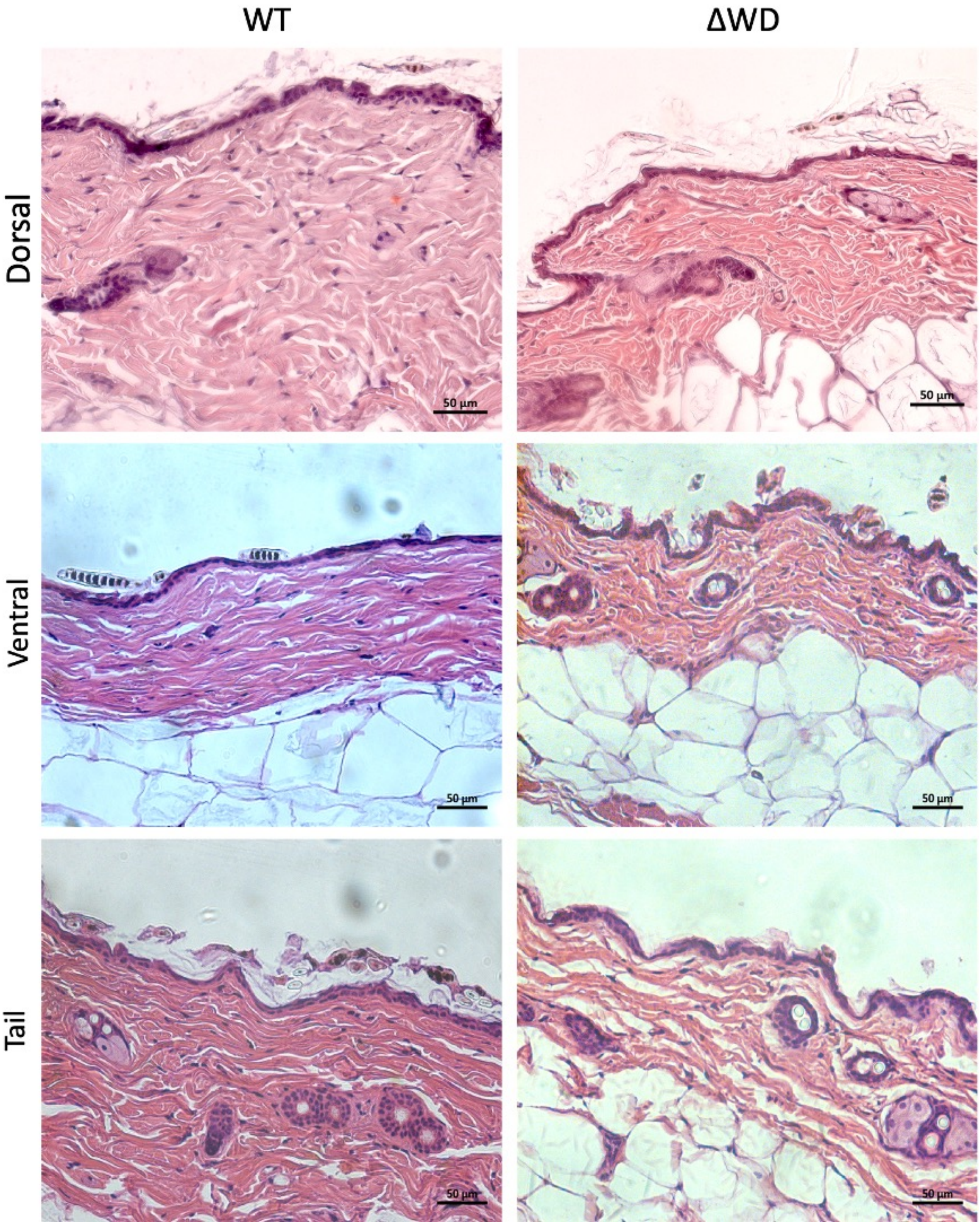

Figure 3.8 Overview of 1-year-old WT littermate controls and ΔWD histology. (A) Representative H&E images showing the general histology of WT and ΔWD at three anatomical locations – dorsal, ventral, and tail. Images taken on Zeiss Axioplan 2. Scale bar: 50 μm.

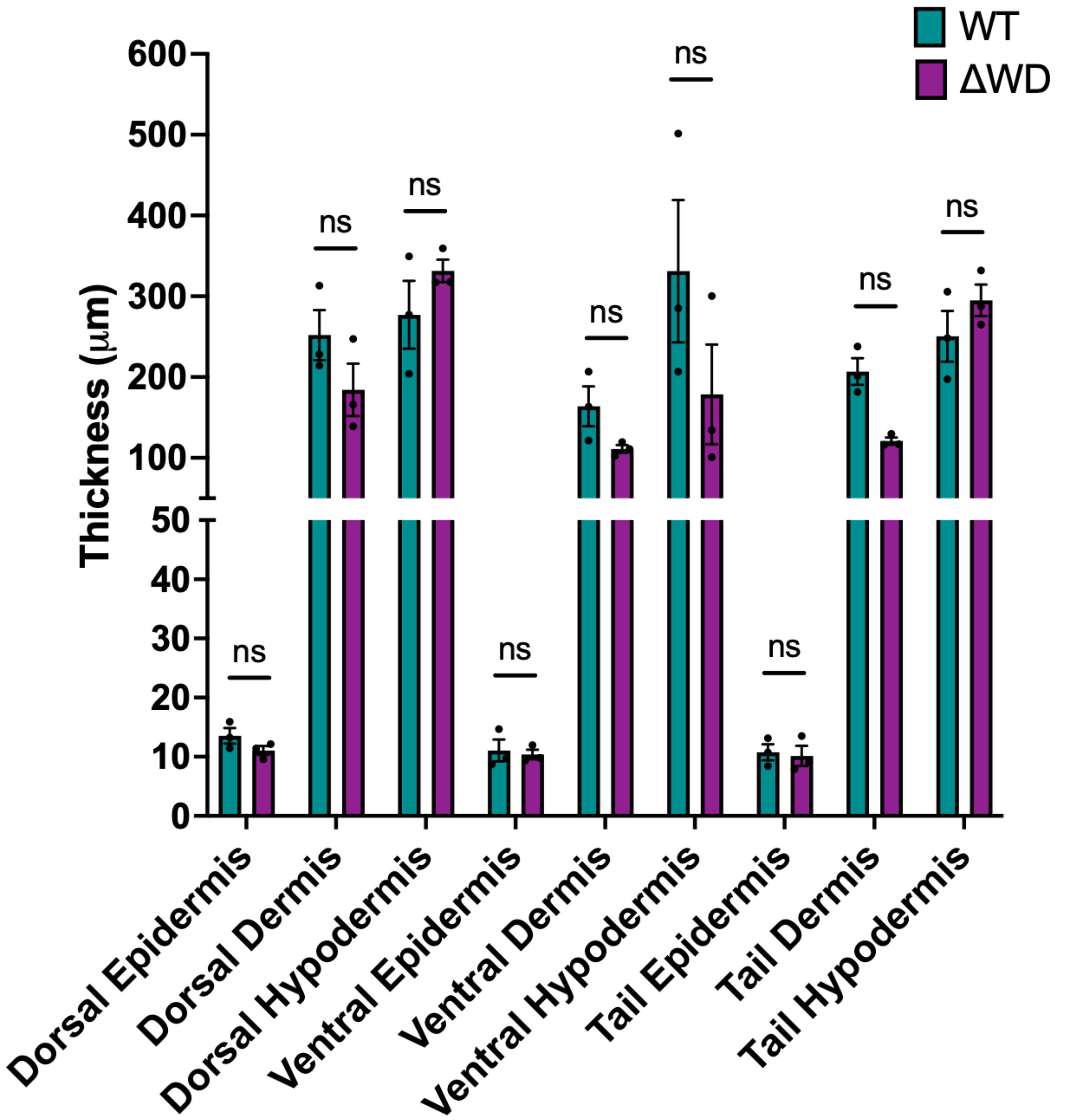

Figure 3.9 Mean thickness (μm) of the skin layers in the dorsal, ventral, and tail region. Mean thickness (μm) quantified using ImageJ with N=3 mice per genotype and n=20 measurements taken in each layer at each location. Error bars represent SE. Means were compared using the multiple unpaired t-tests with Welch and Bonferroni correction (ns = not significant). Figure taken from Conway et al. (2024).

3.2.4 The assessment of the skin permeability barrier of the ΔWD mouse model

3.2.4.1 General histomorphology of E18.5 WT littermate controls and ΔWD mouse embryos

I next sought to examine the epidermal permeability of WT and ΔWD mice. This is typically achieved using embryonic skin at day 18.5. The E18.5 embryos exhibited similar skin architecture, as seen in the 1-year-old mice, yet lacked a hypodermal layer (Figure 3.10). Moreover, the outermost layer of the epidermis, known as the stratum corneum (shown by I), was visible in the left panel by a pink continuous layer, while in the right panel it appeared more purple (Figure 3.10). Positioned beneath the cornified layer were the suprabasal layers (II) and an innermost basal layer (III), containing the proliferative and basal keratinocytes (Figure 3.10). The dermal papillae, which are the precursors of the hair follicles, are also visible on the H&E, and appear in the upper papillary dermis (shown by the asterisk), which can be distinguished by the reticular dermis (shown by the triangle) because of the higher cellular density (Figure 3.10). In addition to the three skin strata, a unique feature, termed the PCM, is found below the dermis, as seen previously in the aged mice. The histology of the dorsal skin revealed a uniform thickness of the epidermis in both WT and ΔWD E18.5 embryos, with one cell layer in the basal layer (III) and three cell layers seen in the suprabasal layer (II) (Figure 3.10).

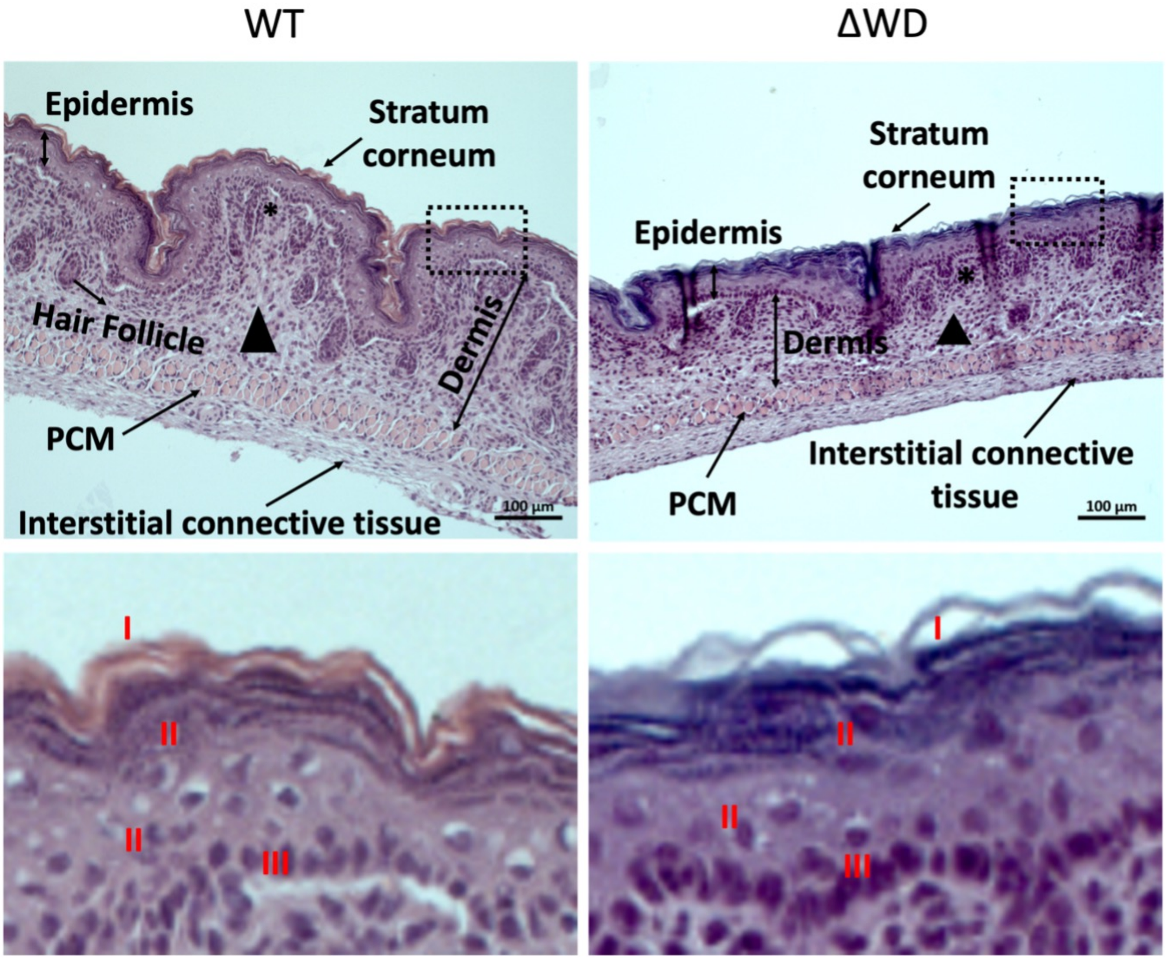

Figure 3.10 Representative H&E images showing overall histology of the ΔWD mouse model at E18.5. Left panel shows the dorsal skin from WT littermate controls, while the right panel shows the dorsal skin of ΔWD. Magnified images of epidermal layer, in the areas marked by the black dashed box, are shown below. Magnified images highlight the epidermal layers: basal layer (III), suprabasal layer (II) and stratum corneum (I). Asterisk shows the papillary dermis, while the triangle shows the reticular dermis. N=2 used for the histological analysis. Images taken on Zeiss Apotome 3 Imager Z.2. Scale bar: 100 µm. Figure taken from Conway et al. (2024).

3.2.4.2 Outside-in assessment of the E18.5 skin barrier

The assessment of barrier function was performed using two approaches. Firstly, embryos were submerged in toluidine blue (TB) and rinsed before macroscopic visualisation of dye retention. Both WT and ΔWD embryos lacked TB retention across the embryonic skin (Figure 3.11). TB dye was retained only at two sites: the remnants of the umbilical cord and at the sites of tail clipping for genotyping. Otherwise, the embryos were comparable to the untreated control (Figure 3.11 A). Secondly, sodium fluorescein (SF) was used as a confirmatory probe that permits examination of epidermal permeability by fluorescence microscopy. Fluorescence microscopy analysis revealed that SF aggregates on top of the uppermost epidermal layer, likely the stratum corneum (Figure 3.12 A). Measurements of SF penetration into the epidermis (Figure 3.12 B) showed a consistent depth of SF dye penetration, with the uptake measuring around 2 μm in both genotypes ($p > 0.05$) (Figure. 3.12 B). The results shown in Figure 3.12 demonstrate that the barrier was intact, thus corroborating the results of the TB penetration assay (Figure 3.11).

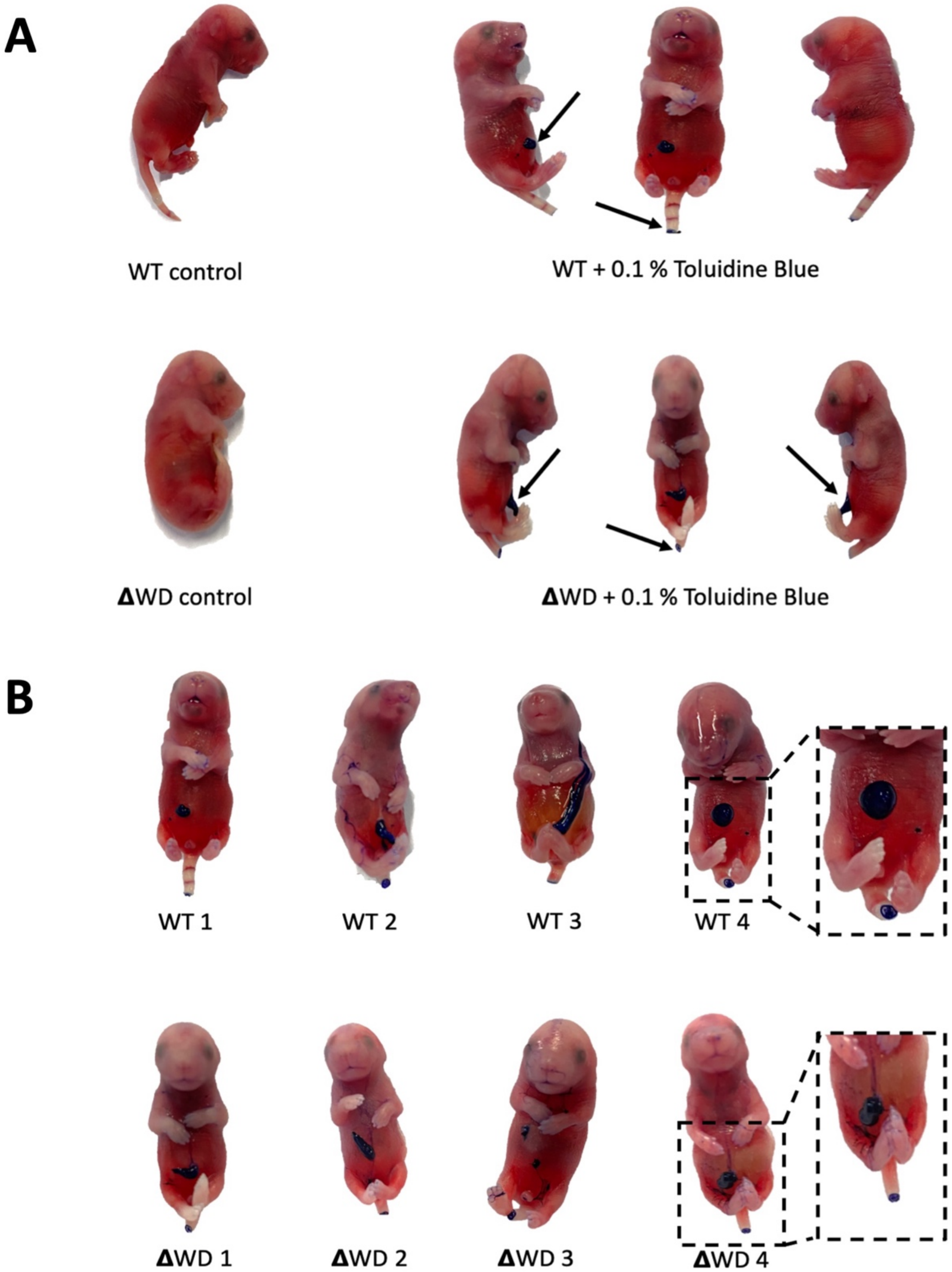

Figure 3.11 Toluidine blue dye permeation assay on E18.5 WT and ΔWD mouse embryos. **(A)** Representative images showing E18.5 embryos stained with 0.1 % toluidine blue. Arrow showing regions of dye uptake. **(B)** Representative images showing consistent toluidine blue dye uptake across embryos in both genotypes (N=4). Figure taken from Conway et al. (2024).

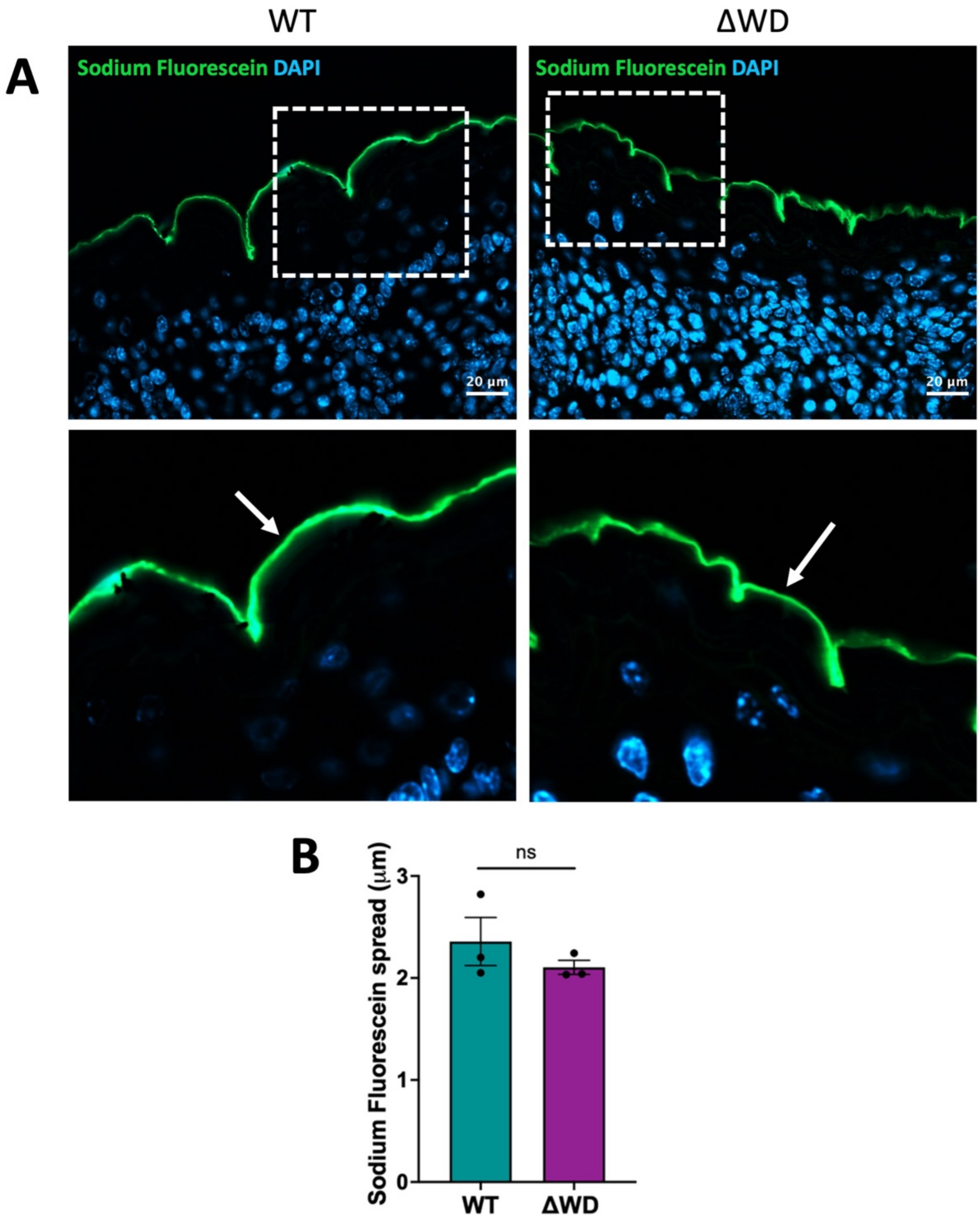

Figure 3.12 Outside-In barrier examination on E18.5 WT and ΔWD mouse embryos. (A) Representative images showing sodium fluorescein (SF) (green) staining in fixed WT and ΔWD embryonic dorsal skin (N=3). DAPI used to stain for nuclei (blue). SF (green) stain accumulating on upper stratum corneum layer (white arrow), shown in magnified insert (highlighted by ROI). Scale bar: 20 µm**. (B)** Dye uptake was measured in ImageJ. Data shown are mean depth of SF permeation (µm). Error bars are SE. N=3 mice per genotype with n= 40 SF measurements taken per mouse. Unpaired t-test used for comparison of means (ns = not significant). Figure taken from Conway et al. (2024).

3.2.5 Assessment of the dermal biomechanical properties of young (2-months) and aged (17-months) WT and ∆WD mice

To complete the cutaneous assessment of the ∆WD mouse model, the gross biomechanical functionality, including net elasticity and elastic recovery, was measured using a suction-based measurement method with the Cutometer® Dual MPA 580 from Enviroderm, UK. The analysis involved utilising young (2-months) and aged (17-months) control and ∆WD mice. This enabled an examination of how the absence of the WD domain, leading to LAP-deficiency, impacted dermal function and integrity over time.

The cutometer calculates a set of parameters, from which the net elasticity (Avg R5%) and elastic recovery (Avg R7%) are calculated (Table 3.2). A series of other parameters are automatically computed by the device and outputted into an excel spreadsheet (Table 3.2) (Qu, 2024). Average R0 (mm) denotes the amplitude at the end of the suction phase (i.e., 5 seconds). The average R1 (mm) exhibits the ability of the skin to return to its original state. The average R2 (%) emphasises the gross elasticity of the sample, with the closer the value is to 100%, the more elastic the sample is. The average R6 exhibits the portion of visco-elasticity on the elastic area of the curve, with a smaller value denoting more elasticity. The average R8 (mm) demonstrates the ability of the skin to return to its normal state. Finally, the average F1 (mm*s) shows the elasticity, with a value closer to 0 implying more elasticity in the sample. The net elastic recovery and elasticity of both WT and ∆WD dorsal skin were statistically indistinguishable at 2 and 17 months ($p > 0.05$) (Figure 3.13). However, in the ∆WD mouse, both the net elasticity and elastic recovery decreased with age ($p < 0.001$; $p < 0.05$, respectively) (Figure 3.13). A similar trend for elasticity was seen in the WT mouse skin yet did not reach statistical significance ($p > 0.05$) (Figure 3.13). The WT mice exhibited similar elastic recovery at 2 and 17 months ($p > 0.05$) (Figure 3.13).

Table 3.2. Overview of 17-month-old sample raw data from Cutometer ® Dual MPA 580 with various automated parameters and n=6 cutometer measurements.

Mouse ID	**Repeats**	**Avg R0 (mm)**	**Avg R1 (mm)**	**Avg R2 (%)**	**Avg R5 (%)**	**Avg R6 (%)**	**Avg R7 (%)**	**Avg R8 (mm)**	**Avg F1 (mm*s)**
4602 - WT	1	0.41	0.24	41.70	25.80	87.00	13.80	0.17	0.18
	2	0.38	0.15	61.10	59.20	60.90	36.80	0.23	0.04
	3	0.55	0.34	39.10	40.10	85.20	21.60	0.22	0.08
	4	0.61	0.43	30.20	27.30	90.40	14.40	0.19	0.07
	5	0.36	0.13	64.90	51.20	60.50	31.90	0.23	0.12
	6	0.49	0.23	53.80	48.20	74.90	27.50	0.26	0.08
4540 - **Δ**WD	1	0.40	0.17	57.10	63.90	55.10	15.70	0.23	0.08
	2	0.37	0.18	51.00	45.90	61.20	28.30	0.19	0.06
	3	0.27	0.13	50.40	58.50	78.70	33.70	0.13	0.05
	4	0.36	0.28	24.20	9.10	50.50	25.40	0.09	0.08
	5	0.38	0.24	37.20	31.50	98.80	27.70	0.14	0.10
	6	0.28	0.16	41.90	44.00	84.70	30.20	0.12	0.06

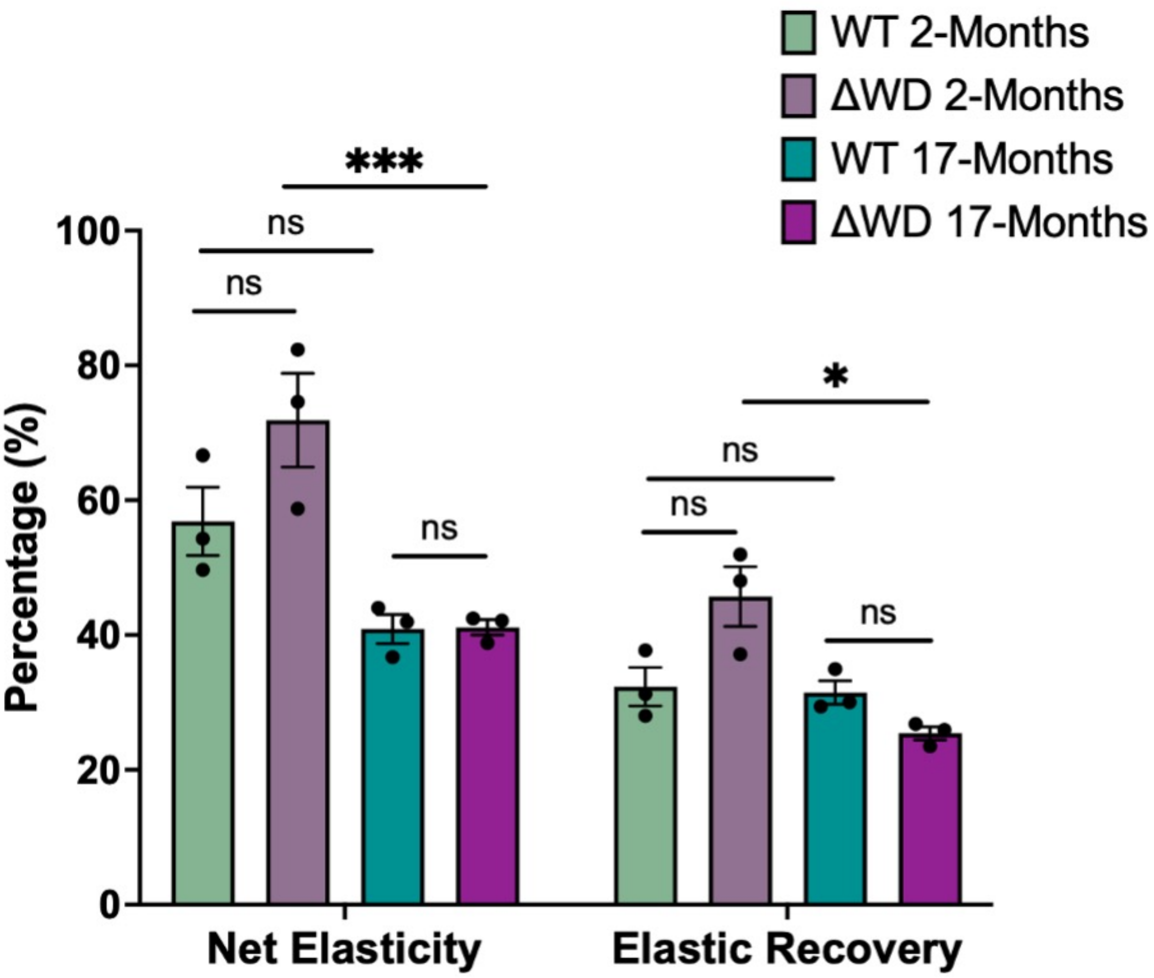

Figure 3.13 Biomechanical properties of young (2-Months) versus aged (17-Months) WT and ΔWD dorsal skin. Net elasticity and elastic recovery were measured using the Cutometer MPA 580. Data represent the mean of n=6 measurements taken per mouse with N=3 mice per genotype. Error bars represent SE. Two-way ANOVA with Tukey's post-hoc test (* ≤ 0.05; *** ≤ 0.001; ns = not significant). Figure taken from Conway et al. (2024).

3.3 Discussion

It is widely acknowledged that abnormalities in autophagy can impair the skin barrier, by preventing the natural process of keratinisation in the epidermis. However, distinguishing whether these disruptions stem from autophagy or other autophagy-related pathways, such as LAP, has posed a challenge. The ΔWD model now offers a novel *in vivo* system for investigating the physiological and pathophysiological roles of LAP. To further our current understanding, this chapter highlights the impact of LAP-deficiency on the integumentary system of 1-year-old mice and explores the relationship of LAP-deficiency on skin barrier formation and function.

3.3.1 Confirming the genetic background of the ΔWD mouse model

Routine genotyping was performed on tail lysates, using pre-designed primers (Arasteh, 2012) to ensure that only homozygous mice were used. The 290-291 primer set can be used to confirm the presence of WT alleles or ΔWD alleles. For WT littermate controls, a single WT allele band at 291 bp is expected, while ΔWD allele bands appear at 639 bp. For heterozygous mice, carrying one WT allele and one ΔWD allele, two PCR products would be expected, with one appearing at 291 bp and the other at 639 bp. The larger PCR product expected for ΔWD is due to the insertion of the two stop codons in exon 6, along with the bovine growth hormone polyadenylation site and the frt-flanked neomycin cassette (Arasteh, 2012; Rai et al., 2019). Further confirmation in terms of protein expression was performed by Western Blot. The truncated ATG16L1 revealed an expected reduced band size of 25 kDa in the ΔWD ATG16L1, compared to the full-length WT ATG16L1 of 75 kDa. The smaller band size was expected in ΔWD, as here, ATG16L1 only consists of the ATG5 binding domain in the N-terminal and the CCD.

3.3.2 Characterising the histology of integumentary system in the ΔWD mouse model

The overall appearance of the 1-year-old WT and ΔWD mice was comparable, and both exhibited similar body sizes and bodyweight, as previously reported by Rai and coworkers

(Rai et al., 2019). In the adult skin, the appendages, such as the hair follicles and sebaceous glands are found in the upper dermal and epidermal layer. Here, both control and ∆WD mice were covered with dense hair, with few white hairs present indicating signs of ageing. The hair follicle comprises three main regions: the bulbar region, the infundibulum and isthmus, with the hair following a defined cycle of growth, starting with the anagen (growth) phase, followed by catagen (regression) and subsequently a telogen (resting) phase (Lin, Zhu, and He, 2022; Wong et al., 2011). The histomorphology of hair in 1-year-old WT and ∆WD mice was evaluated by scanning electron microscopy (SEM). In both genotypes, the scale architecture exhibited the characteristic coronal scaling pattern, commonly observed in the hairs of small rodents (Deedrick and Koch, 2004). Mice deficient for ATG7, demonstrated a more irregular cuticle, which varied from their controls that exhibited normal cuticles in a regular pattern (Yoshihara et al., 2015). Moreover, the diameter of the hairs was reduced in the ATG7-deficient mice, compared to their controls, yet here control and ∆WD mouse hair thickness was comparable at hair follicle regions ($p > 0.05$) (Yoshihara et al., 2015). These results suggest that autophagy may play a role in regulating cornification in the hair, and that LAP-deficiency does not interfere with this process.

It is critical to consider gender when designing mouse model experiments, as anatomical and physiological differences are noted between male and female mice (Calabro et al., 2011). Sex hormones primarily regulate the differences in skin layer thickness, with the male skin around 40 % stronger, due to the thicker dermis providing a richer collagen network, and the female mice exhibiting a thicker epidermis (13 μm) and hypodermis (189 μm) (Calabro et al., 2011; Sabino et al., 2016). Here, for the histological analysis, skin tissue from the dorsal, ventral, and tail region from male ∆WD mice and WT littermate controls was assessed by brightfield microscopy. The average skin thickness of the C57BL/6 mouse is around 540 μm ± 20 μm (Sabino et al., 2016). The epidermis was slightly thinner in the 1-year-old ∆WD mice in the dorsal, ventral and tail skin, compared to age-matched WT littermate controls. However, this was not noted as a significant difference between genotypes ($p > 0.05$). Basal keratinocytes can be clearly visualised by H&E at a higher magnification and are represented as dark purple oval structures at the base of the epidermis, known as the basement membrane. A single layer of basal keratinocytes was observed in our higher magnification images, with thinner suprabasal layers revealed throughout the epidermis. As the control and ΔWD mice were covered by dense hairs throughout the entire body, depilation was done at the dorsal and ventral region, which resulted in the loss of the stratum corneum. Below the epidermis, lies the dermis, composed of high levels of structural proteins (e.g., collagen and elastin) that provide the mechanical integrity and elasticity to the skin (Calabro et al., 2011). Generally, this layer has a reported thickness of 226 μm ± 37 μm in male C57BL/6 mice (Sabino et al., 2016). In the 1-year-old ΔWD mice, the dermis was thinner in the dorsal, ventral and tail skin compared to controls, with statistical significance observed only in the tail dermis ($p < 0.001$). Finally, the hypodermis displayed varying results between the adult WT and ΔWD mice, but again results were not noted as significant differences ($p > 0.05$). Rodents exhibit a unique striated muscle, known as the panniculus carnosus muscle (PCM) and can be found below the hypodermis. It is formed of 3-4 myofibers and has a thickness of around 100 μm in adult mice (Bahri et al., 2019). It predominantly consists of type II fibres and functions to provide rodent skin with twitching and thermoregulation capacities, promoting contractions and supporting revascularisation during wound healing (Naldaiz-Gastesi et al., 2016; Naldaiz-Gastesi et al., 2018).

3.3.3. Evaluating the impact of LAP-deficiency on the epidermal permeability barrier

The subsequent phase of the study concentrated on assessing the epidermal permeability barrier. Both the control and ΔWD E18.5 skin samples displayed a thickened epidermis, characterised by a single layer of basal keratinocytes, seen along the base of the epidermis, followed by three suprabasal layers, and an outermost stratum corneum, distinguishable by its red or purple colour. This epidermal layer starts to develop from the surface ectoderm at E9.5, forming from a single layer of basal keratinocytes that subsequently become covered by a protective layer of squamous cells, known as the periderm (Jacob et al., 2023). Epidermal barrier function is commonly acquired at the later stages of embryonic development, which coincides with hair follicle development and epidermal stratification (Damen et al., 2021; Ding et al., 2016). This enables E18.5 embryos to be a useful tool for the assessment of barrier function. In the control and ΔWD E18.5 skin, the dermis contains the dermal papillae, which serve as the precursors for hair follicles in the murine skin. These epidermal appendages start to develop after E9.5, leading to the complete formation of a stratified epidermis by E19.5 (Jacob et al., 2023). The hypodermal layer was absent in the control and ΔWD E18.5 skin. Schmidt and Horsley report that the murine intradermal adipocyte depot, i.e., the hypodermis, forms postnatally, through the interaction with growing hair follicles (Schmidt and Horsley, 2012). Throughout follicular morphogenesis, intradermal adipocytes develop and grow through lipogenesis, resulting in adipocyte hypertrophy. This study shows that despite the absence of LAP, ΔWD mouse skin still undergoes a healthy process of skin morphogenesis comparable to controls.

To further our understanding of the epidermal barrier of the ΔWD mouse model, dye permeation assays on the E18.5 mouse embryos were performed. For this toluidine blue (TB) and sodium fluorescein (SF) were used. TB is a cationic dye, which can visualise the presence of proteoglycans in desired tissues, as it has a high affinity for the sulfate groups of the proteoglycans (Bergholt et al., 2019). It can also be used to detect changes in chromatin DNA-protein complexes and nucleolus location (Vidal and Mello, 2019). SF is a negatively charged hydrophilic molecule, with a low molecular weight (376 Da) that possesses the advantage of being freely dispersible (Ahishali and Kaya, 2021). In the event of a leaky, disturbed skin barrier, SF would permeate freely into the underlying skin layers. Results on E18.5 ΔWD mice and WT littermates showed a fully developed and functioning skin barrier, noted by the lack of dye retention throughout the body. Areas such as the umbilical stump and tail were rich in TB staining, due to the damage caused by the clipping of the tail for genotyping and the DNA rich umbilical cord. The SF stain was homogenous and continuous throughout the entire WT and ΔWD embryonic epidermis ($p > 0.05$). The results are consistent with the outcomes of the TB staining experiments.

3.3.4 Biomechanical assessment of the dermal function ΔWD skin

To complete the cutaneous examination of the aged ΔWD mouse model, the biomechanical properties of the ΔWD mouse skin were assessed. The biomechanical properties of the skin can be evaluated using a wide range of non-invasive techniques, such as experimental methods of suction, traction, torsion, and indentation (Langton et al., 2017). Commonly, for the assessment of skin elasticity, the suction-based method, using the commercially available Cutometer (Courage + Khazaka Electronic GmbH, Köln, Germany) is used (Langton et al., 2017). Using a probe to apply a negative pressure to the skin, the Cutometer can measure the degree of skin deformation in the probe and measure the recovery of the skin on removal of the suction (Langton et al., 2017). This pressure-release cycle can be repeated, to measure the ability of the skin to both resist the negative pressure and return to its original state (Langton et al., 2017). The analysis was completed using young (2-months) and aged (17-months) control and ΔWD mice, to examine the effects of the loss of the WD domain of ATG16L1, resulting in LAP-deficiency on dermal function over time. WT and ΔWD dorsal skin exhibited decreases in net elasticity and elastic recovery during ageing. The disparities in net elasticity were found to be nonsignificant among WT age groups ($p > 0.05$), whereas in ΔWD mice these differences were statistically significant ($p < 0.001$). At comparable ages across genotypes, there was no difference in net elasticity ($p > 0.05$), suggesting that the absent WD domain of ATG16L1 accelerates intrinsic ageing within the ΔWD mouse. Similarly, at comparable ages across genotypes, minor changes in elastic recovery were demonstrated ($p > 0.05$). While control mice exhibited no alteration in elastic recovery with age ($p > 0.05$), a marked decrease in elastic recovery was observed in ΔWD mice ($p < 0.05$). Age-related microstructural changes primarily affect the collagen fibres, alongside other components of the extracellular matrix (Lynch et al., 2017). There is a progressive decrease in collagen, elastin, and proteoglycan content, with about a 30% decrease in collagen content between 2 month and 22-month-old murine skin (Lynch et al., 2017). As previously stated, Tashiro and colleagues demonstrated that the number of autophagosomes increases in dermal fibroblasts with ages, as well as LC3-II expression is elevated in dermal fibroblasts cultured from elderly donors (Tashiro et al., 2014). Moreover, they showed that autophagy was disrupted at the degradation step in aged fibroblasts; consequently, this could possibly explain why we saw a decline in the net elasticity and elastic recovery in our WT and ΔWD skin. Further research would need to consider whether LAP is involved in degrading aged fibroblasts, alongside autophagy and whether the loss of LAP function accelerates this decline in dermal function and acceleration in collagen fragmentation.

Age-related physiological and pathophysiological changes have already been observed in the ΔWD model. Two-year-old ΔWD mice exhibited a strong deposition of endogenous murine Aβ in the hippocampus and throughout the cerebral cortex, compared to their WT littermate controls (Heckmann et al., 2020). Furthermore, ΔWD mice have demonstrated that the loss of the WD region of ATG16L1 is sufficient to drive spontaneous, age-associated Alzheimer's disease. Therefore, additional research is required to ascertain LAP's involvement in dermal turnover and its contribution to dermal function.

3.4 Conclusions

This chapter has described the general morphology of the ΔWD mouse integument and has revealed that WT littermate controls and ΔWD mice show subtle differences in their skin histology. Assessment of the biomechanical properties of the ΔWD mouse model skin indicated that the loss of the WD domain of ATG16L1, resulting in LAP-deficiency, may accelerate intrinsic skin ageing relative to age-matched littermate controls. Overall, the observed differences were found to have no adverse effects on skin barrier function, demonstrated by an intact skin barrier in both the WT and ΔWD E18.5 skin.

3.5 Limitations and future work

The experiments conducted within this chapter were primarily done on depilated WT and ΔWD mice. Initially, epilation was achieved by using a depilatory cream, yet this was quite difficult, due to the dense fur of the mice. Moreover, these creams can be corrosive and damaging to the skin, due to the potassium thioglycolate and sodium hydroxide (Reichert et al., 2023). Therefore, I decided to trim the hair first and then use a razor for the remaining hair. I believe by using this method, some of the stratum corneum was removed in the process, which is likely why it was not as visible in the 1-year-old skin as it was in the E18.5 skin.

The dye permeation assays were done using embryos from one timed mating. Fortunately, I managed to get 8 embryos from this, yet this represented one technical repeat. Ideally, this experiment would need to be repeated at least another two times. However, considering the 3Rs of animal research (Replacement, Reduction and Refinement), it is important to minimise the number of animal sacrifices; therefore, technical repeats were favoured rather than biological repeats for this experiment. Future work could be done on postnatal day 1, as these mice are born naked, with the hair beginning to appear at 2-4 days post birth.

For the biomechanical assessment of the ∆WD mouse model further analysis would need to include more extensively aged mice with a higher statistical power to gain a greater insight into the cutaneous phenotype of the ∆WD mouse model. Moreover, analysis would need to be conducted on the dermal compartment, gaining a greater understanding into dermal composition and organisation. LAP appears to contribute to the acceleration in ageing. Therefore, exploring autophagic activity in the dermal fibroblasts and its impact on matrix metalloproteinases (MMP) expression would be of interest. Dysregulation in autophagy has been linked to changes in type I procollagen, hyaluronan and elastin, as well collagen fibril breakdown, leading to a decline in dermal structural integrity and skin fragility (Kovacs et al., 2022). Furthermore, it would be intriguing to assess the levels of ROS in both control and ∆WD skin during intrinsic ageing. ROS not only influences LAP function but also contributes to intrinsic ageing by activating signalling pathways associated with diminished collagen production and activation of MMPs, which are responsible for collagen degradation (Gu et al., 2020).

Chapter 4: Comprehensive analysis of key gene and protein expression patterns in the ΔWD epidermis

4.1 Introduction

The skin's primary role is to serve as a protective barrier, to sustain this function and effectively heal injuries, it relies on the regenerative and proliferative capabilities of its stem cells (Ansary et al., 2021). These cells are crucial for replenishing and restoring the damaged skin layers, thereby preventing the body from dehydration, pathogen invasion and environmental factors. The multi-layered structure of the epidermis is continuously renewed by the process of terminal differentiation, where keratinocytes in the basal layer divide and differentiate to form the cells of the spinous, granular and cornified layers (Akinduro et al., 2016). Keratins are key components of this intermediate filament cytoskeleton of the epidermis and are expressed in a cell type and differentiation-specific manner (Santos et al., 2002).

Autophagy has demonstrated roles in skin and differentiation, with autophagy markers being significantly upregulated in granular layer formation during development or in skin conditions such as psoriasis (e.g., p62; ULK1; WIPI1) (Akinduro et al., 2016; Koenig et al., 2020; Lee et al., 2011). The terminal differentiation process is repeated in the adult epidermis and the expression pattern of the autophagy and differentiation markers persists in adult mouse and human skin (Akinduro et al., 2016). The influence of non-canonical autophagy, specifically LAP, on skin differentiation remains unknown.

Therefore, this chapter aims to understand the role played by LAP on epidermal differentiation. I hypothesise that ΔWD mice will display comparable levels of fundamental components of the differentiation (i.e., Keratin 10 and 1; involucrin) and autophagic (i.e., LC3-I/II; p62) pathway. This chapter will aim to meet the following experimental objectives:

- Evaluating the mRNA expression patterns of key keratins (i.e., Keratin 5, 10 & 1) and late differentiation marker (i.e., involucrin) in the 1-year-old epidermal skin of the ΔWD mouse model, using SYBR green qPCR.
- Examine the expression of keratins, proliferative (i.e., Akt; p-Akt & PCNA) and autophagy markers (i.e., LC3-I/II & p62) in the 1-year dorsal skin of the ΔWD mouse model by Western Blot and immunofluorescence.
- Compare the ability of the WT and ΔWD skin, to replace the epidermis by assessing the level of PCNA-positive basal keratinocytes in the embryonic skin tissue.

4.2 Results

4.2.1 Validating the protein expression of key autophagy and LAP markers

As previously stated, keratinocytes undergo a controlled process of terminal differentiation, which is essential for the maintenance of tissue homeostasis. Autophagy has exhibited roles in the process of keratinisation in the epidermis, which led me to evaluate the expression patterns of key autophagy markers in the adult WT and ∆WD epidermis (Figure 4.1). The status of autophagy was examined in epidermal skin lysates of 1-year-old WT and ∆WD mice, by probing for the cytosolic LC3-I and the autophagosome membrane bound form LC3-II, as well as the further autophagy substrate protein p62. The status of LC3-I and LC3-II were comparable in WT and ∆WD mice ($p > 0.05$) (Figure 4.1). The p62 expression also remained unchanged in both groups ($p > 0.05$) (Figure 4.1). Results indicate that there is no defect in autophagy, due to the consistent expression of p62 and LC3-II in both WT and ∆WD (Figure 4.1 B).

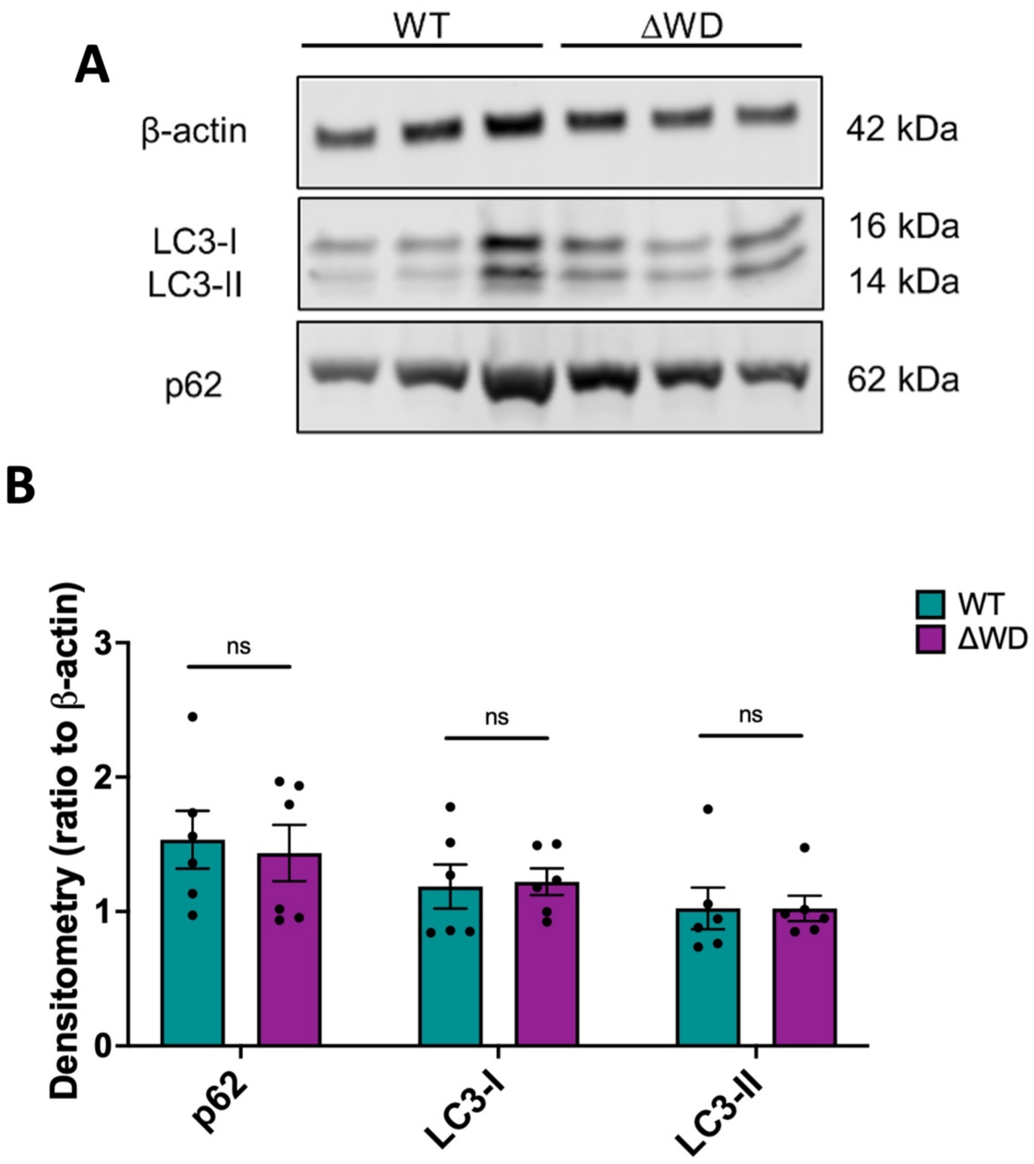

Figure 4.1 Western Blot and densitometry analysis of autophagy markers in 1-year old WT and ΔWD whole skin. (A) Representative Western Blots for β-actin, p62, LC3-I and LC3-II. N=3 mice per genotype. **(B)** Densitometric analysis of Western Blot data in panel A. Band densities were quantified and normalised to β-actin loading control. Data derived from 3 independent experiments. Means represent N=6 mice per genotype. Error bars are SE. Multiple unpaired t-tests with Bonferroni correction (ns = not significant). Figure taken from Conway et al. (2024).

4.2.2 Comparison of LC3B expression in embryonic vs adult epidermal tissue

To further evaluate the expression of LC3 in WT and ΔWD skin, immunohistochemistry was performed on E18.5 embryonic and 1-year-old whole skin (Figure 4.2-4.3). The expression of LC3B (LC3B-I & LC3B-II) appeared confined to the suprabasal layers of the epidermis, in both WT and ΔWD embryonic dorsal skin (Figure 4.2 A). The LC3B expression appeared beneath the stratum corneum, which is represented by the sodium fluorescein stain (green) (Figure 4.2 A). The intensity of LC3B expression was measured in the ImageJ software, using a rectangular region of interest with a horizontal distance of 49 μm (Figure 4.2 B). The intensity of the LC3B pixels was greater in the ΔWD embryonic dorsal skin, yet this was shown to be not statistically significant from the WT embryonic dorsal skin ($p > 0.05$) (Figure 4.2 B-C).

LC3B expression in the adult WT and ΔWD skin was homogenous across genotypes, with LC3B localised to the suprabasal layers of the epidermis, with few LC3B aggregates found in the basal layer of the WT epidermis (Figure 4.3 A). Moreover, in the uppermost WT epidermal layer, an accumulation of LC3B aggregates can be seen, while ΔWD exhibits few LC3B aggregates (Figure 4.3 A). These spherical aggregates may be signs of autophagosomes in the epidermis of WT and ΔWD dorsal skin. In the WT, the LC3B aggregates appear to be localised in the perinuclear region and exhibit a more clustered punctate staining, while in the ΔWD, the staining for LC3B is more diffuse and with few LC3B aggregates found at the cell periphery (Figure 4.3 A). The level of LC3B pixel intensity was measured in ImageJ software, again using a rectangular region of interest with a horizontal distance of 40 μm (Figure 4.3 B-C). The intensity of LC3B expression was greater in the WT dorsal skin, compared to ΔWD (Figure 4.3 B). This greater average pixel intensity of LC3B was shown to be statistically significant when compared to the ΔWD dorsal skin ($p \leq 0.05$) (Figure 4.3 C).

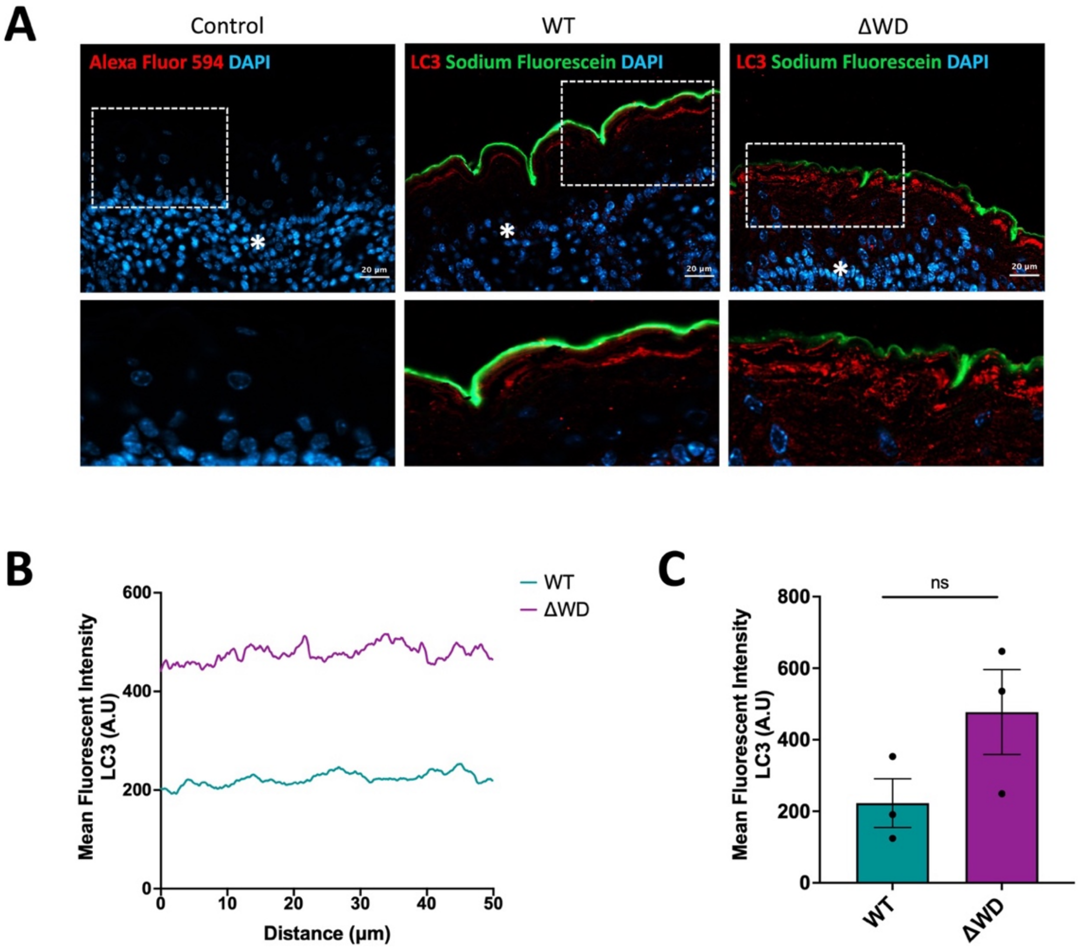

Figure 4.2 LC3B expression (LC3B-I and LC3B-II) in E18.5 mouse skin. Representative immunohistochemistry of LC3B (red) expression in WT and ΔWD dorsal epidermal skin. Secondary antibody control (Alexa Fluor 594) in left panel. Magnified images, shown below, of the areas marked by a white dashed box. Sodium fluorescein (green) exhibiting the stratum corneum. DAPI used to stain for nuclei (blue). Asterisk denotes the basal cell layer in the epidermis. Images are representative from 3 independent experiments on N=3 mice per genotype. Scale bar: 20 µm. **(B)** Line graphs show fluorescent intensities (arbitrary units, A.U) of LC3B expression in embryonic WT and ΔWD epidermal skin, measured across a rectangular selection with 49 µm distance in ImageJ software. Line represents the mean of n=3 fluorescent intensity measurements from N=3 mice per genotype. **(C)** Bars represent the mean fluorescent intensities (arbitrary units) of LC3B gray value from 3 independent experiments with n=6 fluorescent intensity profile measurements taken per animal and N=3 mice per genotype. Error bars are SE. Unpaired t-test with Welch’s correction (ns = not significant).

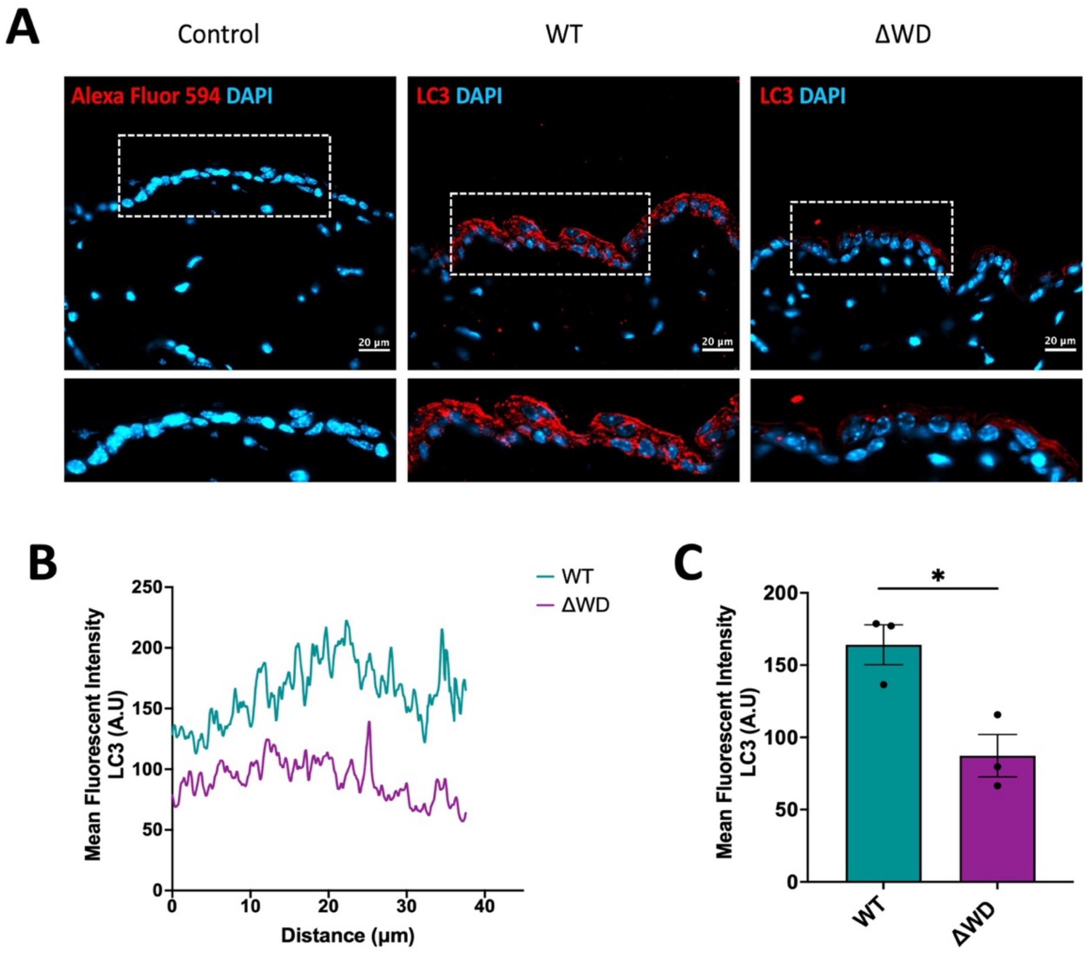

Figure 4.3 LC3B expression (LC3B-I and LC3B-II) in 1-year-old mouse skin. (A) Representative immunohistochemistry of LC3B (red) expression in WT and ΔWD dorsal epidermal skin. Puncta (red) denote LC3B aggregates. Secondary antibody control (Alexa Fluor 594) in left panel. DAPI used to stain for nuclei (blue). Magnified images, shown below, of the areas marked by a white dashed box. Images are representative from 3 independent experiments on N=3 mice per genotype. Scale bar: 20 μm. **(B)** Line graphs show fluorescent intensities (arbitrary units, A.U) of LC3B expression in adult WT and ΔWD epidermal skin, measured across a rectangular selection with 40 μm distance in ImageJ software. Line represents the mean of n=3 fluorescent intensity measurements from N=3 mice per genotype. **(C)** Bars represent the mean fluorescent intensities (arbitrary units) of LC3B gray value from 3 independent experiments with n=6 fluorescent intensity profile measurements taken per animal and N=3 mice per genotype. Error bars are SE. Unpaired t-test (* ≤ 0.05). Figure taken from Conway et al. (2024).

4.2.3 Similar expression of key keratinocyte differentiation and proliferative markers in the ∆WD mouse model

Next, I looked at the relative expression of key keratins (i.e., keratin 5, keratin 10 and keratin 1) and late terminal differentiation marker involucrin, a precursor protein of the epidermal cornified envelope. This was assessed in isolated epidermal tissue from WT and ∆WD mice using SYBR Green qPCR (Figure 4.4). Basal marker keratin 5 showed a comparable expression in the epidermal skin of WT and ∆WD, yet this was shown to not be significant ($p > 0.05$) (Figure 4.4 A). Similarly, keratin 10 and keratin 1, both markers for the early stages of terminal differentiation, exhibited similar levels of expression ($p > 0.05$) (Figure 4.4 A). This was confirmed by Western Blot, which also revealed a comparable expression of keratin 5 and keratin 10 across genotypes ($p > 0.05$) (Figure 4.4 B-C). Involucrin, a marker for granular layer formation, demonstrated equal expression ($p > 0.05$) across both genotypes (Figure 4.4). In addition, the level of p-Akt and Akt was shown to be similar in WT and ∆WD epidermal tissue (Figure 4.4 B-C).

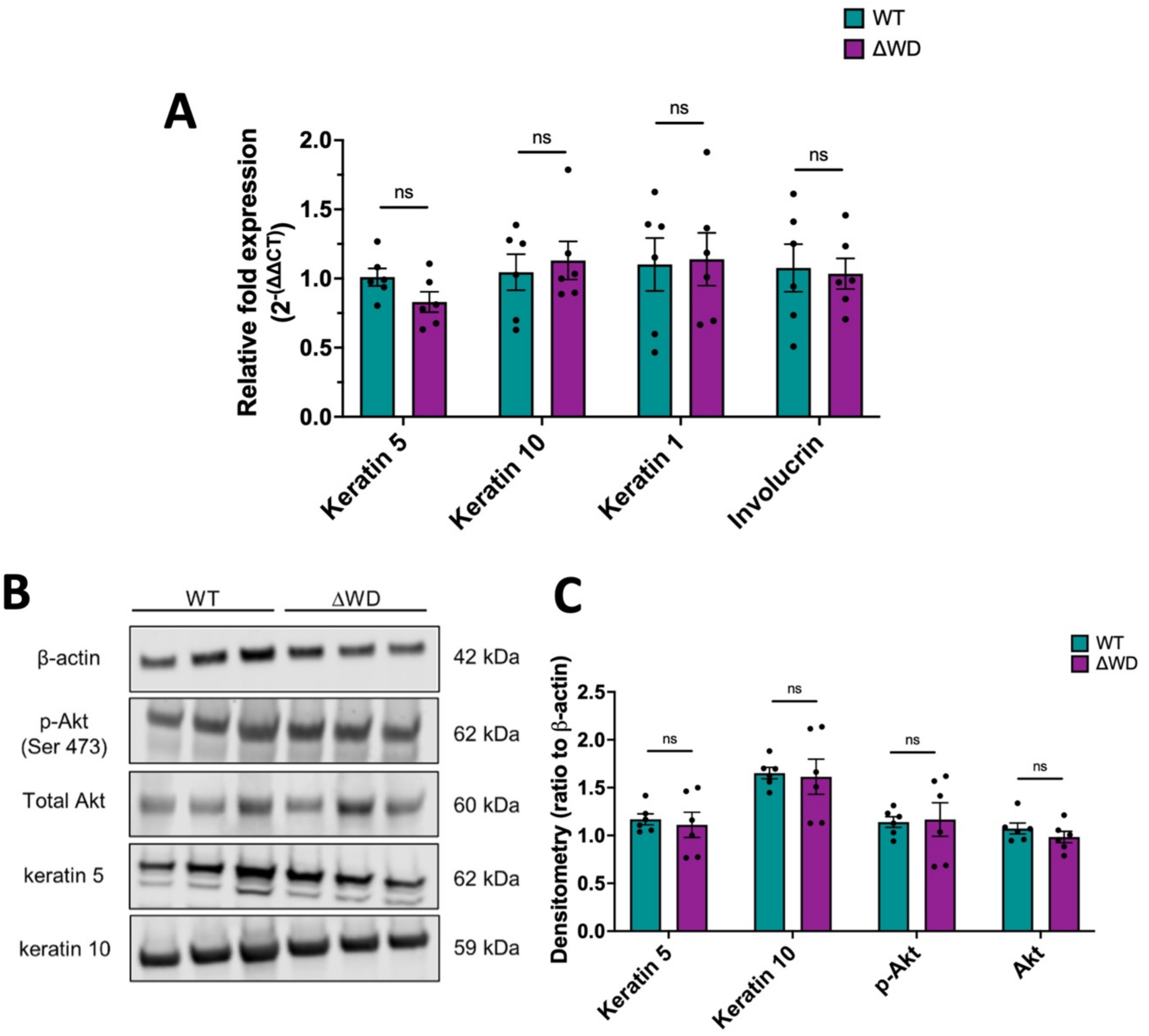

Figure 4.4 Expression of key keratinocyte differentiation and proliferative markers in 1-year old WT and ΔWD epidermal skin. (A) Relative fold expression of Keratin 5, Keratin 10 Keratin 1 and involucrin assessed by SYBR green qPCR. Relative mRNA expression normalised to 18S. Data points represent means of triplicate technical repeats of cDNA samples from individual mice (N=6 mice per genotype). Error bars are SE. Multiple unpaired t-tests (ns = $p > 0.05$). **(B)** Representative Western Blots from 3 independent experiments for β-actin, keratin 5, keratin 10, p-Akt and Akt. N=3 mice per genotype. **(C)** Densitometric analysis of Western blot data in panel B. Band densities were quantified and normalised to the β-actin loading control (n=3). N=6 mice per genotype. Error bars are SE. Multiple unpaired t-tests with Bonferroni correction (ns = not significant). Figure taken from Conway et al. (2024).

4.2.4 Localisation of keratin 10 expression in adult epidermis

To assess the localisation of keratin 10 expression in the adult epidermis, 1-year old dorsal skin was isolated from WT and ΔWD mice and examined by immunohistochemistry (Figure 4.5). Immunofluorescence analysis of keratin 10 revealed a homogenous staining in the WT and ΔWD epidermis (Figure 4.5 A). Keratin 10 expression was confined to the suprabasal layers of the epidermis (Figure 4.5 A). The level of keratin 10 fluorescent intensity was measured in the ImageJ software, by analysing the level of pixel intensities across a rectangular region of interest (Figure 4.5 B). Here, the horizontal distance through the selection was around 45 μm, exhibited by the x-axis (Figure 4.5 B). The mean gray value, which denotes the average keratin 10 pixel intensity in the epidermis, demonstrated an equal amount of keratin 10 expression in WT and ΔWD skin (Figure 4.5 B-C).

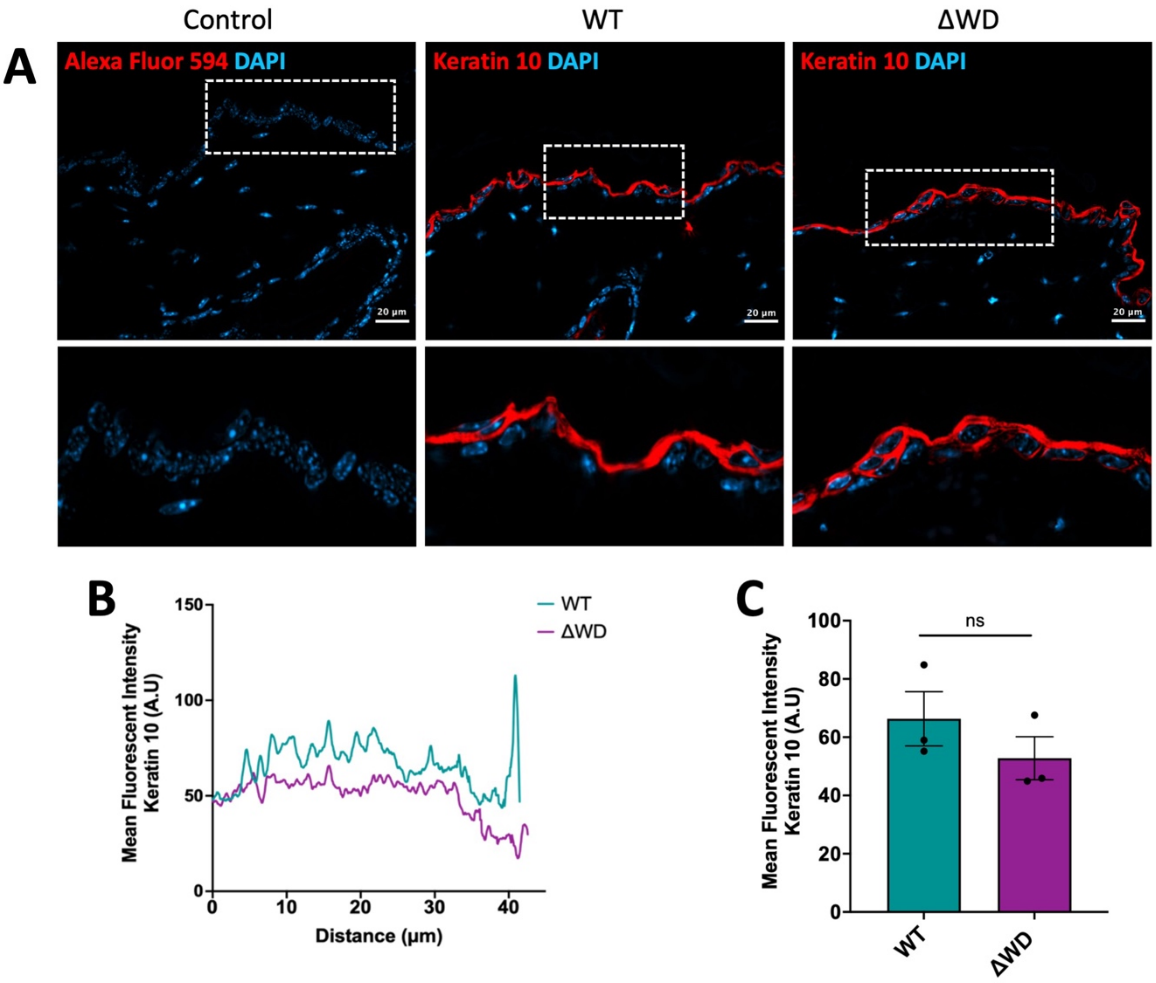

Figure 4.5 Keratin 10 expression in 1-year-old mouse skin. (A) Representative immunohistochemistry of keratin 10 (red) expression in WT and ΔWD dorsal mouse skin. DAPI used to stain for nuclei (blue). Magnified images, shown below, of the areas marked by a white dashed box. Images are representative from 3 independent experiments. N=3 mice per genotype. Scale bar: 20 μm. Secondary antibody control (Alexa Fluor 594) in left panel. **(B)** Line graphs show fluorescent intensities of keratin 10 expression in adult WT and ΔWD epidermal skin, measured across a rectangular selection with 45 μm distance in ImageJ software. Line represents the mean of n=3 fluorescent intensity measurements from N=3 mice per genotype. **(B)** Bars represent the mean fluorescent intensities of keratin 10 gray value from 3 independent experiments with n=6 fluorescent intensity profile measurements taken per animal and N=3 mice per genotype. Error bars are SE. Unpaired t-test (ns = not significant). Figure taken from Conway et al. (2024).

4.2.5 Comparison of PCNA expression in embryonic vs adult epidermal tissue

To examine the contribution of proliferation to the subtle morphological changes observed in the epidermis of the ∆WD mouse model, the expression of the nuclear antigen PCNA was assessed. PCNA expression was evaluated by immunofluorescence of E18.5 and adult WT and ∆WD dorsal skin. PCNA's distribution was primarily confined to the basal layer in adult and embryonic epidermal skin, yet PCNA expression was also found beneath the epidermal-dermal boundary (white dashed line) in the embryonic dorsal skin (Figure 4.6; Figure 4.7). Here, few PCNA positive cell types are visible, which might denote the proliferating fibroblasts of the dermis (Figure 4.6 A). There were few PCNA-stained fibroblasts observed in the 1-year-old dorsal skin (Figure 4.7A) The spatial distribution of PCNA was even in the embryonic basal cell layer and dermis, with no areas showing accumulation of PCNA positive cells in any region (Figure 4.6 A). This is also demonstrated in the adult dorsal skin (Figure 4.7 A). The number of PCNA positive nuclei was further assessed by counting the number of PCNA positive cells compared to total number of cells in the epidermis. In both embryonic and adult skin, the number of PCNA positive basal cells was similar across genotypes ($p > 0.05$) (Figure 4.6-4.7). The comparable levels of PCNA-positive basal cells across genotypes, in both embryonic and adult tissue, provides an indication that both WT and ∆WD mice have the same ability to replace the basal cells of the epidermis.

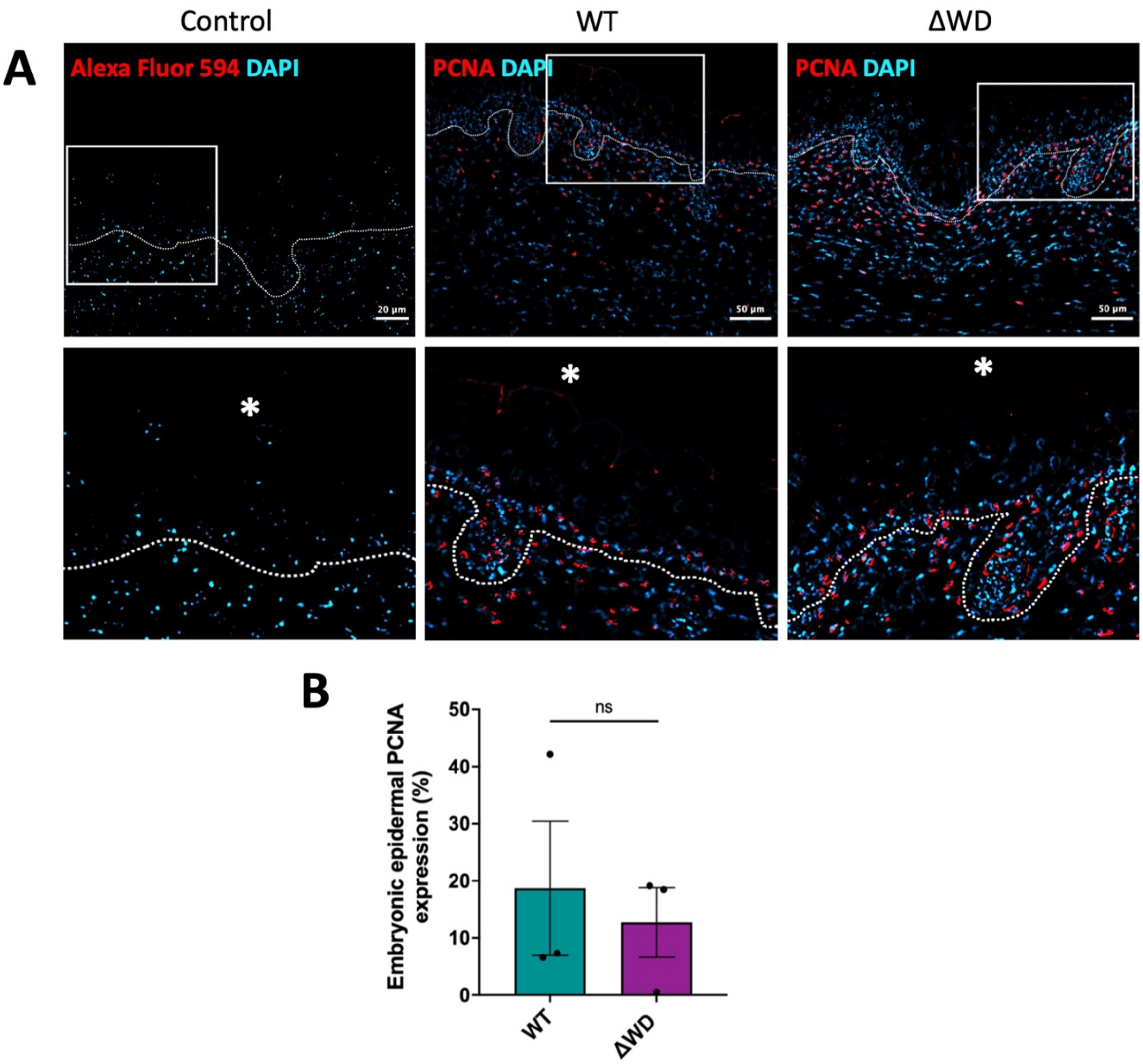

Figure 4.6 PCNA expression in the WT and ΔWD embryonic (E18.5) dorsal skin. (A) Representative immunohistochemistry of PCNA (red) expression in basal cells of WT and ΔWD skin dorsal skin. DAPI used to stain for nuclei (blue). Dashed line highlighting the epidermal-dermal boundary. Secondary antibody control (Alexa Fluor 594) in left panel. Magnified images, shown below, of the areas marked by a white box. Asterisk denotes the stratum corneum. Images are representative from 3 independent experiments on N=3 mice per genotype. Scale bar: 50 μm and 20 μm for control. **(B)** Data represents the mean (%) of PCNA positive basal cells in WT and ΔWD epidermis. N=3 mice per group with 2 epidermal regions used to count PCNA positive basal cells, using Fiji ImageJ. Error bars are SE. Mann-Whitney test (ns = not significant). Figure taken from Conway et al. (2024).

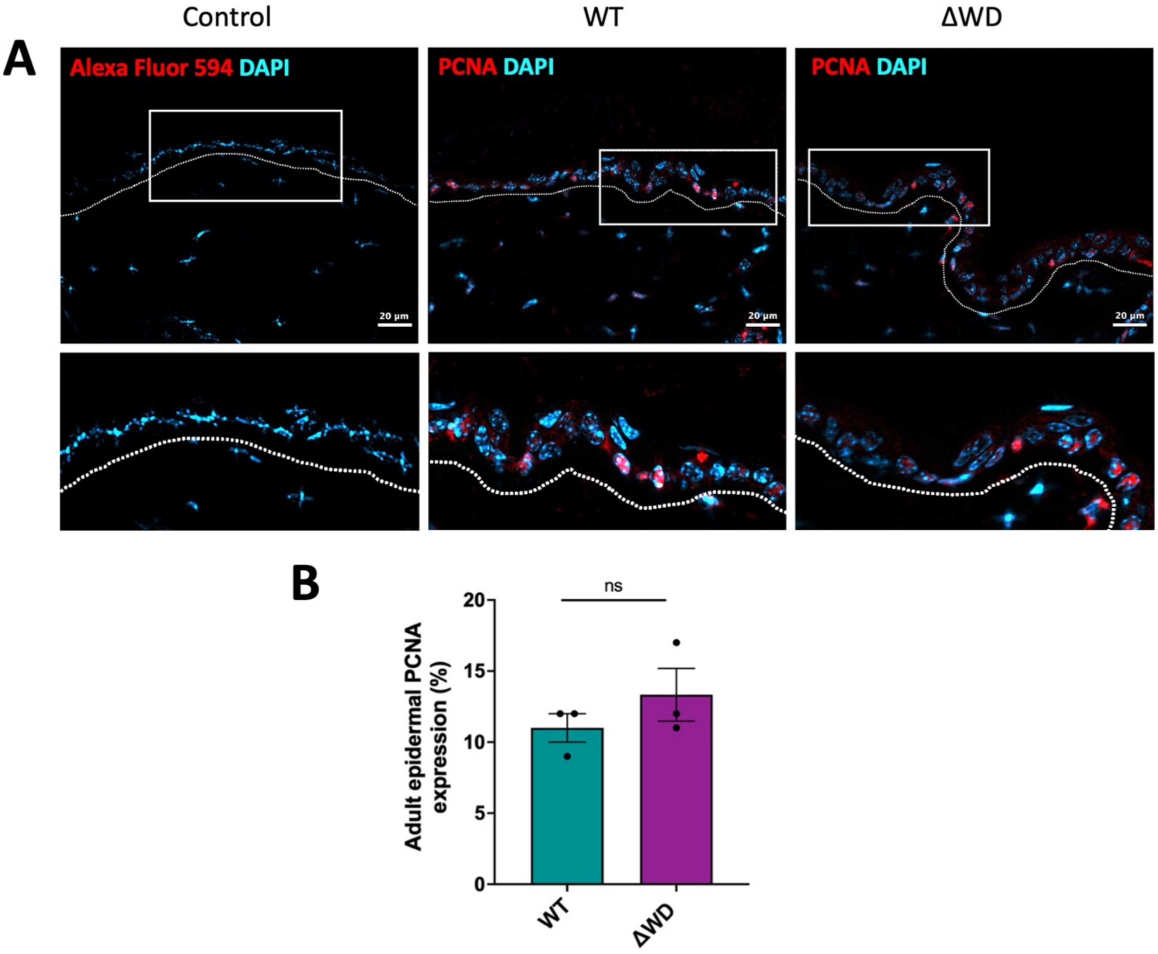

Figure 4.7 PCNA expression in the WT and ΔWD 1-year old dorsal skin. (A) Representative immunohistochemistry of PCNA (red) expression in basal cells of WT and ΔWD skin dorsal skin. DAPI used to stain for nuclei (blue). Dashed line highlighting the epidermal-dermal boundary. Secondary antibody control (Alexa Fluor 594) in left panel. Magnified images, shown below, of the areas marked by a white box. Images are representative from 3 independent experiments on N=3 mice per genotype. Scale bar: 20 µm. **(B)** Data represents the mean (%) of PCNA positive basal cells in WT and ΔWD epidermis. N=3 mice per group with 2 epidermal regions used to count PCNA positive basal cells, using Fiji ImageJ. Error bars are SE. Mann-Whitney test (ns = not significant).

4.3 Discussion

This chapter examined the expression of key keratins (i.e., keratin 5; keratin 10 and keratin 1), a differentiation marker (i.e., involucrin), proliferative markers (i.e., PCNA; p-Akt and Akt) and autophagic markers (i.e., LC3-I/II and p62) in isolated dorsal skin tissue from WT and ∆WD mice. Investigating the effects of LAP deficiency on these markers will help determine whether autophagy or LAP is responsible for maintaining epidermal homeostasis. The research conducted in this chapter enhances our understanding of autophagy in epidermal turnover and outlines the effects of LAP-deficiency on epidermal homeostasis. Utilising the ∆WD mouse model allows us to clearly distinguish between autophagy and LAP, enabling evaluation of the function of LAP in the murine skin and identifying potential therapeutic targets for future dermatological research.

4.3.1 Evaluating the autophagic status in isolated epidermal skin of ∆WD

The level of autophagic status in isolated epidermal tissue was assessed by qPCR, Western Blot and immunohistochemistry. The expression of LC3B in the E18.5 WT and ∆WD was localised in the suprabasal layers but was shown to not be significantly different between control and mutant mice ($p > 0.05$). Akinduro and colleagues showed that autophagy is actively involved in normal epidermal development and differentiation, emphasising that defects in autophagy may result in epidermal disorders such as psoriasis (Akinduro et al., 2016). During embryonic development, the expression of LC3 commences at E15.5, and is present in low levels in the spinous layer of the epidermis. However, as the granular layer begins to form at E16.5, LC3 becomes upregulated in the uppermost layers, which are believed to represent the early granular layers. The elevation in LC3 expression after E16.5 indicates that autophagy occurs during epidermal differentiation and may be involved in the formation of the granular layer (Akinduro et al., 2016). Similar findings were observed in our 1-year-old WT and ∆WD dorsal skin, with LC3B primarily concentrated in the suprabasal layers, indicating that autophagy is mainly active in the later stages of differentiation and persists in adult tissue. A greater expression of LC3B was revealed in the WT dorsal skin, in comparison to the ∆WD ($p \leq 0.05$), with a more clustered LC3B expression around the perinuclear region of the keratinocytes. The expression of LC3 was more homogenous in the ΔWD with few LC3B aggregates found near the cell periphery in the epidermal keratinocytes. The amount of autophagy markers, such as cytosolic LC3-I and lipidated LC3-II, as well as p62, was further assessed by Western Blot and displayed similar levels of expression ($p > 0.05$). An elevated expression of p62 and impaired ability to generate LC3-II would indicate defects in the process of autophagy (Rossiter et al., 2013). Results support the findings, previously observed by Rai and colleagues, who demonstrated that E230 mice (here referred to as ΔWD) were still able to activate autophagy, shown by the similar levels of p62 and LC3-II expression, in comparison to their littermate controls (Rai et al., 2019). These findings further support previous results reported by Rossiter and co-workers, who revealed that LC3-I, LC3-II and p62 show weak expression in control mice, in comparison to the ATG7 deficient mice (Rossiter et al., 2013). Previous ATG5 and ATG7 knock out mice have demonstrated decreases in autophagic flux, thereby causing drastic p62 and ubiquitin accumulation, resulting in skin disorders such as psoriasis (Komatsu et al., 2005; Malhotra et al., 2015).

Since the autophagy genes, ATG5, ATG7 and ATG16L1, are essential for both autophagy and LAP, knock-out mice lacking these genes are not ideal models for studying the effects of non-canonical autophagy on epidermal homeostasis, as they die at the neonatal stage. Therefore, the ΔWD mouse model presents a desirable model to study the effects of LAP on skin homeostasis. The ΔWD mouse can still perform autophagy, due to the presence of the N-terminal and CCD of ATG16L1; therefore, explaining the maintained levels of key autophagy markers in the dorsal skin of 1-year old WT and ΔWD mice. Additionally, these findings reinforce the concept that autophagy is actively occurring in the epidermis, contributing to skin stratification during embryonic development and persisting throughout adult life. This demonstrates that the loss of LAP does not affect the process of epidermal differentiation, providing further evidence that these mice can still fulfil autophagy, regardless of the removal of the WD domain of ATG16L1.

4.3.2 Characterising the expression of epidermal genes in the ΔWD skin

Given that previous work suggests that defects in the autophagy machinery can negatively impact epidermal barrier formation, I aimed to evaluate the expression of key differentiation markers and basal cell proliferation markers in the ∆WD skin. qPCR and Western Blot analysis demonstrated that the expression levels of key keratins (keratin 5, keratin 10 and keratin 1) were comparable across genotypes ($p > 0.05$), indicating that LAP deficiency does not interfere with the commitment of basal keratinocytes to differentiation. Keratins, which constitute the principal structural proteins of the epidermis, contribute about 30-80% towards its intermediate filament cytoskeleton (Ling-Juan, 2018). As noted in the previous chapter, the epidermis is vital for skin barrier integrity and function, with keratins being essential in ensuring the intermediate filament cytoskeleton of the epidermis is resilient to mechanical trauma. The interfollicular epidermis is mainly composed of four major keratins that form the intermediate filament cytoskeleton in pairs, such as keratin 5/14 and keratin 1/10 (Santos et al., 2002). In the basal layer, cells typically express the keratin 5/14 pair, while keratinocytes committed to terminal differentiation express the keratin 1/10 pair. Consequently, keratin 10 is generally localised in the suprabasal spinous layer, which was confirmed through the immunohistochemistry analysis showing homogenous keratin 10 expression in the suprabasal layers of both WT and ∆WD epidermis ($p > 0.05$).

Moreover, both in the embryonic and adult skin, WT and ∆WD mice exhibited similar patterns of PCNA expression, with PCNA primarily localised to the basal layer. PCNA has a vital role in DNA replication and has now been widely accepted to exhibit roles in cellular growth and proliferation (Moore et al., 2004). The level of PCNA expression, in both embryonic and adult tissue, was shown to be comparable across genotypes ($p > 0.05$), indicating that both control and ∆WD mice exhibit similar abilities to replenish the basal layer of the epidermis. In embryonic tissue, proliferating fibroblasts were likely stained with PCNA positive nuclei in the dermal compartment.

Additionally, other markers of differentiation and proliferation, such as involucrin, p-Akt and Akt, were assessed and showed similar levels of expression ($p > 0.05$) across control and ∆WD skin samples. The activation of the PI3K/Akt pathway in skin is involved in maintaining skin homeostasis, with Akt regulating key processes like proliferation, growth, survival, apoptosis, protein synthesis, and transcription (Teng et al., 2021). Akt plays a crucial role in the differentiation and survival of keratinocytes, with mice lacking Akt 1 and Akt2 isoforms exhibiting no stratum corneum (Lu et al., 2007). A study by Monteleon et al.

showed that using small molecule inhibitors for blocking the assembly of autophagosomes, organotypic cultured human skin were undifferentiated and lacked keratin 10 and filaggrin expression (Monteleon et al., 2018). Moreover, ATG7-deficient mice exhibited reduced expression of involucrin in their skin grafts compared to their WT mice, which was further validated by Monteleon and others, who used short hairpin RNAs to knockdown ATG7 in organotypic cultured human skin, resulting in the diminished expression of keratin 1 and filaggrin (Monteleon et al., 2018; Yoshihara et al., 2014). The findings from the current chapter suggest that ∆WD mice do not exhibit any signs of an impaired terminal differentiation pathway and corroborate previous results in Chapter 3, which showed comparable epidermal thickness and a fully established, intact skin barrier in both control and ∆WD mice.

Autophagy has been implicated in several human diseases, including cancer, skin disorders, inflammatory disorders (e.g., inflammatory bowel disease), and neurodegeneration (Douroudis et al., 2011; Hampe et al., 2007). The ATG16L1 protein, encoded by the *ATG16L1* gene, is a fundamental component in the activation of both autophagy and non-canonical autophagy (Douroudis et al., 2011). As previously noted, its amino-terminal binds with ATG5, and ATG12 to form the ATG5-ATG12-ATG16L1 complex, which is essential for phagophore elongation (Li, Chen, and Gu, 2016). The CCD binds to WIPI2, thereby recruiting the ATG5-ATG12-ATG16L1 complex to the phagophore membrane for LC3 conjugation to PE. Furthermore, the C-terminal WD domain of ATG16L1 was shown to be required for LAP (Fletcher et al., 2018; Rai et al., 2019). A study on keratinocyte-selective ATG16L1-deficient mice (Δ^{ker}*ATG16L1*) showed that these mice displayed a thickened cornified layer, suggesting potential defects in desquamation (Van Hove et al., 2023). These mice exhibited similar epidermal thickness and a fully formed skin barrier, when compared to their control, indicating that the defect in keratinocyte autophagy did not compromise the skin. Δ^{ker}*ATG16L1* showed enhanced tumour formation compared to their controls, with increased p62 expression as demonstrated by immunoblotting. Additionally, polymorphisms in the *ATG16L1* gene have been linked to skin conditions such as palmoplantar pustulosis and psoriasis vulgaris, suggesting that autophagy may play a role in immunosurveillance (Douroudis et al., 2011; Douroudis et al., 2012). Overall, these studies suggest that altering the autophagic components in *ATG16L1* can lead to consequential side effects, resulting in skin disorders.

4.4 Conclusion

I have demonstrated that the absence of the WD domain of ATG16L1, leading to LAP-deficiency, does not affect standard epidermal differentiation. The findings show that keratinisation operates independently from LAP, and that ∆WD mice do not exhibit any cellular-level abnormalities in their skin barrier. The presence of healthy tissue homeostasis in the skin of the ∆WD mice supports other observations by Rai and co-workers on other isolated tissues (e.g., liver, kidney, muscle and brain), which displayed no obvious defects on tissue homeostasis *in vivo* (Rai et al., 2019). Altogether, the findings from this chapter and previous studies suggest that despite the truncated ATG16L1 in the ∆WD mouse, autophagy, rather than LAP, is responsible for reducing tissue damage *in vivo*.

4.5 Limitations and future work

To evaluate the expression of key autophagy markers during embryonic development, epidermal lysates of WT and ∆WD E18.5 tissue could be collected to compare the levels of autophagy markers in embryonic versus adult epidermal tissue. Future work could focus on challenging the skin, either by UV or topical reagents and evaluating the wound healing response in LAP-defective mice. This could be explored further by blocking autophagic flux (i.e., chloroquine) and examining the response to injury in this model.

Chapter 5: Evaluation of melanosomal dynamics in ΔWD keratinocytes

5.1 Introduction

In mammals, the pigmentation of the hair, skin, and eyes arises from the synthesis and distribution of melanins (Palmisano et al., 2008). Melanocytes, the neural crest-derived cells located in the basal epidermal layer, are responsible for synthesising and transferring two types of melanin: black/brown eumelanin and yellow/red pheomelanin (Shi et al., 2016). Melanin synthesis occurs in specialised intracellular organelles called melanosomes, which are identified as endo-lysosome-related organelles, due to them being derived from the endosomal system and sharing several features with lysosomes, such as low pH (in early stages) and a cohort of lysosomal resident proteins (e.g., LAMP1/2 and CD63) (Delevoye et al., 2019; Dell'Angelica et al., 2000; Moreiras et al., 2022). During a series of maturation stages, melanosomes are gradually deposited with melanin in premelanosomal protein (PMEL) fibrils, ultimately achieving full pigmentation and maturity at the end of stage IV (Hossain et al., 2022). OA1 is a G-protein-coupled receptor that displays a pivotal role in melanosome biogenesis and is found in the intracellular endolyso-melanosomal membrane (Falletta et al., 2014). Once mature, melanosomes undergo long-range, bidirectional, microtubule-based transport, facilitated by Rab27a, from the perinuclear region to the peripheral dendrites (Hume et al., 2001; Palmisano et al., 2008). There, they interact with the actin cytoskeleton via melanophilin and myosin Va. The capture of the melanosomes at the melanocyte periphery is necessary for the transfer of the melanosomes to the neighbouring keratinocytes (Futter et al., 2004). Keratinocytes constitute approximately 80% of the cell population in the epidermis (Bento-Lopes et al., 2023). Together, keratinocytes and melanocytes form the 'epidermal-melanin units'. Mature pigmented melanosomes once internalised by keratinocytes, are trafficked and deposited in the supranuclear area, where they protect keratinocyte DNA from UV radiation (Nordlund, 2007). The mechanisms underlying melanin transfer in keratinocytes are still poorly understood, with four main hypotheses proposed: the exocytosis-endocytosis model, the cytophagocytosis model, tunnelling nanotube hypothesis, and the shedding-vesicle model (Benito-Martinez et al., 2021).

Keratinocytes can exhibit phagocytic activity through the protease-activated receptor-2 (PAR-2) (Murase et al., 2013; Scott et al., 2001). PAR-2 is suggested to control melanosome ingestion and phagocytosis by keratinocytes, playing a crucial role in skin pigmentation, with higher PAR-2 expression observed in darker skin (Babiarz-Magee et al., 2004). Additionally, autophagy has emerged as an important pathway in maintaining homeostasis by recycling damaged organelles, such as mitochondria, peroxisomes, and ribosomes (Ramkumar et al., 2017). Autophagy has been implicated in determining skin colour, through the regulation of melanosome degradation in keratinocytes (Murase et al.,2013). The function of LAP has not yet been studied in skin pigmentation and melanin transfer; however, it has been studied with regards to fungal melanin (Akoumianaki et al., 2016; Kyrmizi et al., 2018). Studies on *Aspergillus fumigatus* have determined that fungal cell melanin can induce LAP blockage by excluding NOX2 recruitment and inhibiting the NADPH oxidase complex (Akoumianaki et al., 2016; Kyrmizi et al., 2018). It is important to evaluate whether mouse melanin exhibits a similar inhibitory function on LAP. Due to challenges in distinguishing between autophagy and LC3-associated phagocytosis (LAP), our mouse model provides a unique method in distinguishing between the pathways and therefore I aim to evaluate the role of LAP in melanosome uptake and processing in keratinocytes.

This chapter aims to investigate the dynamics of melanosomes within primary keratinocytes that lack LAP, and to assess whether LAP deficiency impacts melanosome uptake and processing in these cells. Previous studies have shown that melanin is not localised in double membrane autophagosomes surrounded by LC3 within keratinocytes, but instead resides in single membrane compartments (Tarafder et al., 2014). To explore this further, primary keratinocytes were isolated from the epidermal tail skin of control and ΔWD mice. I hypothesise that murine melanin, contained within melanosomes, does not exert the same inhibitory effect on LAP as fungal melanin does. LAP is known to target a broad range of cargo, which supports the idea that melanosomes may be a target of this process. Therefore, I propose that OA1-mCherry labelled melanosomes are engulfed by keratinocytes, forming a phagosome with a single membrane that is marked by LC3 and selectively targets the melanosomal membrane. These phagosomes are then directed to acidic compartments (i.e., lysosomes), as indicated by LysoTracker, while being transported toward the perinuclear region. The chapter aims to meet the following experimental objectives:

- Optimising the method of primary keratinocyte isolation and assessment of melanosomal dynamics in control and ΔWD mice.

- Assess the dynamics of OA1-mCherry tagged melanosomes following internalisation by the isolated primary keratinocytes.
- Evaluate whether melanin is processed by autophagy or LAP following internalisation by keratinocytes.

5.2 Results

5.2.1 Isolation of primary WT and ΔWD keratinocytes

To evaluate the effect of LAP deficiency on the uptake and processing of melanosomes in keratinocytes, primary control and ΔWD keratinocytes were isolated from the epidermal tail skin through enzymatic digestion (i.e., trypsin). Primary keratinocytes were isolated in a low calcium (Ca^{2+}) growth medium (EMEM Low Calcium, 0.05 mM), containing chelated foetal bovine serum (FBS), since FBS generally contains high levels of Ca^{2+} (3.5-4.0 mM) (Zoico et al., 2014). Before chelation, FBS had a Ca^{2+} concentration of 2.31 mmol/L, which was reduced to 0.20 mmol/L after chelation (Table 5.1). After adding the chelated serum to the growth medium, the concentration of Ca^{2+} remained low (< 0.20 mmol/L) (Table 5.1). Maintaining low Ca^{2+} levels are essential to preserve the basal and proliferative phenotype of primary keratinocytes.

Table 5.1 Overview of Cobas Calcium analysis. Mean calcium concentration (mmol/L) of growth medium and serum for primary keratinocytes (n=3).

Sample	Value (mmol/L)
FBS before chelation	2.31
FBS after chelation	0.20
EMEM	< 0.20
Low Calcium EMEM	< 0.20

For the long-term culture of primary keratinocytes, the EMEM low Ca^{2+} growth medium proved unsuitable. By day 5 post isolation, both the WT and ΔWD primary keratinocytes demonstrated a low proliferative capacity, making it challenging to culture enough primary keratinocytes for downstream analysis (Figure 5.1). No day 8 image is available for primary keratinocytes cultured in EMEM low Ca^{2+}, as they ceased proliferation and were unable to become confluent (Figure 5.1). Following this observation, EMEM low Ca^{2+} was still used for the isolation of the primary keratinocytes, yet the initial plating was done in an alternative serum-free growth medium called keratinocyte basal medium (KBM). This KBM growth medium consisted of Ca^{2+}-free basal medium supplemented with growth factors, cytokines, and other supplements, which included an antibiotic (i.e., gentamicin),

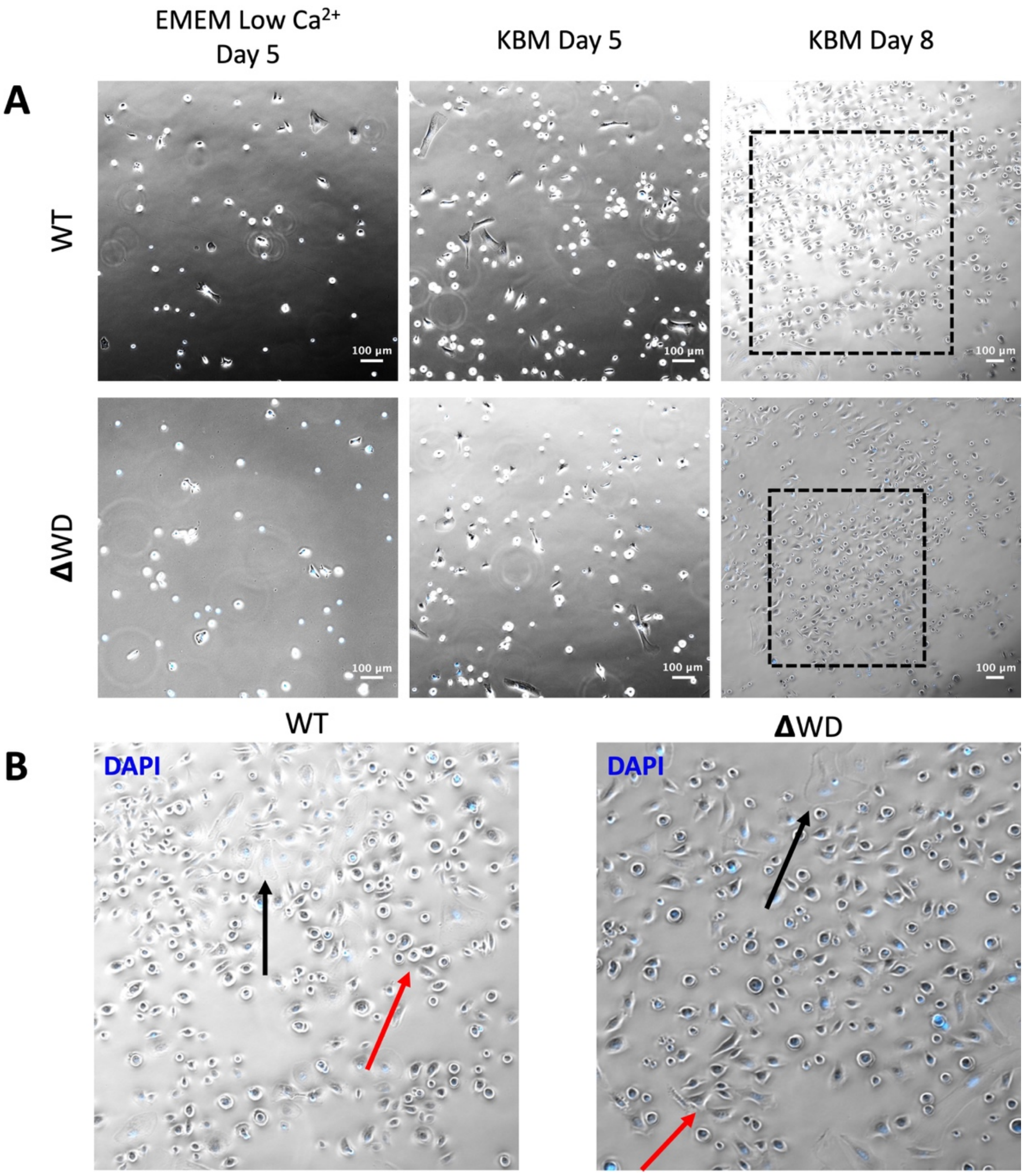

Figure 5.1 Representative images showing primary WT and ΔWD keratinocytes in EMEM low Ca^{2+} and serum-free keratinocyte basal medium (KBM). (A) Phase contrast images showing primary keratinocytes isolated and cultured in EMEM low Ca^{2+} growth media at day 5 post isolation. Phase contrast images showing primary keratinocytes isolated and cultured in KBM keratinocyte serum-free growth media at day 5 and 8. Images taken from a single experiment. Scale bar: 100 µm. **(B)** Magnified inserts, outlined by black dashed box in panel A, showing morphological characteristics of WT and ΔWD keratinocytes. Black arrows showing terminally differentiating keratinocytes, while red arrows show proliferating keratinocytes. DAPI used to stain for nuclei (blue).

hydrocortisone, insulin, human epidermal growth factor and bovine pituitary extract. By day 5 post isolation, the WT and ΔWD keratinocytes were much more confluent, than those in the EMEM growth medium, with the keratinocytes being fully confluent at day 8 (> 70%) (Figure 5.1). Both WT and ΔWD primary keratinocytes grew as a monolayer, with individual cells exhibiting a polygonal shape, resembling cobblestones when confluent (Figure 5.1 B). Few terminally differentiating keratinocytes can be observed by their more flattened shape at day 8 post isolation, despite the presence of low Ca^{2+} growth media (Figure 5.1 B). The typical yield from one well of a six-well plate of primary keratinocytes at day 8 was around 3.0×10^5 cells/ml. The primary keratinocytes could only be maintained until passage one before ceasing proliferation.

Actin remodelling was assessed by staining the primary WT and ΔWD keratinocytes with phalloidin. At day 8, WT and ΔWD keratinocytes showed similar cytoskeletal arrangements with the actin fibres primarily distributed at the cell periphery in both WT and ΔWD keratinocytes (Figure 5.2). However, the ΔWD keratinocytes showed a more prominent circumferential phalloidin staining than the WT keratinocytes (Figure 5.2). Additionally, the keratinocytes appeared flatter at day 8, which is a common characteristic of terminal differentiation. This was further assessed by immunostaining day 8 keratinocytes with keratin 10, a key marker for keratinocytes committing to terminal differentiation, as previously discussed. Keratin 10 expression was observed in both WT and ΔWD keratinocytes at day 8, indicating that these keratinocytes were undergoing terminal differentiation (Figure 5.3).

Next, autophagic activity was evaluated in the WT and ΔWD primary keratinocytes in preparation for the live cell imaging experiment. The repercussions of the removal of the WD domain of ATG16L1 on autophagy and LAP were confirmed using primary keratinocytes (Figure 5.4). The primary keratinocytes were treated with chloroquine, an autophagy inhibitor and LAP inducer, which resulted in the recruitment of LC3 to large endo-lysosomal vacuoles in control keratinocytes (Figure 5.4). The ΔWD keratinocytes failed to recruit LC3 to large endo-lysosomal compartments, when induced by chloroquine (as indicated by the absence of vacuoles) (Figure 5.4). Primary keratinocytes from ΔWD mice recruited LC3 to small puncta, which highlight the autophagosomes that arise during conventional autophagy (Figure 5.4). In non-chloroquine induced primary cultures, results showed a

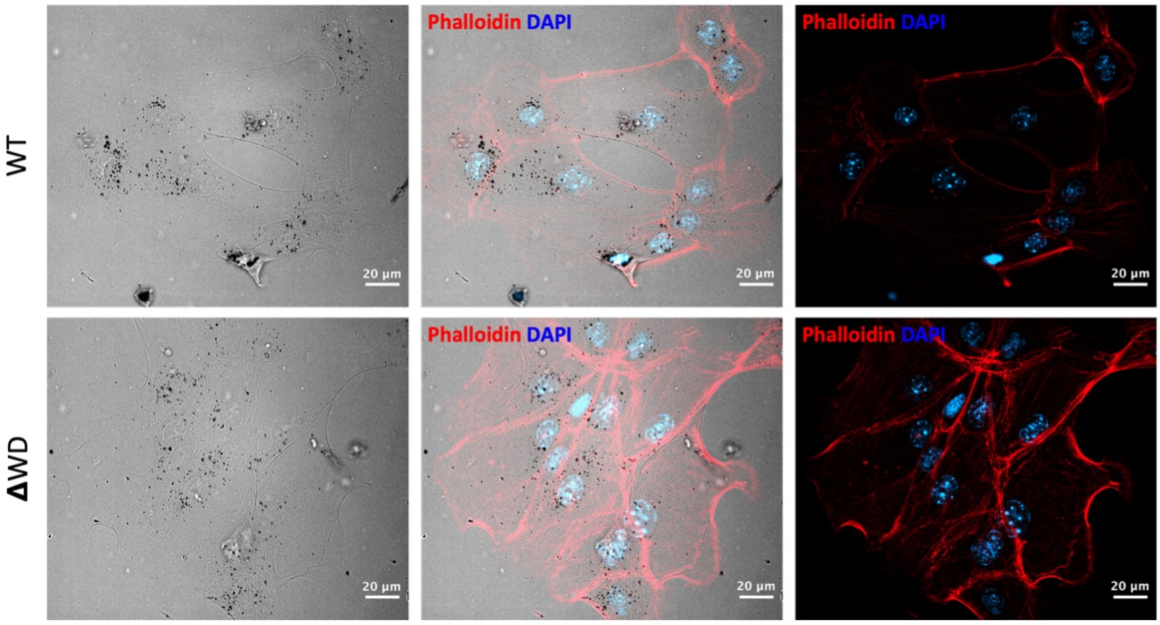

Figure 5.2 Representative immunostaining of F-actin (phalloidin) in 4% PFA fixed WT and ΔWD primary keratinocytes. Phalloidin Atto 647N (red) staining in WT and ΔWD primary keratinocytes. Phalloidin staining overlayed on brightfield images of WT and ΔWD primary keratinocytes. Black puncta in brightfield images are melanin aggregates. DAPI used to stain for nuclei (blue). Images taken from 2 independent experiments. Scale bar: 20 μm.

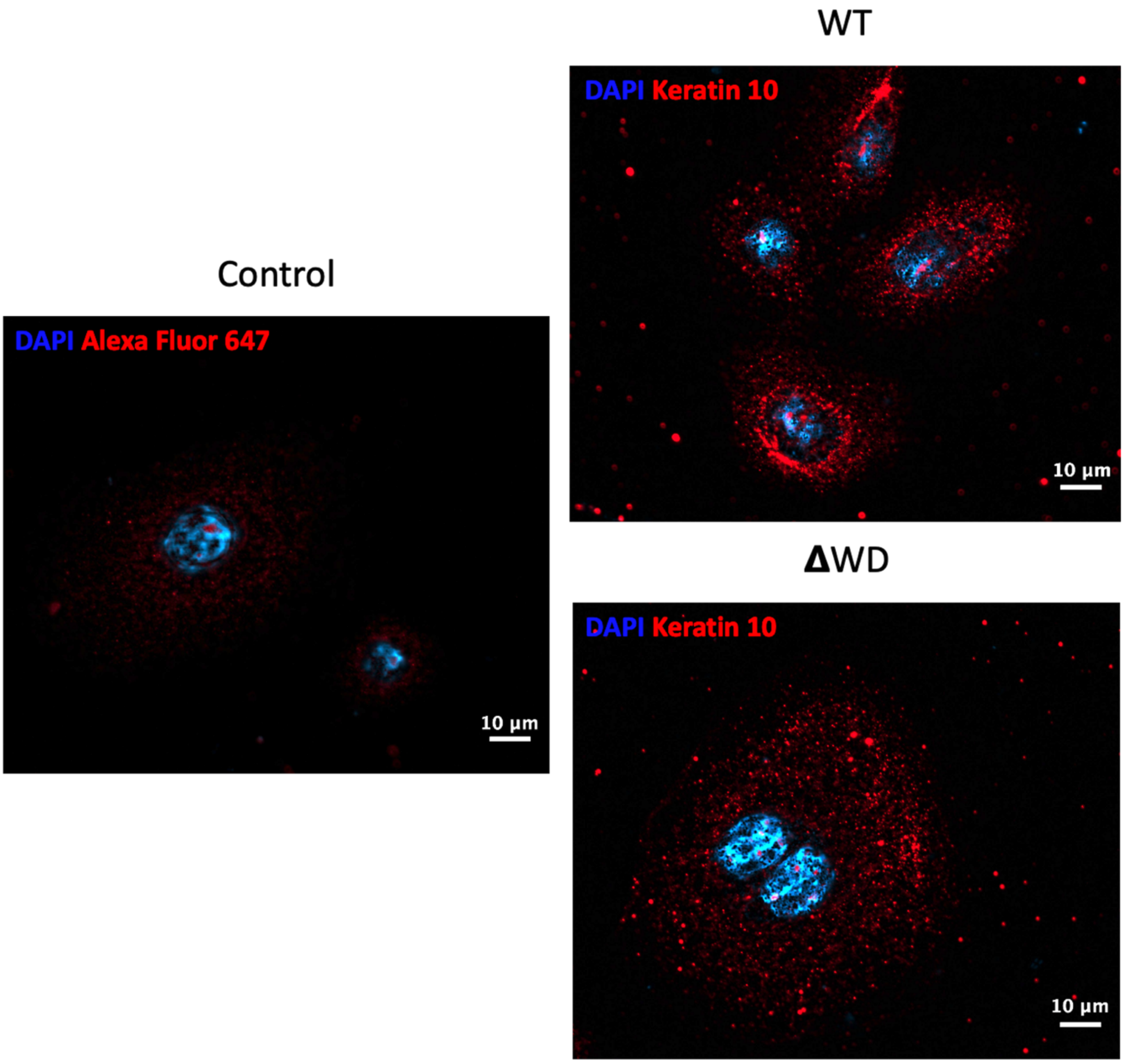

Figure 5.3 Representative keratin 10 immunostaining in isolated primary WT and ΔWD keratinocytes. Primary WT and ΔWD keratinocytes were fixed in 100 % methanol and immunolabelled with keratin 10 (red). Left panel showing secondary antibody control (Alexa Fluor 647). DAPI used to stain for nuclei (blue). Images taken from 2 independent experiments. Scale bar: 10 μm.

diffuse expression of LAMP1, indicating the presence of lysosomes, in both WT and ΔWD keratinocytes (Figure 5.5). In addition, some colocalization of LC3-I/II and LAMP1 was observed, highlighting the presence of autophagosomes in the keratinocytes (Figure 5.5). The Pearson's coefficient (PC) in ΔWD primary keratinocytes between LAMP1 and LC3-I/II was 0.16 ± 0.03, while in the control keratinocytes it was shown to be 0.15 ± 0.02 (Figure 5.5). LC3-I/II appeared more prominent in the perinuclear region in both control and ΔWD keratinocytes (Figure 5.4). It was not possible to distinguish between LC3-I and LC3-II, as the LC3 A/B antibody was used.

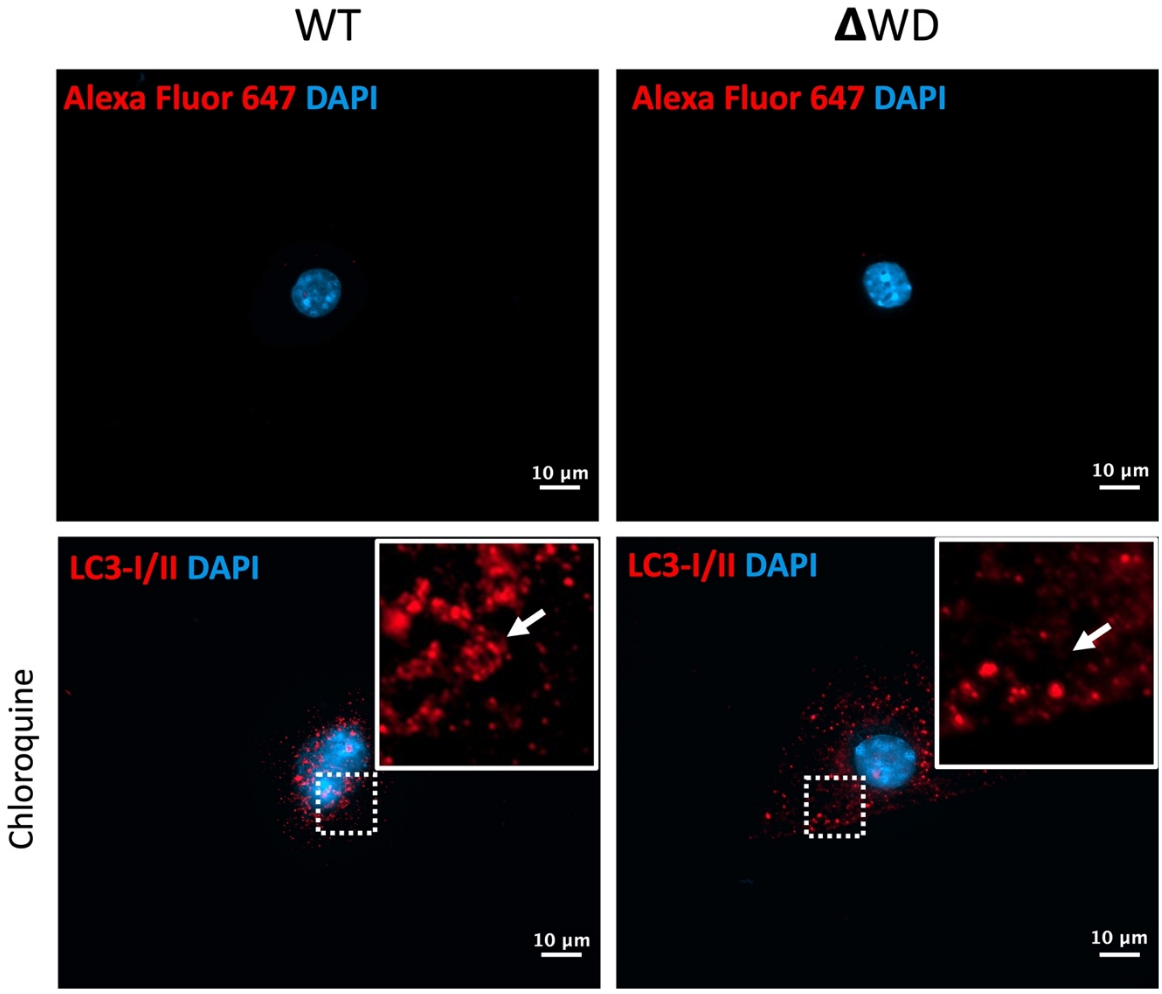

Figure 5.4 Representative immunostaining of chloroquine treated primary WT and ΔWD keratinocytes. Primary keratinocytes were treated for 2 hours with chloroquine (100 µm) as indicated. Primary keratinocytes were fixed with 100% methanol and labelled with LC3-I/II (red). ROI outlined by white box with magnified images shown in top right corner. Arrow shows a ring of LC3 expression surrounding a vacuole in WT keratinocytes and the absence of a vacuole in ΔWD. Secondary antibody control (Alexa Fluor 647) in top panels. DAPI used to stain for nuclei (blue). Images taken from a single experiment. Scale bar: 10 µm.

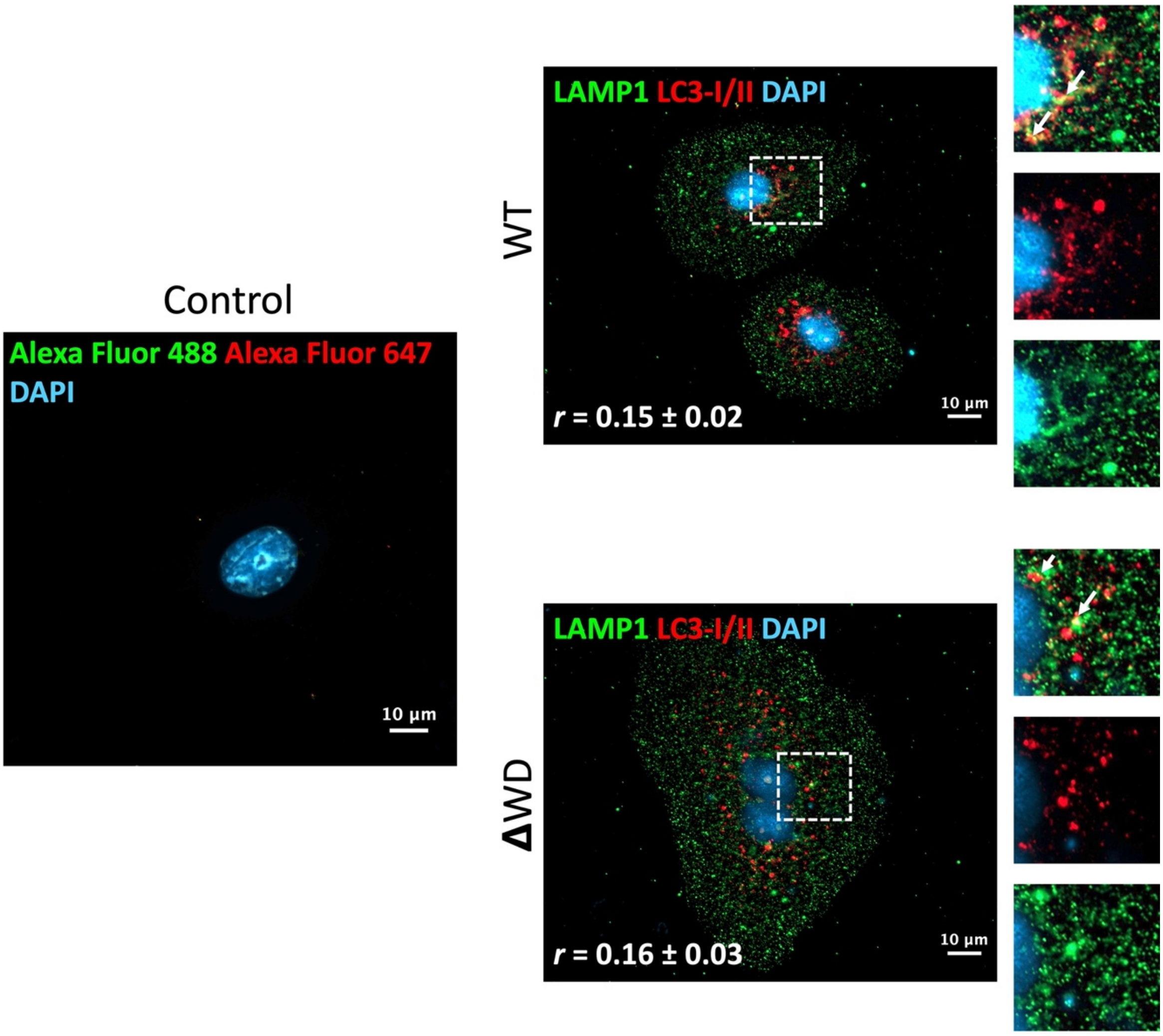

Figure 5.5 Representative LC3-I/II and LAMP1 immunostaining in isolated primary WT and ΔWD keratinocytes. Day 5 primary WT and ΔWD keratinocytes were fixed in 100 % methanol and labelled with LC3 I/II (red) and LAMP1 (green). Magnified images of region outlined by white dashed box, shown on right. Arrows indicate regions of colocalization of LC3-I/II and LAMP1. The degree of colocalization (yellow) (Pearson's coefficient, *r*) between LC3-I/II and LAMP1 is indicated separately (mean ± SE, 5 cells per genotype with n = 3). Left panel showing secondary antibody control (Alexa Fluor 488 and 647). DAPI used to stain for nuclei (blue). Images taken from 3 independent experiments. Scale bar: 10 µm.

5.2.2 Optimising OA1-mCherry transfection and Adenovirus LC3-GFP transduction

To visualise the melanosomes and autophagic activity in our live-cell experiment, I transfected the highly pigmented 1014 murine melanoma cell line with an mCherry reporter of OA1 (GRP143). This protein is involved in the synthesis and maturation of melanosomes and labels the pigmented melanosomes in the 1014 melanocytes red, as it is embedded in their membrane (Figure 5.6) (Burgoyne et al., 2013; Palmisano et al., 2008). Notably, OA1-mCherry expression is concentrated in regions exhibiting high melanin pigmentation (black puncta), corresponding to melanosomes transporting melanin to the cell periphery (Figure 5.6 I). The 1014 melanocyte cell in the background displays limited OA1-mCherry labelling, as it exhibits less pigmentation (Figure 5.6). OA1-mCherry co-localised with Rab27a, a transport protein, at the cell periphery (observed in yellow). Additionally, Rab27a expression was dispersed throughout the cytoplasm, but was more pronounced at the cell periphery, indicating areas of melanosome docking to the cortical actin (Figure 5.6 I-II; Figure 5.7 I-II). OA1-mCherry expression could also be observed in the melanocyte centre, which corresponds to the early stages of melanosome maturation (i.e., stages I and II) (Figure 5.6 II). The pigmentation of the 1014 murine melanoma cells is not homogenous and therefore the OA1-mCherry staining correlates with the amount of melanin (Figure 5.6).

Visualising LC3 expression in the live-cell imaging experiment was achieved by employing an adenovirus encoding LC3-GFP. The adenovirus isolate stock was generated using HEK-293 cells and titrated using the 1014 murine melanoma cells (Table 5.2). A positive control ATG16L1 knock out (KO) MEFs was used to confirm that the 1014 murine melanoma cells were effectively transduced (Figure 5.8). A range (2-8 μl) of adenovirus isolate volumes were tested to establish the optimum transduction efficiency (Figure 5.8; Table 5.2). Results demonstrated that the optimum volume of adenovirus LC3-GFP in a 24 well-plate was 2 μl, which displayed a transduction efficiency of 99% (Table 5.2). As the volume of adenovirus increased, the transduction efficiency declined (Table 5.2; Figure 5.8 B). The recommended 2 μl adenovirus isolate volume was scaled up or down depending on the culture dish used.

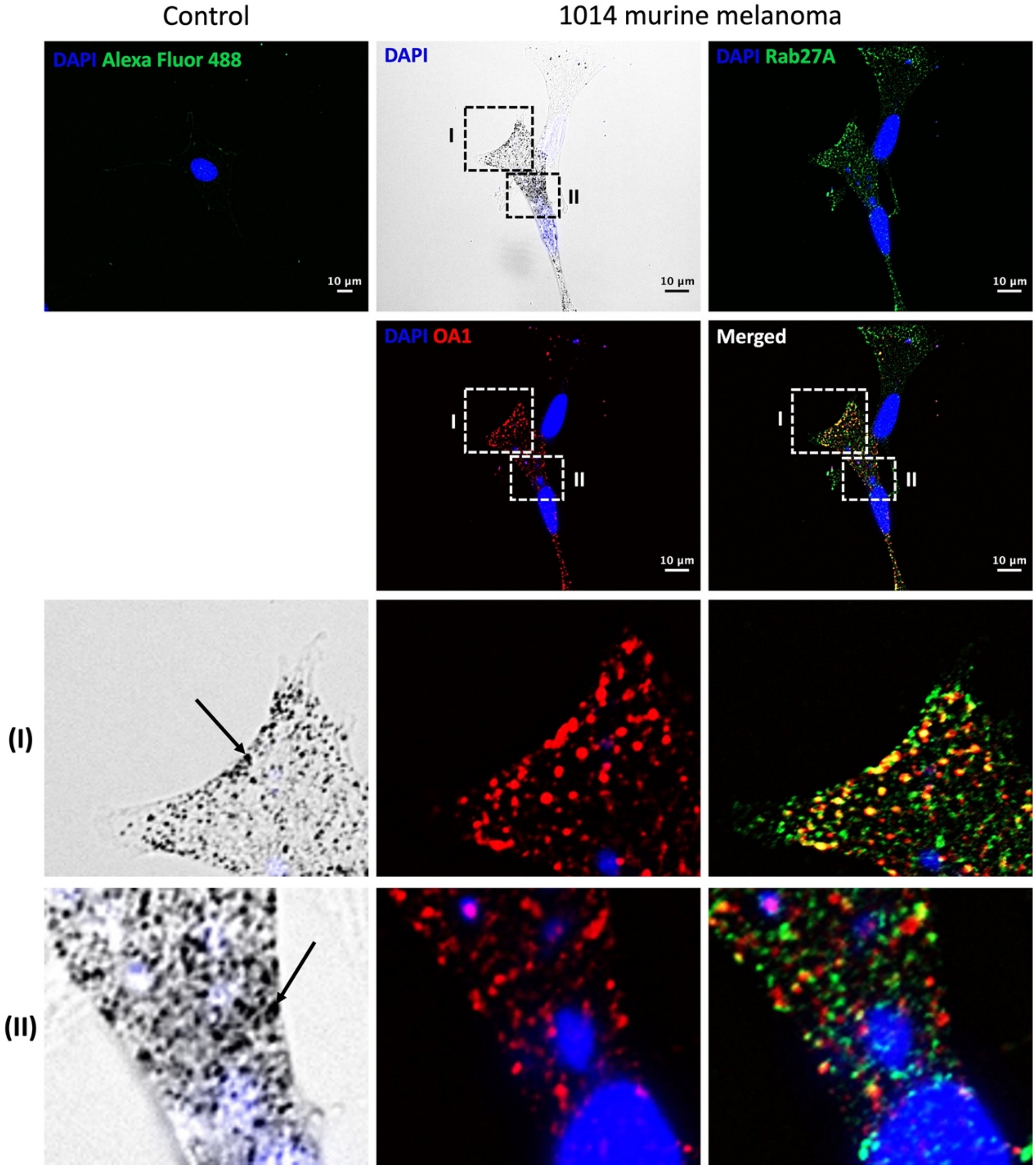

Figure 5.6 Representative Rab27a and OA1-mCherry immunostaining in 1014 murine melanoma cells. 1014 murine melanoma cells were transfected with OA1-mCherry (red). 1014 murine melanoma cells were later fixed in 100% methanol, following transfection and labelled with Rab27a (green). **(I)** Magnified images of melanocyte periphery. **(II)** Magnified images of melanocyte cell centre. Arrow in brightfield images showing melanosomes with melanin at the melanocyte periphery and cell centre. Top left panel showing secondary antibody control for Alexa Fluor 488. DAPI used to stain for nuclei (blue). Images taken from a single experiment. Scale bar: 10 μm

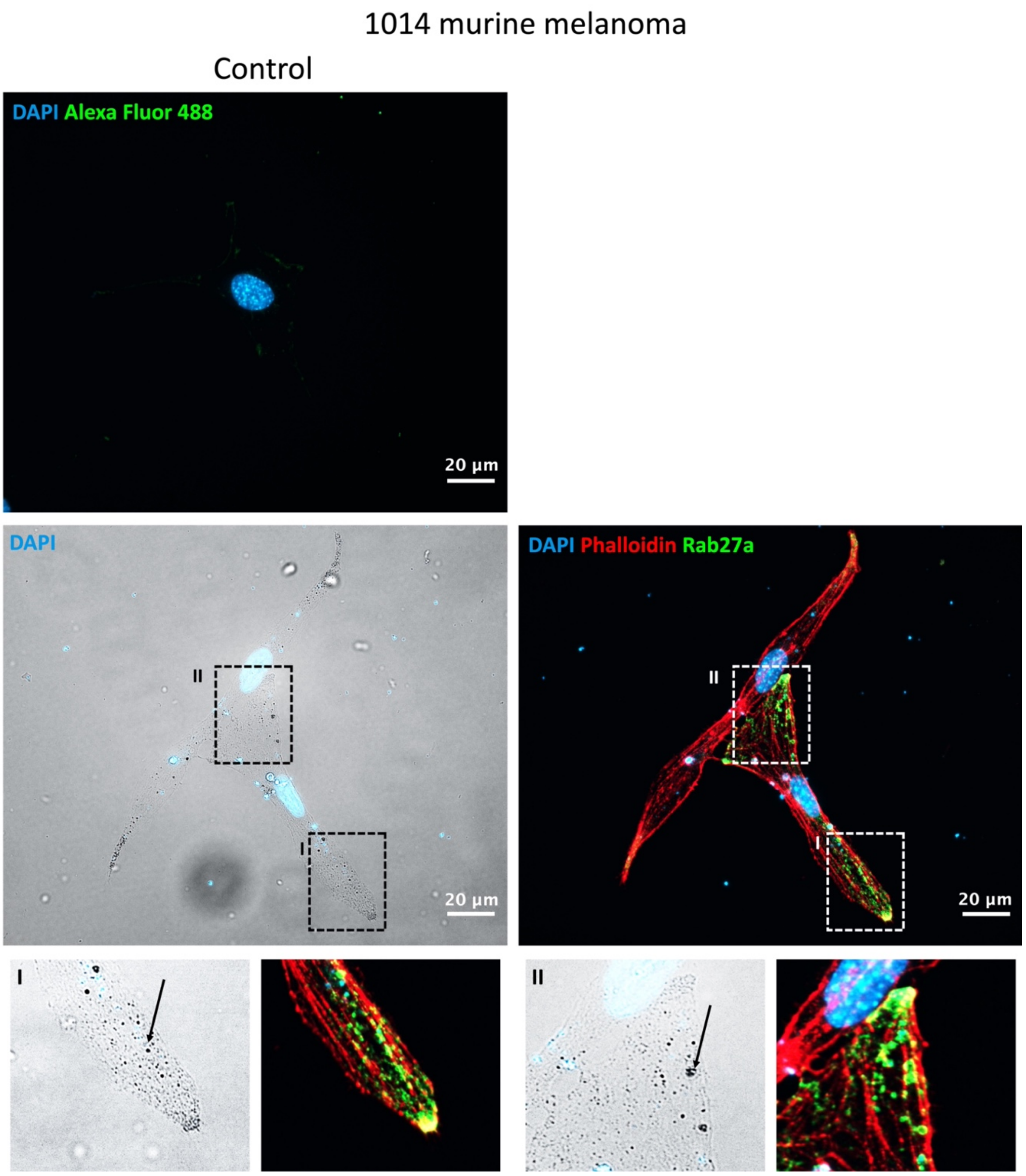

Figure 5.7 Representative Rab27a and F-actin (Phalloidin) immunostaining in 1014 murine melanoma cells. 1014 murine melanoma cells fixed with 4% PFA and labelled with Rab27a (green) and Phalloidin Atto 647N (red). Arrow showing melanin pigment. Secondary antibody control (Alexa Fluor 488) top left panel. (I-II) Magnified inserts of regions outlined by ROI of the melanocyte periphery. Images taken from a single experiment. Scale bar: 20 µm.

Table 5.2 Adenovirus LC3-GFP transduction efficiency (%) in 1014 murine melanoma cells.

Volume of viral isolate (µl)	Total number of cells	LC3-GFP positive cells	Transduction efficiency (%)
2	126	125	99
4	352	210	60
6	322	87	27
8	313	110	35

XB-2 mouse keratinocytes were used to confirm the adenovirus LC3-GFP transduction (Figure 5.9). XB-2 mouse keratinocytes were immunostained with LC3-I/II and transduced with 2 µl of adenovirus LC3-GFP (Figure 5.9). Immunostaining confirmed the effective labelling of LC3 in the XB-2 keratinocytes, with the LC3-GFP co-localising with LC3-I/II (Figure 5.9). To ensure that the adenovirus LC3-GFP infected our primary WT and ΔWD keratinocytes, the keratinocytes were cultured on collagen-coated coverslips and transduced with 2 µl of adenovirus LC3-GFP for 24 hours, before fixing the keratinocytes with 100% methanol. The keratinocytes were successfully transduced with the adenovirus LC3-GFP and showed more prominent LC3-GFP expression around the perinuclear region in both WT and ΔWD keratinocytes (Figure 5.10). Moreover, LC3-GFP appeared in areas with melanin aggregates, providing a first indication that LC3 may be localised to melanosome membranes after ingestion by keratinocytes (Figure 5.10). Findings provide strong evidence that the adenovirus is effectively labelling LC3 in our primary keratinocyte cultures.

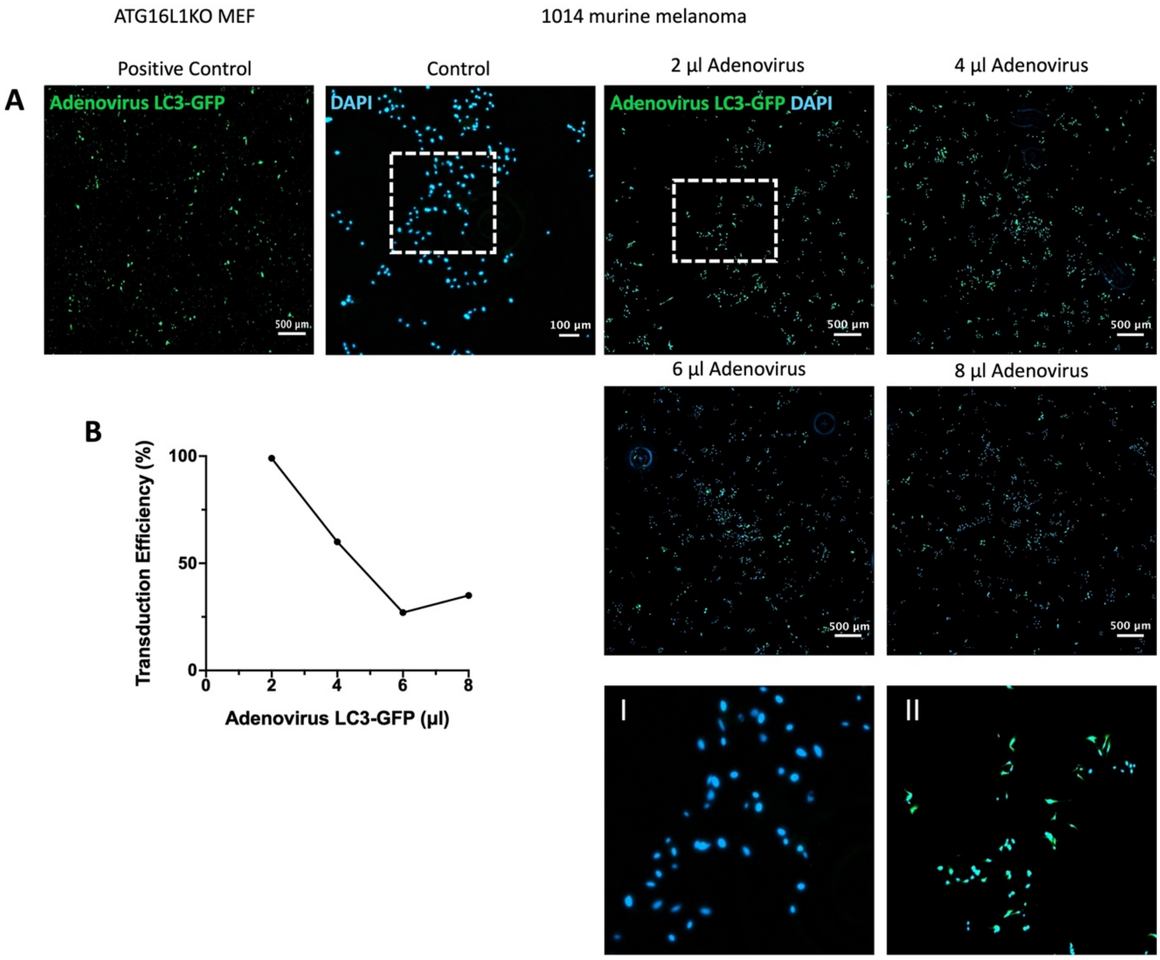

Figure 5.8 Representative images of adenoviral LC3-GFP transduced 1014 murine melanoma cells. (A) Positive control: Representative tiled image (4x4) of ATG16L1 knock out (KO) mouse embryonic fibroblasts (MEF) transduced with 2 µl adenovirus LC3-GFP (green). Scale bar: 500 µm. Untransduced control: 1014 murine melanoma cells. Scale Bar: 100 µm. Titration (2-8 µl) of adenovirus LC3-GFP isolate stock on 1014 murine melanoma cells. Representative images showing tiled image (4x4) of transduced 1014 murine melanoma melanocytes in green. Images taken from a single experiment. Scale bar: 500 µm. DAPI used to stain for nuclei (blue). **(I)** Magnified image of area marked by ROI showing untransduced 1014 murine melanoma cell control. **(II)** Magnified image of area marked by ROI showing 2 µl LC3-GFP transduced 1014 murine melanoma cells. **(B)** Transduction efficiency (%) of adenovirus LC3-GFP isolate stock in 1014 murine melanoma cells, using 2-8 µl of adenovirus LC3-GFP. Analysis conducted in ImageJ.

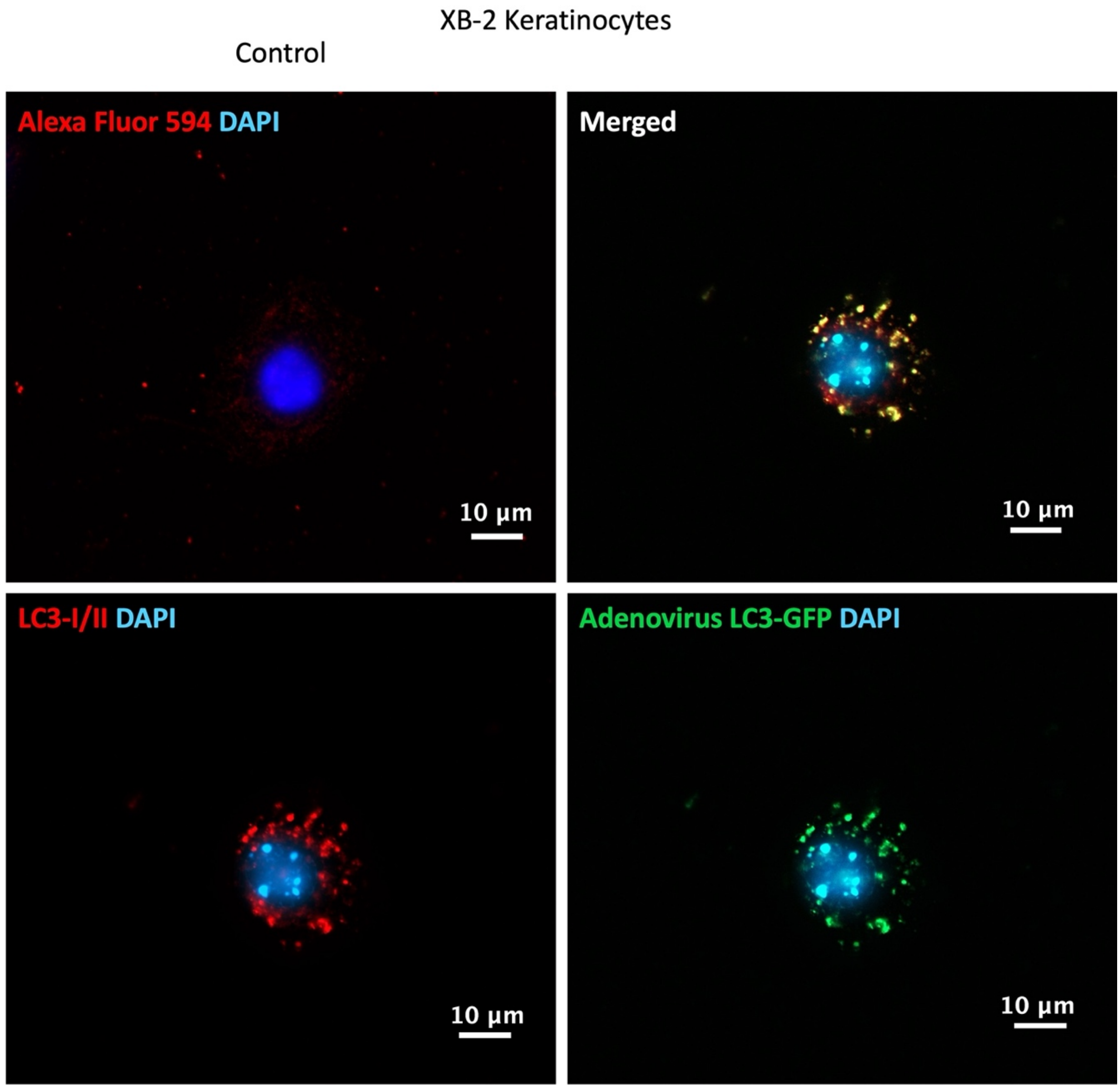

Figure 5.9 Representative images of XB-2 mouse keratinocytes transduced with adenovirus LC3-GFP (green) and immunolabelled with LC3-I/II (red). Colocalisation of LC3-GFP and LC3-I/II shown in yellow. Top left panel showing secondary antibody control (Alexa Fluor 594). DAPI used to stain for nuclei (blue). Images taken from a single experiment. Scale bar: 10 µm.

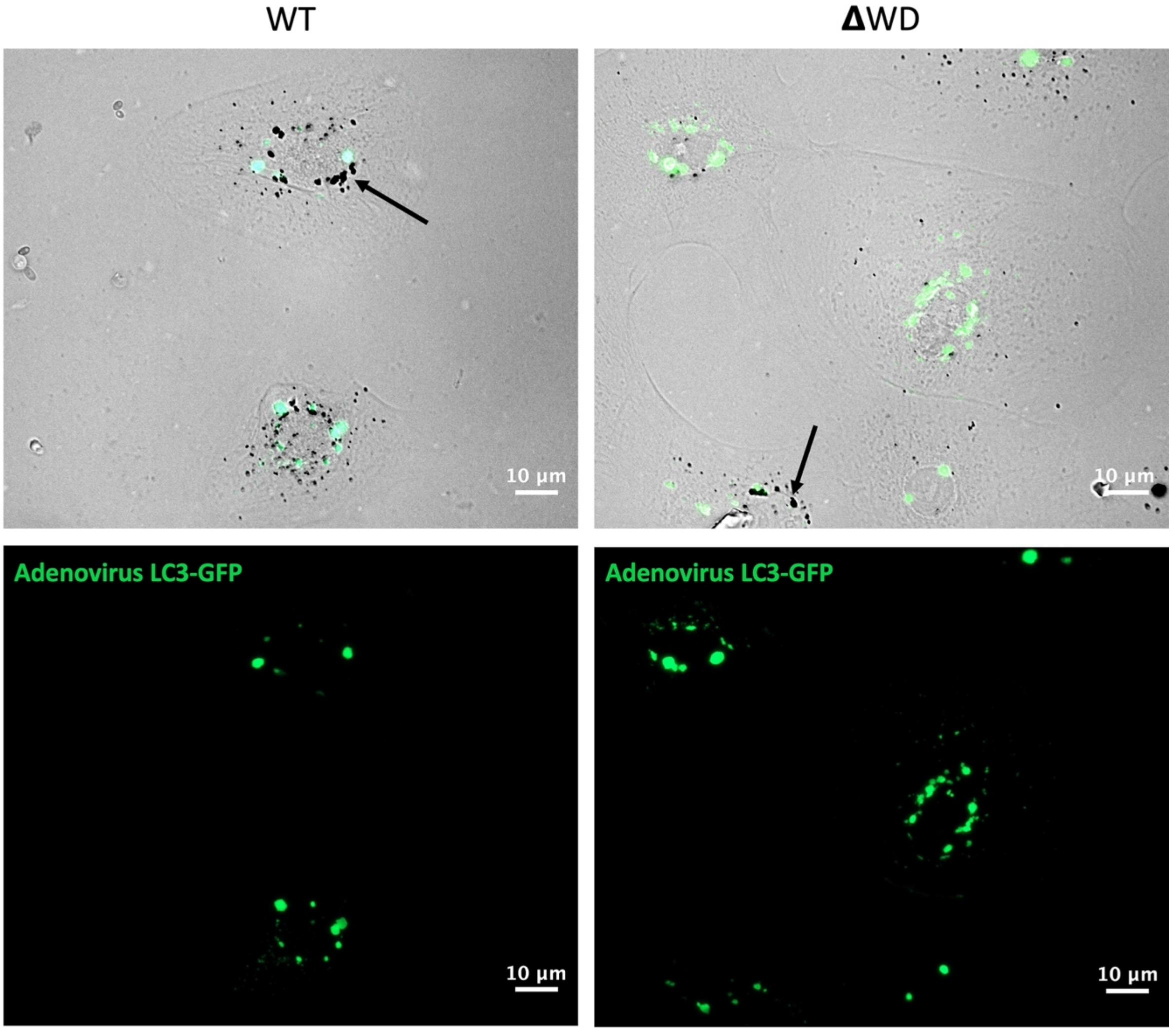

Figure 5.10 Representative images confirming adenoviral LC3-GFP transduction in primary WT and ΔWD keratinocytes. Primary WT and ΔWD keratinocytes were fixed in 100 % methanol. 2 μl of adenovirus LC3-GFP (green) used to transduce WT and ΔWD keratinocytes. Top panels showing brightfield image of WT and ΔWD keratinocytes overlayed with adenovirus LC3-GFP (green). Arrows showing melanin pigment in primary keratinocytes. Images taken from 3 independent experiments. Scale bar: 10 μm.

5.2.3 Optimisation of the experimental design for live cell imaging

After confirming the optimum transfection and transduction conditions for the melanosome donor 1014 cells and recipient primary keratinocytes, I next sought to harvest OA1-mCherry labelled melanosomes from the 1014 murine melanoma cells. This media was used to treat the primary WT and ΔWD keratinocytes with the mCherry tagged melanosomes, which enabled me to visualise the movement of the melanosomes within our live-cell imaging experiment. Results demonstrated that the melanin aggregates overlapped with the OA1-mCherry labelling in both the WT and ΔWD keratinocytes, providing a strong indication that the primary keratinocytes are taking up the OA1-mCherry melanosomes from the growth media (Figure 5.11; Figure 5.12).

LAMP1 expression was diffuse in both WT and ΔWD keratinocytes, with lysosomes seen in the same areas of melanin clusters (Figure 5.11; Figure 5.12). These areas were near the perinuclear region in both the control and ΔWD keratinocytes (Figure 5.11; Figure 5.12). LC3-I/II was prominent in the perinuclear region in both control and ΔWD keratinocytes, as previously described, but exhibited a low expression in the cytosol (Figure 5.11; Figure 5.12). In some areas the OA1-mCherry melanosomes were overlapping with LC3-I/II (shown in yellow) and LAMP1 staining (shown in white), providing a first indication of their interactions in our control and ΔWD keratinocytes (Figure 5.11; Figure 5.12). The areas shown in white, which highlight the association of OA1-mCherry, LC3-I/II and LAMP1, may suggest potential melanosome processing, driven by autophagy (Figure 5.11; Figure 5.12). The areas of magenta overlap (OA1-mCherry and LAMP1) suggest that melanosomes are internalised in lysosomal compartments within keratinocytes after 24 hours of melanosome treatment (Figure 5.11; Figure 5.12). Moreover, it suggests that processing of the melanosomes had not yet occurred, due to the lack of LC3 surrounding the lysosomal compartment.

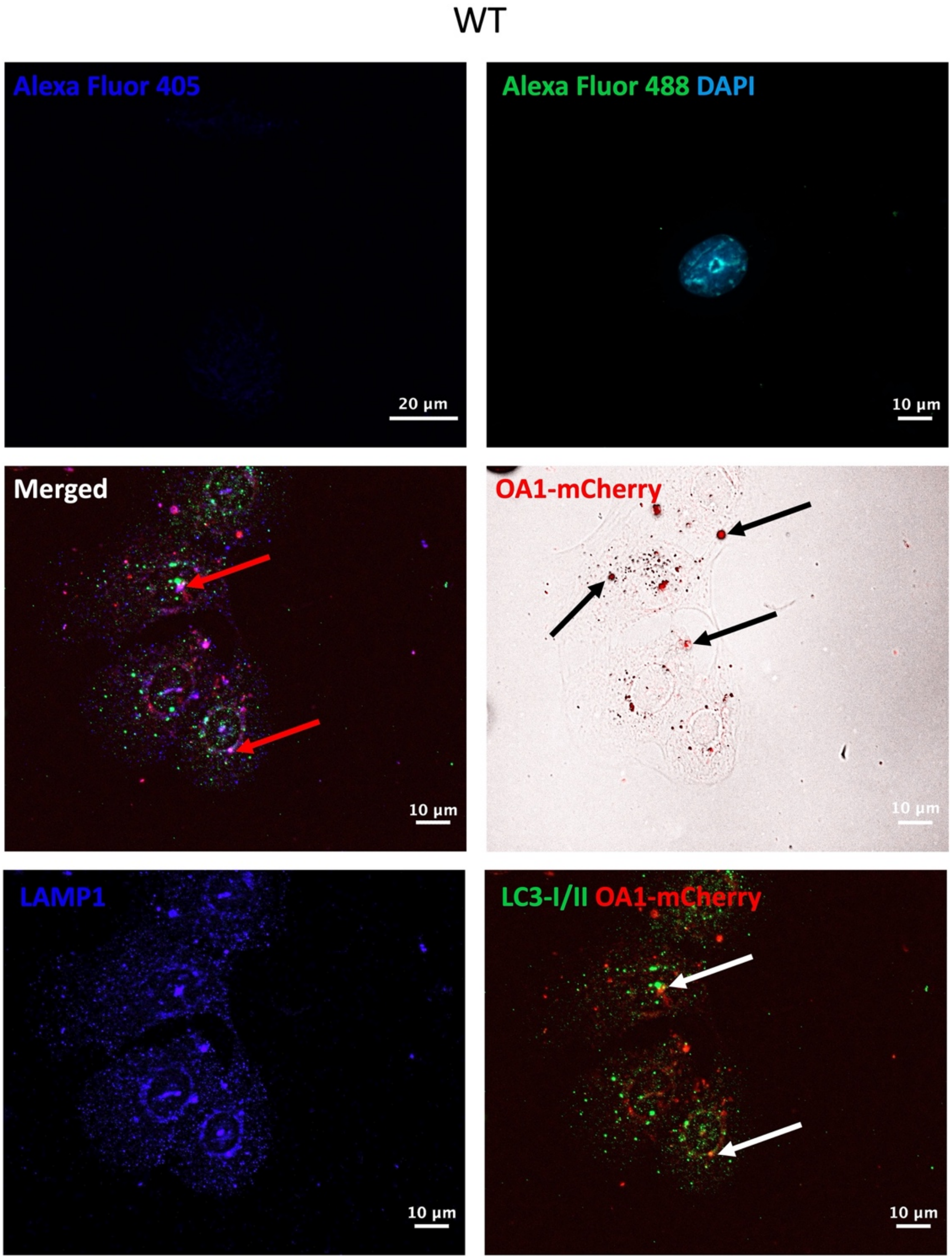

Figure 5.11 Representative immunostaining confirming OA1-mCherry uptake after 24 hours in primary WT keratinocytes. Primary WT keratinocytes fixed in 100 % methanol and labelled with LC3-I/II (green) and LAMP1 (blue). OA1-mCherry positive melanosomes highlighted in red and overlap in regions of melanin aggregates, shown by black arrow in brightfield image (middle right panel). White arrow showing OA1-mCherry with LC3-I/II overlap and red arrow showing LAMP1, LC3-I/II and OA1-mCherry overlap. Secondary antibody controls (Alexa Fluor 405 and 488) in top left panels. Images taken from 3 independent experiments. Scale bar: 20 µm for Alexa Fluor 405 control and 10 µm for remaining panels.

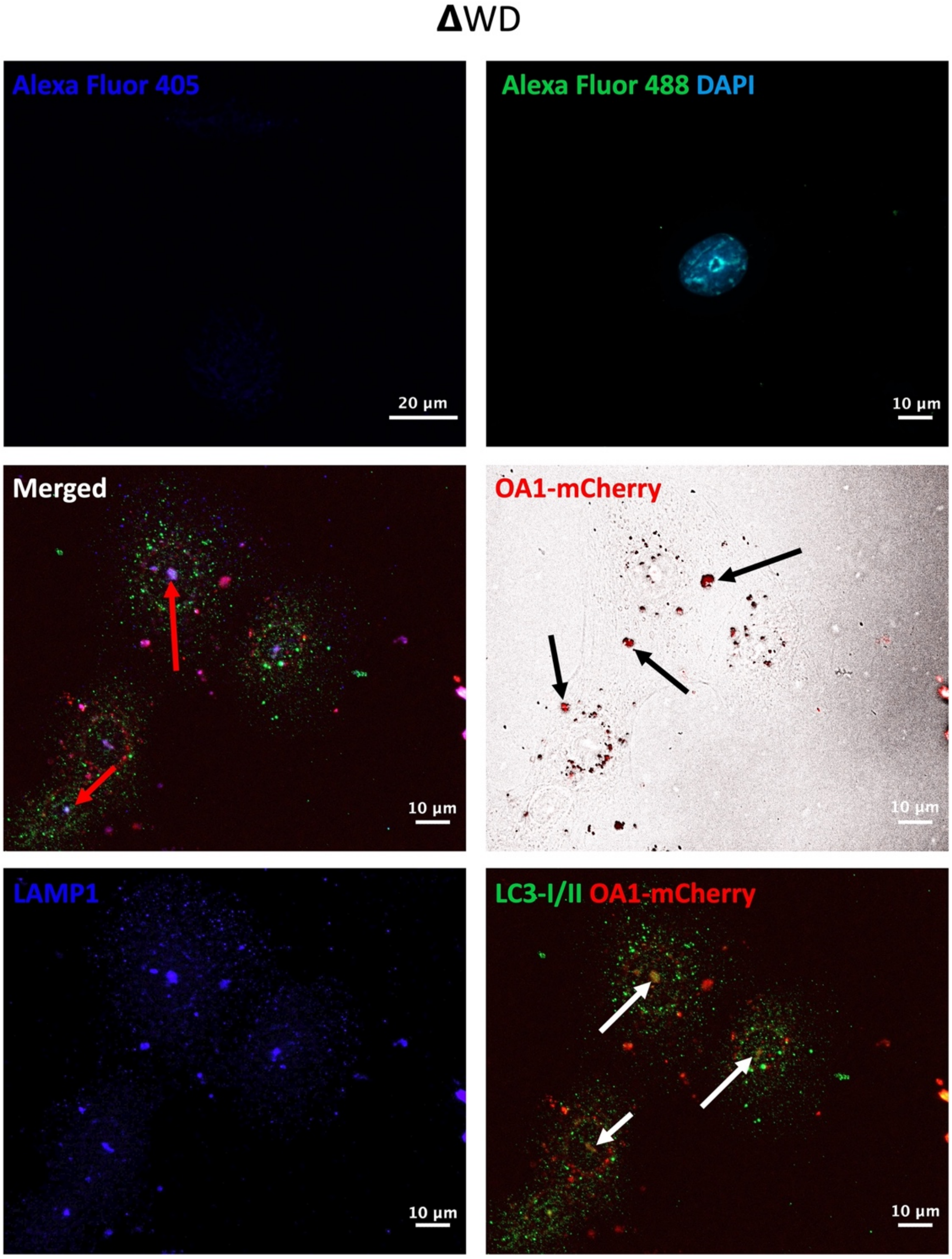

Figure 5.12 Representative immunostaining confirming OA1-mCherry uptake after 24 hours in primary ΔWD keratinocytes. Primary ΔWD keratinocytes fixed in 100 % methanol and labelled with LC3-I/II (green) and LAMP1 (blue). OA1-mCherry positive melanosomes highlighted in red and overlap in regions of melanin aggregates, shown by arrow in brightfield image (middle right panel). White arrow showing OA1-mCherry with LC3-I/II overlap and red arrow showing LAMP1, LC3-I/II and OA1-mCherry overlap. Secondary antibody controls (Alexa Fluor 405 and 488) in top left panels. Images taken from 3 independent experiments. Scale bar: 20 µm for Alexa Fluor 405 control and 10 µm for remaining panels.

5.2.4 Assessing melanosomal dynamics in WT and ΔWD primary keratinocytes

With the system now established in fixed primary keratinocytes, the next step involved monitoring the dynamics in live cells over a 24-hour period, to examine the effects of LAP-deficiency on melanosomal uptake and processing. To investigate the interaction of melanosomes with the autophagic and LAP pathways, primary keratinocytes were transduced with adenovirus LC3-GFP and treated with LysoTracker blue, which monitors lysosomal compartments. Cells were imaged using the confocal Z scanning at 63x magnification for 24 hours.

In WT keratinocytes, LC3 expression displayed perinuclear localisation at 2 hours, with prominent LC3 green puncta indicating autophagosome formation (Figure 5.13). These autophagosomes disappeared by 7 hours, with diffuse LC3-GFP expression becoming visible, which persisted until 9 hours. By 11 hours, LC3 puncta began to reappear, showing OA1-mCherry expression and LysoTracker staining, with these structures remaining visible at 16 hours (Figure 5.13). From 16 hours onwards, LC3 puncta became more prominent and remained punctate until 24 hours (Figure 5.13). This pattern resembled the LC3 expression observed in fixed WT keratinocytes after 24 hours of melanosome treatment (Figure 5.11). In the ΔWD keratinocytes, LC3-GFP expression was more diffuse at 2 hours; however, autophagosome formation began as early as 4 hours post melanosome treatment (Figure 5.14). These bright LC3-GFP puncta clustered in regions of OA1-mCherry at 8 hours and remained visible at 9 hours (Figure 5.14). A strong LC3-GFP signal around the perinuclear region was consistently visible from 9 to 18 hours (Figure 5.14). After 18 hours, the LC3 puncta remained until 24 hours, similar to the observations made in the fixed ΔWD keratinocytes (Figure 5.12; Figure 5.14).

In WT keratinocytes, LysoTracker exhibits diffuse fluorescence at 2 hours, persisting until after autophagosome formation at 16 hours (Figure 5.13). LysoTracker fluorescence becomes much stronger at 19 hours, starting to associate with LC3-GFP and OA1-mCherry. By 24 hours, LysoTracker is more prominent in regions of melanosome processing (Figure 5.13). In the ΔWD keratinocytes, LysoTracker is initially diffuse at 2 hours but begins to aggregate as early as 10 hours in regions of melanosome deposition (Figure 5.14). Between 10 and 17 hours, LysoTracker increasingly associates with LC3-GFP and OA1-mCherry

(Figure 5.14). In the remaining hours, LysoTracker fluorescence remains prominent near melanosome processing sites (Figure 5.14). Similar aggregates of LAMP1 and LC3 can be observed in the fixed WT and ΔWD keratinocytes at 24 hours (Figure 5.11; Figure 5.12).

In WT keratinocytes, results revealed that OA1-mCherry positive melanosomes began to aggregate at 9 hours post-incubation with OA1-mCherry melanosome (Figure 5.13). These melanosomes formed clusters around the perinuclear region during the live-cell imaging time course (Figure 5.13). In ΔWD keratinocytes, melanosome clustering occurred as early as 4 hours and became progressively more aggregated by 9 hours (Figure 5.14). The OA1-mCherry melanosome clusters remain localised to the perinuclear area of the keratinocyte, with the OA1-mCherry signal persisting until 24 hours in WT keratinocytes. However, in the ΔWD keratinocytes, the OA1-mCherry expression begins to disappear at 21 hours in ΔWD cell 1 but remained in the second keratinocyte (Figure 5.14).

The interaction of LysoTracker, LC3-GFP, and OA1-mCherry was further assessed by calculating the co-localisation of the three markers and measuring the fluorescent intensity through line analysis in ImageJ (Table 5.3; Figure 5.15; Figure 5.16). For the colocalization analysis, the Pearson's coefficient (PC) was calculated at several regions of melanosome processing over time. The line analysis for the fluorescent intensity profiles was measured in the same regions, allowing for a comparison of the PC coefficient with the intensity profile (Figure 5.15; Figure 5.16).

For example, at 9 hours, the ROI outlined in Figure 5.15-5.16, exhibited a PC for the interaction between OA1-mCherry and LC3-GFP of 0.02 (WT cell 1) and 0.24 (WT cell 2) (Table 5.3). The fluorescent intensity of these markers at this ROI was weak, with the greatest signal appearing from the LysoTracker (Figure 5.15 A). In contrast, the coefficients at 9 hours were higher in the ΔWD keratinocytes, with values of 0.68 (ΔWD cell 1) and 0.46 (ΔWD cell 2). These higher PC values were reflected in the intensity plots, which showed more pronounced peaks than those observed in the WT keratinocytes (Figure 5.16 A). Moreover, the LC3-GFP and OA1-mCherry plots showed close interaction at 9 hours, as demonstrated by the high PC value (Table 5.3; Figure 5.16). At 16 hours, WT keratinocytes showed subtle differences in the intensities of the LC3-GFP, OA1-mCherry, and LysoTracker signals, except in WT Cell 1, which began to form a large aggregate with stronger OA1-mCherry and LC3-GFP signals (Figure 5.13; Figure 5.15 A). The association of LC3-GFP and

OA1-mCherry at this ROI exhibited a PC of 0.68 (Table 5.4; Figure 5.15 B). At 16 hours, the fluorescent intensities of LC3, OA1, and LysoTracker increased slightly from 9 hours, in both ΔWD cells (Figure 5.16 A). The interaction of OA1 and LC3 was greater at 16 hours than at 9 hours, with a PC of 0.89 for ΔWD cell 1 and 0.71 for ΔWD cell 2 (Table 5.3; Figure 5.16 B). Additionally, the association of OA1-mCherry and LysoTracker increased, with coefficients of 0.62 (ΔWD cell 1) and 0.63 (ΔWD cell 12) (Table 5.3; Figure 5.16 B). This association was much weaker in the WT keratinocytes, with PCs of only 0.22 (WT cell 1) and 0.01 (WT cell 2) (Table 5.3; Figure 5.15 B). The ΔWD keratinocytes exhibited signs of LC3-GFP fusion with lysosomes at 16 hours, indicated through the high PCs of 0.74 (ΔWD cell 1) and 1 (ΔWD cell 2) (Table 5.3; Figure 5.16 B). Correspondingly, the high PCs observed between OA1-mCherry and LysoTracker blue, suggest that melanosomes start to become processed in the lysosomes at around 16 hours (Table 5.3; Figure 5.16 B). This processing was not observed in the WT keratinocytes, with only WT cell 1 showing a strong association of LC3-GFP and LysoTracker blue at 16 hours (*r* = 0.40) (Table 5.3). At 24 hours, the expression and interaction between melanosomes and LC3 increased, with PCs of 0.74 (WT cell 1) and 0.26 (WT cell 2) (Table 5.3; Figure 5.13; Figure 5.15 A-B). The same was true for the association of LC3 and lysosomes, with coefficients of 0.76 (WT cell 1) and 0.34 (WT cell 2) (Table 5.3; Figure 5.13; Figure 5.15 A-B). Moreover, the interaction between melanosomes and lysosomes increased, displaying higher PCs in cell 1 and 2 (*r* = 0.43 and 0.12, respectively) (Table 5.3; Figure 5.15 B). At 24 hours, the ΔWD keratinocytes exhibited increased expression of OA1-mCherry, LC3-GFP and LysoTracker blue, yet the association of OA1-mCherry and LC3-GFP remained comparable, with PCs of 0.81 in ΔWD cell 1 and 0.73 in ΔWD cell 2 (Figure 5.13; Figure 5.16).

However, the interaction of OA1 and lysosomes began to decrease in ΔWD cell 1, with a PC of 0.49 (Table 5.3; Figure 5.16 B). In ΔWD keratinocyte 2, the interaction between lysosomes and melanosomes remained similar to that observed at 16 hours, with a coefficient of 0.64 (Table 5.3; Figure 5.16 B). Moreover, the association of LC3 and lysosomes began to decrease at 24 hours, with subtle changes seen in the PCs, recorded at 0.72 (ΔWD cell 1) and 0.74 (ΔWD cell 2) (Table 5.3; Figure 5.16 B). Despite these changes, the intensity of the LC3 and LysoTracker signals remained high in the intensity plots at 24 hours (Figure 5.16 A).

Table 5.3 Overview of Pearson’s coefficient (*r*) for primary keratinocyte ROIs listed below at 2-24 hrs.

Condition	**Pearson's coefficient (r)**			
	2 hrs	**9 hrs**	**16 hrs**	**24hrs**
WT Cell 1 mCherry + GFP	0.02	0.02	0.68	0.74
WT Cell 1 mCherry + Lysotracker Blue	0.00	0.01	0.22	0.43
WT Cell 1 GFP + Lysotracker Blue	0.00	0.01	0.40	0.76
WT Cell 2 mCherry + GFP	0.01	0.24	0.03	0.26
WT Cell 2 mCherry + Lysotracker Blue	0.00	0.01	0.01	0.12
WT Cell 2 GFP + Lysotracker Blue	0.00	0.00	0.00	0.34
ΔWD Cell 1 mCherry + GFP	0.60	0.68	0.89	0.81
ΔWD Cell 1 mCherry + Lysotracker Blue	0.00	0.08	0.62	0.49
ΔWD Cell 1 GFP + Lysotracker Blue	0.00	0.14	0.74	0.72
ΔWD Cell 2 mCherry + GFP	0.00	0.46	0.71	0.73
ΔWD Cell 2 mCherry + Lysotracker Blue	0.02	0.31	0.63	0.64
ΔWD Cell 2 GFP + Lysotracker Blue	0.00	0.51	1.00	0.74

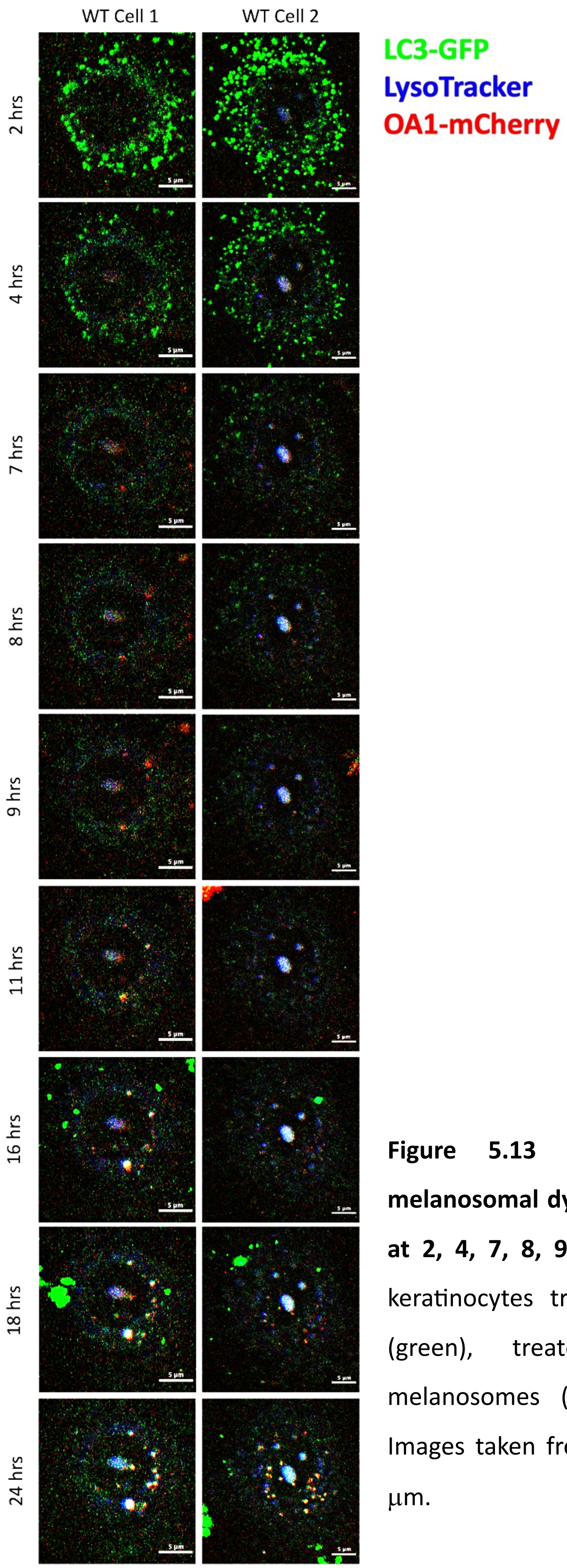

Figure 5.13 Timestamp confocal images of melanosomal dynamics in WT primary keratinocytes at 2, 4, 7, 8, 9, 11, 16, 18 and 24 hours. Primary keratinocytes transduced with adenovirus LC3-GFP (green), treated with OA1-mCherry tagged melanosomes (red) and LysoTracker Blue (blue). Images taken from a single experiment. Scale bar: 5 µm.

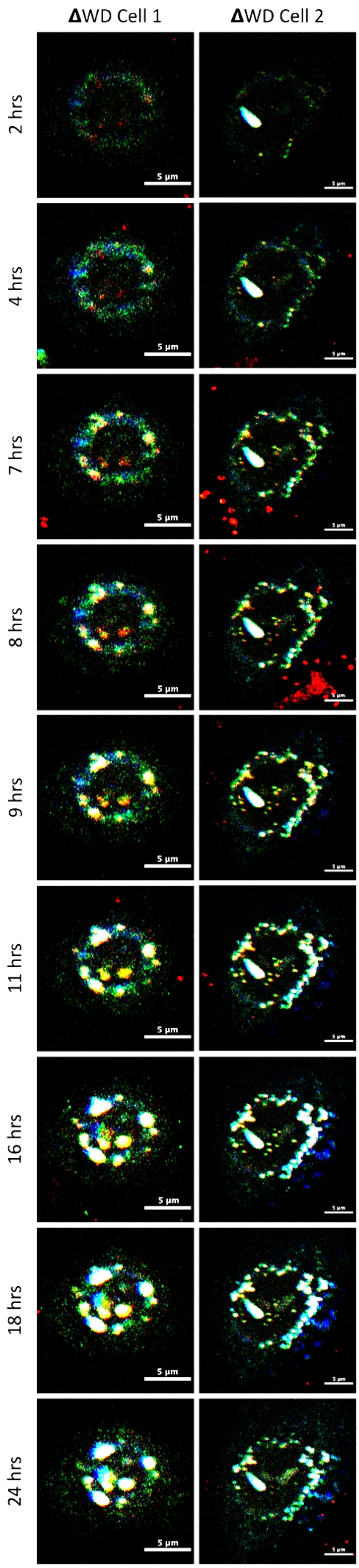

Figure 5.14 Timestamp confocal images of melanosomal dynamics in ΔWD primary keratinocytes at 2, 4, 7, 8, 9, 11, 16, 18 and 24 hours. Primary keratinocytes transduced with adenovirus LC3-GFP (green), treated with OA1-mCherry tagged melanosomes (red) and LysoTracker Blue (blue). Images taken from a single experiment. Scale bar: 5 μm.

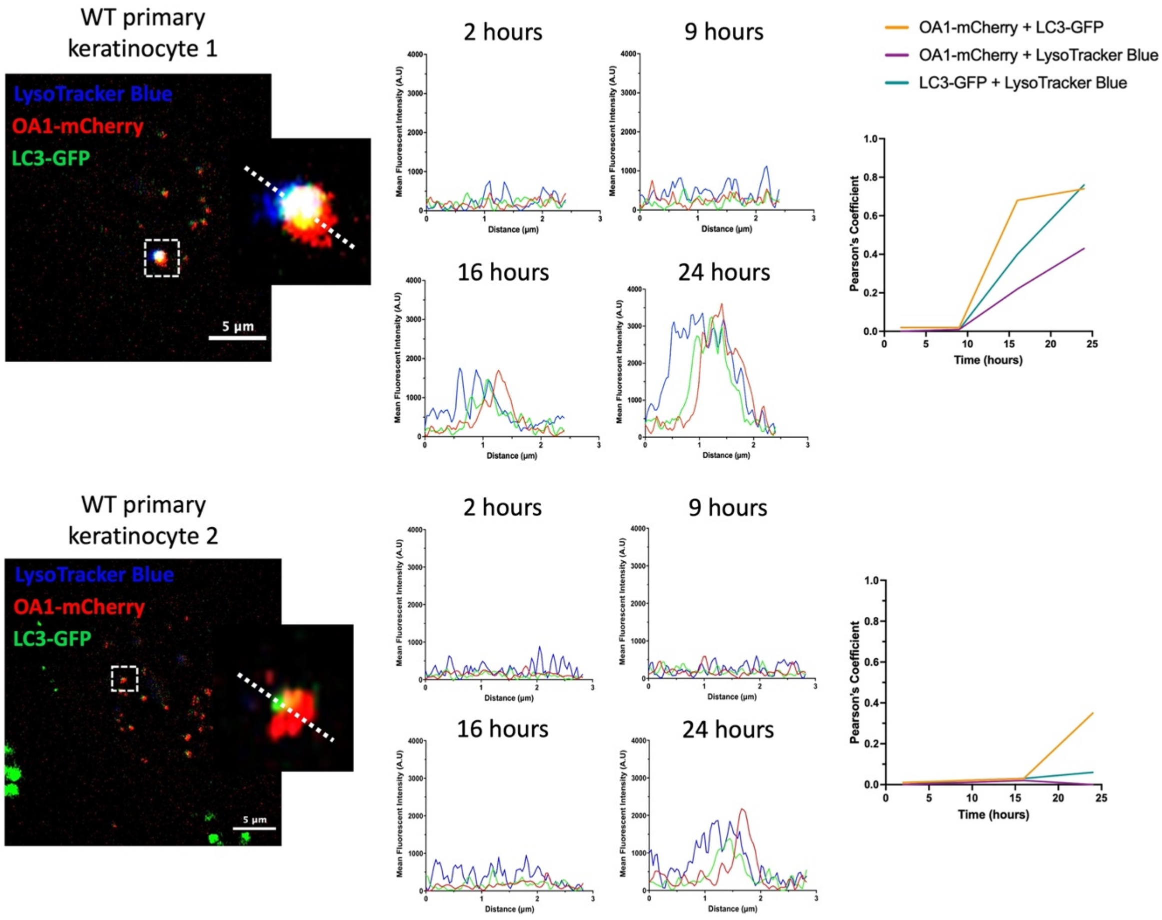

Figure 5.15 WT primary keratinocytes at 24 hours post OA1-mCherry melanosome treatment. (A) WT primary keratinocyte transduced with adenovirus LC3-GFP (green) and treated with LysoTracker Blue (blue) and OA1-mCherry (red) melanosomes. White dashed box highlighting a region of melanosome processing and analysis. Magnified image showing ROI. Images taken from a single experiment. Scale bar: 5 µm. Right panels showing fluorescent intensity profiles (A.U) over time (2-24 hours) at ROI. **(B)** Colocalisation analysis at ROIs, showing Pearson's coefficient of OA1-mCherry and LC3-GFP, OA1-mCherry and LysoTracker Blue, and LC3-GFP and LysoTracker Blue, over time (2-24 hours).

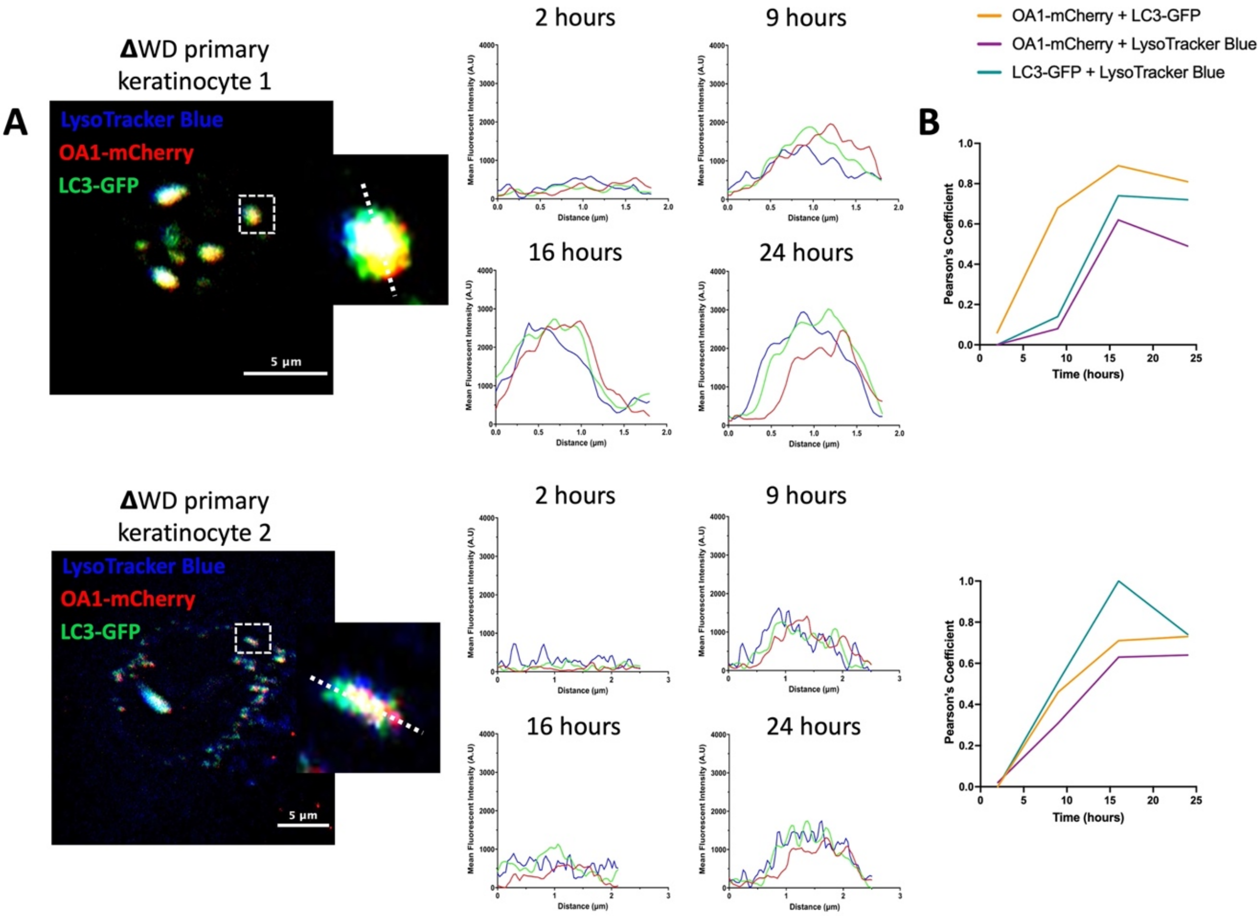

Figure 5.16 ΔWD primary keratinocytes at 24 hours post OA1-mCherry melanosome treatment. (A) ΔWD primary keratinocyte transduced with adenovirus LC3-GFP (green) and treated with LysoTracker Blue (blue) and OA1-mCherry (red) melanosomes. White dashed box highlighting a region of melanosome processing and analysis. Magnified image showing ROI. Images taken from a single experiment. Scale bar: 5 μm. Right panels showing fluorescent intensity profiles (A.U) over time (2-24 hours) at ROI. **(B)** Colocalisation analysis at ROIs, showing Pearson's coefficient of OA1-mCherry and LC3-GFP, OA1-mCherry and LysoTracker Blue, and LC3-GFP and LysoTracker Blue, over time (2-24 hours).

5.3 Discussion

This chapter explored the impact of LAP deficiency on melanosome uptake and processing in primary control and ΔWD keratinocytes. By utilising the ΔWD mouse model I was able to provide a unique system to distinguish between autophagy and LAP in the trafficking of melanosomes in keratinocytes. This work expanded the current understanding of the role of autophagy in melanosome degradation in keratinocytes and offers a novel *in vitro* system for investigating pigmentation dynamics in both autophagy-efficient and LAP-deficient keratinocytes.

5.3.1 Isolation and long-term culture of primary keratinocytes

Primary keratinocytes were isolated from the epidermal tail skin of control and ΔWD mice, and were cultured in rat tail type I collagen-coated dishes until further processing. The tail skin was chosen over dorsal skin due to its lower hair follicle density, making it more suitable for pure keratinocyte isolation (Li et al., 2017). Initially, keratinocytes were isolated and cultured in low Ca^{2+} (0.05 mM) serum-supplemented growth medium (EMEM), but this medium did not promote cell proliferation and cells survived only up to day 5 post-isolation. Instead, serum-free keratinocyte specific medium, supplemented with growth factors, cytokines and other supplements – proved more effective for long-term keratinocyte culture. The proliferation rate increased, and cells sustained growth beyond 8 days, reaching confluency (> 70%) by day 5, when cultured immediately in KBM growth medium. It has been reported that serum-free media supports keratinocyte growth when supplemented with EGF, insulin, transferrin, and hydrocortisone (Ścieżyńska et al., 2018). Increased proliferation rates were observed with this supplemented serum-free media, though the rate of proliferation decreased when the concentration of supplements was reduced. The proliferating keratinocytes exhibited a cobblestone morphology, which is a common characteristic for basal keratinocytes (Zhang, 2019). Despite achieving confluency, primary keratinocytes could not sustain growth as a monolayer in this medium and began to decrease in number after subculturing. Primary murine keratinocytes have shown difficulties in *in vitro* culture compared to human primary keratinocytes, which maintain their division capability for many passages (Hager et al., 1999). Hager and colleagues demonstrated that maintaining murine epidermal keratinocytes (MEK) in EMEM growth medium with 0.06 mM Ca^{2+} was sufficient to subculture primary basal cells (Hager et al., 1999). They isolated the MEKs using collagenase solution, whereas keratinocytes in this project were isolated using trypsin. The use of trypsin for the isolation of primary keratinocytes may influence the keratinocyte viability following culture in KBM or EMEM. A method review by Ścieżyńska and co-workers stated that after enzymatic digestion with trypsin only 3-4% of keratinocytes could form colonies, despite optimal culture conditions (Ścieżyńska et al., 2018). Moreover, Hager's study revealed that adding fibroblast-conditioned medium, along with appropriate growth factors such as EGF, hydrocortisone, cholera toxin and aminoguanidine, allowed cultures to maintain their basal phenotype through to passage 19 (Hager et al., 1999). Similarly, a feeder layer of fibroblast cells is often used when culturing primary keratinocytes (Morris et al., 2019).

In addition to low concentrations of Ca^{2+} and appropriate growth media, the microenvironment in which the primary keratinocytes are cultured *in vitro* also determines the cell fate (Wong et al., 2019). It has been demonstrated that maintaining an acellular ECM assists in preserving the stem-cell like characteristics of the keratinocytes, by providing biochemical and biomechanical cues that regulate migration, adhesion, proliferation, and differentiation (Frantz et al., 2010). A study by Wong and colleagues revealed that primary keratinocytes cultured on collagen I grew as single cells but developed mixed morphologies, with some cells becoming quite large and flat (Wong et al., 2019). This characteristic was also observed in our primary keratinocytes at day 5, increasing progressively at day 8. These flattened cells exhibited F-actin staining around the cell periphery, more prominently in the ΔWD keratinocytes. This circumferential actin network indicates that these ΔWD keratinocytes are less motile and are undergoing terminal differentiation, similar to observations by Nanba and co-workers (Nanba et al., 2013). In the WT keratinocytes, phalloidin staining was not as prominent, but was still localised to the cell periphery. Additionally, both WT and ΔWD keratinocytes began to express keratin 10, an early indicator of terminal differentiation. The association of increased size and prominent F-actin distribution at the cell periphery during terminal differentiation supports findings by Sun and Green (Sun and Green, 1976).

5.3.2 Applications for modelling LC3-associated phagocytosis, autophagy and melanosomal movement *in vitro*

Melanin is an electron-dense, chemically robust, and highly light-absorbing substance, making it challenging to assess melanosomal dynamics using fluorescent techniques (Lazova et al., 2010). An OA1-mCherry plasmid was used to label melanosomes that had undergone synthesis and maturation in 1014 murine melanoma melanocytes. OA1-mCherry positive fluorescent puncta were observed throughout the cytosol of 1014 murine melanoma cells, yet the majority of OA1-mCherry accumulated at the cortical actin network. OA1-mCherry expression was shown to be in regions of melanin aggregates, corresponding to the mature melanosomes carrying the pigment to the melanocyte periphery. These melanin aggregates can be observed in the phase and brightfield images by the black puncta. The 1014 murine melanoma cells did not exhibit homogenous pigmentation throughout cultures. It has been shown that OA1 is localised to the perinuclear area and was mainly associated with endosomal/lysosomal compartment, and co-localised to TYRP1 and LAMP1, however other studies have demonstrated that OA1 is confined to the membrane of melanosomes at all stages of maturation (Samaraweera et al., 2001; Schiaffino et al., 1996). Some of these vesicular OA1-mCherry puncta were also immunolabelled with Rab27a, a binding protein that attaches melanosomes to the distal actin cytoskeleton (Van Gele et al., 2009). Rab27a exhibited an increased expression at this cortical actin network, due to melanosomes docking at the cell periphery. This docking was facilitated by the binding of Rab27a to the actin network, mediated through melanophilin (Strom et al., 2002). Bruder and co-workers also showed that this Rab27a was co-localised to OA1-mCherry, indicating that both markers were localised to melanosomes (Bruder et al., 2012). Using this fluorescently tagged OA1, it was established that OA1-mCherry could be used as an effective melanosomal marker for fixed and live cell imaging experiments. As far as we are aware this is the first report of using OA1-mCherry tagged melanosomes in primary keratinocyte cultures and provides a useful tool for studying and characterising the dynamics of melanosomes in adjacent keratinocytes. The Morris lab at UCL has confirmed through Western Blot that these exocytosed melanosomes, harvested from the 1014 murine melanoma media, are positive for Rab27a and S100 calcium-binding protein B. This marker is secreted by melanocytes, proving that these OA1-mCherry tagged melanosomes are derived from the melanocytes. An exosome control was probed alongside the melanosome to evaluate the nature and origin of the extracellular vesicle (Personal communication).

For monitoring autophagy and LAP, primary WT and ΔWD keratinocytes were transduced with an adenovirus encoding GFP-LC3 for 24 hours, before replenishing with fresh growth medium. Following conventional autophagy inhibition with chloroquine, primary control keratinocytes recruited LC3 to large endo-lysosomal compartments. Here, chloroquine induced the non-conventional LAP pathway in the control keratinocytes, with ΔWD keratinocytes failing to recruit LC3 to these large endo-lysosomal structures. Similar observations were made by Wang and co-workers using WT and ΔWD MEFs (Wang et al., 2021). Autophagy was activated in non-chloroquine induced control and ΔWD keratinocytes, indicated by the LC3 puncta. These LC3 puncta were localised to the perinuclear area in both the WT and ΔWD keratinocytes. Immunolabelling of LC3-I/II exhibited similar expression patterns, with the expression of LC3-I/II primarily confined to the perinuclear region. Several dermatological conditions, such as Hermansky-Pudlak syndrome type 1, vitiligo and melanoma, have been shown to exhibit various levels of autophagic dysregulation (Li et al., 2020; Nagar, 2017). Additionally, studies have indicated that melanosomes may be degraded by autophagy in melanocytes and keratinocytes (Kim et al., 2020; Murase et al., 2013; Zhu et al., 2020). So far, the assumptions have been made that autophagy has a key role in the pathogenesis of these conditions, yet little is known whether an alternative non-canonical process (i.e., LAP) may be involved.

5.3.3 OA1-mCherry associates with LC3-GFP and lysosomes in ΔWD keratinocytes

OA1-mCherry tagged melanosomes were collected from the 1014 murine melanoma growth medium and added to primary keratinocytes cultured in KBM growth medium. The melanosomes were incubated with the keratinocytes for 24 hours before fixing the keratinocytes with 100% methanol for subsequent immunolabelling. This system was established in fixed primary keratinocyte cultures to ensure that the melanosomes would be ingested by the keratinocytes. Results showed that OA1-mCherry melanosomes were engulfed by the keratinocytes and deposited in the supranuclear region. This had been previously reported by Ando and co-workers, who also revealed that within 24 hours, melanosomes accumulated around the perinuclear region after initial phagocytosis in keratinocytes (Ando et al., 2012). Brightfield imaging confirmed that the OA1-mCherry labelling was in areas of melanin aggregation, corroborating the findings from the OA1-mCherry labelling in the 1014 murine melanoma cells. Additionally, control and ΔWD keratinocytes showed co-localisation of LAMP1 with OA1-mCherry, suggesting that these melanosomes might be degraded or stored in lysosomal compartments. In some areas, LAMP1 expression also co-localised with LC3-I/II, indicating a potential autophagic driven degradation process.

Studies have proposed that the melanosome membrane is not internalised by the keratinocyte, with Tarafder and co-workers showing that the single membrane limiting melanin granules in human keratinocytes lacks melanosomal markers (e.g., TYRP1) (Tarafder et al., 2014). In addition, they established a co-culture system between mouse melanocytes (Melan-Inka) and human keratinocytes, and further labelled melanosomes with LAMP1 that specifically detects murine-derived LAMP1. This LAMP1 immunolabelling was present in the mouse melanocytes, yet was absent from the human keratinocytes, further confirming that the melanosome membrane is not present following ingestion by keratinocytes. Given that my study shows OA1-mCherry tagged melanosomes in primary keratinocytes, following 24 hours of treatment, provides a new insight that the melanosome membrane is transferred to keratinocytes in murine skin. Hurbain and colleagues revealed that different modes of transfer are not mutually exclusive and thus may depend on the model system that is used and the region of skin (Hurbain et al., 2018).

Once the system was established in fixed keratinocytes, the dynamics of the melanosomes was further assessed in live WT and ΔWD primary keratinocytes over 24 hours using confocal microscopy. Lysosomal structures were labelled with LysoTracker blue, autophagy and LAP were monitored using an adenovirus LC3-GFP, and melanosomes were fluorescently labelled with OA1-mCherry. Images were captured every hour, revealing that by 2 hours, OA1-mCherry tagged melanosomes had already been ingested by the keratinocytes. Fluorescent intensity analysis indicated a weak mCherry signal in both WT and ΔWD keratinocytes at 2 hours, suggesting that ΔWD keratinocytes show no delay in the uptake of melanosomes compared to controls. At 2 hours, the association between OA1-mCherry and LC3-GFP was weak in controls, as indicated by low PCs. Similarly, the association between OA1-mCherry and LysoTracker blue was low in both controls and ΔWD keratinocytes, suggesting that melanosomal processing had not yet begun. By 9 hours, clustering of OA1-mCherry in the perinuclear area was observed in both WT and ΔWD keratinocytes, with this clustering being more prominent in the ΔWD keratinocytes, as highlighted by fluorescent intensity analysis. The interaction between LC3-GFP and OA1-mCherry increased in both WT and ΔWD keratinocytes, becoming much more pronounced at 16 hours post-melanosome incubation in the ΔWD keratinocytes. This increase was slightly delayed in the WT cells, with only one cell showing a stronger association of OA1-mCherry and LC3-GFP at 16 hours. This increased interaction was coupled with an increase in the co-localisation of lysosomes and LC3, suggesting that melanosomal processing had commenced by 16 hours. By 24 hours, an overlap of LC3-GFP, LysoTracker blue, and OA1-mCherry was observed in both WT and ΔWD keratinocytes, indicating that OA1-mCherry tagged melanosomes were being sequestered by autophagosomes, mediated by LC3. It is possible that the melanosome membrane, where OA1-mCherry is integrated, is targeted by autophagy, and the melanin contained within the lysosome is stored following degradation of the membrane. It has been proposed that melanocores are not degraded by the lysosome, but are stored (Correia et al., 2018; Hurbain et al., 2018). Correia and co-workers revealed that XB-2 keratinocytes treated with melanocores exhibited minimal co-localisation of the melanocores with LysoTracker, and demonstrated that early endosomal antigen 1 (EEA1), LAMP2, and CD63 surround the melanocores (Correia et al., 2018). This suggests that they may be stored in either a hybrid or transitional early-to-late endosome. They demonstrated that these compartments show only moderate acidification and poor hydrolytic capacity, making them convenient for longer term storage of melanin. Yet, Homma and colleagues determined that melanosomes were degraded by lysosomes, which they assessed by using leupeptin, an inhibitor of lysosomal hydrolases (Homma et al., 2018). The studies by Hurbain and co-workers and Correia and colleagues contradict many studies that suggest that melanosomes are degraded by lysosomes (Correia et al., 2018; Homma et al., 2018; Hurbain et al., 2018; Murase et al., 2013).

The phagocytic activity of keratinocytes is regulated by PAR-2. A study by Ando and co-workers revealed that microvillus-associated trapping of the pigment globules occurred in the basal keratinocytes but not in terminally differentiating ones (Ando et al., 2012). In the later stages of keratinocyte phagocytosis, the pigment globule was engulfed by the keratinocyte plasma membrane, a process that could be inhibited by treatment with soybean trypsin inhibitor, known as a PAR-2 inhibitor. This strongly indicates that the incorporation of pigment globules in human epidermal keratinocytes is dependent on PAR-2. In fact, Seiberg and co-workers established that PAR-2 stimulation increased melanin uptake by keratinocytes (Seiberg et al., 2000). Furthermore, Correia and co-workers revealed that PAR-2 was required for melanocore uptake by keratinocytes, with PAR-2 silencing resulting in fewer melanocores being ingested (Correia et al., 2018). Moreover, a study by Babiarz-Magee and others found that PAR-2 was highly expressed in darker skin, suggesting that increased phagocytic activity influences skin colour (Babiarz-Magee et al., 2004). Indeed, Murase and colleagues determined that autophagy plays a role in determining skin colour through the degradation of melanosomes in keratinocytes (Murase et al., 2013). By suppressing ATG7, they reported an increase in the melanosomal protein PMEL, accompanied by a decrease in LC3-II, a marker for autophagosomes. These findings suggest that autophagy is involved in melanosome degradation in normal human epidermal keratinocytes. Further support came from knockdowns of ATG13 and UVRAG, which resulted in the accumulation of p62. Given that autophagy targets organelles such as mitochondria, peroxisomes, the nucleus, and the endoplasmic reticulum for degradation, it is reasonable to assume it would degrade lysosome-related organelle like melanosomes to protect keratinocytes from toxicity (Murase et al., 2013).

A study by Kim and colleagues showed that a synthetic autophagy inducer, PTPD-12, could stimulate melanosome degradation in keratinocytes (Kim et al., 2020). Primary human epidermal keratinocytes treated with PTPD-12 exhibited upregulation of LC3-II and a dose-dependent reduction of p62. Fluorescent microscopy revealed a significant increase in the number of autolysosomes following PTPD-12 treatment, emphasising that this synthetic inducer could enhance autophagic activity. Furthermore, it induced the degeneration of melanosome structures within autophagic vesicles, which was observed by the colocalization of PMEL17 and LC3 and reduced the number of isolated melanosomes in primary human keratinocytes. TEM imaging showed a reduced number of melanosomes, and increased number of autophagosomes and autolysosomes in the primary human keratinocytes, following PTPD-12 treatment. Moreover, they revealed that electron microscopy of L-DOPA showed melanosomes in the perinuclear area within autophagic vacuoles, which they suggest that terminal stage melanosomes are degraded by PTPD-12 mediated autophagy. This was supported by further Western Blot analysis on key melanogenesis proteins, such MITF, TYR and PMEL17, where MITF expression remained unchanged following treatment with PTPD-12, yet PMEL and TYR expression decreased. Interestingly, following chloroquine treatment, an autophagic flux inhibitor, PTPD-12-mediated melanosome degradation decreased.

The relationship between LAP and melanosome processing and degradation remains ambiguous, therefore, the question of whether LAP is involved in the early stages of melanosome trafficking needs to be addressed. Despite promising efforts of autophagy being involved in melanosome biogenesis, processing and degradation, limited research has been conducted on the relationship between human/mouse melanin and LAP. So far, research has only been conducted on fungal melanin, which has demonstrated inhibitory functions on LAP in *Aspergillus fumigatus* (Akoumianaki et al., 2016; Gonçalves et al., 2020; Kyrmizi et al., 2018). Akoumianaki and colleagues revealed that two events must occur in *A.fumigatus* germination that will enable LAP activation, which include unmasking of the PAMPs and removal of melanin from the fungal cell wall (Akoumianaki et al., 2016). They determined that fungal cell wall melanin inhibits the assembly of the NADPH oxidase complex, by excluding the p22*phox* subunit from the phagosome, thereby preventing LAP. They also indicated that not only fungal melanin exhibits this inhibitory role, but also purified melanin from various sources, such as synthetic melanin. This was confirmed by a further study by Chamilos and co-workers, who showed that LAP blockage was not restricted to fungal cell wall melanin but was a general property of other melanin pigments that were tested (Chamilos et al., 2016). In addition, they revealed that melanin did not inhibit macroautophagy, which had been induced by rapamycin, but only inhibited the NADPH oxidase-dependent activation of LAP. If mouse skin melanin is exhibiting similar inhibitory mechanisms on the control primary keratinocytes, this would mean that both our WT and ΔWD keratinocytes are LAP-deficient, despite the removal of the WD domain in *ATG16L1.* Therefore, more research is needed to evaluate whether human and murine skin melanin exhibits similar inhibitory functions on the LAP pathway. By understanding the underlying mechanisms that melanin uses to exploit this pathway, will aid in the future evaluation of dermatological skin conditions.

5.4 Conclusions

This chapter has established a novel system for monitoring melanosomal dynamics in autophagy efficient and LAP-defective primary mouse keratinocytes, using OA1-mCherry tagged melanosomes, an adenovirus LC3-GFP and LysoTracker blue. This study supports previous findings that autophagy is involved in the degradation of melanosomes in keratinocytes and provides a potentially useful tool for assessing the role of LAP in melanosomal degradation. To fully evaluate this involvement, the uptake and processing of melanosomes should be explored at earlier stages in the keratinocytes with shorter time intervals and the potential inhibitory function of melanin on LAP should be examined. Irrespectively, autophagy presents itself as a novel therapeutic approach against pigmentation disorders.

5.5 Limitations and future work

This chapter highlighted several limitations that could be addressed in future experiments.

To expand our primary cultures *in vitro* and maintain them in a basal proliferative state for many passages, one would need to explore the use of a potential fibroblast feeder layer (e.g., Mouse embryonic fibroblasts from the ΔWD) to provide microenvironmental support. This would reduce the number of mice required for primary keratinocyte isolation and thus contribute to maintaining the three Rs principle in animal research.

Insufficient amounts of OA1-mCherry labelled melanosomes were harvested from the media of the 1014 murine melanoma cells. To address this, future experiments should involve large-scale transfection of 1014 murine melanoma cells with OA1-mCherry, followed by purification of melanosomes. This approach will enable us to obtain a more concentrated volume of melanosomes for use with keratinocytes, enhancing the intensity of the mCherry signal and enabling more effective downstream imaging. During my analysis, I encountered difficulties using the confocal microscope due to the weak mCherry signal, which required a higher laser power. This higher power negatively impacted the viability of the primary cultures over the 24-hour imaging period. By increasing the concentration of melanosomes, we should be able to reduce the laser power, thereby preserving the viability of the keratinocytes. The increased laser power and exposure time for the mCherry channel resulted in each time point taking over 10 minutes to image, complicating the evaluation of early time points when LAP commonly occurs, and limiting the number of cells analysed. Therefore, as an alternative, using a light-sheet microscope could improve this process. Light-sheet microscopy requires only a thin sheet of light to excite the fluorophores, which, combined with concentrated melanosomes, would allow for shorter imaging intervals during the first 30 minutes post-melanosome treatment. This would help us better understand whether LAP is involved in the melanosomal movement and processing in primary keratinocytes, as LAP tends to occur 15 minutes post-phagocytosis (Sanjuan et al., 2007). Additional confirmatory immunostaining using TYR or PMEL would help validate that the melanosome membrane is also being ingested by the keratinocyte. Shorter imaging intervals would enable us to monitor the dynamics and tracking of melanosomes entering keratinocytes, allowing for the measurement of the trafficking velocities of these structures post-entry.

Considering that fungal melanin exhibits inhibitory effects on LAP, it would be intriguing to investigate whether human or murine melanin exhibits similar roles. This could be assessed by using extracellular vesicles (e.g., melanosomes & ectosomes), which are released by melanocytes and subsequently taken up the keratinocytes (Wäster et al., 2016). Importantly, the melanosome and the ectosome originate from the lysosome-related organelles, therefore making the ectosome a useful ‘non-melanin’ extracellular vesicle that can be used to study the involvement of LAP in their uptake. This approach would help determine whether human or mouse melanin exhibits inhibitory roles, and whether ectosomes are ingested and contained within a large endo-lysosomal vacuole surrounded by LC3. By evaluating the underlying mechanisms through which melanin potentially exploits the LAP pathway, it would be possible to explore the supplementation of various affected ATGs to rescue those that may be blocked by melanin. This would require extensive research to identify the specific receptors and components that melanin interferes with in the LAP pathway.

The phenotype of the ∆WD keratinocytes could be replicated in human primary keratinocytes or commercially available cell lines, such HaCaT cells. By knocking down the p22*phox* subunit of NADPH complex or silencing of Rubicon in primary human or HaCaT keratinocytes, LAP-deficiency could be induced *in vitro*. This approach would help determine whether human melanin exhibits the same functions as mouse melanin. In addition, using CRISPR technologies, the *ATG16L1* could be manipulated, as demonstrated in the ∆WD mouse model. Given the similarities and differences between mouse and human skin, it is crucial to replicate these studies in human skin models. Mouse skin is thinner than human skin, with fewer cell layers and a greater number of hair follicles. A study by Gerber and colleagues highlighted that there is only 30% identity between the top mouse and human skin associated genes, suggesting that this diversity may explain why results generated from mouse models often fail to translate well to human studies (Gerber et al., 2014). Therefore, mimicking these experiments in human skin is important for more accurate and applicable findings.

Chapter 6: General Discussion & Conclusions

6.1 General Summary

A properly functioning epidermal barrier is a prerequisite for mammalian survival. It serves as a permeability barrier that prevents excessive water loss and shields against external influences such as pathogens, UV light and xenobiotics (Baker et al., 2023; Schmitz et al., 2015). The outermost epidermal layer undergoes a dynamic turnover, driven by proliferating keratinocytes that, upon committing to terminal differentiation, move upward through the individual epidermal layers to form the stratum corneum. In the stratum corneum, corneocytes mitigate UV radiation and contribute to mechanical integrity, while lamellar bodies in the granular layer contribute to the antimicrobial properties of the permeability barrier (Baker et al.,2023). Therefore, proper regulation of the skin barrier components is crucial, as dysregulation can lead to the development of dermatological diseases (e.g., psoriasis). Additionally, melanocytes in the basal epidermal layer produce the pigment melanin, which is transferred to adjacent keratinocytes, resulting in pigmented hair or skin that protects against UV damage (Yang et al., 2014). Similarly, dysregulations in the biosynthesis and distribution of melanin result in dermatological skin conditions, such as vitiligo, melasma and senile lentigo (Lee, 2021).

Several studies have explored the role of autophagy in epidermal differentiation and pigmentation (Akinduro et al., 2016; Montelon et al., 2018; Murase et al., 2013; Ramkumar et al., 2017). Akinduro and colleagues demonstrated that autophagy is constitutively active in the granular layer and is crucial for normal epidermal development and differentiation (Akinduro et al., 2016). Montelon and co-workers found that lysosome activity is essential for normal epidermal development, with its inhibition leading to the accumulation of proteins associated with autophagic vesicles, such as p62 and LC3-I/II (Montelon et al., 2018). Consistent with these findings, Douroudis and others revealed that polymorphisms in ATGs, such as ATG16L1, are associated with the pathogenesis of psoriasis (Douroudis et al., 2012). Additionally, Ramkumar and co-workers discovered that autophagic proteins (e.g., LC3-II and ATG4) expressed in melanocytes facilitate the trafficking of melanosomes from the perinuclear region along cytoskeletal tracks to the melanocyte periphery (Ramkumar et al., 2017). Furthermore, it has been proposed that autophagy plays a role in regulating skin pigmentation, with autophagy-inducers causing depigmentation by promoting melanosome degradation (Kim et al., 2020; Murase et al., 2013; Murase et al., 2020). Building on these findings that autophagy actively regulates the homeostasis of the epidermal permeability barrier, I aimed to evaluate the role of LAP in maintaining skin homeostasis

Limited research exists that investigates the function of LAP in skin pigmentation. So far, LAP has only been studied in microbial pathogenesis with fungal melanin, where studies have demonstrated that certain microbes can survive inside the phagosome by evading LAP (Akoumianaki et al., 2016; Kyrmizi et al., 2018). A study by Akoumianaki and co-workers revealed that fungal melanin can selectively inhibit the assembly of the NADPH oxidase by excluding the p22phox subunit from the phagosome and therefore preventing LAP activation (Akoumianaki et al., 2016). They showed that purified melanin from various sources (e.g., synthetic melanin) inhibits NADPH oxidase-dependent activation of LAP, which many microbes exploit to thrive inside the host. This was further confirmed by a study from Kyrmizi and colleagues, who showed that the fungal cell wall melanin in *Aspergillus fumigatus* causes LAP blockage by excluding NOX2 recruitment on the phagosome, leading to melanin promoting the *Aspergillus fumigatus* virulence *in vivo* (Kyrmizi et al., 2018). While synthetic melanin and fungal cell wall melanin exhibit inhibitory roles in the LAP pathway, it would be crucial to understand whether murine skin melanin exhibits a similar function following uptake by adjacent keratinocytes. The association between LAP blockade and skin pigmentation has not been explored and remains ambiguous. Therefore, this PhD work utilised the LAP-defective ATG16L1$^{\Delta WD}$ mouse model to study the melanosome uptake and processing in LAP-defective keratinocytes compared to controls, to establish the association of LAP in melanosome uptake and processing.

Distinguishing between autophagy and LAP has been challenging; however, our unique ATG16L1$^{\Delta WD}$ mouse model provides a novel tool to study the effects of LAP-deficiency both *in vivo* and *in vitro*. The ATG16L1$^{\Delta WD}$ mouse model has been widely used to study the effects of LAP-deficiency on tissue homeostasis, influenza infection and cognitive disorders (Heckmann et al., 2020; Rai et al., 2019; Wang et al., 2021). Rai and co-workers demonstrated that ΔWD mice did not exhibit any signs of compromised tissue homeostasis in liver, kidney, brain and muscle samples (Rai et al., 2019). Moreover, they determined that these mice grew at similar rates as littermate controls and were fertile. Wang and colleagues found that ΔWD mice were more susceptible to influenza A infection, showing extensive viral replication throughout the lungs and dysregulated cytokine production, which led to fulminant pneumonia and a high mortality rate (Wang et al., 2021). Despite Rai and colleagues' findings of no compromised tissue homeostasis in brain tissue, Heckmann and co-workers discovered that the removal of the WD domain of ATG16L1 in ΔWD mice resulted in increased β-amyloid deposition, increased susceptibility to neuronal death, and β-amyloid neuroinflammation (Heckmann et al., 2020; Rai et al., 2019). Cumulatively, these papers reveal demonstrable roles for ATG16L1 in maintaining healthy tissue homeostasis, which prompts further investigation to elucidate its roles in other diseases and tissues.

This thesis has investigated the impact of LAP-deficiency on skin barrier function and pigmentation dynamics. The study has shown that LAP-deficient mice (ΔWD) exhibit no signs of impaired skin barrier function compared to WT littermate controls. However, these ΔWD mice displayed accelerated skin ageing, evidenced by a significant decrease in net elasticity and elastic recovery in the aged 17-month-old ΔWD mice. Additionally, the research demonstrated that in LAP-deficient primary keratinocytes, melanosomes are trafficked to the perinuclear region and are stored in lysosomal compartments that are co-localised with LC3. Understanding the relationship between LAP, autophagy, and skin barrier function and pigmentation can guide future research toward identifying novel therapeutic targets for treating dermatological diseases.

6.2 Key findings

6.2.1 The skin barrier is not compromised in LAP-deficient mice

In chapter 3 and 4, the skin of 1-year-old WT and ΔWD mice was assessed by immunohistochemistry, revealing comparable skin layer thicknesses across dorsal, ventral and tail regions. Subtle thinning was observed in the ΔWD mice skin layers, yet only reached significance in the tail dermal skin ($p \leq 0.01$). This thinning did not coincide with any abnormalities in the expression profile of key terminal differentiation (i.e., keratin 10; involucrin) or autophagy proteins (i.e., LC3-I/II; p62). Additionally, both WT and ΔWD mice showed comparable levels of proliferative markers (i.e., PCNA, Akt; p-Akt), highlighting their ability to regenerate the epidermal basal cell layer. These findings indicate that removing the WD domain of ATG16L1 does not impact skin barrier permeability and function.

Our results corroborated with earlier studies on the ATG16L1$^{\Delta WD}$ mouse model, revealing that ΔWD mice were still able to activate autophagy, denoted by the comparable levels of p62 and LC3-I/II in the ΔWD compared to littermate controls (Rai et al., 2019). Findings by Fletcher and colleagues determined that the absence of the WD domain in ATG16L1 does not interfere with the capability of the ΔWD mouse to fulfil autophagy (Fletcher et al., 2018). They uncovered a system where they used point mutations or truncations (e.g., ATG16L1 constructs lacking WIPI2b and FIP200 binding sites; Full length ATG16L1; ATG16L1 lacking WD domain) in ATG16L1, to examine whether cells become autophagy/LAP-deficient, or autophagy/LAP-competent. Moreover, Rossiter and co-workers determined that ATG7-deficient mice, defective for autophagy, showed weakened expression of LC3-I/II and p62, which reiterates that the N-terminal and CCD domain of ATG16L1 are essential for autophagic function and thus enables autophagic flux in the ΔWD mouse (Rossiter et al., 2013). The ΔWD mouse exhibits no signs of dermatological disorders and displayed a fully functioning skin barrier in this PhD work. This supports previously established findings that autophagy is actively occurring in the skin and is required for the healthy barrier function (Akinduro et al., 2016). Studies by Douroudis and others revealed that single nucleotide polymorphisms (rs10210302, rs12994971, rs2241880, rs2241879, rs7587633 and rs13005285) in *ATG16L1* increase the susceptibility to psoriasis vulgaris and palmoplantar pustulosis (Douroudis et al., 2011; Douroudis et al., 2012). Additionally, mouse models with keratinocyte-selective ATG16L1 deficiency exhibit a thickened cornified layer and enhanced tumour formation with increased p62 expression (Van Hove et al., 2023). Together, our results and those reported by others suggest that ATG16L1 autophagy is required for healthy skin barrier function (Douroudis et al., 2011; Douroudis et al., 2012; Van Hove et al., 2023).

6.2.2 Skin elastic properties exhibit an accelerated decline in aged ΔWD mice

In chapter 3, the skin of 2-month-old and 17-month-old WT and ΔWD mice was further assessed using a Cutometer MPA 580, a suction-based measurement method. Net elasticity and elastic recovery were measured across ages and genotypes, revealing that ΔWD mice exhibited signs of accelerated intrinsic ageing, indicated by a significant decrease in net elasticity and elastic recovery compared to controls. Fibroblasts play a crucial role in skin maintenance and healing by producing two types of collagens (type I and III) and elastin, with collagen being the primary source of support and mechanical integrity in skin (Everett and Sommers, 2013). Collagen fibres undergo significant age-related microstructural changes, along with other key extracellular components. Lynch and colleagues discovered that murine skin displays a 30% decrease in collagen content between 2 and 22 months of age (Lynch et al., 2017). Further research is necessary to determine whether the thinning of the dermal layer in ΔWD mice contributes to the decline in elastic properties, and whether ΔWD mice exhibit a reduction in ECM components, such as collagen, elastin or fibrillin or an accumulation of aged/apoptotic fibroblasts. Wang and co-workers demonstrated that LAP is active in control embryonic fibroblasts from the ΔWD mouse model (Wang et al., 2021). Control fibroblasts recruited LC3 to large endo-lysosomal vacuoles when LAP was induced by chloroquine, whereas ΔWD fibroblasts were unable to recruit LC3 to large vacuoles despite chloroquine treatment. Moreover, Martinez and colleagues showed that phagosomes in WT macrophages rapidly acidified and eliminated apoptotic fibroblasts within 2h of engulfment, whereas ATG7-deficient macrophages exhibited decreased lysosomal fusion and impaired degradation of dead fibroblasts (Martinez et al., 2011). A study by Tashiro and colleagues revealed that the number of autophagosomes increased in aged dermal fibroblasts and that autophagic flux was impaired at the degradation step in these aged fibroblasts (Tashiro et al., 2014). Further investigations into the dermal compartment of ΔWD mice is necessary to evaluate whether LAP is involved in this fibroblast turnover and if the accumulation of aged fibroblasts contributes to the observed decrease in elastic properties (Lynch et al., 2017; Tashiro et al., 2014).

6.2.3 Melanosomes are internalised and trafficked to the perinuclear area in a potentially autophagy driven process

In chapter 5, pigmentation dynamics in WT and ΔWD primary keratinocytes were assessed by immunofluorescence and live cell confocal microscopy. Transfected melanocytes produced OA1-mCherry tagged melanosomes, which were then added to LC3-GFP transduced WT and ΔWD primary keratinocytes. Over 24 hours, the OA1-mCherry melanosomes co-localised with LC3-GFP after 9 hours at the perinuclear region and subsequently co-localised with LysoTracker Blue, a lysosomal compartment marker, at 24 hours in both WT and ΔWD keratinocytes. In response to UV exposure, melanosomes are transported to neighbouring keratinocytes where they form a perinuclear cap to shield against UV radiation (Yang et al., 2018). Our results corroborate with previously established findings by Ando and co-workers, who demonstrated that melanosomes accumulate around the nucleus within 24 hours post phagocytosis (Ando et al., 2010). A study by Ebanks and colleagues showed that mature stage III and IV melanosomes were incorporated and trafficked to the perinuclear location in keratinocytes (Ebanks et al., 2011). The melanosomes showed ultrastructural disruption at 48 hours, exhibiting visible striations from the melanosome scaffolding and an amorphous shape, with further findings revealing minimal melanosomes in culture by 96 hours. It has been proposed that transferred melanosomes are sorted into LAMP1-positive late endosomes and then transported to the perinuclear region, where they are believed to be degraded in lysosomes (Fukuda, 2021; Murase et al., 2013; Neto et al., 2024). Findings from Hurbain and colleagues determined that melanosomes in keratinocytes showed a greater expression of LAMP1 staining, with no LC3A expression in the melanosome cluster (Hurbain et al., 2018). They proposed that this was due to the mode of transfer rather than the degradative feature. These findings contradict my observations, where I noted co-localisation of LAMP1 and LC3 in areas of OA1-mCherry melanosomes. Moreover, my live cell imaging demonstrated that melanosome clusters co-localise with acidic compartments, as shown by the association with LysoTracker, which exhibits LC3 expression. Similar findings were reported by Correia and colleagues who found that 20% of their melanocores associated with LysoTracker in XB-2 keratinocytes, suggesting that melanocores reside in compartments with moderate acidification and poor hydrolytic capacity, permitting melanin to be preserved for long periods (Correia et al., 2018; Neto et al., 2024).

It has been proposed that autophagy is involved in the trafficking of melanosomes out of the melanocytes. Ramkumar and co-workers established that LC3B knockdown resulted in perinuclear distribution of melanosomes in melanocytes, and thus was required for mobilisation of melanosomes on microtubule tracks (Ramkumar et al., 2017). This LC3B however was not transferred along with the melanosome to adjacent keratinocytes but was disengaged from the melanosome by ATG4. The activity of autophagy in murine melanocytes was previously confirmed by Zhang and colleagues, who showed high levels of LC3-II in murine melanocytes (Zhang et al., 2015). Additionally, they generated ATG7 f/f Tyr::Cre mice, which were deficient for ATG7 and exhibited less pigmentation in their tail and coat compared to ATG7 f/f control mice. They concluded that melanocytes required ATG7-dependent autophagy to achieve full pigmentation of the hair and epidermis yet stated that melanogenesis can still occur in the absence of autophagy. Building on these findings, studies by Murase and co-workers established that autophagic activity is involved in skin pigmentation, with autophagic activity being higher in Caucasian keratinocytes compared to African American keratinocytes (Murase et al., 2013; Murase et al., 2020). They determined that melanosomes could be degraded in a lysosome-dependent manner in keratinocytes, shown by incubation with lysosome inhibitors (e.g., pepstatin A), which increased cellular melanin content and enhanced accumulation of melanosomes (Murase et al., 2013). A study by Homma and co-workers exhibited similar findings when examining skin tissue with hyperpigmentation (Homma et al., 2018). They revealed that cathepsin V, a cysteine protease in lysosomes, was marginally expressed in dark skin compared to light skin and halted melanosome degradation when it was suppressed. Murase and colleagues also reported that melanosomes were labelled with LC3 when human keratinocytes were co-cultured with human melanocytes, hinting at a sequestration of melanosomes by autophagosomes. This supports the observations made in my study that LC3 was co-localised to melanosome membranes in both WT and ∆WD primary keratinocytes and was subsequently co-localised with LysoTracker blue. Results provide an indication that melanosome degradation in the ATG16L1 mouse model is not driven by LAP but rather by ATG16L1-dependent autophagy.

Knowing that autophagy is involved in this melanosome degradation process and has exhibited roles in skin pigmentation, research has found that by exploiting autophagy inducers, hyperpigmentation disorders could be treated. Kim and co-workers discovered an autophagy-regulating peptide, called PTPD-12, which following treatment in primary human epidermal keratinocytes significantly upregulated autophagy proteins (e.g., LC3-II and p62) and resulted in more melanosomes being degraded in autophagic vacuoles, which they had determined by transmission electron microscopy (Kim et al., 2020). They tested this autophagy-regulating peptide in *ex vivo* and 3D skin and determined a decline in melanin content with an increase in autophagic activity. Autophagy inducers and inhibitors have proven useful in the fight against skin cancers, as autophagy aids in tumour cell survival (Ali et al., 2024). Consequently, using an autophagy inhibitor presents a promising treatment approach in skin cancer. The use of natural compounds such as curcumin, α-mangostin, and reseveratrol function as autophagy inducers in skin cancers, by targeting the PI3K/Akt/mTOR pathway (Zhao et al., 2016). Other natural compounds induce autophagy by accumulating ROS or by increasing the expression of ATGs. Similarly, synthetic and semisynthetic compounds (e.g., ibrutinib, protoapigenone) are used to induce autophagy in skin cancer (Ali et al., 2024). Chloroquine, a lysosomal autophagy inhibitor, has demonstrated the ability to kill melanoma cells in an autophagy-independent manner (Xu et al., 2018). Overall, the findings support a favourable therapeutic approach by modulating autophagic function, either by induction or inhibition, in the treatment of hypo/and hyper pigmentary disorders as well as skin cancer.

6.3 Final conclusions & future work

This thesis investigated skin barrier integrity, function, and pigmentation dynamics in keratinocytes derived from LAP-deficient mice, employing live-cell imaging analysis, immunofluorescence, and various biochemical and histological techniques. Histological analysis of the ∆WD mouse revealed a skin phenotype comparable to that of WT littermate controls. The ∆WD mouse exhibited an intact skin barrier, evidenced by similar expression levels of key differentiation and autophagy proteins, and the absence of toluidine blue dye retention in embryonic skin. The findings indicate that ∆WD mice experience age-related deterioration in dermal biomechanics. Additionally, I provided insights into the melanosomal dynamics in LAP-deficient primary keratinocytes, suggesting that melanosomes are degraded through an autophagy-driven process in both primary WT and ∆WD keratinocytes.

The findings from this thesis supported previous research indicating that autophagy plays a role in the keratinisation of the epidermis and the degradation of melanosomes in keratinocytes. This work introduced a unique method to evaluate the function of LAP in skin homeostasis and pigmentation by utilising the ATG16L1$^{\Delta WD}$ mouse model. I have validated that using an OA1-mCherry reporter, it is possible to label mature melanosomes in live cell imaging experiments. This will enable future research to examine the fate of melanosomes following their uptake in keratinocytes, and determine whether early LAP events occur after melanosome ingestion by the keratinocyte.

Overall, the ∆WD mouse model remains a unique tool for distinguishing between autophagy and LAP, and it should be further utilised to assess dermal biomechanics and early pigmentation dynamics. As previously discussed, the phenotype of ∆WD mice could be mimicked in human keratinocytes, by employing CRISPR technologies or by utilising inhibitors to knock-down LAP activity in cell lines. By enhancing our understanding of LAP function in skin and pigmentation, this research offers new insights into potential strategies and therapeutics for the treatment of dermatological disorders.

Chapter 7: References

ADEREM, A. 2003. Phagocytosis and the inflammatory response. *J Infect Dis,* 187 Suppl 2**,** S340-5.

AHISHALI, B. & KAYA, M. 2021. Evaluation of Blood-Brain Barrier Integrity Using Vascular Permeability Markers: Evans Blue, Sodium Fluorescein, Albumin-Alexa Fluor Conjugates, and Horseradish Peroxidase. *In:* TURKSEN, K. (ed.) *Permeability Barrier: Methods and Protocols.* New York, NY: Springer US.

AHN, S. K., HWANG, S. M., JIANG, S. J., CHOI, E. H. & LEE, S. H. 1999. The changes of epidermal calcium gradient and transitional cells after prolonged occlusion following tape stripping in the murine epidermis. *J Invest Dermatol,* 113**,** 189-95.

AKINDURO, O., SULLY, K., PATEL, A., ROBINSON, D. J., CHIKH, A., MCPHAIL, G., BRAUN, K. M., PHILPOTT, M. P., HARWOOD, C. A., BYRNE, C., O'SHAUGHNESSY, R. F. L. & BERGAMASCHI, D. 2016. Constitutive Autophagy and Nucleophagy during Epidermal Differentiation. *J Invest Dermatol,* 136**,** 1460-1470.

AKOUMIANAKI, T., KYRMIZI, I., VALSECCHI, I., GRESNIGT, MARK S., SAMONIS, G., DRAKOS, E., BOUMPAS, D., MUSZKIETA, L., PREVOST, M.-C., KONTOYIANNIS, DIMITRIOS P., CHAVAKIS, T., NETEA, MIHAI G., VAN DE VEERDONK, FRANK L., BRAKHAGE, AXEL A., EL-BENNA, J., BEAUVAIS, A., LATGE, J.-P. & CHAMILOS, G. 2016. Aspergillus Cell Wall Melanin Blocks LC3-Associated Phagocytosis to Promote Pathogenicity. *Cell Host & Microbe,* 19**,** 79-90.

ALEXANDER, C. M., KASZA, I., YEN, C. L. E., REEDER, S. B., HERNANDO, D., GALLO, R. L., JAHODA, C. A. B., HORSLEY, V. & MACDOUGALD, O. A. 2015. Dermal white adipose tissue: a new component of the thermogenic response. *Journal of Lipid Research,* 56**,** 2061-2069.

ALI, L., ROKY, A. H., AZAD, A. K., SHAIKAT, A. H., MEEM, J. N., HOQUE, E., AHASAN, A. M. F., ISLAM, M. M., ARIF, S. R., MOSTAQ, S., MAHMUD, Z., AMIN, M. N. & MAHMUD, A. 2024. Autophagy as a targeted therapeutic approach for skin cancer: Evaluating natural and synthetic molecular interventions. *Cancer Pathogenesis and Therapy*.

ALI, N., HOSSEINI, M., VAINIO, S., TAÏEB, A., CARIO-ANDRÉ, M. & REZVANI, H. R. 2015. Skin equivalents: skin from reconstructions as models to study skin development and diseases. *British Journal of Dermatology,* 173**,** 391-403.

ALONSO, L. & FUCHS, E. 2003. Stem cells of the skin epithelium. *Proceedings of the National Academy of Sciences,* 100**,** 11830-11835.

ANDL, T., REDDY, S. T., GADDAPARA, T. & MILLAR, S. E. 2002. WNT signals are required for the initiation of hair follicle development. *Dev Cell,* 2**,** 643-53.

ANDO, H., NIKI, Y., ITO, M., AKIYAMA, K., MATSUI, M. S., YAROSH, D. B. & ICHIHASHI, M. 2012. Melanosomes are transferred from melanocytes to keratinocytes through the processes of packaging, release, uptake, and dispersion. *Journal of Investigative Dermatology,* 132**,** 1222-1229.

ANSARY, T. M., HOSSAIN, M. R., KAMIYA, K., KOMINE, M. & OHTSUKI, M. 2021. Inflammatory Molecules Associated with Ultraviolet Radiation-Mediated Skin Aging. *International Journal of Molecular Sciences* [Online], 22.

ARASTEH, J.M (2012). *Generation of mouse models to study the role of Atg16L1 in inflammatory bowel disease (IBD).* Ph.D. thesis. University of East Anglia.

ASARE, P. F., ROSCIOLI, E., HURTADO, P. R., TRAN, H. B., MAH, C. Y. & HODGE, S. 2020. LC3-Associated Phagocytosis (LAP): A Potentially Influential Mediator of Efferocytosis-Related Tumor Progression and Aggressiveness. *Frontiers in Oncology,* 10.

BABIARZ-MAGEE, L., CHEN, N., SEIBERG, M. & LIN, C. B. 2004. The Expression and Activation of Protease-Activated Receptor-2 Correlate with Skin Color. *Pigment Cell Research,* 17**,** 241-251.

BAHRI, O. A., NALDAIZ-GASTESI, N., KENNEDY, D. C., WHEATLEY, A. M., IZETA, A. & MCCULLAGH, K. J. A. 2019. The panniculus carnosus muscle: A novel model of striated muscle regeneration that exhibits sex differences in the mdx mouse. *Scientific Reports,* 9**,** 15964.

BAKER, P., HUANG, C., RADI, R., MOLL, S. B., JULES, E. & ARBISER, J. L. 2023. Skin Barrier Function: The Interplay of Physical, Chemical, and Immunologic Properties. *Cells,* 12**,** 2745.

BAZZI, H., FANTAUZZO, K. A., RICHARDSON, G. D., JAHODA, C. A. B. & CHRISTIANO, A. M. 2007. Transcriptional profiling of developing mouse epidermis reveals novel patterns of coordinated gene expression. *Developmental Dynamics,* 236**,** 961-970.

BEALE, R., WISE, H., STUART, A., RAVENHILL, BENJAMIN J., DIGARD, P. & RANDOW, F. 2014. A LC3-Interacting Motif in the Influenza A Virus M2 Protein Is Required to Subvert Autophagy and Maintain Virion Stability. *Cell Host & Microbe,* 15**,** 239-247.

BEDELL, M. A., JENKINS, N. A. & COPELAND, N. G. 1997. Mouse models of human disease. Part I: techniques and resources for genetic analysis in mice. *Genes & Development,* 11**,** 1-10.

BELLEUDI, F., PURPURA, V., SCROFANI, C., PERSECHINO, F., LEONE, L. & TORRISI, M. R. 2011. Expression and signaling of the tyrosine kinase FGFR2b/KGFR regulates phagocytosis and melanosome uptake in human keratinocytes. *The FASEB Journal,* 25**,** 170-181.

BENITO-MARTÍNEZ, S., SALAVESSA, L., RAPOSO, G., MARKS, M. S. & DELEVOYE, C. 2021. Melanin Transfer and Fate within Keratinocytes in Human Skin Pigmentation. *Integr Comp Biol,* 61**,** 1546-1555.

BENTO-LOPES, L., CABAÇO, L. C., CHARNECA, J., NETO, M. V., SEABRA, M. C. & BARRAL, D. C. 2023. Melanin's Journey from Melanocytes to Keratinocytes: Uncovering the Molecular Mechanisms of Melanin Transfer and Processing. *International Journal of Molecular Sciences,* 24**,** 11289.

BERGHOLT, N. L., LYSDAHL, H., LIND, M. & FOLDAGER, C. B. 2019. A Standardized Method of Applying Toluidine Blue Metachromatic Staining for Assessment of Chondrogenesis. *Cartilage,* 10**,** 370-374.

BIKLE, D. D., XIE, Z. & TU, C. L. 2012. Calcium regulation of keratinocyte differentiation. *Expert Rev Endocrinol Metab,* 7**,** 461-472.

BREITKREUTZ, D., KOXHOLT, I., THIEMANN, K. & NISCHT, R. 2013. Skin basement membrane: the foundation of epidermal integrity--BM functions and diverse roles of bridging molecules nidogen and perlecan. *Biomed Res Int,* 2013**,** 179784.

BROHEM, C. A., DA SILVA CARDEAL, L. B., TIAGO, M., SOENGAS, M. S., DE MORAES BARROS, S. B. & MARIA-ENGLER, S. S. 2011. Artificial skin in perspective: Concepts and applications. *Pigment Cell and Melanoma Research,* 24**,** 35-50.

BRUDER, J. M., PFEIFFER, Z. A., CIRIELLO, J. M., HORRIGAN, D. M., WICKS, N. L., FLAHERTY, B. & OANCEA, E. 2012. Melanosomal Dynamics Assessed with a Live-Cell Fluorescent Melanosomal Marker. *PLOS ONE,* 7**,** e43465.

BURGOYNE, T., JOLLY, R., MARTIN-MARTIN, B., SEABRA, M. C., PICCIRILLO, R., SCHIAFFINO, M. V. & FUTTER, C. E. 2013. Expression of OA1 limits the fusion of a subset of MVBs with lysosomes – a mechanism potentially involved in the initial biogenesis of melanosomes. *Journal of Cell Science,* 126**,** 5143-5152.

CALABRO, K., CURTIS, A., GALARNEAU, J.-R., KRUCKER, T. & BIGIO, I. 2011. Gender variations in the optical properties of skin in murine animal models. *Journal of biomedical optics,* 16**,** 011008.

CANDI, E., SCHMIDT, R. & MELINO, G. 2005. The cornified envelope: A model of cell death in the skin. *Nature Reviews Molecular Cell Biology,* 6**,** 328-340.

CHAMILOS, G., AKOUMIANAKI, T., KYRMIZI, I., BRAKHAGE, A., BEAUVAIS, A. & LATGE, J.-P. 2016. Melanin targets LC3-associated phagocytosis (LAP): A novel pathogenetic mechanism in fungal disease. *Autophagy,* 12**,** 888-889.

CHEN, J. & ROOP, D. R. 2008. Genetically engineered mouse models for skin research: taking the next step. *J Dermatol Sci,* 52**,** 1-12.

CHEN, T., WANG, H., LIU, Y., ZHAO, B., ZHAO, Y., FAN, R., WANG, P. & DONG, C. 2016. Ocular Albinism Type 1 Regulates Melanogenesis in Mouse Melanocytes. *Int J Mol Sci,* 17.

CHINWALLA, A. T., COOK, L. L., DELEHAUNTY, K. D., FEWELL, G. A., FULTON, L. A., FULTON, R. S., GRAVES, T. A., HILLIER, L. W., MARDIS, E. R., MCPHERSON, J. D., MINER, T. L., NASH, W. E., NELSON, J. O., NHAN, M. N., PEPIN, K. H., POHL, C. S., PONCE, T. C., SCHULTZ, B., THOMPSON, J., TREVASKIS, E., WATERSTON, R. H., WENDL, M. C., WILSON, R. K., YANG, S.-P., AN, P., BERRY, E., BIRREN, B., BLOOM, T., BROWN, D. G., BUTLER, J., DALY, M., DAVID, R., DERI, J., DODGE, S., FOLEY, K., GAGE, D., GNERRE, S., HOLZER, T., JAFFE, D. B., KAMAL, M., KARLSSON, E. K., KELLS, C., KIRBY, A., KULBOKAS, E. J., LANDER, E. S., LANDERS, T., LEGER, J. P., LEVINE, R., LINDBLAD-TOH, K., MAUCELI, E., MAYER, J. H., MCCARTHY, M., MELDRIM, J., MELDRIM, J., MESIROV, J. P., NICOL, R., NUSBAUM, C., SEAMAN, S., SHARPE, T., SHERIDAN, A., SINGER, J. B., SANTOS, R., SPENCER, B., STANGE-THOMANN, N., VINSON, J. P., WADE, C. M., WIERZBOWSKI, J., WYMAN, D., ZODY, M. C., BIRNEY, E., GOLDMAN, N., KASPRZYK, A., MONGIN, E., RUST, A. G., SLATER, G., STABENAU, A., URETA-VIDAL, A., WHELAN, S., AINSCOUGH, R., ATTWOOD, J., BAILEY, J., BARLOW, K., BECK, S., BURTON, J., CLAMP, M., CLEE, C., COULSON, A., CUFF, J., CURWEN, V., CUTTS, T., DAVIES, J.,

EYRAS, E., GRAFHAM, D., GREGORY, S., HUBBARD, T., HUNT, A., JONES, M., JOY, A., LEONARD, S., LLOYD, C., et al. 2002. Initial sequencing and comparative analysis of the mouse genome. *Nature,* 420**,** 520-562.

CONWAY, S., JEFFERSON, M., WARREN, D. T., WILEMAN, T. & MORRIS, C. J. 2024. The WD Domain of Atg16l1 Crucial for LC3-Associated Phagocytosis Is Not Required for Preserving Skin Barrier Function in Mice. *JID Innovations,* 4.

CORREIA, M. S., MOREIRAS, H., PEREIRA, F. J. C., NETO, M. V., FESTAS, T. C., TARAFDER, A. K., RAMALHO, J. S., SEABRA, M. C. & BARRAL, D. C. 2018. Melanin Transferred to Keratinocytes Resides in Nondegradative Endocytic Compartments. *Journal of Investigative Dermatology,* 138**,** 637-646.

CUNHA, L. D., YANG, M., CARTER, R., GUY, C., HARRIS, L., CRAWFORD, J. C., QUARATO, G., BOADA-ROMERO, E., KALKAVAN, H., JOHNSON, M. D. L., NATARAJAN, S., TURNIS, M. E., FINKELSTEIN, D., OPFERMAN, J. T., GAWAD, C. & GREEN, D. R. 2018. LC3-Associated Phagocytosis in Myeloid Cells Promotes Tumor Immune Tolerance. *Cell,* 175**,** 429-441.e16.

D'ISCHIA, M., WAKAMATSU, K., CICOIRA, F., DI MAURO, E., GARCIA-BORRON, J. C., COMMO, S., GALVÁN, I., GHANEM, G., KENZO, K., MEREDITH, P., PEZZELLA, A., SANTATO, C., SARNA, T., SIMON, J. D., ZECCA, L., ZUCCA, F. A., NAPOLITANO, A. & ITO, S. 2015. Melanins and melanogenesis: From pigment cells to human health and technological applications. *Pigment Cell and Melanoma Research,* 28**,** 520-544.

D’MELLO, S. A. N., FINLAY, G. J., BAGULEY, B. C. & ASKARIAN-AMIRI, M. E. 2016. Signaling pathways in melanogenesis. *International Journal of Molecular Sciences,* 17.

DAMEN, M., WIRTZ, L., SOROKA, E., KHATIF, H., KUKAT, C., SIMONS, B. D. & BAZZI, H. 2021. High proliferation and delamination during skin epidermal stratification. *Nature Communications,* 12**,** 3227.

DE ARAÚJO, R., LÔBO, M., TRINDADE, K., SILVA, DARIZY F. & PEREIRA, N. 2019. Fibroblast Growth Factors: A Controlling Mechanism of Skin Aging. *Skin Pharmacology and Physiology,* 32**,** 275-282.

DECKERS, J., HAMMAD, H. & HOSTE, E. 2018. Langerhans cells: Sensing the environment in health and disease. *Frontiers in Immunology,* 9.

DEEDRICK, D. & KOCH, S. 2004. Microscopy of Hair Part II: A Practical Guide and Manual for Animal Hairs. *Forensic Science Communications,* 6.

DELEVOYE, C., MARKS, M. S. & RAPOSO, G. 2019. Lysosome-related organelles as functional adaptations of the endolysosomal system. *Current Opinion in Cell Biology,* 59**,** 147-158.

DELL'ANGELICA, E., MULLINS, C., CAPLAN, S. & BONIFACINO, J. 2000. Lysosome-related organelles. *FASEB journal: official publication of the Federation of American Societies for Experimental Biology,* 14**,** 1265-78.

DELLAMBRA, E., ODORISIO, T., D'ARCANGELO, D., FAILLA, C. M. & FACCHIANO, A. 2019. Non-animal models in dermatological research. *Altex,* 36**,** 177-202.

DEMIROVIC, D., NIZARD, C. & RATTAN, S. I. S. 2015. Basal Level of Autophagy Is Increased in Aging Human Skin Fibroblasts In Vitro, but Not in Old Skin. *PLOS ONE,* 10**,** e0126546.

DING, X., BLOCH, W., IDEN, S., RÜEGG, M., HALL, M., LEPTIN, M., PARTRIDGE, L. & EMING, S. 2016. mTORC1 and mTORC2 regulate skin morphogenesis and epidermal barrier formation. *Nature Communications,* 7**,** 13226.

DOMINGUES, L., HURBAIN, I., GILLES-MARSENS, F., SIRÉS-CAMPOS, J., ANDRÉ, N., DEWULF, M., ROMAO, M., VIARIS DE LESEGNO, C., MACÉ, A. S., BLOUIN, C., GUÉRÉ, C., VIÉ, K., RAPOSO, G., LAMAZE, C. & DELEVOYE, C. 2020. Coupling of melanocyte signaling and mechanics by caveolae is required for human skin pigmentation. *Nature Communications,* 11.

DOUROUDIS, K., KINGO, K., TRAKS, T., RÄTSEP, R., SILM, H., VASAR, E. & KÕKS, S. 2011. ATG16L1 gene polymorphisms are associated with palmoplantar pustulosis. *Human Immunology,* 72**,** 613-615.

DOUROUDIS, K., KINGO, K., TRAKS, T., REIMANN, E., RAUD, K., RÄTSEP, R., MÖSSNE, R., SILM, H., VASAR, E. & KÕKS, S. 2012. Polymorphisms in the ATG16L1 Gene are Associated with Psoriasis Vulgaris. *Acta dermato-venereologica,* 92**,** 85-7.

DRAAIJERS, L. J., BOTMAN, Y. A. M., TEMPELMAN, F. R. H., KREIS, R. W., MIDDELKOOP, E. & VAN ZUIJLEN, P. P. M. 2004. Skin elasticity meter or subjective evaluation in scars: a reliability assessment. *Burns,* 30**,** 109-114.

EBANKS, J. P., KOSHOFFER, A., WICKETT, R. R., SCHWEMBERGER, S., BABCOCK, G., HAKOZAKI, T. & BOISSY, R. E. 2011. Epidermal Keratinocytes from Light vs. Dark Skin Exhibit Differential Degradation of Melanosomes. *Journal of Investigative Dermatology,* 131**,** 1226-1233.

ECKERT, R. L. & RORKE, E. A. 1989. Molecular biology of keratinocyte differentiation. *Environmental Health Perspectives,* 80**,** 109-116.

ECKHART, L., DECLERCQ, W., BAN, J., RENDL, M., LENGAUER, B., MAYER, C., LIPPENS, S., VANDENABEELE, P. & TSCHACHLER, E. 2000. Terminal differentiation of human keratinocytes and stratum corneum formation is associated with caspase-14 activation. *Journal of Investigative Dermatology,* 115**,** 1148-1151.

ELSHOLZ, F., HARTENECK, C., MULLER, W. & FRIEDLAND, K. 2014. Calcium--a central regulator of keratinocyte differentiation in health and disease. *Eur J Dermatol,* 24**,** 650-61.

EVERETT, J. S. & SOMMERS, M. S. 2013. Skin viscoelasticity: physiologic mechanisms, measurement issues, and application to nursing science. *Biol Res Nurs,* 15**,** 338-46.

FALLETTA, P., BAGNATO, P., BONO, M., MONTICONE, M., SCHIAFFINO, M. V., BENNETT, D. C., GODING, C. R., TACCHETTI, C. & VALETTI, C. 2014. Melanosome-autonomous regulation of size and number: the OA1 receptor sustains PMEL expression. *Pigment Cell & Melanoma Research,* 27**,** 565-579.

FEINGOLD, K. R. 2012. Lamellar bodies: The key to cutaneous barrier function. *Journal of Investigative Dermatology,* 132**,** 1951-1953.

FLETCHER, K., ULFERTS, R., JACQUIN, E., VEITH, T., GAMMOH, N., ARASTEH, J. M., MAYER, U., CARDING, S. R., WILEMAN, T., BEALE, R. & FLOREY, O. 2018. The WD40 domain of ATG16L1 is required for its non-canonical role in lipidation of LC3 at single membranes. *Embo j,* 37.

FORNI, M. F., TROMBETTA-LIMA, M. & SOGAYAR, M. C. 2012. Stem cells in embryonic skin development. *Biological research,* 45 3**,** 215-22.

FRANTZ, C., STEWART, K. M. & WEAVER, V. M. 2010. The extracellular matrix at a glance. *Journal of Cell Science,* 123**,** 4195-4200.

FUCHS, E. 2007. Scratching the surface of skin development. *Nature,* 445**,** 834-842.

FUCHS, E. & GREEN, H. 1980. Changes in keratin gene expression during terminal differentiation of the keratinocyte. *Cell,* 19**,** 1033-42.

FUCHS, E. & HORSLEY, V. 2008. More than one way to skin. *Genes & Development,* 22**,** 976-985.

FUKUDA, M. 2021. Rab GTPases: Key players in melanosome biogenesis, transport, and transfer. *Pigment Cell & Melanoma Research,* 34**,** 222-235.

FUTTER, C. E., RAMALHO, J. S., JAISSLE, G. B., SEELIGER, M. W. & SEABRA, M. C. 2004a. The Role of Rab27a in the Regulation of Melanosome Distribution within Retinal Pigment Epithelial Cells. *Molecular Biology of the Cell,* 15**,** 2264-2275.

GAMMOH, N. 2021. The multifaceted functions of ATG16L1 in autophagy and related processes. *Journal of Cell Science,* 133.

GANESAN, A. K., HO, H., BODEMANN, B., PETERSEN, S., ARURI, J., KOSHY, S., RICHARDSON, Z., LE, L. Q., KRASIEVA, T., ROTH, M. G., FARMER, P. & WHITE, M. A. 2008. Genome-Wide siRNA-Based Functional Genomics of Pigmentation Identifies Novel Genes and Pathways That Impact Melanogenesis in Human Cells. *PLOS Genetics,* 4**,** e1000298.

GATSEVA, A., SIN, Y. Y., BREZZO, G. & VAN AGTMAEL, T. 2019. Basement membrane collagens and disease mechanisms. *Essays Biochem,* 63**,** 297-312.

GERBER, P. A., BUHREN, B. A., SCHRUMPF, H., HOMEY, B., ZLOTNIK, A. & HEVEZI, P. 2014. The top skin-associated genes: a comparative analysis of human and mouse skin transcriptomes. *Biol Chem,* 395**,** 577-91.

GHETTI, M., TOPOUZI, H., THEOCHARIDIS, G., PAPA, V., WILLIAMS, G., BONDIOLI, E., CENACCHI, G., CONNELLY, J. T. & HIGGINS, C. A. 2018. Subpopulations of dermal skin fibroblasts secrete distinct extracellular matrix: implications for using skin substitutes in the clinic. *British Journal of Dermatology,* 179**,** 381-393.

GIORDANO, F., BONETTI, C., SURACE, E. M., MARIGO, V. & RAPOSO, G. 2009. The ocular albinism type 1 (OA1) G-protein-coupled receptor functions with MART-1 at early stages of melanogenesis to control melanosome identity and composition. *Human Molecular Genetics,* 18**,** 4530-4545.

GONÇALVES, S. M., DUARTE-OLIVEIRA, C., CAMPOS, C. F., AIMANIANDA, V., TER HORST, R., LEITE, L., MERCIER, T., PEREIRA, P., FERNÁNDEZ-GARCÍA, M., ANTUNES, D., RODRIGUES, C. S., BARBOSA-MATOS, C., GAIFEM, J., MESQUITA, I., MARQUES, A., OSÓRIO, N. S., TORRADO, E., RODRIGUES, F., COSTA, S., JOOSTEN, L. A. B., LAGROU, K., MAERTENS, J., LACERDA, J. F., CAMPOS, A., BROWN, G. D., BRAKHAGE, A. A., BARBAS, C., SILVESTRE, R., VAN DE VEERDONK, F. L., CHAMILOS, G., NETEA, M. G., LATGÉ, J.-P., CUNHA, C. & CARVALHO, A. 2020. Phagosomal removal of fungal melanin reprograms macrophage metabolism to promote antifungal immunity. *Nature Communications,* 11**,** 2282.

GREEN, K. J., JAIGANESH, A. & BROUSSARD, J. A. 2019. Desmosomes: Essential contributors to an integrated intercellular junction network. *F1000Res,* 8.

GRIJMANS, B. J. M., VAN DER KOOIJ, S. B., VARELA, M. & MEIJER, A. H. 2022. LAPped in Proof: LC3-Associated Phagocytosis and the Arms Race Against Bacterial Pathogens. *Frontiers in Cellular and Infection Microbiology,* 11.

GROSS, S. P., TUMA, M. C., DEACON, S. W., SERPINSKAYA, A. S., REILEIN, A. R. & GELFAND, V. I. 2002. Interactions and regulation of molecular motors in Xenopus melanophores. *J Cell Biol,* 156**,** 855-65.

GU, Y., HAN, J., JIANG, C. & ZHANG, Y. 2020. Biomarkers, oxidative stress and autophagy in skin aging. *Ageing Research Reviews,* 59**,** 101036.

GUDJONSSON, J., JOHNSTON, A., DYSON, M., VALDIMARSSON, H. & ELDER, J. 2007. Mouse Models of Psoriasis. *The Journal of investigative dermatology,* 127**,** 1292-308.

HAGER, B., FLECKMAN, P. & BICKENBACH, J. R. 1999. Long-Term Culture of Murine Epidermal Keratinocytes. *Journal of Investigative Dermatology,* 112**,** 971-976.

HAMPE, J., FRANKE, A., ROSENSTIEL, P., TILL, A., TEUBER, M., HUSE, K., ALBRECHT, M., MAYR, G., DE LA VEGA, F. M., BRIGGS, J., GÜNTHER, S., PRESCOTT, N. J., ONNIE, C. M., HÄSLER, R., SIPOS, B., FÖLSCH, U. R., LENGAUER, T., PLATZER, M., MATHEW, C. G., KRAWCZAK, M. & SCHREIBER, S. 2007. A genome-wide association scan of nonsynonymous SNPs identifies a susceptibility variant for Crohn disease in ATG16L1. *Nature Genetics,* 39**,** 207-211.

HARUNA, K., SUGA, Y., MURAMATSU, S., TANEDA, K., MIZUNO, Y., IKEDA, S., UENO, T., KOMINAMI, E., TANIDA, I., TANIDA, I. & HANADA, K. 2008. Differentiation-specific expression and localization of an autophagosomal marker protein (LC3) in human epidermal keratinocytes. *Journal of Dermatological Science,* 52**,** 213-215.

HARVIMA, I. T. & NILSSON, G. 2011. Mast cells as regulators of skin inflammation and immunity. *Acta dermato-venereologica,* 91**,** 644-650.

HECKMANN, B., TEUBNER, B., BOADA-ROMERO, E., TUMMERS, B., GUY, C., FITZGERALD, P., MAYER, U., CARDING, S., ZAKHARENKO, S., WILEMAN, T. & GREEN, D. 2020. Noncanonical function of an autophagy protein prevents spontaneous Alzheimer's disease. *Science Advances,* 6**,** eabb9036.

HECKMANN, B. L., BOADA-ROMERO, E., CUNHA, L. D., MAGNE, J. & GREEN, D. R. 2017. LC3-Associated Phagocytosis and Inflammation. *Journal of Molecular Biology,* 429**,** 3561-3576.

HENNINGS, H., MICHAEL, D., CHENG, C., STEINERT, P., HOLBROOK, K. & YUSPA, S. H. 1980. Calcium regulation of growth and differentiation of mouse epidermal cells in culture. *Cell,* 19**,** 245-254.

HERB, M., GLUSCHKO, A. & SCHRAMM, M. 2020. LC3-associated phagocytosis - The highway to hell for phagocytosed microbes. *Seminars in Cell and Developmental Biology,* 101**,** 68-76.

HIDA, T., KAMIYA, T., KAWAKAMI, A., OGINO, J., SOHMA, H., UHARA, H. & JIMBOW, K. 2020. Elucidation of Melanogenesis Cascade for Identifying Pathophysiology and Therapeutic Approach of Pigmentary Disorders and Melanoma. *Int J Mol Sci,* 21.

HIROBE, T. 1995. Structure and function of melanocytes: Microscopic morphology and cell biology of mouse melanocytes in the epidermis and hair follicle. *Histology and histopathology,* 10**,** 223-37.

HIROBE, T. 2014. Keratinocytes regulate the function of melanocytes. *Dermatologica Sinica,* 32**,** 200-204.

HO, H., KAPADIA, R., AL-TAHAN, S., AHMAD, S. & GANESAN, A. K. 2011. WIPI1 Coordinates Melanogenic Gene Transcription and Melanosome Formation via TORC1 Inhibition . *Journal of Biological Chemistry,* 286**,** 12509-12523.

HOMMA, T., KAGEYAMA, S., NISHIKAWA, A. & NAGATA, K. 2018. Melanosome degradation in epidermal keratinocytes related to lysosomal protease cathepsin V. *Biochemical and Biophysical Research Communications,* 500**,** 339-343.

HOOPER, K. M., JACQUIN, E., LI, T., GOODWIN, J. M., BRUMELL, J. H., DURGAN, J. & FLOREY, O. 2022. V-ATPase is a universal regulator of LC3-associated phagocytosis and non-canonical autophagy. *J Cell Biol,* 221.

HOSSAIN, M. R., KIMURA-SASHIKAWA, M. & KOMINE, M. 2022. Genetic Abnormalities, Melanosomal Transfer, and Degradation inside Keratinocytes Affect Skin Pigmentation. *Keratinocyte Biology-Structure and Function in the Epidermis.* IntechOpen.

HOUSCHYAR, KHOSROW S., BORRELLI, MIMI R., TAPKING, C., POPP, D., PULADI, B., OOMS, M., CHELLIAH, MALCOLM P., REIN, S., PFÖRRINGER, D., THOR, D., REUMUTH, G., WALLNER, C., BRANSKI, LUDWIK K., SIEMERS, F., GRIEB, G., LEHNHARDT, M., YAZDI, AMIR S., MAAN, ZESHAAN N. & DUSCHER, D. 2020. Molecular Mechanisms of Hair Growth and Regeneration: Current Understanding and Novel Paradigms. *Dermatology,* 236**,** 271-280.

HU, M. S., BORRELLI, M. R., HONG, W. X., MALHOTRA, S., CHEUNG, A. T. M., RANSOM, R. C., RENNERT, R. C., MORRISON, S. D., LORENZ, H. P. & LONGAKER, M. T. 2018. Embryonic skin development and repair. *Organogenesis,* 14**,** 46-63.

HUANG, Y.-C., WANG, T.-W., SUN, J.-S. & LIN, F.-H. 2006. Effect of calcium ion concentration on keratinocyte behavior in the defined media. *Biomedical Engineering-applications Basis Communications - BIOMED ENG-APPL BASIS COMMUN,* 18.

HUME, A. N., COLLINSON, L. M., RAPAK, A., GOMES, A. Q., HOPKINS, C. R. & SEABRA, M. C. 2001. Rab27a Regulates the Peripheral Distribution of Melanosomes in Melanocytes. *Journal of Cell Biology,* 152**,** 795-808.

HURBAIN, I., ROMAO, M., SEXTIUS, P., BOURREAU, E., MARCHAL, C., BERNERD, F., DUVAL, C. & RAPOSO, G. 2018. Melanosome Distribution in Keratinocytes in Different Skin Types: Melanosome Clusters Are Not Degradative Organelles. *Journal of Investigative Dermatology,* 138**,** 647-656.

JACOB, T., ANNUSVER, K., CZARNEWSKI, P., DALESSANDRI, T., KALK, C., LEVRA LEVRON, C., CAMPAMÀ SANZ, N., KASTRITI, M. E., MIKKOLA, M. L., RENDL, M., LICHTENBERGER, B. M., DONATI, G., BJÖRKLUND, Å. K. & KASPER, M. 2023. Molecular and spatial landmarks of early mouse skin development. *Developmental Cell,* 58**,** 2140-2162.e5.

JEONG, D., QOMALADEWI, N. P., LEE, J., PARK, S. H. & CHO, J. Y. 2020. The Role of Autophagy in Skin Fibroblasts, Keratinocytes, Melanocytes, and Epidermal Stem Cells. *Journal of Investigative Dermatology,* 140**,** 1691-1697.

JIANG, Y., TSOI, L. C., BILLI, A. C., WARD, N. L., HARMS, P. W., ZENG, C., MAVERAKIS, E., KAHLENBERG, J. M. & GUDJONSSON, J. E. 2020. Cytokinocytes: the diverse contribution of keratinocytes to immune responses in skin. *JCI Insight,* 5.

JIN, S., OH, Y. N., SON, Y. R., KWON, B., PARK, J.-H., GANG, M. J., KIM, B. W. & KWON, H. J. 2022. Three-Dimensional Skin Tissue Printing with Human Skin Cell Lines and Mouse Skin-Derived Epidermal and Dermal Cells. *Journal of Microbiology and Biotechnology,* 32**,** 238-247.

JOHNSON, J. L., NAJOR, N. A. & GREEN, K. J. 2014. Desmosomes: regulators of cellular signaling and adhesion in epidermal health and disease. *Cold Spring Harb Perspect Med,* 4**,** a015297.

JOOST, S., ANNUSVER, K., JACOB, T., SUN, X., DALESSANDRI, T., SIVAN, U., SEQUEIRA, I., SANDBERG, R. & KASPER, M. 2020. The Molecular Anatomy of Mouse Skin during Hair Growth and Rest. *Cell Stem Cell,* 26**,** 441-457.e7.

KALIE, E., RAZI, M. & TOOZE, S. A. 2013. ULK1 Regulates Melanin Levels in MNT-1 Cells Independently of mTORC1. *PLOS ONE,* 8**,** e75313.

KIM, H. J., PARK, J., KIM, S. K., PARK, H., KIM, J. E. & LEE, S. 2022. Autophagy: Guardian of Skin Barrier. *Biomedicines,* 10**,** 1817.

KIM, J. Y., KIM, J., AHN, Y., LEE, E. J., HWANG, S., ALMURAYSHID, A., PARK, K., CHUNG, H.-J., KIM, H. J., LEE, S.-H., LEE, M.-S. & OH, S. H. 2020. Autophagy induction can regulate skin pigmentation by causing melanosome degradation in keratinocytes and melanocytes. *Pigment Cell & Melanoma Research,* 33**,** 403-415.

KOENIG, U., ROBENEK, H., BARRESI, C., BRANDSTETTER, M., RESCH, G. P., GRÖGER, M., PAP, T. & HARTMANN, C. 2020. Cell death induced autophagy contributes to terminal differentiation of skin and skin appendages. *Autophagy,* 16**,** 932-945.

KOIKE, S., YAMASAKI, K., YAMAUCHI, T., SHIMADA-OMORI, R., TSUCHIYAMA, K., ANDO, H. & AIBA, S. 2019. TLR3 stimulation induces melanosome endo/phagocytosis through RHOA and CDC42 in human epidermal keratinocyte. *Journal of Dermatological Science,* 96**,** 168-177.

KOMATSU , M., WAGURI , S., UENO , T., IWATA , J., MURATA , S., TANIDA , I., EZAKI , J., MIZUSHIMA , N., OHSUMI , Y., UCHIYAMA , Y., KOMINAMI , E., TANAKA , K. & CHIBA , T. 2005. Impairment of starvation-induced and constitutive autophagy in Atg7-deficient mice. *Journal of Cell Biology,* 169**,** 425-434.

KOROSEC, A., FRECH, S., GESSLBAUER, B., VIERHAPPER, M., RADTKE, C., PETZELBAUER, P. & LICHTENBERGER, B. M. 2019. Lineage Identity and Location within the Dermis Determine the Function of Papillary and Reticular Fibroblasts in Human Skin. *Journal of Investigative Dermatology,* 139**,** 342-351.

KOVACS, D., CARDINALI, G., PICARDO, M. & BASTONINI, E. 2022. Shining Light on Autophagy in Skin Pigmentation and Pigmentary Disorders. *Cells,* 11**,** 2999.

KYRMIZI, I., FERREIRA, H., CARVALHO, A., FIGUEROA, J. A. L., ZARMPAS, P., CUNHA, C., AKOUMIANAKI, T., STYLIANOU, K., DEEPE, G. S., SAMONIS, G., LACERDA, J. F., CAMPOS, A., KONTOYIANNIS, D. P., MIHALOPOULOS, N., KWON-CHUNG, K. J., EL-BENNA, J., VALSECCHI, I., BEAUVAIS, A., BRAKHAGE, A. A., NEVES, N. M., LATGE, J.-P. & CHAMILOS, G. 2018. Calcium sequestration by fungal melanin inhibits calcium–calmodulin signalling to prevent LC3-associated phagocytosis. *Nature Microbiology,* 3**,** 791-803.

LANGTON, A. K., GRAHAM, H. K., MCCONNELL, J. C., SHERRATT, M. J., GRIFFITHS, C. E. M. & WATSON, R. E. B. 2017. Organization of the dermal matrix impacts the biomechanical properties of skin. *British Journal of Dermatology,* 177**,** 818-827.

LAZOVA, R., KLUMP, V. & PAWELEK, J. 2010. Autophagy in cutaneous malignant melanoma. *Journal of Cutaneous Pathology,* 37**,** 256-268.

LEE, A. Y. 2021. Skin Pigmentation Abnormalities and Their Possible Relationship with Skin Aging. *Int J Mol Sci,* 22.

LEE, S. E. & LEE, S. H. 2018. Skin Barrier and Calcium. *Ann Dermatol,* 30**,** 265-275.

LEE, H.-M., SHIN, D.-M., YUK, J.-M., SHI, G., CHOI, D.-K., LEE, S.-H., HUANG, S. M., KIM, J.-M., KIM, C. D., LEE, J.-H. & JO, E.-K. 2011. Autophagy Negatively Regulates Keratinocyte Inflammatory Responses via Scaffolding Protein p62/SQSTM1. *The Journal of Immunology,* 186**,** 1248-1258.

LEE, H. J., WOO, Y., HAHN, T. W., JUNG, Y. M. & JUNG, Y. J. 2020. Formation and Maturation of the Phagosome: A Key Mechanism in Innate Immunity against Intracellular Bacterial Infection. *Microorganisms,* 8.

LEE, S. H., JIANG, S., CHOI, E. H., FEINGOLD, K. R. & AHN, S. K. 1998. Iontophoresis Itself on Hairless Mouse Skin Induces the Loss of the Epidermal Calcium Gradient Without Skin Barrier Impairment. *Journal of Investigative Dermatology,* 111**,** 39-43.

LEI, Y. & KLIONSKY, D. J. 2022. The coordination of V-ATPase and ATG16L1 is part of a common mechanism of non-canonical autophagy. *Autophagy,* 18**,** 2267-2269.

LEIDAL, A. M. & DEBNATH, J. 2021. Emerging roles for the autophagy machinery in extracellular vesicle biogenesis and secretion. *FASEB BioAdvances,* 3**,** 377-386.

LEVIN, R., GRINSTEIN, S. & CANTON, J. 2016. The life cycle of phagosomes: formation, maturation, and resolution. *Immunological Reviews,* 273**,** 156-179.

LEVY, J. M. M., TOWERS, C. G. & THORBURN, A. 2017. Targeting autophagy in cancer. *Nature Reviews Cancer,* 17**,** 528-542.

LI, F., ADASE, C. A. & ZHANG, L. J. 2017. Isolation and Culture of Primary Mouse Keratinocytes from Neonatal and Adult Mouse Skin. *J Vis Exp*.

LI, L., CHEN, X. & GU, H. 2016. The signaling involved in autophagy machinery in keratinocytes and therapeutic approaches for skin diseases. *Oncotarget,* 7**,** 50682-50697.

LI, Q. X., ZHOU, X., HUANG, T. T., TANG, Y., LIU, B., PENG, P., SUN, L., WANG, Y. H. & YUAN, X. L. 2017. The Thr300Ala variant of ATG16L1 is associated with decreased risk of brain metastasis in patients with non-small cell lung cancer. *Autophagy,* 13**,** 1053-1063.

LI, X. M., JUNG, K. E., YIM, S. H., HONG, D. K., KIM, C. D., HONG, J. Y., LEE, H. J., LEE, S. Y., KIM, J. E. & PARK, C. W. 2020. Autophagy Suppresses Toll-Like Receptor 3-Mediated Inflammatory Reaction in Human Epidermal Keratinocytes. *Biomed Res Int,* 2020**,** 4584626.

LIAKATH-ALI, K., VANCOLLIE, V. E., HEATH, E., SMEDLEY, D. P., ESTABEL, J., SUNTER, D., DITOMMASO, T., WHITE, J. K., RAMIREZ-SOLIS, R., SMYTH, I., STEEL, K. P. & WATT, F. M. 2014. Novel skin phenotypes revealed by a genome-wide mouse reverse genetic screen. *Nature Communications,* 5**,** 3540.

LIM, J. J., GRINSTEIN, S. & ROTH, Z. 2017. Diversity and Versatility of Phagocytosis: Roles in Innate Immunity, Tissue Remodeling, and Homeostasis. *Frontiers in Cellular and Infection Microbiology,* 7.

LIN, J. Y. & FISHER, D. E. 2007. Melanocyte biology and skin pigmentation. *Nature,* 445**,** 843-850.

LIN, C. B., CHEN, N., SCARPA, R., GUAN, F., BABIARZ-MAGEE, L., LIEBEL, F., LI, W.-H., KIZOULIS, M., SHAPIRO, S. & SEIBERG, M. 2008. LIGR, a protease-activated receptor-2-derived peptide, enhances skin pigmentation without inducing inflammatory processes. *Pigment Cell & Melanoma Research,* 21**,** 172-183.

LIN, X., ZHU, L. & HE, J. 2022. Morphogenesis, Growth Cycle and Molecular Regulation of Hair Follicles. *Frontiers in Cell and Developmental Biology,* 10.

LING-JUAN, Z. 2018. Keratins in Skin Epidermal Development and Diseases. *In:* MIROSLAV, B. (ed.) *Keratin.* Rijeka: IntechOpen.

LIU, A., LONG, Y., LI, J., GU, L., KARIM, A., WANG, X. & GIBSON, A. L. F. 2021a. Accelerated complete human skin architecture restoration after wounding by nanogenerator-driven electrostimulation. *Journal of Nanobiotechnology,* 19**,** 280.

LIU, C., GU, L., DING, J., MENG, Q., LI, N., DAI, G., LI, Q. & WU, X. 2021b. Autophagy in skin barrier and immune-related skin diseases. *The Journal of Dermatology,* 48**,** 1827-1837.

LIVAK, K. J. & SCHMITTGEN, T. D. 2001. Analysis of Relative Gene Expression Data Using Real-Time Quantitative PCR and the 2−ΔΔCT Method. *Methods,* 25**,** 402-408.

LOHI, J. 2001. Laminin-5 in the progression of carcinomas. *International Journal of Cancer,* 94**,** 763-767.

LU, J., RHO, O., WILKER, E., BELTRAN, L. & DIGIOVANNI, J. 2007. Activation of Epidermal Akt by Diverse Mouse Skin Tumor Promoters. *Molecular Cancer Research,* 5**,** 1342-1352.

LYNCH, B., BANCELIN, S., BONOD-BIDAUD, C., GUEUSQUIN, J.-B., RUGGIERO, F., SCHANNE-KLEIN, M.-C. & ALLAIN, J.-M. 2017. A novel microstructural interpretation for the biomechanics of mouse skin derived from multiscale characterization. *Acta Biomaterialia,* 50**,** 302-311.

MADDALENO, A. S., CAMARGO, J., MITJANS, M. & VINARDELL, M. P. 2021. Melanogenesis and Melasma Treatment. *Cosmetics,* 8**,** 82.

MAIER, H. J., COTTAM, E. M., STEVENSON-LEGGETT, P., WILKINSON, J. A., HARTE, C. J., WILEMAN, T. & BRITTON, P. 2013. Visualizing the autophagy pathway in avian cells and its application to studying infectious bronchitis virus. *Autophagy,* 9**,** 496-509.

MALHOTRA, R., WARNE, J. P., SALAS, E., XU, A. W. & DEBNATH, J. 2015. Loss of Atg12, but not Atg5, in pro-opiomelanocortin neurons exacerbates diet-induced obesity. *Autophagy,* 11**,** 145-154.

MANSY, M., SOLIMAN, M., MUBARAK, R. & SHAMEL, M. 2020. The role of exogenous epidermal growth factor on Ki-67 proliferation marker expression in the submandibular salivary gland of albino rats receiving doxorubicin. *F1000Res,* 9**,** 1393.

MARTINEZ, J. 2020. Detection of LC3-Associated Phagocytosis (LAP). *Current Protocols in Cell Biology,* 87**,** e104.

MARTINEZ, J., ALMENDINGER, J., OBERST, A., NESS, R., DILLON, C. P., FITZGERALD, P., HENGARTNER, M. O. & GREEN, D. R. 2011. Microtubule-associated protein 1 light chain 3 alpha (LC3)-associated phagocytosis is required for the efficient clearance of dead cells. *Proceedings of the National Academy of Sciences,* 108**,** 17396-17401.

MATSUI, T. & AMAGAI, M. 2015. Dissecting the formation, structure and barrier function of the stratum corneum. *International Immunology,* 27**,** 269-280.

MENON, G. K., ELIAS, P. M., LEE, S. H. & FEINGOLD, K. R. 1992. Localization of calcium in murine epidermis following disruption and repair of the permeability barrier. *Cell and Tissue Research,* 270**,** 503-512.

MENON, G. K., LEE, S. E. & LEE, S. H. 2018. An overview of epidermal lamellar bodies: Novel roles in biological adaptations and secondary barriers. *Journal of Dermatological Science,* 92**,** 10-17.

MICHALAK-MIĆKA, K., BÜCHLER, V. L., ZAPIÓRKOWSKA-BLUMER, N., BIEDERMANN, T. & KLAR, A. S. 2022. Characterization of a melanocyte progenitor population in human interfollicular epidermis. *Cell Reports,* 38**,** 110419.

MOAZENI-ROODI, A., TABASI, F., GHAVAMI, S. & HASHEMI, M. 2019. Investigation of ATG16L1 rs2241880 polymorphism with cancer risk: A meta-analysis. *Medicina (Lithuania),* 55.

MONTELEON, C. L., AGNIHOTRI, T., DAHAL, A., LIU, M., REBECCA, V. W., BEATTY, G. L., AMARAVADI, R. K. & RIDKY, T. W. 2018. Lysosomes Support the Degradation, Signaling, and Mitochondrial Metabolism Necessary for Human Epidermal Differentiation. *Journal of Investigative Dermatology,* 138**,** 1945-1954.

MOORE, J. A., MISTRY, J. J., HELLMICH, C., HORTON, R. H., WOJTOWICZ, E. E., JIBRIL, A., JEFFERSON, M., WILEMAN, T., BERAZA, N., BOWLES, K. M. & RUSHWORTH, S. A. 2022. LC3-associated phagocytosis in bone marrow macrophages suppresses acute myeloid leukemia progression through STING activation. *The Journal of Clinical Investigation,* 132.

MOORE, J. O., PALEP, S. R., SALADL, R. N., GAO, D., WANG, Y., PHELPS, R. G., LEBWOHL, M. G. & WEI, H. 2004. Effects of Ultraviolet B Exposure on the Expression of Proliferating Cell Nuclear Antigen in Murine Skin. *Photochemistry and Photobiology,* 80**,** 587-595.

MOREIRAS, H., SEABRA, M. C. & BARRAL, D. C. 2021. Melanin Transfer in the Epidermis: The Pursuit of Skin Pigmentation Control Mechanisms. *International Journal of Molecular Sciences,* 22**,** 4466.

MOREIRAS, H., BENTO-LOPES, L., NETO, M. V., ESCREVENTE, C., CABAÇO, L. C., HALL, M. J., RAMALHO, J. S., SEABRA, M. C. & BARRAL, D. C. 2022. Melanocore uptake by keratinocytes occurs through phagocytosis and involves protease-activated receptor-2 internalization. *Traffic,* 23**,** 331-345.

MORRIS, R. J., READIO, N., BOLAND, K., JOHNSON, K., LAD, S., SINGH, A., SINGH, A., HOLTORF, S. & SKAAR, S. 2019. Isolation of Mouse Epidermal Keratinocytes and Their In Vitro Clonogenic Culture. *JoVE***,** e58701.

MÜLLER, L., HATZFELD, M. & KEIL, R. 2021. Desmosomes as Signaling Hubs in the Regulation of Cell Behavior. *Frontiers in Cell and Developmental Biology,* 9.

MUNDE, P. B., KHANDEKAR, S. P., DIVE, A. M. & SHARMA, A. 2013. Pathophysiology of merkel cell. *Journal of Oral and Maxillofacial Pathology,* 17**,** 408-412.

MÜNZ, C. 2022. Canonical and Non-Canonical Functions of the Autophagy Machinery in MHC Restricted Antigen Presentation. *Frontiers in Immunology,* 13.

MURASE, D., HACHIYA, A., TAKANO, K., HICKS, R., VISSCHER, M. O., KITAHARA, T., HASE, T., TAKEMA, Y. & YOSHIMORI, T. 2013. Autophagy Has a Significant Role in Determining Skin Color by Regulating Melanosome Degradation in Keratinocytes. *Journal of Investigative Dermatology,* 133**,** 2416-2424.

MURASE, D., KUSAKA-KIKUSHIMA, A., HACHIYA, A., FULLENKAMP, R., STEPP, A., IMAI, A., UENO, M., KAWABATA, K., TAKAHASHI, Y., HASE, T., OHUCHI, A., NAKAMURA, S. & YOSHIMORI, T. 2020. Autophagy Declines with Premature Skin Aging resulting in Dynamic Alterations in Skin Pigmentation and Epidermal Differentiation. *Int J Mol Sci,* 21.

NAGAR, R. 2017. Autophagy: A brief overview in perspective of dermatology. *Indian J Dermatol Venereol Leprol,* 83**,** 290-297.

NAKAMURA, T., YOSHITOMI, Y., SAKAI, K., PATEL, V., FUKUMOTO, S. & YAMADA, Y. 2014. Epiprofin orchestrates epidermal keratinocyte proliferation and differentiation. *Journal of Cell Science,* 127**,** 5261-5272.

NALDAIZ-GASTESI, N., GOICOECHEA, M., ALONSO-MARTÍN, S., AIASTUI, A., LÓPEZ-MAYORGA, M., GARCÍA-BELDA, P., LACALLE, J., SAN JOSÉ, C., ARAÚZO-BRAVO, M. J., TROUILH, L., ANTON-LEBERRE, V., HERRERO, D., MATHEU, A., BERNAD, A., GARCÍA-VERDUGO, J. M., CARVAJAL, J. J., RELAIX, F., LOPEZ DE MUNAIN, A., GARCÍA-PARRA, P. & IZETA, A. 2016. Identification and Characterization of the Dermal Panniculus Carnosus Muscle Stem Cells. *Stem Cell Reports,* 7**,** 411-424.

NALDAIZ-GASTESI, N., BAHRI, O. A., LÓPEZ DE MUNAIN, A., MCCULLAGH, K. J. A. & IZETA, A. 2018. The panniculus carnosus muscle: an evolutionary enigma at the intersection of distinct research fields. *J Anat,* 233**,** 275-88.

NANBA, D., TOKI, F., MATSUSHITA, N., MATSUSHITA, S., HIGASHIYAMA, S. & BARRANDON, Y. 2013. Actin filament dynamics impacts keratinocyte stem cell maintenance. *EMBO Molecular Medicine,* 5**,** 640-653.

NEAGU, M., CONSTANTIN, C., JUGULETE, G., CAUNI, V., DUBRAC, S., SZÖLLŐSI, A. G. & ZURAC, S. 2022. Langerhans Cells-Revising Their Role in Skin Pathologies. *J Pers Med,* 12.

NETO, M. V., HALL, M. J., CHARNECA, J., ESCREVENTE, C., SEABRA, M. C. & BARRAL, D. C. 2024. Photoprotective melanin is maintained within keratinocytes in a storage lysosome. *bioRxiv***,** 2024.02.05.578910.

NGUYEN, A. V. & SOULIKA, A. M. 2019. The dynamics of the skin's immune system. *International Journal of Molecular Sciences,* 20.

NISHIMURA, M., NISHIE, W., SHIRAFUJI, Y., SHINKUMA, S., NATSUGA, K., NAKAMURA, H., SAWAMURA, D., IWATSUKI, K. & SHIMIZU, H. 2015. Extracellular cleavage of collagen XVII is essential for correct cutaneous basement membrane formation. *Human Molecular Genetics,* 25**,** 328-339.

NORDLUND, J. J. 2007. The Melanocyte and the Epidermal Melanin Unit: An Expanded Concept. *Dermatologic Clinics,* 25**,** 271-281.

O'SHAUGHNESSY, R. & CHRISTIANO, A. 2004. Inherited disorders of the skin in human and mouse: From development to differentiation. *The International journal of developmental biology,* 48**,** 171-9.

OKAZAKI, K., UZUKA, M., MORIKAWA, F., TODA, K. & SEIJI, M. 1976. Transfer mechanism of melanosomes in epidermal cell culture. *J Invest Dermatol,* 67**,** 541-7.

PALMISANO, I., BAGNATO, P., PALMIGIANO, A., INNAMORATI, G., ROTONDO, G., ALTIMARE, D., VENTURI, C., SVIDERSKAYA, E. V., PICCIRILLO, R., COPPOLA, M., MARIGO, V., INCERTI, B., BALLABIO, A., SURACE, E. M., TACCHETTI, C., BENNETT, D. C. & SCHIAFFINO, M. V. 2008. The ocular albinism type 1 protein, an intracellular G protein-coupled receptor, regulates melanosome transport in pigment cells. *Human Molecular Genetics,* 17**,** 3487-3501.

PARK, S. 2022. Hair Follicle Morphogenesis During Embryogenesis, Neogenesis, and Organogenesis. *Frontiers in Cell and Developmental Biology,* 10.

PARKHOUSE, R., EBONG, I.-O., ROBINSON, C. V. & MONIE, T. P. 2013. The N-Terminal Region of the Human Autophagy Protein ATG16L1 Contains a Domain That Folds into a Helical Structure Consistent with Formation of a Coiled-Coil. *PLOS ONE,* 8**,** e76237.

PARZYCH, K. R. & KLIONSKY, D. J. 2013. An Overview of Autophagy: Morphology, Mechanism, and Regulation. *Antioxidants & Redox Signaling,* 20**,** 460-473.

PASPARAKIS, M., HAASE, I. & NESTLE, F. O. 2014. Mechanisms regulating skin immunity and inflammation. *Nature Reviews Immunology,* 14**,** 289-301.

PIIPPONEN, M., LI, D. & LANDÉN, N. X. 2020. The Immune Functions of Keratinocytes in Skin Wound Healing. *International Journal of Molecular Sciences,* 21**,** 8790.

PRABHU, V., RAO, B. S. S., RAO, A. C. K., PRASAD, K. & MAHATO, K. K. 2022. Photobiomodulation invigorating collagen deposition, proliferating cell nuclear antigen and Ki67 expression during dermal wound repair in mice. *Lasers in Medical Science,* 37**,** 171-180.

PRIGENT, L., MERCIER-GOUY, P., BOVIO, S., AUBERT, A., LIOT, S., LAMBERT, E. & VALCOURT, U. 2023. Analysis of biomechanical properties of mouse skin dermis through atomic force microscopy: Application to demonstrate a sexual dimorphism. *Experimental Dermatology,* 32**,** 1016-1027

Qu, D. 2024. Cutometer® Dual MPA 580 - Mechanical parameters of the skin. [Pamphlet]. Courage + Khazaka electronic GmbH.

RAI, S., ARASTEH, M., JEFFERSON, M., PEARSON, T., WANG, Y., ZHANG, W., BICSAK, B., DIVEKAR, D., POWELL, P. P., NAUMANN, R., BERAZA, N., CARDING, S. R., FLOREY, O., MAYER, U. & WILEMAN, T. 2019. The ATG5-binding and coiled coil domains of ATG16L1 maintain autophagy and tissue homeostasis in mice independently of the WD domain required for LC3-associated phagocytosis. *Autophagy,* 15**,** 599-612.

RAJESH, A., WISE, L. & HIBMA, M. 2019. The role of Langerhans cells in pathologies of the skin. *Immunology and Cell Biology,* 97**,** 700-713.

RAMKUMAR, A., MURTHY, D., RAJA, D. A., SINGH, A., KRISHNAN, A., KHANNA, S., VATS, A., THUKRAL, L., SHARMA, P., SIVASUBBU, S., RANI, R., NATARAJAN, V. T. & GOKHALE, R. S. 2017. Classical autophagy proteins LC3B and ATG4B facilitate melanosome movement on cytoskeletal tracks. *Autophagy,* 13**,** 1331-1347.

REICHERT, M. N., KOEWLER, N. J., HARGIS, A. M., FELGENHAUER, J. L. & IMPELLUSO, L. C. 2023. Effects of Depilatory Cream Formulation and Contact Time on Mouse Skin. *J Am Assoc Lab Anim Sci,* 62**,** 153-162.

ROMAO, S. & MÜNZ, C. 2014. LC3-associated phagocytosis. *Autophagy,* 10**,** 526-8.

ROSALES, C. & URIBE-QUEROL, E. 2017. Phagocytosis: A Fundamental Process in Immunity. *Biomed Res Int,* 2017**,** 9042851.

ROSSITER, H., KÖNIG, U., BARRESI, C., BUCHBERGER, M., GHANNADAN, M., ZHANG, C.-F., MLITZ, V., GMEINER, R., SUKSEREE, S., FÖDINGER, D., ECKHART, L. & TSCHACHLER, E. 2013. Epidermal keratinocytes form a functional skin barrier in the absence of Atg7 dependent autophagy. *Journal of Dermatological Science,* 71**,** 67-75.

ROUSSELLE, P., LAIGLE, C. & ROUSSELET, G. 2022. The basement membrane in epidermal polarity, stemness, and regeneration. *American Journal of Physiology-Cell Physiology,* 323**,** C1807-C1822.

SABINO, C. P., DEANA, A. M., YOSHIMURA, T. M., DA SILVA, D. F. T., FRANÇA, C. M., HAMBLIN, M. R. & RIBEIRO, M. S. 2016. The optical properties of mouse skin in the visible and near infrared spectral regions. *Journal of Photochemistry and Photobiology B: Biology,* 160**,** 72-78.

SALAZAR, J., CARMONA, T., ZACCONI, F. C., VENEGAS-YAZIGI, D., CABELLO-VERRUGIO, C., IL CHOI, W. & VILOS, C. 2023. The Human Dermis as a Target of Nanoparticles for Treating Skin Conditions. *Pharmaceutics,* 15**,** 10.

SALGADO, G., NG, Y. Z., KOH, L. F., GOH, C. S. M. & COMMON, J. E. 2017. Human reconstructed skin xenografts on mice to model skin physiology. *Differentiation,* 98**,** 14-24.

SAMARAWEERA, P., SHEN, B., NEWTON, J. M., BARSH, G. S. & ORLOW, S. J. 2001. The Mouse Ocular Albinism 1 Gene Product is an Endolysosomal Protein. *Experimental Eye Research,* 72**,** 319-329.

SANJUAN, M. A., DILLON, C. P., TAIT, S. W. G., MOSHIACH, S., DORSEY, F., CONNELL, S., KOMATSU, M., TANAKA, K., CLEVELAND, J. L., WITHOFF, S. & GREEN, D. R. 2007. Toll-like receptor signalling in macrophages links the autophagy pathway to phagocytosis. *Nature,* 450**,** 1253-1257.

SANTOS, M., PARAMIO, J. M., BRAVO, A., RAMIREZ, A. & JORCANO, J. L. 2002. The Expression of Keratin K10 in the Basal Layer of the Epidermis Inhibits Cell Proliferation and Prevents Skin Tumorigenesis *. *Journal of Biological Chemistry,* 277**,** 19122-19130.

SCHIAFFINO, M. V. 2010. Signaling pathways in melanosome biogenesis and pathology. *International Journal of Biochemistry and Cell Biology,* 42**,** 1094-1104.

SCHIAFFINO, M. V., BASCHIROTTO, C., PELLEGRINI, G., MONTALTI, S., TACCHETTI, C., DE LUCA, M. & BALLABIO, A. 1996. The ocular albinism type 1 gene product is a membrane glycoprotein localized to melanosomes. *Proceedings of the National Academy of Sciences,* 93**,** 9055-9060.

SCHILLE, S., CRAUWELS, P., BOHN, R., BAGOLA, K., WALTHER, P. & VAN ZANDBERGEN, G. 2018. LC3-associated phagocytosis in microbial pathogenesis. *International Journal of Medical Microbiology,* 308**,** 228-236.

SCHINDELIN, J., ARGANDA-CARRERAS, I., FRISE, E., KAYNIG, V., LONGAIR, M., PIETZSCH, T., PREIBISCH, S., RUEDEN, C., SAALFELD, S., SCHMID, B., TINEVEZ, J.-Y., WHITE, D. J., HARTENSTEIN, V., ELICEIRI, K., TOMANCAK, P. & CARDONA, A. 2012. Fiji: an open-source platform for biological-image analysis. *Nature Methods,* 9**,** 676-682.

SCHMIDT, B. & HORSLEY, V. 2012. Unravelling hair follicle–adipocyte communication. *Experimental Dermatology,* 21.

SCHMITZ, A., LAZI'Ć, E., KOUMAKI, D., KUONEN, F., VERYKIOU, S. & RÜBSAM, M. 2015. Assessing the In Vivo Epidermal Barrier in Mice: Dye Penetration Assays. *Journal of Investigative Dermatology,* 135**,** 1-4.

ŚCIEŻYŃSKA, A., NOGOWSKA, A., SIKORSKA, M., KONYS, J., KARPIŃSKA, A., KOMOROWSKI, M., OŁDAK, M. & MALEJCZYK, J. 2019. Isolation and culture of human primary keratinocytes—a methods review. *Experimental Dermatology,* 28**,** 107-112.

SCOTT, G., LEOPARDI, S., PRINTUP, S. & MADDEN, B. C. 2002. Filopodia are conduits for melanosome transfer to keratinocytes. *Journal of Cell Science,* 115**,** 1441-1451.

SCOTT, G., RODRIGUEZ-BURFORD, C., SEIBERG, M., HAN, R., BABIARZ, L., GRIZZLE, W., BELL, W., PENTLAND, A. & DENG, A. 2001. Protease-Activated Receptor 2, a Receptor Involved in Melanosome Transfer, is Upregulated in Human Skin by Ultraviolet Irradiation. *Journal of Investigative Dermatology,* 117**,** 1412-1420.

SEIBERG, M., PAINE, C., SHARLOW, E., ANDRADE-GORDON, P., COSTANZO, M., EISINGER, M. & SHAPIRO, S. S. 2000. The Protease-Activated Receptor 2 Regulates Pigmentation via Keratinocyte-Melanocyte Interactions. *Experimental Cell Research,* 254**,** 25-32.

SERRAMITO-GÓMEZ, I., BOADA-ROMERO, E., VILLAMUERA, R., FERNÁNDEZ-CABRERA, Á., CEDILLO, J. L., MARTÍN-REGALADO, Á., CARDING, S., MAYER, U., POWELL, P. P., WILEMAN, T., GARCÍA-HIGUERA, I. & PIMENTEL-MUIÑOS, F. X. 2020. Regulation of cytokine signaling through direct interaction between cytokine receptors and the ATG16L1 WD40 domain. *Nature Communications,* 11**,** 5919.

SHARLOW, E. R., PAINE, C. S., BABIARZ, L., EISINGER, M., SHAPIRO, S. & SEIBERG, M. 2000. The protease-activated receptor-2 upregulates keratinocyte phagocytosis. *Journal of Cell Science,* 113**,** 3093-3101.

SHI, Z., JI, K., YANG, S., ZHANG, J., YAO, J., DONG, C. & FAN, R. 2016. Biological characteristics of mouse skin melanocytes. *Tissue and Cell,* 48**,** 114-120.

SHIN, J.-M., KO, J.-W., CHOI, C.-W., LEE, Y., SEO, Y.-J., LEE, J.-H. & KIM, C.-D. 2020. Deficiency of Crif1 in hair follicle stem cells retards hair growth cycle in adult mice. *PLOS ONE,* 15**,** e0232206.

SHIN, S. H., LEE, Y. H., RHO, N.-K. & PARK, K. Y. 2023. Skin aging from mechanisms to interventions: focusing on dermal aging. *Frontiers in Physiology,* 14.

SIL, P., MUSE, G. & MARTINEZ, J. 2018. A ravenous defense: canonical and non-canonical autophagy in immunity. *Current Opinion in Immunology,* 50**,** 21-31.

SLOWICKA, K., SERRAMITO-GÓMEZ, I., BOADA-ROMERO, E., MARTENS, A., SZE, M., PETTA, I., VIKKULA, H. K., DE RYCKE, R., PARTHOENS, E., LIPPENS, S., SAVVIDES, S. N., WULLAERT, A., VEREECKE, L., PIMENTEL-MUIÑOS, F. X. & VAN LOO, G. 2019. Physical and functional interaction between A20 and ATG16L1-WD40 domain in the control of intestinal homeostasis. *Nat Commun,* 10**,** 1834.

SNOECK, H. W. 2020. Calcium regulation of stem cells. *EMBO reports,* 21**,** e50028.

SOLANO, F. 2014. Melanins: Skin Pigments and Much More—Types, Structural Models, Biological Functions, and Formation Routes. *New Journal of Science***,** 1-28.

SOTIROPOULOU, P. A. & BLANPAIN, C. 2012. Development and Homeostasis of the Skin Epidermis. *Cold Spring Harbor Perspectives in Biology,* 4.

SPRENKELER, E. G. G., GRESNIGT, M. S. & VAN DE VEERDONK, F. L. 2016. LC3-associated phagocytosis: a crucial mechanism for antifungal host defence against Aspergillus fumigatus. *Cellular Microbiology,* 18**,** 1208-1216.

STAPPERS, M. H. T., CLARK, A. E., AIMANIANDA, V., BIDULA, S., REID, D. M., ASAMAPHAN, P., HARDISON, S. E., DAMBUZA, I. M., VALSECCHI, I., KERSCHER, B., PLATO, A., WALLACE, C. A., YUECEL, R., HEBECKER, B., DA GLÓRIA TEIXEIRA SOUSA, M., CUNHA, C., LIU, Y., FEIZI, T., BRAKHAGE, A. A., KWON-CHUNG, K. J., GOW, N. A. R., ZANDA, M., PIRAS, M., ZANATO, C., JAEGER, M., NETEA, M. G., VAN DE VEERDONK, F. L., LACERDA, J. F., CAMPOS, A., CARVALHO, A., WILLMENT, J. A., LATGÉ, J. P. & BROWN, G. D. 2018. Recognition of DHN-melanin by a C-type lectin receptor is required for immunity to Aspergillus. *Nature,* 555**,** 382-386.

STROM, M., HUME, A. N., TARAFDER, A. K., BARKAGIANNI, E. & SEABRA, M. C. 2002. A Family of Rab27-binding Proteins: MELANOPHILIN LINKS Rab27a AND MYOSIN Va FUNCTION IN MELANOSOME TRANSPORT *. *Journal of Biological Chemistry,* 277**,** 25423-25430.

SUN, T.-T. & GREEN, H. 1976. Differentiation of the epidermal keratinocyte in cell culture: Formation of the cornified envelope. *Cell,* 9**,** 511-521.

SUN, K., DENG, W., ZHANG, S., CAI, N., JIAO, S., SONG, J. & WEI, L. 2013. Paradoxical roles of autophagy in different stages of tumorigenesis: Protector for normal or cancer cells. *Cell & bioscience,* 3**,** 35.

TARAFDER, A. K., BOLASCO, G., CORREIA, M. S., PEREIRA, F. J. C., IANNONE, L., HUME, A. N., KIRKPATRICK, N., PICARDO, M., TORRISI, M. R., RODRIGUES, I. P., RAMALHO, J. S., FUTTER, C. E., BARRAL, D. C. & SEABRA, M. C. 2014. Rab11b Mediates Melanin Transfer between Donor Melanocytes and Acceptor Keratinocytes via Coupled Exo/Endocytosis. *Journal of Investigative Dermatology,* 134**,** 1056-1066.

TASHIRO, K., SHISHIDO, M., FUJIMOTO, K., HIROTA, Y., YO, K., GOMI, T. & TANAKA, Y. 2014. Age-related disruption of autophagy in dermal fibroblasts modulates extracellular matrix components. *Biochemical and Biophysical Research Communications,* 443**,** 167-172.

TENG, Y., FAN, Y., MA, J., LU, W., LIU, N., CHEN, Y., PAN, W. & TAO, X. 2021. The PI3K/Akt Pathway: Emerging Roles in Skin Homeostasis and a Group of Non-Malignant Skin Disorders. *Cells,* 10**,** 1219.

THINGNES, J., LAVELLE, T. J., HOVIG, E. & OMHOLT, S. W. 2012. Understanding the melanocyte distribution in human epidermis: an agent-based computational model approach. *PLoS One,* 7**,** e40377.

TIAN, X., CUI, Z., LIU, S., ZHOU, J. & CUI, R. 2020. Melanosome transport and regulation in development and disease. *Pharmacology and Therapeutics*.

TU, C.-L. & BIKLE, D. D. 2013. Role of the calcium-sensing receptor in calcium regulation of epidermal differentiation and function. *Best Practice & Research Clinical Endocrinology & Metabolism,* 27**,** 415-427.

URIBE-QUEROL, E. & ROSALES, C. 2020. Phagocytosis: Our Current Understanding of a Universal Biological Process. *Frontiers in Immunology,* 11.

VACHTENHEIM, J. & BOROVANSKÝ, J. 2010. "Transcription physiology" of pigment formation in melanocytes: central role of MITF. *Experimental Dermatology,* 19**,** 617-627.

VAN DEN BERG, L. M., ZIJLSTRA-WILLEMS, E. M., RICHTERS, C. D., ULRICH, M. M. W. & GEIJTENBEEK, T. B. H. 2014. Dectin-1 activation induces proliferation and migration of human keratinocytes enhancing wound re-epithelialization. *Cellular Immunology,* 289**,** 49-54.

VAN DEN BOSSCHE, K., NAEYAERT, J.-M. & LAMBERT, J. 2006. The Quest for the Mechanism of Melanin Transfer. *Traffic,* 7**,** 769-778.

VAN DER VEEN, C., HANDJISKI, B., PAUS, R., MÜLLER-RÖVER, S., MAURER, M., EICHMÜLLER, S., LING, G., HOFMANN, U., FOITZIK, K. & MECKLENBURG, L. 1999. A Comprehensive Guide for the Recognition and Classification of Distinct Stages of Hair Follicle Morphogenesis. *Journal of Investigative Dermatology,* 113**,** 523-532.

VAN GELE, M., DYNOODT, P. & LAMBERT, J. 2009. Griscelli syndrome: a model system to study vesicular trafficking. *Pigment Cell & Melanoma Research,* 22**,** 268-282.

VAN HOVE, L., TONIOLO, A., GHIASLOO, M., LECOMTE, K., BOONE, F., CIERS, M., RAAIJMAKERS, K., VANDAMME, N., ROELS, J., MASCHALIDI, S., RAVICHANDRAN, K. S., KASPER, M., VAN LOO, G. & HOSTE, E. 2023. Autophagy critically controls skin inflammation and apoptosis-induced stem cell activation. *Autophagy,* 19**,** 2958-2971.

VIDAL, B. D. C. & MELLO, M. L. S. 2019. Toluidine blue staining for cell and tissue biology applications. *Acta Histochemica,* 121**,** 101-112.

WANG, Y (2020). Role of WD domain of ATG16L1 and LC3-associated endocytosis in control of influenza virus infection. Ph.D. thesis. University of East Anglia.

WANG, Y., MARSHALL, K. L., BABA, Y., GERLING, G. J. & LUMPKIN, E. A. 2013. Hyperelastic Material Properties of Mouse Skin under Compression. *PLOS ONE,* 8**,** e67439.

WANG, Y., RAMOS, M., JEFFERSON, M., ZHANG, W., BERAZA, N., CARDING, S., POWELL, P. P., STEWART, J. P., MAYER, U. & WILEMAN, T. 2022. Control of infection by LC3-associated phagocytosis, CASM, and detection of raised vacuolar pH by the V-ATPase-ATG16L1 axis. *Sci Adv,* 8**,** eabn3298.

WANG, Y., SHARMA, P., JEFFERSON, M., ZHANG, W., BONE, B., KIPAR, A., BITTO, D., COOMBES, J. L., PEARSON, T., MAN, A., ZHEKOVA, A., BAO, Y., TRIPP, R. A., CARDING, S. R., YAMAUCHI, Y., MAYER, U., POWELL, P. P., STEWART, J. P. & WILEMAN, T. 2021. Non-canonical autophagy functions of ATG16L1 in epithelial cells limit lethal infection by influenza A virus. *Embo j,* 40**,** e105543.

WANG, Y. & YANG, X. 2013. Identification and Analysis of Epidermal Stem Cells from Primary Mouse Keratinocytes. *In:* TURKSEN, K. (ed.) *Skin Stem Cells: Methods and Protocols.* Totowa, NJ: Humana Press.

WÄSTER, P., ERIKSSON, I., VAINIKKA, L., ROSDAHL, I. & ÖLLINGER, K. 2016. Extracellular vesicles are transferred from melanocytes to keratinocytes after UVA irradiation. *Scientific Reports,* 6**,** 27890.

WATABE, H., VALENCIA, J., LE PAPE, E., YAMAGUCHI, Y., NAKAMURA, M., ROUZAUD, F., HOASHI, T., KAWA, Y., MIZOGUCHI, M. & HEARING, V. 2008. Involvement of Dynein and Spectrin with Early Melanosome Transport and Melanosomal Protein Trafficking. *The Journal of investigative dermatology,* 128**,** 162-74.

WATT, F. M. & FUJIWARA, H. 2011. Cell-extracellular matrix interactions in normal and diseased skin. *Cold Spring Harbor Perspectives in Biology,* 3**,** 1-14.

WENG, T., WU, P., ZHANG, W., ZHENG, Y., LI, Q., JIN, R., CHEN, H., YOU, C., GUO, S., HAN, C. & WANG, X. 2020. Regeneration of skin appendages and nerves: Current status and further challenges. *Journal of Translational Medicine,* 18.

WICKETT, R. R. & VISSCHER, M. O. 2006. Structure and function of the epidermal barrier. *American Journal of Infection Control,* 34**,** S98-S110.

WIKRAMANAYAKE, T. C., STOJADINOVIC, O. & TOMIC-CANIC, M. 2014. Epidermal Differentiation in Barrier Maintenance and Wound Healing. *Adv Wound Care (New Rochelle),* 3**,** 272-280.

WONG, C. W., LEGRAND, C., KINNEAR, B., SOBOTA, R., RAMALINGAM, R., DYE, D., RAGHUNATH, M., LANE, E. & COOMBE, D. 2019. In Vitro Expansion of Keratinocytes on Human Dermal Fibroblast-Derived Matrix Retains Their Stem-Like Characteristics. *Scientific Reports,* 9.

WONG, R., GEYER, S., WENINGER, W., GUIMBERTEAU, J. C. & WONG, J. K. 2016. The dynamic anatomy and patterning of skin. *Experimental Dermatology,* 25**,** 92-98.

WONG, T., MCGRATH, J. A. & NAVSARIA, H. 2007. The role of fibroblasts in tissue engineering and regeneration. *British Journal of Dermatology,* 156**,** 1149-1155.

WONG, V. W., SORKIN, M., GLOTZBACH, J. P., LONGAKER, M. T. & GURTNER, G. C. 2011. Surgical approaches to create murine models of human wound healing. *J Biomed Biotechnol,* 2011**,** 969618.

WU, X. & HAMMER, J. A. 2014. Melanosome transfer: It is best to give and receive. *Current Opinion in Cell Biology,* 29**,** 1-7.

WU, X. S., MARTINA, J. A. & HAMMER, J. A. 2012. Melanoregulin is stably targeted to the melanosome membrane by palmitoylation. *Biochemical and Biophysical Research Communications,* 426**,** 209-214.

XU, R., JI, Z., XU, C. & ZHU, J. 2018. The clinical value of using chloroquine or hydroxychloroquine as autophagy inhibitors in the treatment of cancers: A systematic review and meta-analysis. *Medicine,* 97.

YAMAMOTO, O. & BHAWAN, J. 1994. Three Modes of Melanosome Transfers in Caucasian Facial Skin: Hypothesis Based on an Ultrastructural Study. *Pigment Cell Research,* 7**,** 158-169.

YANG, R., ZHENG, Y., LI, L., LIU, S., BURROWS, M., WEI, Z., NACE, A., HERLYN, M., CUI, R., GUO, W., COTSARELIS, G. & XU, X. 2014. Direct conversion of mouse and human fibroblasts to functional melanocytes by defined factors. *Nature Communications,* 5**,** 5807.

YANG, Y., JANG, G.-B., YANG, X., WANG, Q., HE, S., LI, S., QUACH, C., ZHAO, S., LI, F., YUAN, Z., LEE, H.-R., ZHONG, H. & LIANG, C. 2018. Central role of autophagic UVRAG in melanogenesis and the suntan response. *Proceedings of the National Academy of Sciences,* 115**,** E7728-E7737.

YOSHIHARA, N., UENO, T., TAKAGI, A., TREJO, J. A. O., HARUNA, K., SUGA, Y., KOMATSU, M., TANAKA, K. & IKEDA, S. 2015. The significant role of autophagy in the granular layer in normal skin differentiation and hair growth. *Archives of Dermatological Research,* 307**,** 159-169.

YUAN, J., ZHANG, Q., CHEN, S., YAN, M. & YUE, L. 2022. LC3-Associated Phagocytosis in Bacterial Infection. *Pathogens,* 11.

ZHANG, C.-F., GRUBER, F., NI, C., MILDNER, M., KOENIG, U., KARNER, S., BARRESI, C., ROSSITER, H., NARZT, M.-S., NAGELREITER, I. M., LARUE, L., TOBIN, D. J., ECKHART, L. & TSCHACHLER, E. 2015. Suppression of Autophagy Dysregulates the Antioxidant Response and Causes Premature Senescence of Melanocytes. *Journal of Investigative Dermatology,* 135**,** 1348-1357.

ZHANG, J., XIANG, X., SHU, S., ZHANG, C., LIANG, Y., JIANG, T., ZHANG, W., GUO, T., LIANG, X. & TANG, X. 2018. Advanced oxidation protein products inhibit the autophagy of renal tubular epithelial cells. *Exp Ther Med,* 15**,** 3908-3916.

ZHANG, L.-J. 2019. Isolation, Culture, and Characterization of Primary Mouse Epidermal Keratinocytes. *In:* BERTONCELLO, I. (ed.) *Mouse Cell Culture: Methods and Protocols.* New York, NY: Springer New York.

ZHAO, G., HAN, X., ZHENG, S., LI, Z., SHA, Y., NI, J., SUN, Z., QIAO, S. & SONG, Z. 2016. Curcumin induces autophagy, inhibits proliferation and invasion by downregulating AKT/mTOR signaling pathway in human melanoma cells. *Oncol Rep,* 35**,** 1065-1074.

ZHU, W., ZHAO, Z. & CHENG, B. 2020. The role of autophagy in skin pigmentation. *European Journal of Dermatology,* 30**,** 655-662.

ZINGKOU, E., PAMPALAKIS, G. & SOTIROPOULOU, G. 2022. Keratinocyte differentiation and proteolytic pathways in skin (patho) physiology. *The International Journal of Developmental Biology,* 66**,** 269-275.

ZOICO, E., FRANCESCHETTI, G., CHIRUMBOLO, S., ROSSI, A. P., MAZZALI, G., RIZZATTI, V., BUDUI, S. & ZAMBONI, M. 2014. Phenotypic Shift of Adipocytes by Cholecalciferol and 1α,25 Dihydroxycholecalciferol in Relation to Inflammatory Status and Calcium Content. *Endocrinology,* 155**,** 4178-4188.

ZOMER, H. D. & TRENTIN, A. G. 2018. Skin wound healing in humans and mice: Challenges in translational research. *Journal of Dermatological Science,* 90**,** 3-12.